HYDRODEOXYGENATION OF BIO-OIL MODEL COMPOUNDS IN SOLVENTS AND OVER CARBON-BASED CATALYST USING DENSITY FUNCTIONAL THEORY

A Thesis

submitted in partial fulfilment of the

requirements for the degree

of

DOCTOR OF PHILOSOPHY

by

Kushagra Agrawal

(Roll No.: 166107102)

DEPARTMENT OF CHEMICAL ENGINEERING

INDIAN INSTITUTE OF TECHNOLOGY GUWAHATI

GUWAHATI, ASSAM – 781039, INDIA

March 2021

Department of Chemical Engineering

Indian Institute of Technology Guwahati

Guwahati, Assam,

India

STATEMENT

I hereby declare that the content embodied in this thesis titled "**Hydrodeoxygenation of Bio-Oil Model Compounds in Solvents and Over Carbon-Based Catalyst Using Density Functional Theory**" is the result of investigations and experiments carried out by me at 210L Non-Newtonian flow laboratory, Department of Chemical Engineering, Indian Institute of Technology Guwahati, India under the guidance of Prof. Nanda Kishore. In keeping with the general practice of reporting scientific observations, due acknowledgements have been made wherever the work described is based on the findings of other investigators.

March 2021 Kushagra Agrawal

Department of Chemical Engineering
Indian Institute of Technology Guwahati
Guwahati, Assam,
India

CERTIFICATE

It is certified that the work contained in this thesis titled "**Hydrodeoxygenation of Bio-Oil Model Compounds in Solvents and Over Carbon-based Catalyst Using Density Functional Theory**" done by **Mr. Kushagra Agrawal** (Roll No 166107102) has been carried out under my supervision, and this work has not been submitted elsewhere for a degree.

March 2021

Dr. Nanda Kishore
Professor
Department of Chemical Engineering
Indian Institute of Technology Guwahati
Guwahati, Assam
India - 781039

ACKNOWLEDGEMENTS

This thesis and my PhD is a realization of the support and encouragement of so many people that I don't think it is possible to thank everyone in the limited few pages here. But let me attempt to recognize and thank some of them who has had a lasting impact on me, and those who stood by me during this journey.

First and foremost, I am thankful to my parents for letting me choose my own career path, and being so supportive of my decision to pursue a PhD. I wouldn't be where I am today, if not for their encouragement and support. Next, I want to thank Prof. Santosh K. Gupta who believed in me and encouraged me to pursue a career in research. His constant mentorship and counselling during my masters helped me choose a career which I thoroughly enjoy. If not for him, I would be doing a mundane 9 to 5 job somewhere. Thank you sir.

I can't thank Prof. Nanda Kishore enough for all the faith he put in me as my supervisor. His strict but supportive attitude truly shaped me as a researcher, and as a professional. His guidance allowed me to decide my own free path, but also ensured that I was not going astray. He constantly pushed me to excel, a trait which has almost become a habit in me now. Whether for trying out new ideas, or for applying for overseas scholarships, you never said no to me for anything sir. Thank you for always being my support.

There is one person who has had a profound effect on my outlook about life and leadership during my PhD, and this acknowledgment wouldn't be complete without thanking him. Dr Andrew Logsdail, I want to thank you for the fantastic support and mentorship you provided me with in the time that we worked together. Your support and motivation, in and outside the lab, provided me with exactly the kind of experience I was hoping for, and more. Thank you for hosting me at Cardiff University.

I am also highly indebted to Dr Anand Mohan Verma who taught me all the basic skills of my research, and helped me build a strong profile early in my career. I would be lost in the world of computational catalysis if not for him. Thank you Dr Anand for always looking out for me.

We all know that PhD is a long journey, and has its share of highs and lows. I am blessed to have friends like Shivani, Jena, Bhaskar and Nihal who shared my happiness as their own, and cheered me during the difficult times. It's because of them that I never realised how fast the time flew by. My PhD wouldn't be half as exciting if not for you guys. Thank you.

When it comes to the lab, I don't think I could have asked for a friendlier and more easy going peers. Thank you Abhipshit, Ogene, Harshal, Gaffer, Sneha, Pritam, Owain and Igor. You guys were absolutely brilliant. You guys gave me the feeling that we are all in this together, and we will get by.

Nilesh, Rahul, Vineet, Jinesh, Sutapa, Surabhi, Bharath, Anusuya, the A-15X lobby, Prateek, Mohit, Smruti bhaiya, Shekhar, Becca, Jordan, Niamh, Shannon thank you so much guys. I am sure there are more people I am missing out. Please know that I am thankful to each one of you for making my PhD journey so joyful.

At last, I want to thank all the staff from the department of chemical engineering, and from the institute administration who provided assistance for all the official paperwork. A special mention for Gourish sir and Ms George Summers for always helping me out with academic formalities.

Kushagra Agrawal

Contents

List of Figures:

List of Tables:

Abstract:

In the quest for a viable renewable source of energy, biomass energy has emerged as a strong contender primarily because of the abundance of flora on the planet, a resource which is renewable in nature. However, bio-oil obtained from the thermal treatment of biomass contains oxygen carrying compounds like guaiacol, phenol, and ferulic acid; and these oxy-compounds need to be reduced before being suitable as fuel. The reduction of the oxy-compounds can be achieved through a process called hydrodeoxygenation (HDO), Unfortunately, the conditions required for HDO are economically prohibitive for scale-up, and so, catalysts and solvents are actively being sought to facilitate the reaction at milder conditions. The presence of solvent facilitates better heat and mass transfer resulting in better reaction kinetics. Introduction of solvents like water is also shown to promote hydrolysis of guaiacol to catechol and methanol which led to reduction in char and increase in single ringed aromatics. Several different classes of metals have also been tested as catalysts for the HDO process. While most of the transition give low yield and high rates of char formation, the noble metals Ru, Pt and Pd have shown good performance; however, their low earth abundance and subsequent high cost makes catalyst price a limiting factor for application towards HDO.

In this dissertation, the hydrodeoxygenation of bio-oil model compounds like xylose, dibenzofuran, guaiacol and formic acid is studied in the solvent environment, as well as over carbon-based catalyst using the density functional theory. First, the upgrading of xylose is studied using B3LYP and M06-2X functional to establish a comparison between the two functionals for thermochemistry calculations. For incorporating the solvation effect, an implicit solvation model – SMD, was used. Next, the upgrading of dibenzofuran is studied in the gas phase, in water solvent and in methanol solvent. The reaction scheme converting dibenzofuran to benzene and cyclohexane was proposed and the thermochemistry was calculated for the proposed mechanism. Further, the upgrading of guaiacol is also studies in an implicit water

solvent environment to produce benzene, toluene and *o*-cresol via important intermediates like phenol and anisole. The subsequent chapter highlights the adsorption characteristics of guaiacol and phenol over nitrogen doped graphene. Non-defective and defective graphene sheets were considered for this study, and the adsorption is conducted for different orientations and arrangements of the adsorbate. Finally, the kinetics and thermochemistry of the upgrading of formic acid and guaiacol is studied over β-Mo_2C (100) surface to gain insight into the HDO mechanism of carboxylic group and phenols present in the crude bio-oil.

It is found that both B3LYP and M06-2X are equally good/bad in predicting the thermochemistry of the system of interest. Xylose hydrodeoxygenation showed that saturation of furan ring is most favourable reaction in the entire reaction scheme, and the presence of solvent improved the thermochemistry when compared to the gas phase. Dibenzofuran also showed similar trends where the presence of water solvent was found to be most suitable medium over methanol and gas phase, and the conversion to cyclohexane was preferred. The saturation of oxygenated intermediates was more favourable over non-oxygenated intermediates. The guaiacol upgrading showed formation of benzene to be thermochemically most favourable upgraded product, and solvent environment to be equal or better than gas phase. In the adsorption of phenol and guaiacol over nitrogen doped graphene, it was observed that the presence of nitrogen increased the adsorption energy, when compared to pristine graphene by more than double. However, the adsorption was still not strong enough to facilitate hydrodeoxygenation on the surface. Upgrading studies of HCOOH and guaiacol over molybdenum carbide show that the surface is susceptible to poisoning by carbon containing species like CO and CH_2 due to high carburization potential. The surface is also found to be selective towards the dehydrogenation over dehydration reactions. Lower temperatures are favourable for high yield, but the conversion is faster at higher temperatures.

INTRODUCTION

1.1 Background

The energy demand of the world has risen at very rapid pace in last two decades. The rise in the world population and the emergence of technology in our day to day lives has contributed to this demand [11]. According to the international energy agency, the world energy demand increased by 2.1% in 2017 and is rising at an exponential rate [12]. The trend has been no different in India. As per the Indian energy statistics 2018 released by the government of India, the country consumed about 1 million GWh of electricity in 2016-17 [13]. And this consumption is rising at a rate of 7.82% per year. With such high rate of energy consumption, the known national reserves of conventional sources of energy like coal and petroleum are projected to run out in next 40 years.

The conventional sources of energy are also not very eco-friendly. Coal, petroleum and natural gas emit harmful greenhouse gases like carbon dioxide and carbon monoxide on combustion into the atmosphere. They are also responsible for the emission of other pollutants like NOx and SOx in the environment which, among other hazards, cause acid rain and damage crops and deplete ground water table [14].

Thus the world is looking at alternative resources to sustain its energy demand. The search is on for a resource which is abundant, easily obtainable and non-polluting in nature. Several different alternatives have emerged in this quest for clean energy. Few of them like wind energy, solar energy, tidal energy, hydro power energy and biomass energy have emerged as the promising source [15]. These resources are abundant and freely available and do not cause any harm to the environment. But among all these, biomass energy has been of particular interest to researchers and industry. Biomass energy provides sustainable carbon fuel which is compatible with the current energy infrastructure of the world. The transportation fuel obtained

from biomass can be used in the current power systems without any modifications [16]. Biomass energy is also non-polluting since the net carbon release to the environment is zero [17]. The sources of biomass are also abundant such as agricultural residue, municipal wastes, forest timber, etc. These factors make it a strong contender as a replacement of conventional sources. However, if biomass is such a good alternative, it bodes an important question - why has the world not shifted to this energy source yet?

Biomass energy is tapped in the form of bio-oil and syngas which are obtained through treatment of biomass *via* different methods like thermochemical conversion method, biochemical conversion method and others [18]. The obtained bio-fuel contain over 400 compounds; from linear alkanes to highly complex aromatics [19]. These compounds contain oxy-functionals like aldehyde, carboxylic, hydroxyl groups which degrades the quality of the fuel. The oxy rich bio-oil has low pour point, poor viscosity, low calorific value, low pH and low energy density [20]. Thus the obtained bio-fuel has to be upgraded by different methods like zeolite upgrading, emulsification with diesel, Hydrodeoxygenation, etc. before being used as a transport fuel [21]. The thermochemical treatment of biomass and its subsequent upgrading is a complex phenomenon and several reactions occur simultaneously during the process. In order to have a better control on the product distribution and to obtain higher yield, it is desirable to know the exact mechanism of the reactions and the kinetic parameters influencing the output. Catalysts and solvents are being employed to make the upgrading process more economical, but without the knowledge of true mechanism and kinetics of the upgrading process, it is very difficult to design an appropriate catalyst and choose the best solvent.

Determination of kinetic parameters of a reaction is a two pronged approach in the modern science. While the conventional way is to determine the kinetics by fitting experimental data into the mathematical models, the emergence of higher computational power has given rise to superior computational tools which can predict the thermochemistry of the

system accurately by studying the system at quantum level. The study at the micro level can be used to describe the macro level thermochemical properties with the help of statistical thermodynamics. These computational tools can be classified broadly into two types based on the approach they take to determine the properties. These are - molecular mechanics and quantum mechanics [22]. The molecular mechanics approach uses the laws of classical physics to determine observable properties of the system. A set of equations are used to determine the potential energy of molecules with respect to its constituent atoms, which are then parameterized against experimental data to obtain force fields. The force fields are then used on the system of interest to determine the unknown observable properties. Molecular mechanics do not consider electrons individually and hence they cannot accurately describe chemical process such as bond breaking and bond formations where the electronic effects play major role [23]. On the other hand, in quantum mechanics, the solution of Schrödinger's equation ($\hat{H}\Psi=E\Psi$) can provide a better approximation for the energy of the system. It can potentially predict the bond breaking and formation energies accurately. But unfortunately, the true form of wavefunction (Ψ) is unknown. Hence approximations are made and the equation is solved iteratively to obtain desirably accurate results.

In this study, the kinetics of hydrodeoxygenation of bio-oil compounds along with the thermochemical parameters of the reaction is determined using quantum mechanics under the density functional framework with suitable solvents and catalysts.

It is practically impossible to determine the kinetics of bio-oil upgrading by considering bio-oil as a single entity because of the large number of compounds present in any pyrolysis/liquefaction reactant and product. Thus model compounds like guaiacol, xylose, dibenzofuran, etc. are selected based on their occurrence in feed. The molecular structure of few model compounds have been shown in Figure 1.1.1. The possible upgrading routes in gas as well as solvents are proposed and the upgrading is discussed in the subsequent sections.

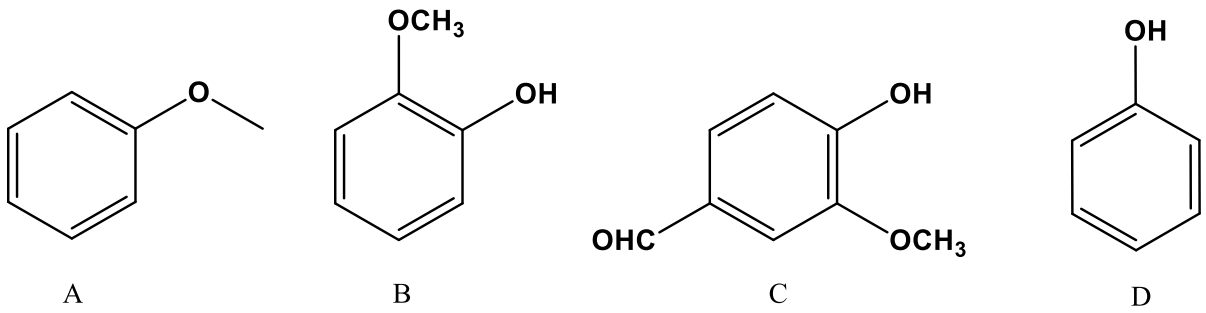

Figure 1.1.1. Schematic representation of the molecular structure of bio-oil model compounds (A) anisole (B) guaiacol (C) vanillin (D) phenol.

1.2 Bio-oil and its challenges

The plant derived biomass (trunks, barks, etc.), among other sources of biomass like municipal waste, crop residue, etc., are the major source of biomass energy. This biomass, also called the lignocellulosic biomass, contains three major components – cellulose, hemi-cellulose and lignin, of which, lignin forms about 15-30 wt% of total biomass [24]. Lignin, which forms the outer layer of plants, protects the plants by being rigid and resistant to permeation. It has a three dimensional polymeric structure made up of three different types of monomers namely *p*-coumaryl alcohol, coniferyl alcohol and sinapyl alcohol [25–27]. These polymeric hydrocarbons (lignin, cellulose and hemicellulose), when treated under suitable conditions, break down to produce biofuel in the form of liquid bio-oil and syngas.

The breakdown of lignocellulosic biomass to bio-oil can be primarily achieved by thermochemical conversion or biochemical conversion [26]. The thermochemical conversion process employs gasification, liquefaction and pyrolysis to convert biomass to biofuel whereas the biochemical conversion methods use acid/enzyme hydrolysis or fermentation to produce bio-ethanol and bio-diesel. Biochemical conversion processes are expensive and time consuming, and the products obtained are very specific from the application point of view. Thermochemical conversion methods, on the other hand, are cheaper and produce a variety of fuels like syngas and bio-oil [28] . In liquefaction, the biomass is subjected to moderate

temperature and pressure (550-600 K, 5-20 MPa) condition in the presence of a catalysts and a solvent. This causes the macromolecules present in the biomass to decompose into lighter compounds, which further re-polymerizes to form molecules of appropriate size. On the other hand, pyrolysis occurs at extreme conditions (650-800 K, 0.1-0.5 MPa) where the macromolecules directly decompose into stable hydrocarbons in the absence of air and catalyst. But the bio-oil obtained after thermochemical treatment contain high amount of oxy-compounds (50-80 wt%) which compromise the quality of the fuel by providing it high viscosity (125 mm^2/s), low pH (2-3), poor flash point (70-110 °C) and low energy density (13–18 MJ/kg wet basis) [29–31]. Also, the biofuel which contain large number of oxy-compounds, forms large deposits on exposure to air making the mixture unstable [32]. Thus the obtained bio-oil compounds are upgraded before being used as fuel. Several methods such as zeolite upgrading, emulsion treatment, hydrodeoxygenation, catalytic hydro-treatment and others are used for this purpose [29]. Of the several ways of upgrading, hydrodeoxygenation (HDO) has emerged as the leading and most promising method due to its efficiency and cost effectiveness. HDO involves the introduction of hydrogen into the oxy-compound and simultaneous removal of water molecule. HDO has been studied by researchers with different catalysts and solvents for a long time now. The review article by Furimsky [33] published in 1983 was one of the first articles to outline the catalytic HDO of fuel oil and its implications in the energy industry. Furimsky proposed that just as hydrodesulfurization (HDS) and hydrodenitrogenation (HDN) are performed over crude oil to remove sulphur and nitrogen impurities, it is possible to eliminate oxygen and upgrade the crude oil by HDO to increase the stability of the fuel. However, from the time of industrial revolution to the late 1980's, fossil fuel was the only major source of energy; a fuel with less oxygen content in it. Due to this, HDO was not given much importance by early researcher. Though the formation of oil from carbonaceous matter was already demonstrated in the works of Fischer and Schrader in 1921 [34] , it was only in

the late 1980's and early 1990's that the world acknowledged the polluting nature and the limited reserves of the fossil fuel, and the search for alternative energy lead to interest in biomass energy. Since then, a lot of work has been done on synthesis and upgrading of biofuels.

1.3 Emergence of Hydrodeoxygenation

In the early days, Furimsky [35] performed a qualitative comparison of HDS, HDN and HDO of heavy gas oil over Ni/MoO_3 and Co/MoO_3 catalyst and found that the removal of S, N and O was proportional to the bond strength of C-S, C-N and C-O in the heterocyclic compounds. He reported the breaking of C-O bond to be least energy demanding. He also reported that the formation of char had no measurable effect on the relative rates of HDS, HDN & HDO, and thereby, on the catalyst activity. When comparing the two catalysts, an insignificant promoting effect was observed between Ni and Co for HDN and HDO by Furimsky. In another work, liquefaction of wood was attempted by Elliot & Baker [36] followed by hydrogenation at 300 – 350 °C and 136 atm pressure with Ni/MoO_3 and CoS/MoO_3 catalyst. They reported 80 wt% conversion of oxygenated compounds to non-oxygenated compounds and 90% removal of oxygen from the feed mixture. In the year 2000, Furimsky published another review article on the catalytic HDO of bio-oil [37] with the perspective of kinetics of the reactions. In this article, he discussed the effect of HDO on bio-oil by considering model compounds. He reported the general reaction for HDO to be $CH_2O + H_2 \rightarrow CH_2 + H_2O$. Since then, HDO reaction and its mechanism has been extensively studied in detail. And so we now know that other than the one reaction proposed by Furimsky, there can be several more reactions occurring during the HDO, such as the dehydration reaction arising due to the polymerization of the smaller compounds [38], the decarboxylation reaction with the elimination of water molecule [39] , the hydrocracking reaction resulting in breaking of high molecular weight compounds into the lighter ones [40], saturation of unsaturation compounds by hydrogenation [41] and hydrogenolysis causing the breakage of C-O bonds [42].

1.4 Role of catalyst in hydrodeoxyegantion

1.4.1 *Transition metal catalysts - CoMo and NiMo*:

With consideration of knowledge of reactions occurring during HDO, many other studies were conducted to study the effect of catalysts. In a study conducted by Rollman [43], the formation of benzene and cyclohexane from dibenzofuran and benzofuran on sulphided CoMo catalyst at 344 K temperature and 5 MPa pressure was reported. It was also observed that unsaturated bonds of oxygen atom connected to the aromatic ring needed to undergo saturation before HDO of the compound. The effect of CoMo and NiMo catalyst supported on γ-alumina support for the removal of carbonyl, carboxylic and guaiacyl type oxygenated groups during the HDO was also studied by Laurent & Delmon [44]. They reported that while ketonic group showed 100% conversion to methylene group at 200°C, the conversions of carboxylic and guaiacyl to methyl groups and decarboxylation were possible only above 300 °C with NiMo catalyst. The adsorption of phenol over CoMo and sulphided CoMo catalysts supported over oxides of silica and alumina was studied by Popov et al. [45] where they reported that the phenol dissociates on the catalyst surface and gets chemisorbed on acid-base pair catalyst like CoMo over alumina oxide. Thus, they proposed that by decreasing the acid-base strength of the catalyst and its support, functionality of the catalyst could be enhanced. Massoth et al. [46] also carried out HDO of methyl substituted phenol over sulphided CoMo at 300°C and 2.85 MPa pressure in a microreactor. They obtained methyl substituted benzene and cyclohexanes as the end product. To determine the reaction pathway, they further conducted a computational study and reported two major possible routes of upgrading; one leading to aromatic end products and the other leading to saturated cyclohydrocarbons. The HDO of phenol and methyl heptanoate was also conducted by Ryymin et al. [47] over sulphided NiMo/γ-Al_2O_3 at 250 °C and 7.5 MPa where they reported that the hydrogenation occurred at coordination unsaturated sites for aromatic as well as aliphatic hydrocarbons. While the CoMo and NiMo catalysts provided 88-99.9%

deoxygenation, they were not ideal for upgrading as they were susceptible to high poisoning and lead to formation of coke [48]. While Co, Mo and Ni were the most favoured catalyst in the industry in general due to their cost, it was not giving very good results due to quick poisoning and char formation. This led the researchers to study the prospects of noble metals as catalyst for HDO.

1.4.2 *Noble metal catalyst – Pt, Pd, Rh and Ru:*

Sheu et al. conducted a study [49] to compare the upgrading of pine pyrolytic oil using $Pt/Al_2O_3/SiO_2$ and sulphided $CoMo/\gamma\text{-}Al_2O_3$, $Ni\text{-}W/\gamma\text{-}Al_2O_3$ and $Ni\text{-}Mo/\gamma\text{-}Al_2O_3$ at 623 K – 673 K from 750 psig to 1500 psig. The experiment was conducted in a trickle bed reactor with varying space velocity. They reported that the $Pt/Al_2O_3/SiO_2$ gave the best hydrotreated product with an activation energy of 45.5 ± 3.2 kJ/mol. They also reported that the oxygen removal from the pine oil was not dependent on the space velocity. In another study, Gutierrez et al. [50] performed the HDO of bio-oil by considering guaiacol as model compound over ZrO_2 supported noble metals. They studied Pd, Pt, Rh and Ru as a catalyst individually, as well as in combination of two noble metals. They reported that with Rh and RhPt catalyst, HDO at 100 °C yielded hydrocarbons with H/C ratio identical to gasoline (~2.0). The major products obtained were cyclohexanol, cyclohexane and 1-methyl-1,2-cyclohexandiol. Taking acetic acid as model compound, HDO of hydrocarbons was also studied by Ying et al. [51] where they report upto 30.98 % conversion with the $CoRu/\gamma\text{-}Al_2O_3$ catalyst. In a different study by Gagnon & Kaliaguine [52], the effect of hydrogen pre-treatment of vacuum pyrolysis oil along with the support of Ru catalyst was analysed. The pre-treatment was followed by HDO of the oil with NiO, Ru and $Cu_2Cr_2O_5$ catalysts supported on alumina in a batch slurry reactor. They reported the inhibition of polymerization/coking during HDO due to the pre-treatment of the feed. In the study conducted by Payormhorm et al. [53], the bio-oil obtained from the trunk of Leucaena Leucocephala was deoxygenated over Pt/Al_2O_3 catalyst. It was reported that the O/C

ratio decreased from 0.43 to 0.14 at 340 °C and 2 bar pressure. The reactions occurring during the HDO were C-C cleavage, reforming, water–gas shift and methanation to produce methane and water. The HDO of guaiacol was also studied with Pd catalyst supported over tungsten and alumina by Lee et al. [54] . It was reported that 100% guaiacol conversion was achieved at 32 wt% Pd to produce cyclohexane as major product. In a computational study conducted by Chiu et al. [55], DFT was used to determine the energetics of the conversion of guaiacol to different specialty chemicals like catechol, phenol and benzene on Ru (0001) surface. They reported the activation energy to be around 69 kJ/mol for the bond scission of the aliphatic side of guaiacol. However, scission of other bonds like oxy bonds in phenolate were reported to have as high as 189 kJ/mol of activation barrier. The full kinetic modelling done by Lu and Heyden [56] for guaiacol dissociation over Ru (0001) suggested that the dehydrogenation of H atoms from the hydroxyl group and the methoxy group are the most favourable initiation step. Another computational study conducted by Verma and Kishore [57] over Pd (111) surface of guaiacol reported the activation energy of 23.06 kcal/mol for the formation of catechol. The cleavage of CH_2 bond from the 2-methylene-oxy-phenol was determined to be the rate limiting step. The thermochemical parameters were reported to be favourable even for temperatures as low as 473 K. The formation of catechol from guaiacol over Pt (111) followed by conversion to phenol was also been reported by Vlachos et al. [58]. They reported that direct demethylation and demethoxylation of catechol to phenol was not feasible due to high energy barrier (> 4.5 eV) and should be further explored. The HDO of phenol was also been studied by Li et al. [59] over Pt (111) and Pd (111) where they reported the formation of phenoxy to be favourable only over Pd (E_a = 0.20 eV). Formation of cyclohexanol from phenol was reported to be the dominant pathway over Pt whereas cyclohexanone was reported as the major product over Pd catalyst. Though the noble metals have shown good potential as a standard catalyst for HDO of bio-oil,

the high cost of these metals due to limited availability has rendered them uneconomical for the industrial application.

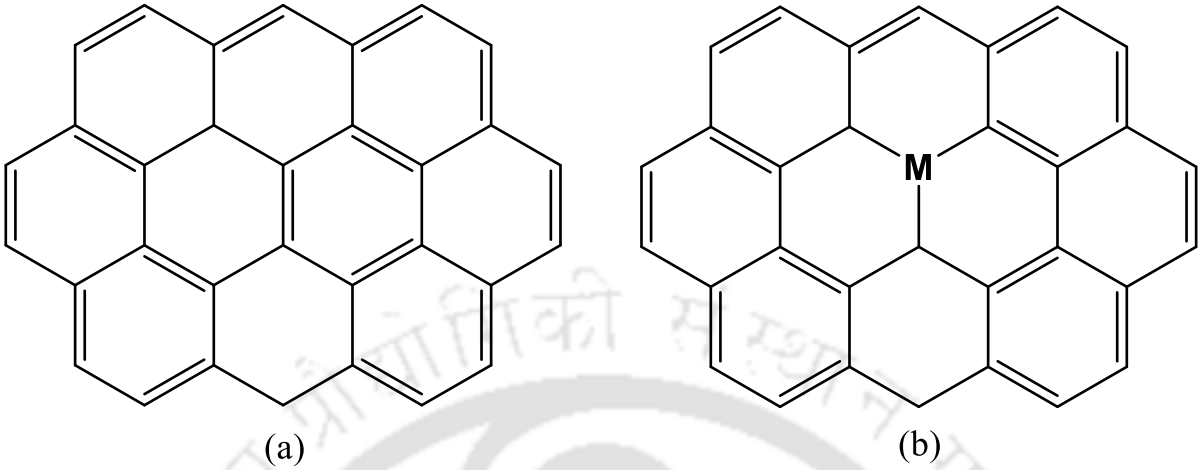

Figure 1.4.2. Schematic representation of (a) pristine graphene (b) M doped graphene where M is Pt or Pd

1.4.3 *Carbon based catalyst – Chemically Modified Graphene*

With the synthesis of carbon based catalyst, its application in the bio-fuel field has gained interest of researchers due to less char formation and high temperature resistance to deformation (up to 800 °C) [60]. Though pristine graphene has not shown good catalyst characteristics like electron density distortion, charge distortion, etc., the chemically modified graphene like Ni doped [61], noble metal doped [62,63], Al doped and Fe doped graphene have found wide application as catalyst in different fields. In a study conducted by Xu et al. [64], Ni doped graphene was used to determine the kinetics of CO oxidation between 400-800 K using DFT. They reported a high metal binding energy (-7.57 eV) for the Ni on a single defect site in graphene suggesting high stability of the chemically modified graphene (CMG). They investigated the Eley-Rideal and Langmuir-Hinshelwood mechanism for CO oxidation and reported 0.63 eV and 0.77 eV as the activation barrier, respectively. Wanno and Tabtimsai [65] also studied CO adsorption over a range of CMG including Fe, Ru, Os, Co, Rh, Ir, Ni, Pd and Pt-doped. They reported that at different orientation of CO, Fe and Os doped graphene showed

most stable configuration (E_{ads} = -10.96 kcal/mol). The metal adsorption characteristics on the graphene sheet was studied by Lopez et al. [66] where they reported the binding energy of different metal over graphene. From the bio-oil perspective, Verma and Kishore [67] studied the adsorption characteristics of different model compounds like guaiacol, vanillin, anisole and others over Pt and Pd doped graphene. Figure 1.4.2 shows the schematic representation of pristine and noble metal doped graphene. They also reported that while both the CMG are stable, the adsorption of compounds are selective and orientation dependent on Pt or Pd doping. While Pt doped graphene showed better stability with aromatic ring adsorption of salicylaldehyde, the Pd doped graphene showed better stability of adsorption of hydroxyl group. In another study conducted by Kunaseth et al. [68] , transition metal deposited over graphite was used as catalyst to study the adsorption behaviour of volatile organic compounds like benzene, furan, pyrrole, pyridine and thiophene. They reported that among Pt, Pd, Ag and Au metal deposits, the most negative binding energy for pyridine was observed with Pt (-2.11 eV). Due to the several advantages like high surface area, tuneable properties, resistance to structural deformation at high temperatures and increased electronic activity, chemically modified graphene has a lot of potential as a catalyst in bio-oil upgrading. Thus, in this study we are looking at nitrogen doped graphene which has recently been successfully synthesized by different research groups [69–74] as a catalyst towards upgrading of model bio-oil compounds into value added products.

1.4.4 *Carbon based catalyst – Carbides*

While transition metals like platinum, palladium and ruthenium are good HDO catalysts [20], their high cost due to their scarcity, hinders their industrial implementation; however, the beneficial properties of the active catalysts can be used to design new catalysts composed of earth-abundant elements. For precious metals, the positioning of their *d*-band electronic states correlates significantly with the catalytic activity [75]. The importance of the *d*-band can be

rationalised thus: as an adsorbate approaches the catalytic surface, the *s* and *d* orbitals of the metal catalyst interact with the frontier orbitals of the adsorbate, forming both bonding and anti-bonding states; the relative energy of the anti-bonding state, compared to the centre of the *d*-band, then determine the strength of the bond between the surface and the adsorbate. Therefore, the *d*-band centre correlates with reactivity [76]. Although the high Pt like reactivity of metal carbides were know for a long time [77], it is only recently that molybdenum carbide and Tungsten carbide has been identified to have similar *d*-band characteristics to that of noble metals [78]. This, together with their thermal stability, offer an exciting opportunity for application of these lower cost material in domains that have previously been limited to precious metals. The nature of the *d*-band centre in metal carbides (W and Mo), and specifically its contraction to favour catalytic applications, arises due to the increase in the interatomic bond length of the Mo/W lattice as it is carburized [79]. As a result of the *d*-band contraction, the *d*-electron states are increased at the Fermi level, akin to the density of states observed for noble metals [80].

.

LITERATURE REVIEW

2.1 Xylose

Lignocellulose biomass contains three major building blocks– cellulose, hemicellulose and lignin [24]. Hemicellulose, which is the second most abundant fraction present in the lignocellulose, forms about 25-30% of the total lignocellulose [26,81]. Xylose is one of the several compounds present in the hemicellulose fraction of the lignocellulose. It has a cyclic structure containing 5 carbon atoms with chemical formula $C_5H_{10}O_5$ and forms about 10-35% of the hemicellulose [82]. This represents a potential of xylose for conversion into value-added products by appropriate upgrading routes. In general, this upgrading is done in a two-step process. First, the xylose is converted into C4-C6 compounds with less number of oxy groups, for instance, furan, furfural, etc. Then these compounds are converted into the desired high-value products like methyl-hydrofuran, butanol, butane, etc. by further deoxygenation and bond saturation reactions. These conversion steps have been studied by several researchers, for instance, conversion of xylose to furfural by Choudhary et al. [83], conversion of xylose to furan by Zhang [84], conversion of xylose to 5-hydroxymethylfurfural by Agirrezabal-Telleria et al. [85].

In a study conducted by Pholjaroen et al. [86], xylose is converted into jet fuel grade branched alkanes over Ru based catalyst. The process involved three steps: in the first step, xylose is dehydrated to furfural in a biphasic solvent; in the second step furfural undergoes aldol condensation with methyl isobutyl ketone; and in the third step hydrodeoxygenation of aldol condensate occurs over Ru/H-ZSM-5 catalyst to yield branched C10 and C11 alkanes. A similar study has been conducted by Xing et al. [87] where C12 and C13 alkanes are synthesized in a four-step process. Xylose is first subjected to acid-catalyzed biphasic

dehydration to produce furfural which is then extracted into tetrahydrofuran phase and fed into aldol condensation. The reaction of furfural with acetone yields difurfurylideneacetone (F-Ac-F) dimer. This dimer (F-Ac-F) is then hydrogenated to produce H-FAF (2-(2-(tetrahydrofuran-2-yl)ethyl)-1,6-dioxaspiro[4.4]nonane or AHD) dimers over Ru/C catalyst. Finally, H-FAF is hydrodeoxygenated to produce target alkanes. Several other researchers [88–90] have numerically studied the conversion of cellulose derived chemicals into valuable alkanes. For instance, Liu et al. [91] and Verma & Kishore [92] have studied thermochemical aspects of conversion of furan/furfural and glucose to alkanes, respectively. Liu et al. [91] have determined the energy requirements of the conversion of furan to ethers by Diels-Alder type reaction using low molecular weight compounds. They have also studied the conversion of furfural transformation to linear alkanes. Verma and Kishore [92] have also investigated thermochemical parameters, eg., Gibbs free energy change (ΔG), enthalpy change (ΔH) and rate constant at equilibrium (K_{eq}) for the conversion of glucose to linear alkanes (C9, C12 and C15) computationally.

2.2 Dibenzofuran

Dibenzofuran has been considered as a model compound in several biomass HDO study to represent high molecular weight oxy-compounds and the effect of various catalysts has been studied for upgrading the compound. For example, Shah et al. [93] studied the effect of NiMo/γ-Al_2O_3 catalyst on the HDO of DBF at 616-649 K temperature and 6.89-13.78 MPa hydrogen pressure. They reported that the HDO proceeds via two routes: one with the direct elimination of oxygen without any ring saturation, and the other with hydrogenation of the aromatics followed by oxygen removal. The later route was found to be energetically preferrable with catalyst. The C-O bond scission was also found to be preceded by ring saturation. Similarly, Liang et al. [94] also studied the HDO of DBF with platinum loaded over modified mesoporous silica with zirconia and alumina oxide catalyst and reported

bicyclohexane as the major product. They observed close to 80% conversion of DBF with aluminium oxide added to the silica. The hydrogenation of the aromatic ring and the cleavage of saturated C-O bond was promoted with the same catalyst. Upgrading DBF and 2-methoxy phenol at 40 bar and 250 °C temperature with two different zeolites- Pt/mesoporous-Y and Pt/mesoporous-MFI was studied by Park et al. [95]. It was reported that the acidity of the catalyst was an important factor in determining product distribution during HDO. In another study by Jiménez-López et al. [96], the conversion of DBF was studied over silica-supported nickel phosphide catalysts with varying P/Ni atomic ratios. It was reported that close to 100% conversion was achieved with 7.5 wt % nickel phosphide loading. While bicyclohexane was obtained as a major product, water was reported as an undesirable side product. In a computational study [97], degradation of DBF was reported in the presence of OH radicals in atmospheric conditions using density functional theory. One of the prime findings of the study was the possible fragmentation of the aromatic ring due to the OH attack.

However, the effect of solvent has not been properly explored. In one of the studies conducted by Cai et al.[98], bimetallic nickel/platinum (Ni/Pt) catalyst was used at 200 °C and 1.2 MPa with water as a solvent. The most energetically favoured mechanism for the upgrading was found to initiate with hydrogenation of the aromatic rings, followed by the cleavage of the C–O ether bond. Finally, the cyclohexanol was deoxygenated to produce cyclohexylbenzene. But no further experimental or computational study has been conducted explicitly to study solvent behaviour in upgrading heavy bio-oil compounds.

2.3 Guaiacol

Guaiacol is one of the important components of pyrolytic bio-oil which comprise of two oxy-functional groups in it- the hydroxyl group and the methoxy group. This makes it a suitable representative compound to study deoxygenation for the production of several platform

chemicals. Thus, extensive study has been conducted towards guaiacol deoxygenation; both experimentally and computationally [2, 10-26]. Some of them are detailed below.

Experimentally, a number of researchers report the formation of anisole, catechol, phenol and cyclohexane as major products [10-17] of hydrodeoxygenation (HDO) of guaiacol. In a study conducted by Zhou et al. [99], guaiacol is converted to cyclohexane, cyclohexanol and cyclohexanone over NiCo/CNT catalyst. They report a conversion rate of 93% with cyclohexanol as major product. Bykova et al. also report the formation of cyclic products like cyclohexanol and cyclohexane from guaiacol in the presence of Ni [100] and Ni–Cu/SiO_2–ZrO_2–La_2O_3 [101], while phenol and catechol are reported as intermediates. Further, Bykova et al. [101] report the formation of 1-methylcyclohexane-1,2-diol as major product at relatively low temperature (280 °C) along with cyclohexane and cyclohexanone; and show that with increase in temperature to 360 °C, guaiacol conversion decreases from 96.8% to 50%. In a two stage study by Van et al. [102,103], HDO of guaiacol over Co-Mo and sulphided Co-Mo catalyst is shown to yield benzene as major product with catechol and phenol as major intermediates. HDO of guaiacol over bimetallic catalyst PtPd supported over mesoporous aluminosilicate with methanol as solvent was studied by Roldugina et al. [104] and they report the formation of anisole with 17% selectivity at 200 °C. With the increase in temperature, selectivity of phenol increases till 350 °C and selectivity of catechol reach 42% at 300 °C. Wahyudiono et al. studied the effect of water as solvent and they report catechol as major derivative among other products [105]. In a study by Ma et al. [106], the effect of alcohol as solvent is studied to upgrade guaiacol using activated carbon supported α-molybdenum carbide catalyst (MoC_{1-x}/AC). Their study report high selectivity (85%) towards the formation of mono-oxygenated phenols such as o-cresol and others with catechol as intermediate.

Similarly, the kinetics of guaiacol deoxygenation was also studied using computational tools. Lu et al. [56,107] studied the reaction kinetics of guaiacol over Pt catalyst and reported

phenol and catechol to be the major products in gaseous phases. Similarly, Chiu et al. [55] used Ru catalyst to study gaseous phase guaiacol HDO and reported similar product formation. Gao et al. [108] conducted an experimental as well as a computational HDO study and they report the formation of cyclopentanone as major end product in gas phase. Lee et al. [58] and Verma and Kishore [57] show catechol as major product in studies conducted over Pt catalyst and Pd catalyst respectively.

It is evident that presence of solvent during the catalytic HDO of guaiacol affects the reaction mechanism. However, the role of solvent in non-catalytic system, and the kinetics of solvated reactions have not been studied in detail. In fact, literatures report solution phase reactions as beneficial in terms of high selectivity, high yield and low temperature required systems compared to their gas phase counterparts. In the gas phase, the free radical mechanism dominates the reaction progress whereas ionic hydrolysis pathways are favoured in the aqueous medium [109]. This pathway may lead to formation of acidic entities which can catalyse the reaction homogeneously. In a study conducted by Zhou et al. [110], demethoxylation of guaiacol is reported as the route to phenol formation in aqueous medium over NiCo/γ-Al_2O_3 catalyst giving 96.1 % conversion. In another experimental study conducted by a Lawson and Klein [111], catechol is reported as major product in gas phase pyrolysis along with phenol and methanol. Introduction of water solvent is shown to promote hydrolysis of guaiacol to catechol and methanol which led to reduction in char and increase in single ringed aromatics.

2.4 Nitrogen doped graphene

Recently, due to the successful synthesis of N doped graphene by various methods like arc discharge [69,70], chemical vapour deposition [71], segregation growth approach [72] and others [73,74], N doped graphene has found applications in different fields like fuel cell, field effect transistor, Li-ion batteries and ultracapacitors [112]. Zhufeng et al. conducted a study to

determine the stability and formation of N doped graphene[113]. They reported that the doping of N on a graphene with defects leads to lower formation energy of the graphene, suggesting higher stability. They also reported that in a monovacancy defect, pyridinlike defect is more stable whereas in multivacancy defects, pyrrholiclike defects show better stability. Figure 2.4.1 shows various types of defects and the corresponding N doped graphene. In a study conducted by Siburian et al. [114], N doped graphene has been used as support for Pt catalyst for half-cell cathode reaction in hydrogen fuel cell towards oxygen reduction reaction (ORR) and have reported that N doped graphene can potentially replace Pt. In another study, Fiorentin et al. [2] studied the adsorption of CO_2 over different N doped graphene sheets like graphiticlike, pyridiniclike and pyrroliclike defect, computationally. They reported high stability of the N doped graphene and thermodynamically feasible adsorption of CO_2 on pyrroliclike defect. However, they studied CO_2 adsorption only at N doped sites and proposed the possibility of better adsorption at neighbouring sites for pyridiniclike and graphiticlike defects. In order to understand the effect of N doping on neighbouring atoms, Zhang and Xia [115] studied the active sites of the N doped graphene with the help of atomic charge density and atomic

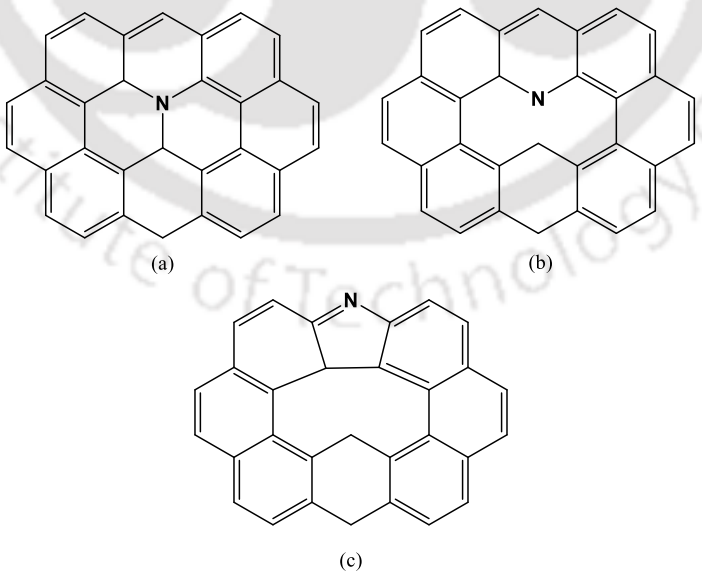

Figure 2.4.1: Schematic representation of (a)quaternary (b)pyridinelike (c)pyrrholiclike N-doped graphene

spin density. They reported that the neighbouring atoms of the defect site had significant potential to act as an adsorption site due to large positive atomic charge/spin density. A study conducted by Gao et. al [116] concurred with this finding where they tried to determine the role of N doped graphene as catalyst for C-H bond activation. They reported that the N doped site itself, when compared with pristine graphene, did not enhance the rate of reaction. However, it influenced the *ortho* carbons in the graphitic doping, which acted as a strong activator for C-H oxidation reaction. They achieved 98.6% conversion of ethyl benzene with acetophenone yield of 91.3% using N doped graphene as catalyst at 373 K, which was better than some transition metals and metal complex catalysts. They also reported that increasing the doping did not have any effect on the C-H oxidation reaction kinetics. Lai et al. [117] have also reported that the electrocatalytic activity of the N doped graphene was highly dependent on the graphitic N content of the graphene sheet. The synthesis of N doped graphene has recently been possible due to different novel synthesis techniques. Thus, its potential as catalyst in bio-oil upgrading is yet to be explored.

2.5 Molybdenum Carbide

Mo_2C has been applied as a catalyst in the HDO process in several experimental investigations. Mai *et al.* [118] studied the conversion of levulinic acid to γ-valerolactone catalysed by carbon nanotube (CNT) supported molybdenum carbide, identifying that the CNT support is crucial to prevent catalyst deactivation; at operating conditions of 30 bar H_2 and 200 °C, the conversion and selectivity with this system is >90%, which is similar to the performance of noble metals. Han *et al.* [119] upgraded a range of different vegetable oils (soybean oil, rapeseed oil, maize oil, sunflower oil) to transport-grade fuel over a molybdenum carbide catalyst, reporting an ability to recycle the catalyst 16 times for the upgrading process with no leaching observed; however, the product distribution with the Mo_2C catalyst differed from when using a palladium

catalyst, due to different acyl-to-alkyl rearrangement on the surfaces. McManus and Vohs [120] investigated the deoxygenation of glycoldehyde and furfural with a Mo_2C catalyst on a Mo (100) support. The catalyst was prepared as per the method described by Farkas and Solymosi [121] by which an orthorhombic structure of the molybdenum carbide is obtained with a molybdenum like facet. They observed an initial interaction with the surface through the aldehyde groups, and also noticed the weakening of the carbonyl C-O bond at temperatures of 200-300 K, which facilitates its dissociation. Bhan *et al.* also extensively studied the appropriateness of molybdenum carbide towards the HDO of hydrocarbons [122–126]. For the HDO of acetone over acidified molybdenum carbide [126], sequential hydrogenation led to formation of isopropyl alcohol, which was then followed by dehydration to form propylene and finally propane. For a similar investigation of the HDO of anisole in gas phase over the Mo_2C catalyst surface [125], desirable high selectivity and efficiency was observed towards the cleavage of C-O bond, and high stability of the catalyst, at conditions of 420-520 K and 1 atm of pressure.

To understand the fundamental aspects of the reaction mechanism, computational studies provide important insights. Shi *et al.* [127] investigated, using density functional theory (DFT), the Mo_2C (101) surface for catalytic conversion of butyric acid to butane, considering the reaction as representative of conversions of fatty acids to long-chain alkanes. The highest energy barrier in the reaction profile is observed for the dissociation of butanol. In complementary calculations, they also showed that the Mo_2C (001) surface was able to adsorb water, OH, and O, more strongly than the (101) surface. Shi *et al.* [128] also investigated the conversion of furfural to 2-methylfuran on the Mo_2C (101) surface, comparing bare surfaces with those pre-saturated with H atoms. At the elevated hydrogen coverage, the selectivity of the products could be tuned: at “high” H_2 pressure, the formation of 2-methylfuran was promoted whereas the furan formation was suppressed. Luo *et al*. [129] studied the formic acid

decomposition over β-Mo_2C (101) surface using DFT and report the cleavage of HCO-OH to be thermochemically most favourable route for formic acid decomposition.

OBJECTIVE

It is quite evident from the literature survey that the potential of biomass as an alternative fuel is very high. A lot of work has already been done to improve the quality of the fuel by both – experimental and computational approaches. However, the synthesis and upgrading studies have still not solved the problems associated with the commercialization of the process. This is because a good catalyst which is cheap, recyclable and resistant to poisoning has not been found for the biomass application yet. Most of the research is focussed on transition and noble metal catalysts like nickel, platinum, ruthenium, etc. which either provide low yield and selectivity, or are prohibitively expensive. Carbon based catalyst like CMG and carbides, on the other hand, could potentially provide high yield at a cheaper price, due to them having superior properties than pure transition metals.

The use of solvent in the liquefaction has also been very limited and not found much importance in the research and industrial community in the biomass context. With the development of universal solvation model methods like SMD and CPCM, the effect of solvent on the kinetics of HDO can be now calculated with more reliability than before. Also, the modern catalyst synthesis methods and tools are opening up new possibilities for better and commercially viable carbon-based catalyst. Thus, this study highlights the kinetics and thermochemical parameters of HDO of bio-oil model compounds in the presence of solvents and over carbon-based catalyst using the density functional theory framework.

Aim:

To study the thermochemical and kinetic parameters of upgrading of bio-oil model compounds in the presence of solvents, and over carbon-based catalyst using the density functional theory.

Objectives:

1. To study the effect of solvent on the hydrodeoxygenation of bio-oil model compounds.

   1.1 To decide on the simulation parameters by standardizing the functionals to be used for system of interest.

   Article(s) published:

   (i) DFT Investigation on Thermochemical Analyses of Conversion of Xylose to Linear Alkanes in Aqueous Phase

   1.2 To study the effect of solvents on the HDO of bio-oil model compounds

   Article(s) published:

   (i) DFT Study on Dibenzofuran Conversion to Cyclohexane and Benzene in Gas, Water and Methanol Solvents

   (ii) Thermochemical Conversion of Guaiacol in Aqueous Phase by Density Functional Theory

2. To study the performance of carbon-based catalyst on the hydrodeoxygenation of bio-oil model compounds

   2.1 To study the effect of chemically modified graphene as catalyst in the bio-oil upgrading.

   Article(s) submitted for publishing:

   (i) Computational Study on Adsorption Characteristics of Phenol and Guaiacol Over Single and Multiple Nitrogen Doped Graphene

   2.2 To study the effect of metal-carbides as catalyst in the bio-oil upgrading.

   Article(s) submitted for publishing:

   (i) Dehydrogenation and Dehydration of Formic Acid over Orthorhombic Molybdenum Carbide

   (ii) Hydrodeoxygenation of Guaiacol Over Orthorhombic Molybdenum Carbide: A DFT and Microkinetic Study

COMPUTATIONAL DETAILS

One of the early methods of solving the Schrödinger equation, called the Born-Oppenheimer (BO) approximation, considered the nuclei to be fixed in the space while electrons to be mobile [130]. This method simplified the Hamiltonian ($\hat{H}$) by neglecting any interaction arising due to the movement of nucleus, which simplified the mathematics involved with the solution. The approximation provided a remarkable way of solving Schrödinger's equation. However, finding the solution of Schrödinger's equation for large systems with many electrons was still very challenging due to the sheer number of variables (spatial coordinates and electron spin for each electron). To overcome this problem, the observable electron density was proposed to be used to determine all the necessary information for creating the $\hat{H}$ like the nucleus position, atomic number and the number of electrons. This idea of determination of system properties from the electron density was first put forth by E. Fermi and P. A. M. Dirac independently in 1920s [131]. They considered the atom to be a sphere with nucleus in the centre surrounded by a uniform electron cloud, and provided approximations for calculating the kinetic energy of the system. After improvements in calculating different interatomic potentials by Dirac in the model, it was renamed as Thomas-Fermi-Dirac model [132,133]. Though the model proved to be highly accurate in predicting energy for atoms, it failed miserably for molecules. Despite the Thomas-Fermi-Dirac's model's inability to predict the molecular properties, it introduced the idea of electron cloud approximation to the scientific community which later led to the formulation of density functional theory (DFT).

4.1 Density Functional Theory

In the subsequent years, Hohenberg and Kohn gave two theorems, called the Hohenberg-Kohn theorems, which later went on to form the basis of the density functional theory. The first

Hohenberg-Kohn theorem [131] stated that all the properties of a system in a ground electronic state can be determined by the ground state electron density function $\rho_o(\mathbf{r})$ for any point **r** in the space. In other words,

$$E_o = E[\rho_o(\mathbf{r})] \tag{4.1}$$

While the second Hohenberg-Kohn theorem stated that any electron density $\rho(\mathbf{r})$ will give energy E, equal to or greater than the true ground state energy of system. In other words

$$E[\rho(\mathbf{r})] \geq E[\rho_o(\mathbf{r})] \tag{4.2}$$

The Hohenberg-Kohn theorem related the ground state energy of the system to ground state electron density [134]. This reduced the number of variables in the solution of the Schrodinger's equation to only three spatial coordinates irrespective of the number of electrons. But the limitation of these theorems was that though the theorems described the ground state energy, they did not describe the method to determine the ground state energy. To overcome this limitation, Kohn and Sham applied the variational approach [135]. The ground state electronic energy of any system can be expressed as the sum of electron kinetic energies (T), the electron-nucleus attraction potential (V_{Ne}) and the electron-electron repulsion potential (V_{ee}). Since each of these terms are being considered as a function of electron density, they can be written as $T[\rho_o(\mathbf{r})]$, $V_{Ne}[\rho_o(\mathbf{r})]$ and $V_{ee}[\rho_o(\mathbf{r})]$, respectively. Thus, the ground state energy E_o can be written as:

$$E_o = \langle T[\rho_o(\mathbf{r})] \rangle + \langle V_{Ne}[\rho_o(\mathbf{r})] \rangle + \langle V_{ee}[\rho_o(\mathbf{r})] \rangle \tag{4.3}$$

Where the angle brackets $\langle\ \rangle$ describe the quantum-mechanical average values, commonly referred to as expectation value, of the term contained within.

Calculating the quantum-mechanical average for the nucleus-electron potential $\langle V_{Ne}[\rho_o(\mathbf{r})] \rangle$ for all the electron in the system gives

$$\langle V_{Ne}[\rho_o(\mathbf{r})] \rangle = \int \rho_o(\mathbf{r}) \nu(\mathbf{r}) d\mathbf{r} \tag{4.4}$$

Where the $\nu(\mathbf{r})$ describe the external potential due to the attraction of electrons to all the nuclei within the system.

Hence equation (4.3) becomes

$$E_o = \langle T[\rho_o(\mathbf{r})]\rangle + \int \rho_o(\mathbf{r})\,\nu(\mathbf{r})d\mathbf{r} + \langle V_{ee}[\rho_o(\mathbf{r})]\rangle \tag{4.5}$$

Kohn and Sham proposed to write the kinetic term $\langle T[\rho_o(\mathbf{r})]\rangle$ and the electron-electron potential term $\langle V_{ee}[\rho_o(\mathbf{r})]\rangle$ in terms of a fictitious reference system of non-interacting electrons.

$$\langle T[\rho_o(\mathbf{r})]\rangle = \langle T[\rho_o(\mathbf{r})]\rangle_{ref} + \Delta\,\langle T[\rho_o(\mathbf{r})]\rangle \tag{4.6}$$

and

$$\langle V_{ee}[\rho_o(\mathbf{r})]\rangle = \langle V_{ee}[\rho_o(\mathbf{r})]\rangle_{ref} + \Delta\,\langle V_{ee}[\rho_o(\mathbf{r})]\rangle = \frac{1}{2}\int\int \frac{\rho_o(\mathbf{r}_1)\rho_o(\mathbf{r}_2)}{\mathbf{r}_{12}}\,d\mathbf{r}_1 d\mathbf{r}_2 + \Delta\,\langle V_{ee}[\rho_o(\mathbf{r})]\rangle \tag{4.7}$$

Where $\langle T[\rho_o(\mathbf{r})]\rangle_{ref}$ and $\langle V_{ee}[\rho_o(\mathbf{r})]\rangle_{ref}$ is the kinetic energy and electron-electron potential energy of the non-interacting system, respectively, and $\Delta\,\langle T[\rho_o(\mathbf{r})]\rangle$ and $\Delta\,\langle V_{ee}[\rho_o(\mathbf{r})]\rangle$ are the respective deviations in the two terms due to interactions between electrons.

As the electron- electron potential can be described by the classical electrostatic repulsion correlation of electron density between any two points $\mathbf{r}_1$ and $\mathbf{r}_2$ in the space, the $\langle V_{ee}[\rho_o(\mathbf{r})]\rangle_{ref}$ can be formulated as $\frac{1}{2}\int\int \frac{\rho_o(\mathbf{r}_1)\rho_o(\mathbf{r}_2)}{\mathbf{r}_{12}}\,d\mathbf{r}_1 d\mathbf{r}_2$ where $\mathbf{r}_{12}$ is the distance between $\mathbf{r}_1$ and $\mathbf{r}_2$.

Therefore, E_o can be written as:

$$E_o = \int \rho_o(\mathbf{r})\,\nu(\mathbf{r})d\mathbf{r} + \langle T[\rho_o(\mathbf{r})]\rangle_{ref} + \frac{1}{2}\int\int \frac{\rho_o(\mathbf{r}_1)\rho_o(\mathbf{r}_2)}{\mathbf{r}_{12}}\,d\mathbf{r}_1 d\mathbf{r}_2 + E_{xc}[\rho_o(\mathbf{r})] \tag{4.8}$$

Where $E_{xc}[\rho_o(\mathbf{r})]$ is the exchange correlation energy containing the unknows:

$$E_{xc}[\rho_o(\mathbf{r})] = \Delta\langle T[\rho_o(\mathbf{r})]\rangle + \Delta\langle V_{ee}[\rho_o(\mathbf{r})]\rangle \tag{4.9}$$

When the attraction potential of all the nucleus of system A with atomic number Z_A and a small fraction of charge cloud is summed, the first term in equation (4.8) becomes

$$\int \rho_o(\mathbf{r})\,\nu(\mathbf{r})d\mathbf{r} = \int \left[\rho_o(\mathbf{r}_1)\sum - \frac{Z_A}{\mathbf{r}_{1A}}\right] d\mathbf{r}_1 = -\sum Z_A \int \frac{\rho_o(\mathbf{r}_1)}{\mathbf{r}_{1A}}\,d\mathbf{r}_1 \tag{4.10}$$

Expanding the second term in equation (4.8) in terms of Dirac notation for integrals [136], and by Slater-Condon rule [137] for a four electron system

$$\langle T[\rho_o(\mathbf{r})]\rangle_{\text{ref}} = \langle \psi_{ref} \left| \sum -\frac{1}{2} \nabla_i^2 \right| \psi_{ref} \rangle = -\frac{1}{2} \sum \langle \psi_1^{KS}(1) \left| \nabla_i^2 \right| \psi_1^{KS}(1) \rangle \qquad (4.11)$$

Where ψ_{ref} is the wavefunction of the reference system, $\psi_1^{KS}(1)$ is the first slater determinant of the Kohn-Sham orbital.

Putting equation (4.9), (4.10) and (4.11) in energy equation (4.8):

$$E_o = -\sum Z_A \int \frac{\rho_o(\mathbf{r}_1)}{\mathbf{r}_{1A}} d\mathbf{r}_1 - \frac{1}{2} \sum \langle \psi_1^{KS}(1) \left| \nabla_i^2 \right| \psi_1^{KS}(1) \rangle + \frac{1}{2} \int \int \frac{\rho_o(\mathbf{r}_1)\rho_o(\mathbf{r}_2)}{\mathbf{r}_{12}} d\mathbf{r}_1 d\mathbf{r}_2 + E_{xc}[\rho_o(\mathbf{r})] \qquad (4.12)$$

The term $E_{XC}[\rho(\mathbf{r})]$ constitutes all the unknowns and is called exchange correlation potential whose exact mathematical form is unknown [138]. Different functionals have been developed by various researchers over time to provide approximate solution for this exchange-correlation (XC) potential. The accuracy of the DFT results depends largely on the choice of the functional. Functionals which considers only electron density at each point and do not account for interactions between the particles, like the local density approximation (LDA), is computationally cheap; but they come at the expense of accuracy [134]. Thus, they are not employed in the study where more accurate (error < 10 kcal/mol) results are desired. As of now, meta-generalized gradient approximation (GGA) and hybrid meta-GGA class of functionals are a popular choice among chemists. These class of functionals considers the Kohn-Sham kinetic energy density along with the electron density and gradient of electron density [139]. They provide a good trade-off between accuracy and computational time and are suitable for specific systems. Some of the most commonly employed functionals are PBE, BEEF, B3LYP, ωB97XD, M05, M06-2X.

The electron density can be expressed as

$$\rho_o = \rho_r = \sum_{i=1}^{2n} \left| \psi_i^{KS}(1) \right|^2 \qquad (4.13)$$

Where ψ_i^{KS} is the KS spatial orbital. When the energy equation (4.12) is differentiated with respect to ψ_i^{KS} with the orthonormal condition, the KS equation is obtained which is:

$$\left[-\frac{1}{2}\nabla_i^2 - \sum_{nuclei\ A}\frac{Z_A}{r_{1,A}} + \int\frac{\rho(r_2)}{r_{12}}d\boldsymbol{r_2} + v_{XC}(1)\right]\psi_i^{KS}(1) = \varepsilon_i^{KS}\psi_i^{KS}(1) \quad (4.14)$$

Where ε_i^{KS} are the Kohn-Sham energy levels. The $v_{xc}(\mathbf{r})$ is a functional derivative of the exchange correlation energy ($E_{XC}[\rho(\mathbf{r})]$) and is expressed as

$$v_{XC}(\boldsymbol{r}) = \frac{\delta E_{XC}[\rho(\boldsymbol{r})]}{\delta\rho(\boldsymbol{r})} \quad (4.15)$$

In simple notations, the KS equation can also be written as;

$$h_i^{KS}(1)\psi_i^{KS}(1) = \varepsilon_i^{KS}\psi_i^{KS}(1) \quad (4.16)$$

Where the Kohn-Sham operator h_i^{KS} is defined by comparing equation 4.14 with 4.16

4.2 Solvation model with DFT

The Schrödinger's equation contains Hamiltonian operator whose solution provides the ground state energy of any molecule in the gas phase. However, not all reactions occur in gas phase. Sometimes the temperature conditions of reactions are not sufficient to vaporise the reactants. Also, often the reactions are purposely conducted in solvents to enhance yield and selectivity [140] of the product mixture. In such cases, solvation effect plays a major role in the kinetics of reaction. One way to include these effects in the simulation environment could be to surround a solute molecule with several solvent molecules. But whether the number of solvent molecules considered are sufficient to accurately describe the solution system, can't be said with certainty. Also, the interaction of solute molecule with the distant solvent molecules cannot be accounted in such case [22]. Thus a need to define the solvent implicitly led to the development of solvent models like polarizable continuum model (PCM) [141], Onsager model [142] and SMx [143] models. These models consider the solute molecule to be present in a cavity created by superimposing vacuum spheres of particular radii over the atoms of the molecule, which is surrounded by a dielectric medium. The medium is defined by the solvent polarity strength; and

the electrostatic interactions between the continuum and the solute are accounted during the energy calculation. The way the models define the radii of the solute cavity and the continuum strength to determine all interactions between the solute and the solvent varies for each model. For instance, the Onsager model [142] considers the van der Waals radius for the cavity and only the dielectric constant of the solvent for the continuum. In the polarized continuum (PCM) model [141,144], van der Waals radius is used for cavity radius but apart from the electrostatic interaction, the dispersion-repulsion and the cavitation energy are also accounted by defining dielectric constant, molar volume, thermal expansion coefficient, etc. The SMD model, developed by Truhler et al. [145], uses seven different descriptors for defining the medium such as dielectric constant, refractive index, Abraham's hydrogen bond acidity, Abraham's hydrogen bond basicity, etc. and defines the cavity by superposition of nuclear-centred spheres. The SMD model, a universal solvation model based on the solute electron density, has two components: a) the electrostatic component and b) a non-electrostatic component. The components can be expressed in terms of free energy as:

$$\Delta G_S^o = \Delta G_{ENP} + \Delta G_{CDS} + \Delta G_{conc}^o \quad (4.17)$$

Where ΔG_S^o is standard state free energy of solvation, ΔG_{ENP} denotes the electrostatic component of the energy of solvation which includes electronic, nuclear and polarization contributions. ΔG_{CDS} is the cavity-dispersion-solvent structure contribution to the solvation free energy. ΔG_{conc}^o is the change in the free energy due to change of concentration between gas phase standard state and liquid phase standard state.

The electrostatic component is largely based on the integral equation formalism polarizable continuum model (IEFPCM) [146] but with a new set of parameterized atomic radii. The electrostatic effect is incorporated by solving the non-homogenous Poisson's equation (NPE) which relates the solute charge density (ρ_f) to the dielectric constant (ε) with total potential ϕ as

$$\nabla \cdot (\varepsilon \nabla \phi) = -4\pi\rho_f \tag{4.18}$$

The NPE when solved for the solute (in terms of quantum descriptors) provides electric potential called reaction field (φ). The free energy change can then be calculated using the reaction field as

$$\Delta G_{EP} = \langle \Psi \left| H^{(0)} - \frac{e}{2}\varphi \right| \Psi \rangle + \frac{e}{2}\sum_k Z_k \varphi_k - \langle \Psi^{(0)} \left| H^{(0)} \right| \Psi^{(0)} \rangle \tag{4.19}$$

Where *e* is the unit atomic charge, Z_k and φ_k are atomic number and reaction field of atom *k* and $H^{(o)}$ and $\Psi^{(0)}$ are Hamiltonian and electronic wavefunction of solute in gas phase and Ψ is the polarized electronic wavefunction of solute in the solution. The reaction field inside the molecular cavity for the solute can be defined for any location **r** as

$$\varphi\,(\mathbf{r}) = \sum_m \frac{q_m}{|\mathbf{r}-\mathbf{r}_m|} \tag{4.20}$$

Where $\mathbf{r}_m$ is the position of any part of surface are on the solute-solvent boundary and q_m is the corresponding charge. The non-electrostatic part, which can also be called cavity-dispersion-solvent structure (CDS) term is the sum of following descriptors:

$$G_{CDS} = \sum_k^{atoms} \sigma_k A_k \left(\mathbf{R}, \{R_{Z_k} + r_s\}\right) + \sigma^{[\mathrm{M}]} \sum_k^{atoms} A_k \left(\mathbf{R}, \{R_{Z_k} + r_s\}\right) \tag{4.21}$$

Where **R** is the geometry parameter for solvent accessible surface area (SASA) which is dependent on set $\{R_{Z_k}\}$ of atomic van der Waal's radii and the solvent radius r_s. σ_k, $\sigma^{[M]}$ and A_k are the atomic surface tension, molecular surface tension and SASA of any atom *k* respectively. The atomic surface tension can be further calculated as:

$$\sigma_k = \tilde{\sigma}\,\tilde{\sigma}_{Z_k} + \sum_{k`}^{atoms} \tilde{\sigma}\,\tilde{\sigma}_{Z_k Z_{k`}} T_k(\{Z_{k`}, R_{kk`}\}) \tag{4.22}$$

Where $\tilde{\sigma}\,\tilde{\sigma}_{Z}$ and $\tilde{\sigma}\,\tilde{\sigma}_{ZZ}$ represents the specific parameter for atomic number *k* and *k`*, $T_k(\{Z_{k`}, R_{kk`}\})$ is called cut off tan and is the switching function dependent of the molecular geometry. $\tilde{\sigma}\,\tilde{\sigma}_{Z}$ and $\tilde{\sigma}\,\tilde{\sigma}_{ZZ}$ can be further calculated using a set of solvent parameters described as

$$\tilde{\sigma}\ \tilde{\sigma}_{i} = \tilde{\sigma}\ \tilde{\sigma}_{i}^{[n]} n + \tilde{\sigma}\ \tilde{\sigma}_{i}^{[\alpha]} \alpha + \tilde{\sigma}\ \tilde{\sigma}_{i}^{[\beta]} \beta \quad (4.23)$$

Where $\tilde{\sigma}\ \tilde{\sigma}_{i}$ is either $\tilde{\sigma}\ \tilde{\sigma}_{Z}$ or $\tilde{\sigma}\ \tilde{\sigma}_{ZZ}$, n is the refractive index of solvent at room temperature, α is the Abraham's hydrogen bond acidity and β is the Abraham's hydrogen bond basicity with corresponding empirical parameters. The molecular surface tension $\sigma^{[M]}$ is also dependent on a set of descriptors and is calculated as:

$$\sigma^{[M]} = \tilde{\sigma}\ \tilde{\sigma}^{[\gamma]} \left(\frac{\gamma}{\gamma_o}\right) + \tilde{\sigma}\ \tilde{\sigma}^{[\phi^2]} \phi^2 + \tilde{\sigma}\ \tilde{\sigma}^{[\psi^2]} \psi^2 + \tilde{\sigma}\ \tilde{\sigma}^{[\beta^2]} \beta^2 \quad (4.24)$$

Where γ is the macroscopic surface tension of the solvent at air-solvent interface at room temperature, ϕ is fraction of solvent atoms which are aromatic carbon, ψ is the fraction of solvent atoms which are halogens (F, Cl and Br) and β is the Abraham's hydrogen bond basicity with corresponding empirical constants. Altogether, a total of seven independent descriptors are used to define any solvent using SMD solvation model. The descriptors have been parametrized against the experimental data to yield mean unsigned error as low as 0.60 kcal/mol in the optimal conditions. This makes it one of the most accurate and comprehensive models to include solvation effect in the simulation environment.

4.3 DFT Algorithm

The density functional theory employed for this study is based upon the Kohn-Sham method for finding the ground state energy of a system. The computational package used for implementing DFT will be Gaussian [147]. The procedure and the algorithm used for solving the Kohn-Sham equation in the Gaussian package are as follows [148].

First the *i*th K-S orbitals are expanded in terms of basis function for the *i*th orbital (ϕ_i) as:

$$\psi_i^{KS} = \sum_{s=1}^{m} c_{si}\phi_i \ ; i = 1,2,3 \ldots, m \quad (4.25)$$

Where c_{si} is the basis function coefficient of the *s*th basis function of the *i*th orbital.

Putting this basis function in KS equation (4.16) gives

$$\sum_{s=1}^{m} c_{si}\hat{h}^{KS}\phi_s = \varepsilon_i^{KS}\sum_{s=1}^{m} c_{si}\phi_s \tag{4.26}$$

Multiplying equation (4.2) with ϕ_i gives

$$\sum_{s=1}^{m} c_{si}h_{rs}^{KS} = \sum_{s=1}^{m} c_{si}S_{rs}\varepsilon_i^{KS} \tag{4.27}$$

Where

$$h_{rs}^{KS} = \int \phi_r \hat{h}^{KS}\phi_s dv \qquad and \qquad S_{rs} = \int \phi_r\phi_s dv \tag{4.28}$$

The h_{rs}^{KS} and S_{rs} assumes the matrix form when *r* varies from 1 to *m*, and *i* varies from 1 to *m*. Thus, in the matrix notation, equation 4.27 can be written as:

$$\mathbf{HC=SC\varepsilon} \tag{4.29}$$

Where **H**, **C** and **S** are m x m matrix and ε is an m x m diagonal matrix with non-zero elements. Gaussian package uses statistical thermodynamics to calculate the thermochemical parameters of the structures. The equations which govern the thermochemical parameter calculations in the package are [149,150]:

$$S = R\left(ln(q) + T\left(\frac{\partial lnq}{\partial T}\right)_V\right) \tag{4.30}$$

$$E = Nk_BT^2\left(\frac{\partial lnq}{\partial T}\right)_V \tag{4.31}$$

Where S is the entropy of the system, E is the internal energy of the system, T is the temperature, k_B is the Boltzmann constant, q is the partition function and comprise of q_{elect}, q_{transl}, q_{rot} and q_{vib}; which are the electronic, translation, rotational and the vibrational contribution to the partition function respectively.

Each molecular partition function can be calculated as:

4.3.1 *Electronic energy contribution*

$$q_{elec} = \exp(\frac{-E_{elec,ground}}{k_BT}) \tag{4.32}$$

Where k_B is the Boltzmann constant and T is temperature. This equation is valid for cases where the spin multiplicity is one. For all other spin multiplicities, a degeneracy factory (2s+1) is added, where s is the total spin.

4.3.2 Translational motion contribution

$$q_{trans} = \left(\frac{2\pi M k_B T}{h^2}\right)^{\frac{3}{2}} V \tag{4.33}$$

Where V is the volume of a very large cube with side *a* such that $a \gg$ molecule size, *h* is planck's constant and *M* is the molecular weight

4.3.3 Rotational motion contribution

a. Linear molecules:

$$q_r = \frac{1}{\sigma_r}\left(\frac{T}{\theta_r}\right) \tag{4.34}$$

Where σ_r represents the symmetry number which tells the number of indistinguishable orientations of the molecule and $\theta_r = h^2/8\pi^2 I k_B$ where *I* is the moment of inertia.

b. Non-linear molecules:

$$q_r = \frac{\pi^{1/2}}{\sigma_r}\left(\frac{T^{3/2}}{(\theta_{r,x}\theta_{r,y}\theta_{r,z})^{1/2}}\right) \tag{4.35}$$

Where $\theta_{r,x}$, $\theta_{r,y}$ and $\theta_{r,z}$ describes the rotational temperature associated with the moment of inertia in x, y and z directions.

4.3.4 Vibrational motion contribution

$$q_v = \prod_K \frac{e^{-\theta_{v,K}/2T}}{1-e^{-\theta_{v,K}/T}} \tag{4.36}$$

Where $\theta_{v,K}$ is the characteristic vibrational temperature defined as $-\theta_{v,K} = h\nu_j / k_B$

The total partition function *q* can be calculated as:

$$q = q_{elect} \cdot q_{transl} \cdot q_{rot} \cdot q_{vib} \tag{4.37}$$

The total partition functions are then used to calculate the entropy contributions from the individual partition functions using equation (4.30) and (4.37). The energy contributions are also calculated using equation (4.31). Once the entropy and energy has been calculated, the following equations are used to calculate the overall enthalpy (H) and Gibbs free energy (G):

$$H=E+k_BT \tag{4.38}$$

$$G=H-TS \tag{4.39}$$

RESULTS AND DISCUSSION

5.1 DFT Investigation on Thermochemical Analyses of Conversion of Xylose to Linear Alkanes in Aqueous Phase

The xylose is converted to butane, pentane, tridecane and octane by five major pathways shown in schemes 1-5 as detailed below.

In RS 1, xylose (XYL) is dehydrated to produce furfural (FF) which upon decarbonylation gives rise to furan (FRN). FRN then undergoes hydrogenation to obtain butanol (BOL) with tetrahydrofuran (THF) as intermediate. BOL upon subsequent hydrogenation and deoxygenation produce butane (BAN).

In RS 2, XYL is dehydrated to produce FF which upon hydrogenation yield furfuryl alcohol (FOL). FOL is further hydrodeoxygenated to produce 2-methylfuran (2MF). Further hydrogenation of 2MF yields 2-methyltetrahydrofuran (MTHF). Ring opening of MTHF yields pentaldehyde (PAD) *via* RS 2a which upon further hydrogenation produce propanol (POL). Also, direct hydrogenation of MTHF yields POL which upon hydrogenation and deoxygenation gives rise to pentane (PAN) *via* RS 2b.

RS 3a/3b initiates with ring and formyl hydrogenation of FF resulting in saturation of all C=C bonds and a C=O bond to produce hydroxymethyl tetrahydrofuran (THFOL). Then ring opening of THFOL occurs by hydrogenation which leads to the possibility of formations of pentane-1,5-diol (PDOL) and pentane-1,2-diol (PAOL) *via* RS 3a and 3b, respectively. PDOL and PAOL upon simultaneous hydrodeoxygenation yield PAN.

RS 4 produce tridecane (TDC) *via* two sub-pathways, i.e., RS 4a and RS 4b. XYL is first dehydrated to produce FF which is then subjected to aldol condensation with acetone to

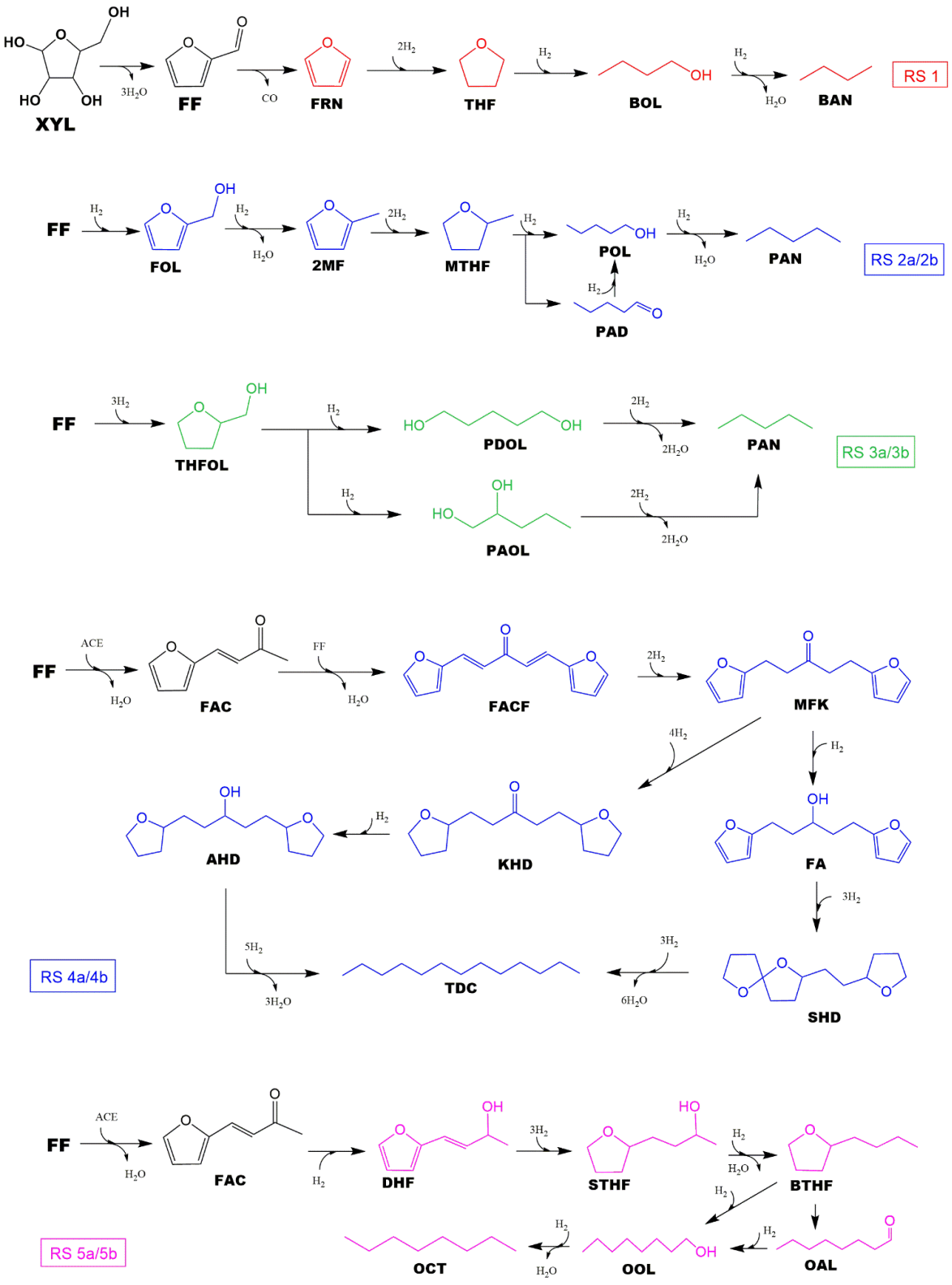

Reaction Scheme: All reaction scheme describing the conversion of xylose to linear C4, C5, C8 and C13

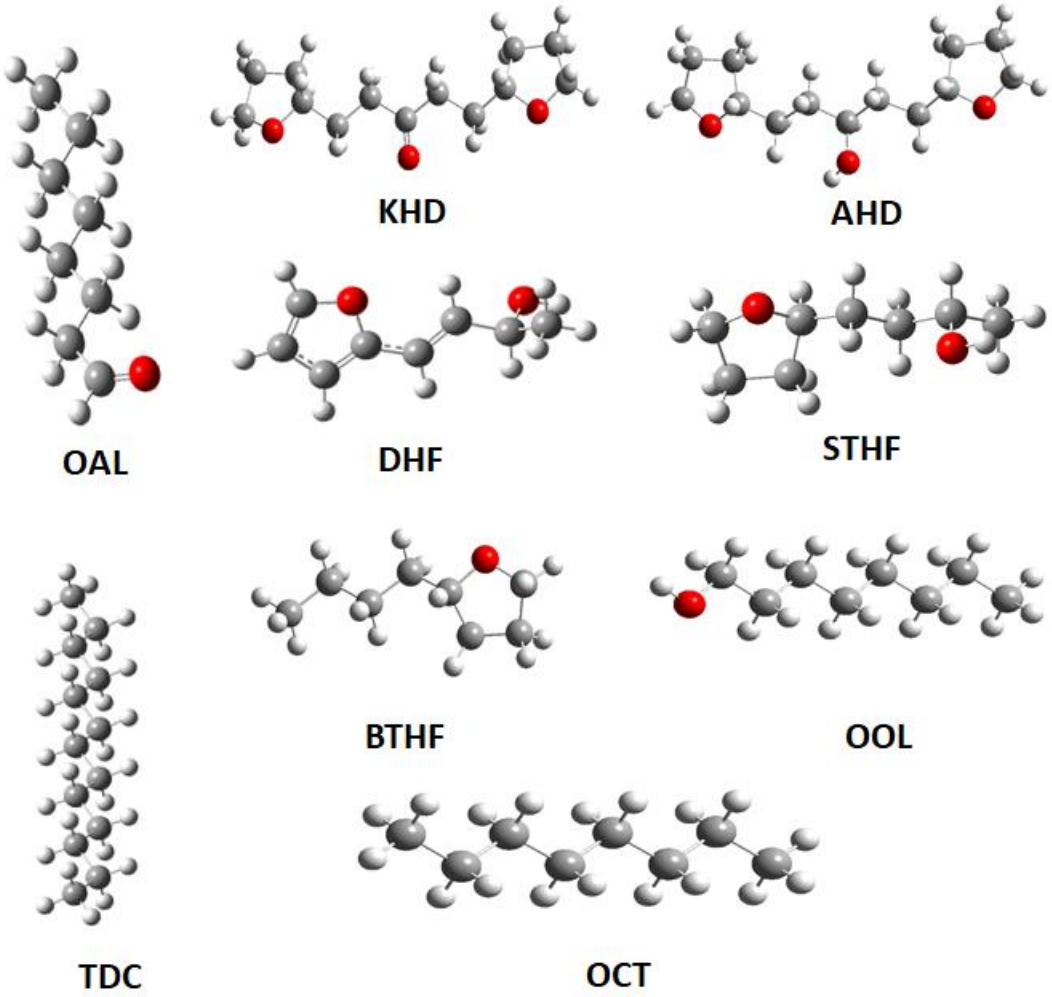

Figure 5.1.1. Optimized geometrical structure of few compounds using B3LYP functional in aqueous phase.

produce furfural acetone (FAC). Further aldol condensation of FF with FAC yields difurfurylideneacetone (FACF) and a water molecule *via* RS 4a. The FACF is then hydrogenated to saturate the C=C chain bonds to produce 1,5-di(furan-2-yl)pentan-3-one (MFK) which is then hydrogenated to yield 1,5-di(furan-2-yl)pentan-3-ol (FA). Further addition of 3 hydrogen molecules to FA yields 2-(2-(tetrahydrofuran-2-yl)ethyl)-1,6-dioxaspiro[4.4]nonane (SHD) *via* RS 4a which upon simultaneous hydrodeoxygenation gives rise to TDC. Alternatively, hydrogenation of the furan rings of MFK produces 1,5-bis(tetrahydrofuran-2-yl)pentan-3-one (KHD). The hydrogenation of C=O group of KHD

occurs to produce 1,5-bis(tetrahydrofuran-2-yl)pentan-3-ol (AHD) *via* RS 4b. Further, hydrodeoxygenation of AHD gives rise to TDC.

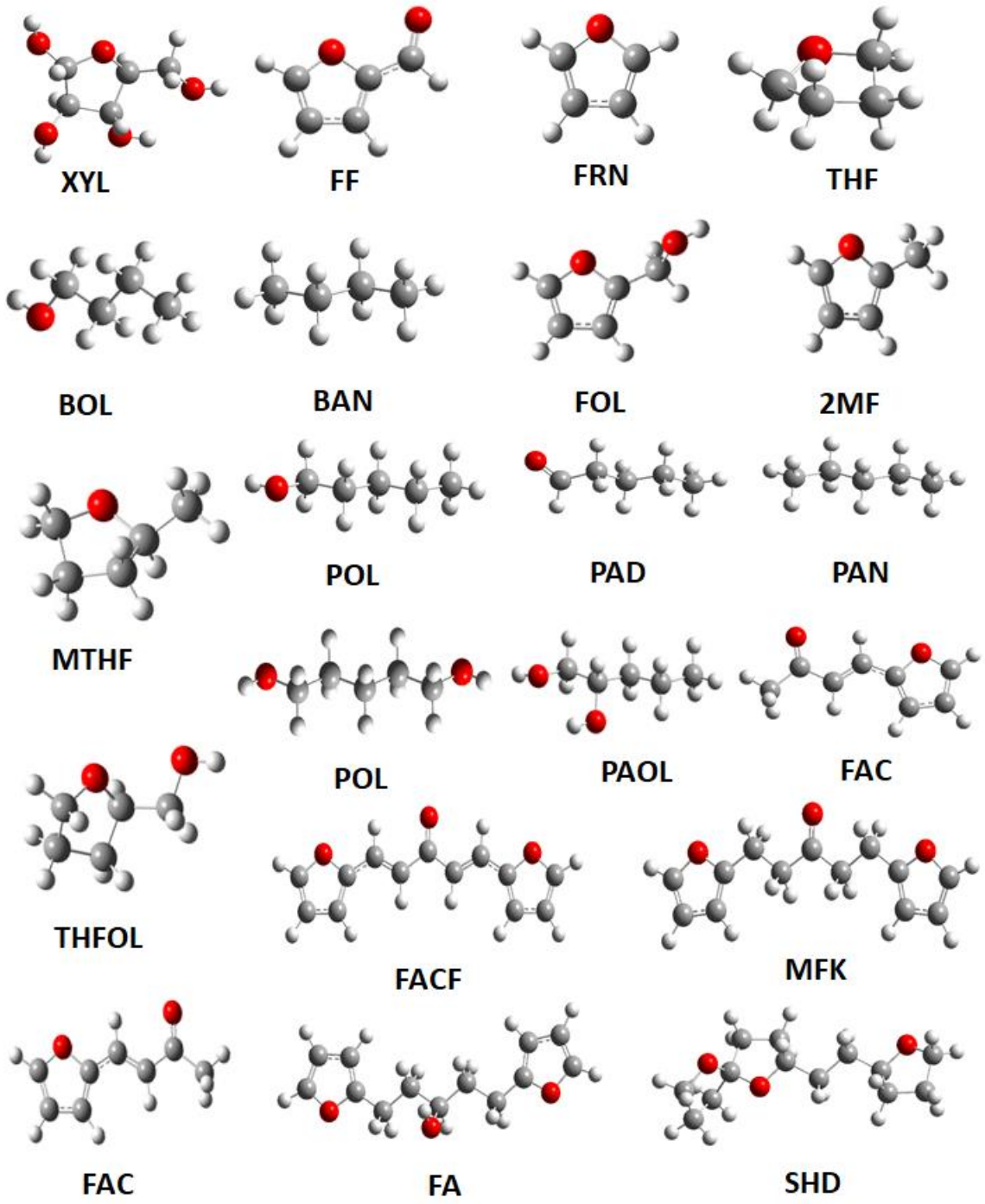

Figure 5.1.2: optimized geometrical structure of remaining few compounds using B3LYP functional

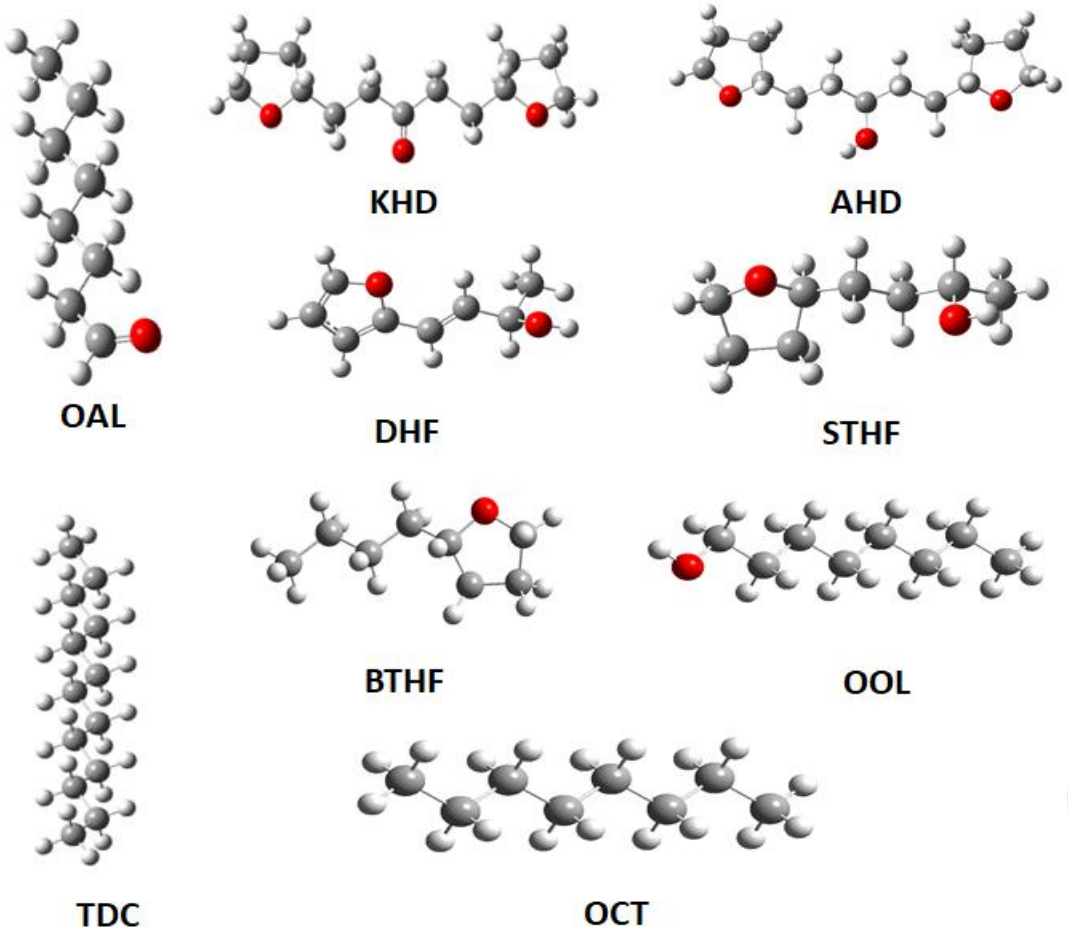

Figure 5.1.3: optimized geometrical structure of remaining few compounds using M06-2X functional in aqueous phase.

In RS 5, hydrogenation of all unsaturated carbon of FAC is performed in two steps to produce 4-(tetrahydrofuran-2-yl)butan-2-ol (STHF) followed by hydrodeoxygenation to produce 2-butyltetrahydrofuran (BTHF). Direct hydrogenation of BTHF yields octanol (OOL) in RS 5a, whereas in RS 5b, BTHF first undergoes ring opening to produce octaldehyde (OAL) followed by hydrogenation of OAL to produce OOL. Finally, hydrodeoxygenation of OOL yields octane (OCT).

All structures are first optimized using B3LYP functional with Pople's split valence basis set [151] with diffuse function on non-hydrogen atoms and polarization function on all

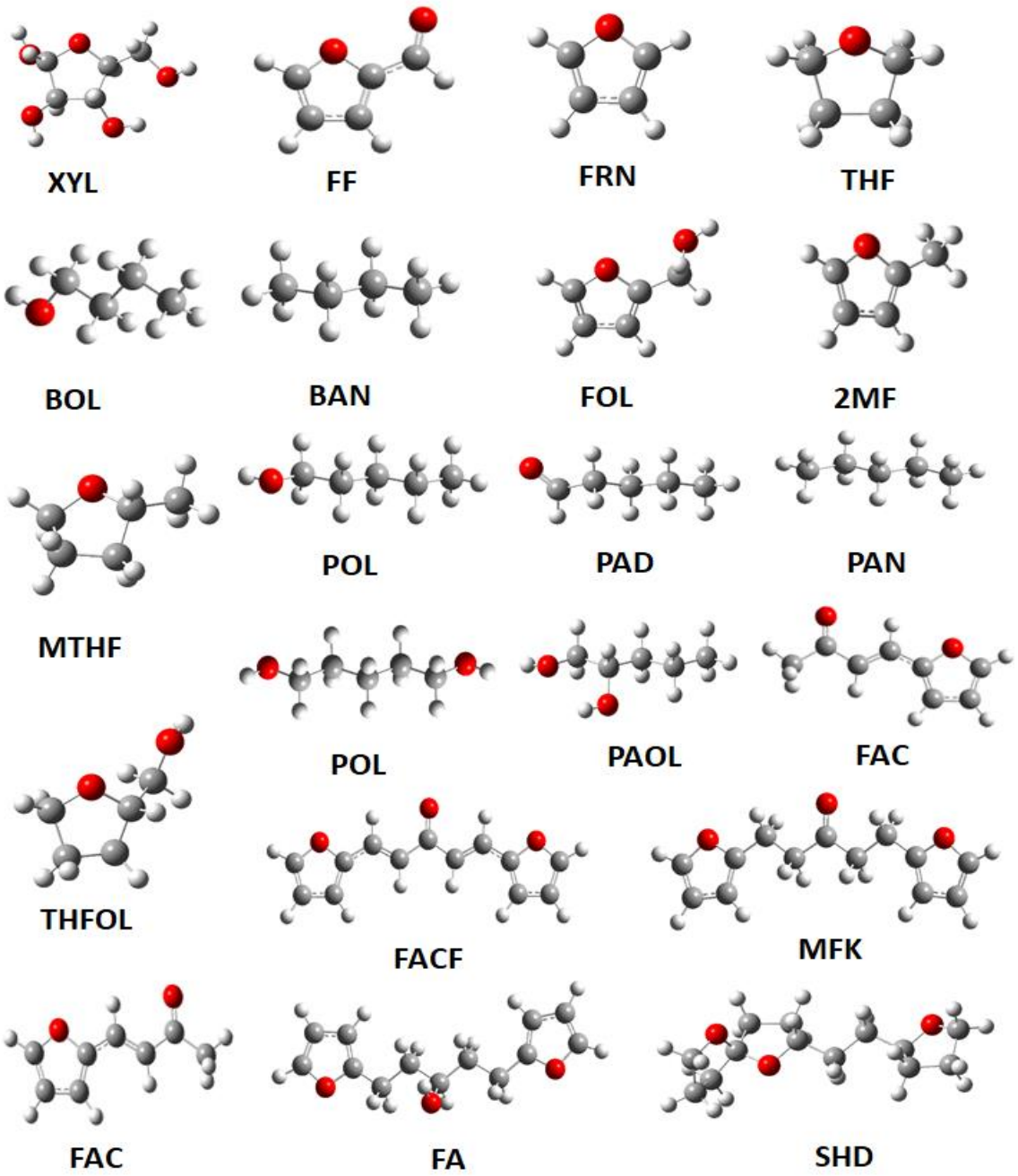

Figure 5.1.4: optimized geometrical structure of remaining few compounds using M06-2X functional in aqueous phase.

atoms, 6-31+g(d,p) in the gas phase. The resultant molecule structure is again optimized in aqueous phase using SMD [145] solvation model and the thermochemical parameters are derived at a varying temperature at the same level of theory. The optimized structures of all the molecules by both functionals are provided in Figure 5.1.1 and 5.1.2. Further, in the study

conducted by Simón & Goodman [152], it is reported that the single point energy (SPE) calculation conducted using M05-2X functional [153] can be more accurate than some of the more computationally expensive methods. Thus, the single point energetics of the optimized structures of the aqueous phase is then calculated at M05-2X/6-311++g(3df,2p) level of theory in aqueous phase using SMD solvation model. Sample Gaussian input codes are provided in Annexure 2 for reference.

Alternatively, molecules are also optimized in the gas phase at M06-2X/6-31+g(d,p) level of theory. The resultant structure is then re-optimized in the aqueous phase using SMD solvation model at the same level of theory and are given in Figure 5.1.3 and Figure 5.1.4. Thermochemical parameters are also calculated at the same level of theory.

All simulations are performed using Gaussian 09 software package [147] with the aid of GaussView 5 visualization tool [154].

5.1.1 Thermochemistry

The thermochemical parameters- ΔG, ΔH and K_{eq} of all the conversions for all the reaction schemes have been discussed in this section. The M and C values of the equation $\ln K_{eq} = \frac{M}{T} + C$ is also provided in Table 5.1.1 for all conversions. The conversion of XYL to FF is common in all reaction schemes and is discussed below.

Table 5.1.1: M and C values for the equation $\ln K_{eq} = \frac{M}{T} + C$ where K_{eq} is the rate constant in s^{-1} at equilibrium and T is the temperature in Kelvin.

	M06-2X		B3LYP	
	M	C	M	C
XYL → FF	-2425.60	56.50	6478.10	57.39
FF → FRN	-7193.20	18.35	-8846.70	18.10
FRN → THF	22342.00	-30.11	20097.00	-28.32
THF → BOL	12974.00	-10.85	12651.00	-10.17

BOL → BAN	12068.00	1.99	13046.00	1.51
FF → FOL	10210.00	-14.13	6933.60	-13.16
FOL → 2MF	13531.00	2.86	14335.00	3.09
2MF → MTHF	22129.00	-30.72	19358.00	-29.86
MTHF → POL	10592.00	-11.49	10724.00	-10.86
MTHF → PAD	-634.02	4.37	1919.80	4.45
PAD → POL	11226.00	-15.87	8803.80	-15.31
POL →PAN	11876.00	2.41	12870.00	2.49
FF → THFOL	33525.00	-45.43	27126.00	-43.72
THFOL → PDOL	10884.00	-11.22	11232.00	-10.84
PDOL → PAN	23920.00	5.58	25862.00	5.96
THFOL → PAOL	12834.00	-12.14	12510.00	-11.17
PAOL → PAN	21971.00	6.50	24584.00	6.28
FF → FAC	2827.00	-2.91	2182.10	-1.98
FAC → FACF	3171.80	-2.12	2296.70	-2.59
FACF → MFK	29327.00	-30.22	22188.00	-28.54
MFK → FA	8808.90	-15.35	6142.20	-13.47
FA → SHD	37626.00	-50.39	31790.00	-51.87
SHD → TDC	62126.00	-22.58	69645.00	-35.13
MFK → KHD	44534.00	-62.23	39371.00	-62.96
KHD → AHD	8455.50	-16.41	5364.00	-13.26
AHD → TDC	55572.00	-9.67	62843.00	-24.25
FAC → DHF	8164.00	-15.37	5078.40	-15.20
DHF → STHF	37565.00	-46.35	32007.00	-44.77
STHF → BTHF	9899.60	2.79	11291.00	3.99
BTHF → OOL	10770.00	-10.02	11146.00	-11.34
OOL → OCT	11991.00	3.25	12932.00	3.68
BTHF → OAL	121.09	4.23	2688.00	2.84
OAL → OOL	10649.00	-14.25	8458.50	-14.18

5.1.1.1 Formation of Furfural

The conversion of XYL to FF is achieved by the dehydration of XYL molecule by eliminating three molecules of water. The associated enthalpy change is -14.32 kcal/mol using B3LYP functional at 298 K which decreases to -16.32 kcal/mol at 698 K (Table 5.1.2). However, M06-2X calculation for the same conversion shows the associated enthalpy change of 4.59 kcal/mol at 298 K which decreases to 4.25 kcal/mol at 698 K. ΔH difference of 18.91 kcal/mol between

both functionals at 298 K is the largest difference calculated across all the reaction schemes. To determine the actual error between the two functionals, XYL to FF conversion step is simulated with two very high accuracy methods – MP2/aug-ccPVDZ and G4MP2 in the aqueous phase with SMD solvation model [155,156]. ΔH is found to be -5.52 kcal/mol and -4.89 kcal/mol for MP2 and G4MP2 at 298 K respectively. At 698 K, the enthalpy change is found to be -5.82 kcal/mol and -5.55 kcal/mol for MP2 and G4MP2 respectively. This suggests that while the reaction step is exothermic in nature, the error in both the functionals (B3LYP and M06-2X) is almost of the same magnitude but in opposite direction.

The free energy change (ΔG) of the XYL to FF conversion is calculated to be -46.45 kcal/mol using B3LYP functional in the aqueous phase. The gas phase study conducted by Luo et al. [157] with the same functional report ΔG = -69.8 kcal/mol making the reaction more favorable in the gas phase. Using M06-2X functional, ΔG of the conversion is found to be -28.63 kcal/mol at 298 K. While the low free energy shows the reaction step to be favorable in nature, the actual spontaneity of the reaction is confirmed by the MP2/aug-ccPVDZ and G4MP2 methods, which estimate ΔG to be -38.01 kcal/mol and -37.62 kcal/mol at 298 K respectively. At 698 K, the ΔG for B3LYP and M06-2X is -91.68 kcal/mol and -73.48 kcal/mol respectively. Luo et al. [157] report ΔG of -119.5 kcal/mol for gas phase at this temperature. Calculations with MP2 and G4MP2 in aqueous phase show ΔG equal to -82.14 kcal/mol and -81.67 kcal/mol respectively. Thus, here too, the error associated with B3LYP and M06-2X is of the same magnitude. The spontaneity is found to increase with an increase in temperature from 298 K to 698 K for both B3LYP and M06-2X by the same magnitude of 45.00±1 kcal/mol (Figure 5.1.5(a)). This in accordance with the findings of Xu et al. [158] which reports the activation energy of this conversion to be quite high. Thus, a high temperature can be favorable for this conversion step.

Table 5.1.2. Enthalpy change (ΔH) in Kcal/mol using B3LYP and M06-2X functional for all conversion steps at varying temperature.

	298 K		**398 K**		**498 K**		**598 K**		**698 K**	
	M06-2X	B3LYP	M06-2X	B3LYP	M06-2X	B3LYP	M06-2X	B3LYP	M06-2X	B3LYP
XYL → FF	4.59	-14.32	4.95	-15.57	4.98	-15.58	4.73	-15.84	4.26	-16.32
FF → FRN	14.32	17.78	14.34	17.91	14.29	17.86	14.17	17.75	14.01	17.60
FRN → THF	-43.16	-39.49	-44.14	-41.48	-44.95	-42.24	-45.57	-42.82	-46.02	-43.21
THF → BOL	-25.72	-25.43	-25.76	-25.91	-25.80	-25.97	-25.82	-26.01	-25.82	-26.02
BOL → BAN	-23.59	-25.38	-23.85	-25.55	-24.14	-25.86	-24.44	-26.18	-24.74	-26.49
FF → FOL	-19.87	-13.70	-20.22	-14.37	-20.47	-14.58	-20.65	-14.72	-20.75	-14.78
FOL → 2MF	-26.48	-28.09	-26.75	-28.51	-27.04	-28.82	-27.35	-29.15	-27.66	-29.46
2MF → MTHF	-42.76	-37.73	-43.74	-39.26	-44.52	-40.01	-45.11	-40.56	-45.51	-40.93
MTHF → POL	-20.86	-21.36	-21.00	-21.72	-21.13	-21.84	-21.22	-21.93	-21.27	-21.98
MTHF → PAD	0.96	-4.08	1.22	-3.78	1.40	-3.62	1.52	-3.52	1.61	-3.45
PAD → POL	-21.82	-17.28	-22.22	-17.94	-22.52	-18.22	-22.74	-18.41	-22.87	-18.53
POL →PAN	-23.16	-25.17	-23.44	-25.60	-23.75	-25.92	-24.07	-26.25	-24.39	-26.57
FF → THFOL	-64.99	-53.09	-66.31	-55.29	-67.35	-56.25	-68.10	-56.93	-68.61	-57.37
THFOL → PDOL	-21.46	-22.37	-21.58	-22.73	-21.70	-22.86	-21.79	-22.95	-21.84	-23.01
PDOL → PAN	-46.70	-50.58	-47.26	-51.44	-47.86	-52.07	-48.49	-52.71	-49.12	-53.35
THFOL → PAOL	-25.41	-25.00	-25.48	-25.26	-25.54	-25.32	-25.57	-25.36	-25.58	-25.36

PAOL → PAN	-42.75	-47.96	-43.36	-48.91	-44.03	-49.61	-44.71	-50.31	-45.38	-50.99
FF → FAC	-6.02	-5.32	-5.70	-4.80	-5.43	-4.54	-5.20	-4.34	-5.03	-4.18
FAC → FACF	-6.70	-4.56	-6.39	-4.54	-6.12	-4.24	-5.89	-3.99	-5.72	-3.80
FACF → MFK	-57.12	-43.43	-58.05	-44.88	-58.78	-45.56	-59.32	-46.06	-59.69	-46.39
MFK → FA	-17.03	-11.98	-17.42	-12.65	-17.72	-12.93	-17.93	-13.12	-18.06	-13.24
FA → SHD	-72.60	-61.74	-74.35	-64.34	-75.74	-65.65	-76.79	-66.61	-77.52	-67.26
SHD → TDC	-121.54	-130.65	-122.89	-124.94	-124.25	-126.37	-125.52	-127.69	-126.66	-128.85
MFK → KHD	-86.05	-76.45	-88.02	-79.71	-89.60	-81.42	-90.78	-82.72	-91.60	-83.66
KHD → AHD	-16.31	-10.73	-16.72	-11.22	-17.03	-11.31	-17.24	-11.31	-17.38	-11.23
AHD → TDC	-108.81	-117.20	-109.92	-110.99	-111.08	-112.23	-112.21	-113.40	-113.25	-114.47
FAC → DHF	-15.78	-9.42	-16.15	-10.29	-16.43	-10.51	-16.62	-10.66	-16.74	-10.73
DHF → STHF	-72.80	-62.49	-74.29	-64.79	-75.47	-65.91	-76.35	-66.74	-76.96	-67.28
STHF → BTHF	-19.17	-21.93	-19.51	-22.47	-19.88	-22.86	-20.26	-23.24	-20.62	-23.61
BTHF → OOL	-21.25	-22.21	-21.36	-22.55	-21.47	-22.67	-21.54	-22.75	-21.57	-22.79
OOL → OCT	-23.42	-25.32	-23.69	-25.73	-23.99	-26.03	-24.29	-26.34	-24.60	-26.65
BTHF → OAL	-0.56	-5.60	-0.29	-5.29	-0.09	-5.13	0.05	-5.02	0.15	-4.94
OAL → OOL	-20.69	-16.61	-21.08	-17.26	-21.37	-17.54	-21.58	-17.73	-21.72	-17.84

Table 5.1.3. Equilibrium rate constant (K_{eq}) values using B3LYP and M06-2X functional for all conversion steps at varying temperature.

	298 K		**398 K**		**498 K**		**598 K**		**698 K**	
	M06-2X	B3LYP	M06-2X	B3LYP	M06-2X	B3LYP	M06-2X	B3LYP	M06-2X	B3LYP
XYL → FF	1.01E+21	1.22E+34	7.50E+21	2.73E+32	2.66E+22	5.22E+30	6.08E+22	3.67E+29	1.05E+23	5.28E+28
FF → FRN	3.03E-03	9.87E-06	1.32E+00	1.46E-02	5.02E+01	1.37E+00	5.58E+02	2.79E+01	3.06E+03	2.36E+02
FRN → THF	2.64E+19	5.69E+16	2.43E+11	9.70E+09	2.97E+06	2.35E+05	1.41E+03	1.77E+02	5.61E+00	9.88E-01
THF → BOL	1.56E+14	8.66E+13	2.81E+09	3.31E+09	4.02E+06	4.56E+06	5.12E+04	5.63E+04	2.27E+03	2.44E+03
BOL → BAN	2.70E+18	4.65E+19	1.15E+14	7.73E+14	2.60E+11	1.12E+12	4.29E+09	1.38E+10	2.21E+08	5.74E+08
FF → FOL	5.27E+08	1.51E+04	1.07E+05	6.95E+01	6.11E+02	1.76E+00	1.89E+01	1.49E-01	1.55E+00	2.51E-02
FOL → 2MF	8.69E+20	1.56E+22	1.08E+16	1.10E+17	1.17E+13	7.58E+13	1.18E+11	5.65E+11	4.26E+09	1.65E+10
2MF → MTHF	7.03E+18	1.21E+15	7.67E+10	2.44E+08	1.04E+06	1.04E+04	5.33E+02	1.14E+01	2.25E+00	8.40E-02
MTHF → POL	2.72E+10	7.19E+10	3.79E+06	1.17E+07	1.80E+04	4.62E+04	5.02E+02	1.14E+03	3.87E+01	8.09E+01
MTHF → PAD	9.79E+00	5.63E+04	1.55E+01	1.00E+04	2.16E+01	3.91E+03	2.76E+01	2.14E+03	3.33E+01	1.41E+03
PAD → POL	2.78E+09	1.28E+06	2.45E+05	1.17E+03	8.34E+02	1.18E+01	1.82E+01	5.34E-01	1.16E+00	5.76E-02
POL →PAN	2.09E+18	6.24E+19	1.06E+14	1.51E+15	2.66E+11	2.18E+12	4.67E+09	2.66E+10	2.51E+08	1.10E+09
FF → THFOL	1.11E+29	2.02E+20	9.09E+16	9.26E+10	3.87E+09	6.57E+04	4.11E+04	4.61E+00	1.08E+01	4.69E-03
THFOL → PDOL	9.56E+10	4.04E+11	1.04E+07	4.30E+07	4.25E+04	1.31E+05	1.08E+03	2.73E+03	7.74E+01	1.71E+02
PDOL → PAN	1.72E+37	1.57E+40	3.79E+28	8.28E+30	2.16E+23	1.62E+25	6.28E+19	2.31E+21	1.74E+17	3.86E+18
THFOL → PAOL	2.67E+13	2.16E+13	5.47E+08	7.48E+08	8.38E+05	1.21E+06	1.11E+04	1.67E+04	5.09E+02	7.86E+02

PAOL → PAN	6.17E+34	2.93E+38	7.18E+26	4.76E+29	1.09E+22	1.76E+24	6.05E+18	3.78E+20	2.65E+16	8.39E+17
FF → FAC	7.49E+02	2.00E+02	6.20E+01	3.61E+01	1.51E+01	1.10E+01	6.12E+00	5.18E+00	3.30E+00	3.10E+00
FAC → FACF	5.27E+03	1.82E+02	3.26E+02	2.15E+01	6.66E+01	7.05E+00	2.41E+01	3.53E+00	1.20E+01	2.21E+00
FACF → MFK	3.60E+29	6.15E+19	8.91E+18	1.09E+12	3.21E+12	1.13E+07	1.48E+08	4.89E+03	1.13E+05	1.85E+01
MFK → FA	1.41E+06	1.07E+03	9.52E+02	9.20E+00	1.10E+01	3.58E-01	5.38E-01	3.95E-02	6.14E-02	8.06E-03
FA → SHD	6.92E+32	3.54E+23	2.06E+19	3.45E+12	1.09E+11	2.35E+05	2.73E+05	3.28E+00	2.48E+01	1.02E-03
SHD → TDC	4.26E+80	2.52E+87	1.29E+58	7.12E+58	3.06E+44	9.80E+44	2.07E+35	4.61E+35	5.14E+28	8.77E+28
MFK → KHD	5.62E+37	5.06E+29	5.33E+21	1.26E+16	8.56E+11	1.65E+07	2.04E+05	1.56E+01	3.40E+00	6.85E-04
KHD → AHD	1.48E+05	9.87E+01	1.35E+02	1.55E+00	1.86E+00	8.88E-02	1.02E-01	1.31E-02	1.27E-02	3.37E-03
AHD → TDC	5.01E+76	1.91E+82	3.53E+56	1.15E+56	2.30E+44	5.61E+43	1.46E+36	2.92E+35	1.82E+30	3.13E+29
FAC → DHF	1.58E+05	5.73E+00	1.83E+02	9.97E-02	2.91E+00	7.14E-03	1.78E-01	1.20E-03	2.38E-02	3.30E-04
DHF → STHF	3.33E+34	9.19E+26	9.56E+20	6.80E+15	5.27E+12	4.22E+08	1.41E+07	5.71E+03	1.35E+03	1.76E+00
STHF → BTHF	4.08E+15	1.37E+18	1.12E+12	1.32E+14	7.52E+09	4.18E+11	2.53E+08	8.50E+09	2.15E+07	5.04E+08
BTHF → OOL	2.16E+11	1.84E+11	2.57E+07	2.08E+07	1.11E+05	6.66E+04	2.94E+03	1.43E+03	2.18E+02	9.19E+01
OOL → OCT	7.30E+18	2.54E+20	3.33E+14	5.88E+15	7.82E+11	8.19E+12	1.32E+10	9.76E+10	6.93E+08	3.98E+09
BTHF → OAL	1.07E+02	1.49E+05	8.88E+01	1.37E+04	8.46E+01	3.65E+03	8.41E+01	1.55E+03	8.51E+01	8.47E+02
OAL → OOL	2.03E+09	1.24E+06	2.89E+05	1.51E+03	1.32E+03	1.82E+01	3.49E+01	9.27E-01	2.56E+00	1.08E-01

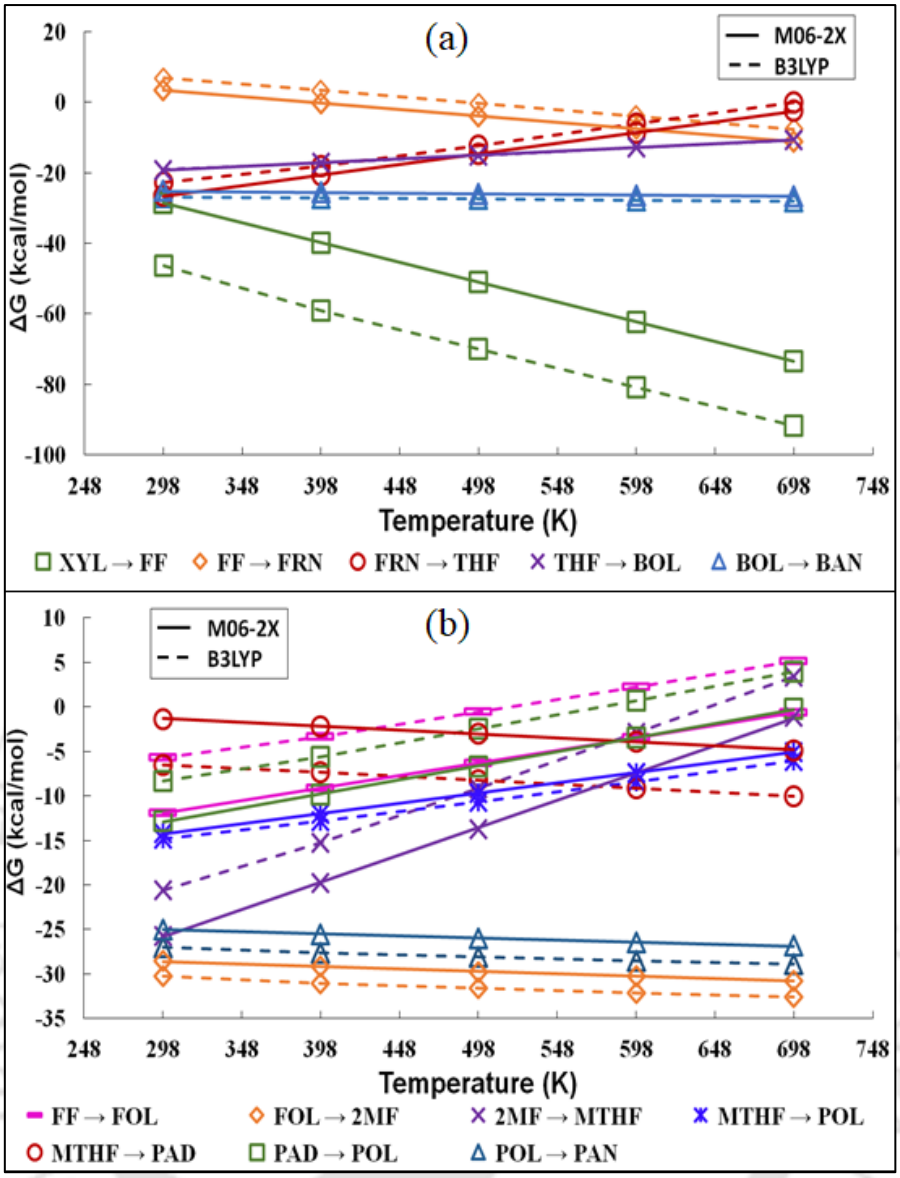

Figure 5.1.5. ΔG vs T plot with B3LYP and M06-2X functional for (a) all conversions of RS 1 (b) all conversions of RS 2

5.1.1.2 Formation of Butane

The conversion of FF to BAN starts with the decarbonylation of FF. With ΔG of 6.82 kcal/mol and 3.43 kcal/mol using B3LYP and M06-2X respectively at 298 K (Figure 5.1.5(a)), this step is observed to be the most unfavorable reaction step in RS 1. With ΔG = 9.56 kcal/mol, this conversion is unfavorable even in the gas phase as reported by Banerjee & Mushrif [159]. The equilibrium constant for the reaction is also found to be almost zero suggesting minimum

conversion (Table 5.1.3). But with an increase in temperature, the spontaneity increases and at 698 K, ΔG is found to be -7.57 kcal/mol and -11.12 kcal/mol for B3LYP and M06-2X respectively. The enthalpy change for FF to FRN is calculated to be 17.78 kcal/mol and 14.32 kcal/mol for B3LYP and M06-2X at 298 K respectively (Table 5.1.2). The increase in temperature does not seem to have any significant effect on its reaction enthalpy. Further conversion of FRN to THF is highly spontaneous at 298 K with ΔG as -22.83 kcal/mol and -26.47 kcal/mol for B3LYP and M06-2X respectively. However, the spontaneity decreases with increase in the temperature and reaches almost 0.02 kcal/mol for B3LYP and -2.39 kcal/mol for M06-2X at 698 K. The enthalpy change for the reaction step suggest exothermic reaction with resistance to the temperature change and show only a deviation of ±3 kcal/mol with the increase in temperature. Similarly, the conversion of THF to BOL and BOL to BAN is exothermic and does not change significantly with the increase in temperature. However, the reaction free energy change of THF to BOL increases from -18.99 kcal/mol to -10.81 kcal/mol as per B3LYP functional and -19.34 kcal/mol to -10.71 kcal/mol as per M06-2X functional from 298 K to 698 K temperature. On the contrary, the free energy change for BOL to BAN decreases from -26.80 kcal/mol to -27.96 kcal/mol as per B3LYP functional and -25.12 kcal/mol to –26.63 kcal/mol as per M06-2X functional suggesting minimal temperature effect on the spontaneity of the conversion.

5.1.1.3 Formation of Pentane

In RS 2, the conversion of FF to FOL is spontaneous with ΔG equal to -5.70 kcal/mol and -11.89 kcal/mol at 298 K using B3LYP and M06-2X functional respectively. When this is compared to the gas phase ΔG of ~14 kcal/mol reported by Banarjee & Mushrif [159], the conversion in the aqueous phase is more likely to occur. However, the same does not hold true at a higher temperature. As the temperature increase, ΔG increases to 5.11 kcal/mol and -0.61 kcal/mol at 698 K with B3LYP and M06-2X functional respectively, suggesting an unfavorable

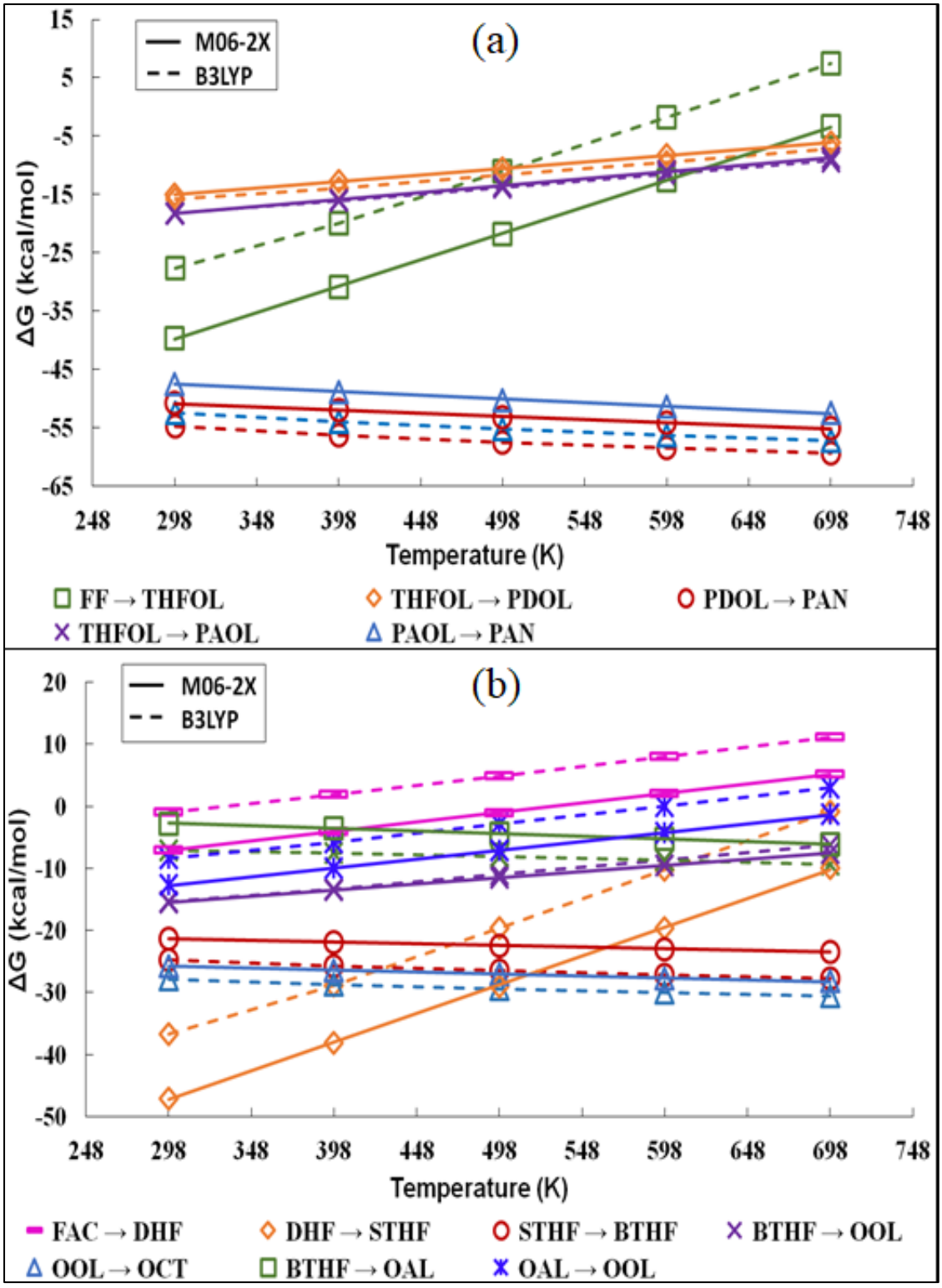

Figure 5.1.6: ΔG vs T plot with B3LYP and M06-2X functional for (a) all conversions of RS 3 (d) all conversions of RS 5

environment at high temperature. Further, K_{eq} also reduces to less than zero at 698 K suggesting no likelihood of the conversion to proceed. A similar trend is observed in conversion of 2MF

to MTHF, MTHF to POL and PAD to POL as well (Figure 5.1.5(b)). In RS 2a/2b, all reactions are exothermic by nature and an increase in temperature is favorable, except for MTHF to PAD conversion steps. The predicted ΔH by both functionals suggests that this step is not very exothermic and may require energy to proceed. Also, ΔH is observed to increase with an increase in temperature suggesting an unfavorable condition at a higher temperature.

In RS 3, the reaction free energy for the conversion of FF to THFOL is calculated to be -27.67 kcal/mol and -39.58 kcal/mol for B3LYP and M06-2X functionals, respectively. This suggests that the reaction step is spontaneous. It is also observed that with an increase in temperature, the spontaneity decreases and reaches 7.43 kcal/mol at B3LYP and -3.29 kcal/mol at M06-2X level of theories signifying an unfavorable condition. Conversion of THFOL to PDOL and THFOL to PAOL show similar trend where ΔG increases with increase in temperature (Figure 5.1.6(a)). However, the enthalpy change for the conversion of FF to THFOL decrease from -53.09 kcal/mol at 298 K to -57.37 kcal/mol at 698 K for B3LYP functional showing increase in the exothermicity. Similarly, for M06-2X, enthalpy change decreases from -64.99 kcal/mol at 298 K to -68.61 kcal/mol at 689 K. No significant change is observed in ΔH of THFOL to PDOL and THFOL to PAOL conversion. A decrease in the enthalpy change of less than 2 kcal/mol is observed for the PDOL to PAN and PAOL to PAN conversion step at each interval of 100 K temperature for both functionals. Also, Gibbs energy change decreases with temperature from 298 K to 698 K for PDOL to PAN and PAOL to PAN for both functionals, signifying increasing feasibility of the conversion with an increase in temperature.

5.1.1.4 Formation of Tridecane

In RS 4, FF to FAC conversion is an exothermic step with ΔH_{298} value of -5.32 kcal/mol at B3LYP and -6.02 kcal/mol at M06-2X at 298 K. As reported by Liu et el. [91] this reaction

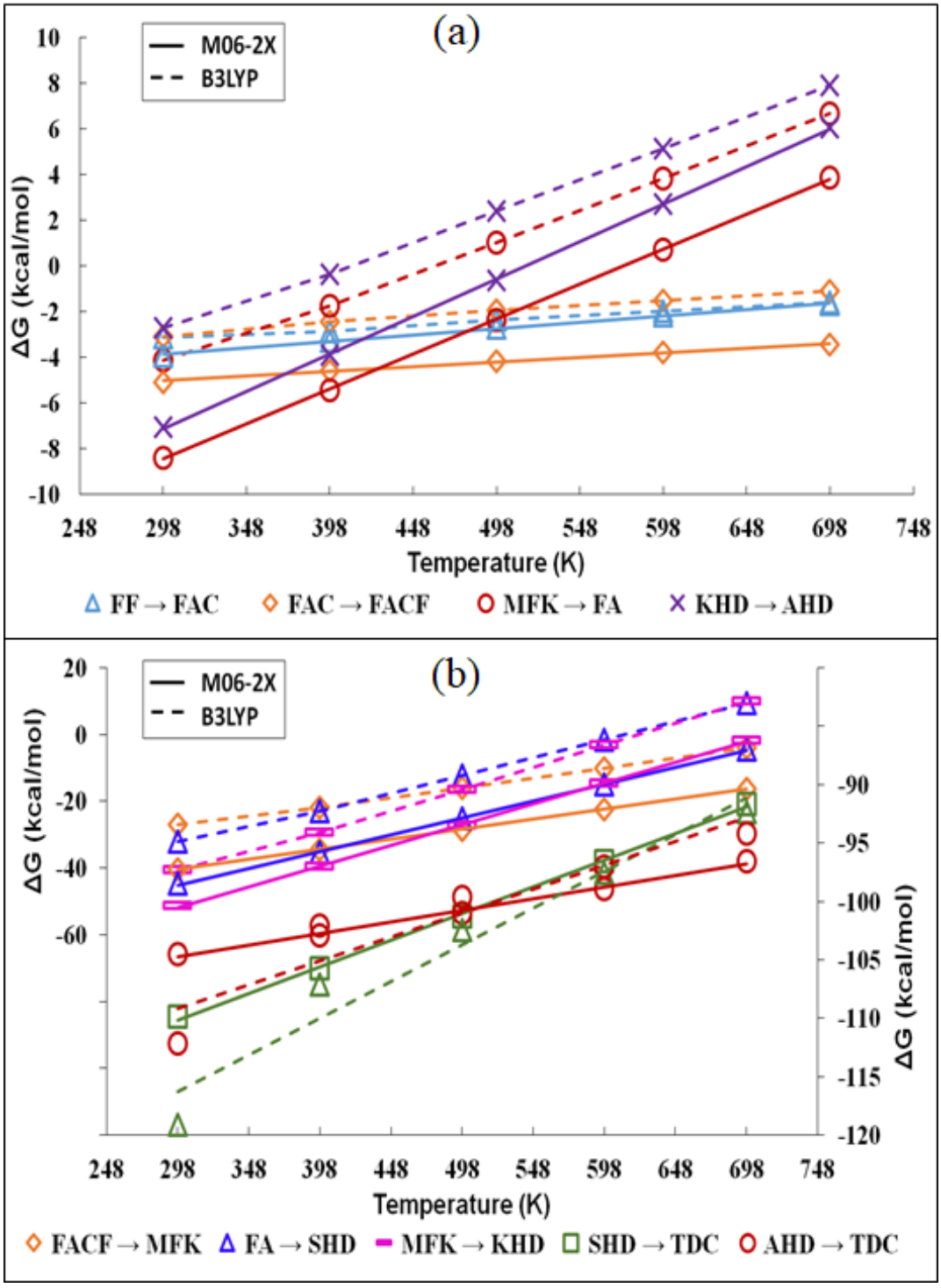

Figure 5.1.7: ΔG vs T plot with B3LYP and M06-2X functional for conversions of RS 4

has an enthalpy change of 1.4 kcal/mol in the gas phase. This makes the aqueous phase energetically favorable for FF to FAC conversion. Increase in temperature does not have much influence as ΔH increase to -4.18 kcal/mol and -5.02 kcal/mol at 698 K for respective

functionals. Also, ΔG remains mostly unaffected by rising temperature and increase by less than 2 kcal/mol; from -3.14 kcal/mol at 298 K to -1.57 kcal/mol at 698 K for B3LYP and -3.92 kcal/mol to -1.66 kcal/mol for M06-2X (Figure 5.1.7(a)). In RS 4a, FAC to FACF conversion exhibit ΔH = -4.55 kcal/mol and -6.70 kcal/mol with B3LYP and M06-2X functionals respectively. Liu et al. [91] report enthalpy change as 2.8 kcal/mol for this reaction in gas phase making the reaction more favorable in the aqueous phase. The ΔG and ΔH are not much influenced by temperature increment for this reaction either. However, FACF to MFK conversion exhibit strong temperature dependence which leads to increase in ΔG from -26.97 kcal/mol at 298 K to -4.05 kcal/mol at 698 K for B3LYP and -40.28 kcal/mol to -16.13 kcal/mol for M06-2X at respective temperatures. With ΔG = -15.7 kcal/mol, the reaction is less favorable in the gas phase as reported by Liu et al. [91]. ΔH for this conversion is found to be -43.43 kcal/mol with B3LYP and -57.12 kcal/mol with M06-2X functional whereas the gas phase enthalpy change reported by Liu et al. [91] is -23.5 kcal/mol. This again shows that aqueous medium can be preferred phase for the conversion to occur. With the difference of less than 3 kcal/mol between 298 K and 698 K for both the functionals, enthalpy change does not seem to be affected much by rise in temperature. With the increase in temperature, ΔG is found to increase in most of the reaction steps in RS 4a. As a consequence, conversion of MFK to FA and FA to SHD reach positive or close to zero ΔG at a higher temperature, showing the conversion to be not very feasible at extreme conditions. However, SHD to TDC and AHD to TDC show very high spontaneity at all temperatures. They have been depicted on the secondary y-axis (see Figure 5.1.7(b)). The enthalpy change for the conversion of AHD to TDC is reported by Liu et al. [91] as -71.9 kcal/mol whereas this study found it to be -108.81 kcal/mol with M06-2X and -117.19 kcal/mol with B3LYP functional. This is significantly lower than the gas phase ΔH suggesting high enthalpy change favorability in the aqueous phase. Similarly, in RS 4b, MFK to KHD and KHD to AHD show positive or close to zero ΔG at higher temperatures.

Table 5.1.4: Entropy change (ΔS) in Kcal $mol^{-1}K^{-1}$ for all conversion steps at varying temperature using B3LYP and M06-2X functional.

	298 K		**398 K**		**498 K**		**598 K**		**698 K**	
	M06-2X	B3LYP	M06-2X	B3LYP	M06-2X	B3LYP	M06-2X	B3LYP	M06-2X	B3LYP
XYL → FF	0.45	0.45	0.46	0.46	0.46	0.46	0.45	0.45	0.45	0.45
FF → FRN	0.15	0.15	0.15	0.15	0.15	0.15	0.15	0.15	0.15	0.15
FRN → THF	-0.23	-0.23	-0.24	-0.24	-0.25	-0.25	-0.26	-0.26	-0.26	-0.26
THF → BOL	-0.09	-0.09	-0.09	-0.09	-0.09	-0.09	-0.09	-0.09	-0.09	-0.09
BOL → BAN	0.02	0.02	0.02	0.02	0.01	0.01	0.01	0.01	0.01	0.01
FF → FOL	-0.11	-0.11	-0.12	-0.12	-0.12	-0.12	-0.12	-0.12	-0.12	-0.12
FOL → 2MF	0.03	0.03	0.03	0.03	0.02	0.02	0.02	0.02	0.02	0.02
2MF → MTHF	-0.24	-0.24	-0.25	-0.25	-0.26	-0.26	-0.26	-0.26	-0.27	-0.27
MTHF → POL	-0.09	-0.09	-0.09	-0.09	-0.09	-0.09	-0.09	-0.09	-0.10	-0.10
MTHF → PAD	0.03	0.03	0.04	0.04	0.04	0.04	0.04	0.04	0.04	0.04
PAD → POL	-0.13	-0.13	-0.13	-0.13	-0.13	-0.13	-0.13	-0.13	-0.13	-0.13
POL →PAN	0.03	0.03	0.02	0.02	0.02	0.02	0.02	0.02	0.01	0.01
FF → THFOL	-0.36	-0.36	-0.37	-0.37	-0.38	-0.38	-0.39	-0.39	-0.39	-0.39
THFOL → PDOL	-0.09	-0.09	-0.09	-0.09	-0.09	-0.09	-0.09	-0.09	-0.10	-0.10
PDOL → PAN	0.06	0.06	0.05	0.05	0.04	0.04	0.04	0.04	0.04	0.04
THFOL → PAOL	-0.10	-0.10	-0.10	-0.10	-0.10	-0.10	-0.10	-0.10	-0.10	-0.10

PAOL → PAN	0.06	0.06	0.05	0.05	0.05	0.05	0.04	0.04	0.04	0.04
FF → FAC	-0.03	-0.03	-0.02	-0.02	-0.02	-0.02	-0.02	-0.02	-0.02	-0.02
FAC → FACF	-0.02	-0.02	-0.02	-0.02	-0.02	-0.02	-0.02	-0.02	-0.02	-0.02
FACF → MFK	-0.23	-0.23	-0.24	-0.24	-0.25	-0.25	-0.25	-0.25	-0.25	-0.25
MFK → FA	-0.11	-0.11	-0.11	-0.11	-0.12	-0.12	-0.12	-0.12	-0.12	-0.12
FA → SHD	-0.42	-0.42	-0.44	-0.44	-0.45	-0.45	-0.46	-0.46	-0.46	-0.46
SHD → TDC	-0.16	-0.16	-0.19	-0.19	-0.20	-0.20	-0.21	-0.21	-0.22	-0.22
MFK → KHD	-0.50	-0.50	-0.53	-0.53	-0.55	-0.55	-0.56	-0.56	-0.56	-0.56
KHD → AHD	-0.11	-0.11	-0.11	-0.11	-0.12	-0.12	-0.12	-0.12	-0.11	-0.11
AHD → TDC	-0.07	-0.07	-0.09	-0.09	-0.11	-0.11	-0.11	-0.11	-0.12	-0.12
FAC → DHF	-0.12	-0.12	-0.13	-0.13	-0.13	-0.13	-0.13	-0.13	-0.13	-0.13
DHF → STHF	-0.36	-0.36	-0.38	-0.38	-0.39	-0.39	-0.40	-0.40	-0.40	-0.40
STHF → BTHF	0.04	0.04	0.03	0.03	0.03	0.03	0.03	0.03	0.02	0.02
BTHF → OOL	-0.10	-0.10	-0.10	-0.10	-0.10	-0.10	-0.10	-0.10	-0.10	-0.10
OOL → OCT	0.03	0.03	0.03	0.03	0.03	0.03	0.03	0.03	0.02	0.02
BTHF → OAL	0.02	0.02	0.02	0.02	0.03	0.03	0.03	0.03	0.03	0.03
OAL → OOL	-0.12	-0.12	-0.12	-0.12	-0.12	-0.12	-0.12	-0.12	-0.13	-0.13

It is worth noting here that in MFK → KHD conversion, the entropy change is found to be highly negative (Table 5.1.4), suggesting that the increase in the enthalpy change is being offset by the entropy. As a result the free energy change is close to zero. Though not substantially but ΔH of both pathways, i.e., RS 4a and RS 4b, decrease with increase in temperature except for final conversion step, i.e., SHD to TDC and AHD to TDC. The reaction steps SHD to TDC and AHD to TDC show an increase in enthalpy change with the increase in temperature. With ΔH_{298} of -130.65 kcal/mol at B3LYP and -121.54 kcal/mol at M06-2X at 298 K, SHD to TDC is the most exothermic step in RS 4a.

5.1.1.5 Formation of Octane

In RS 5, FAC to 4-(furan-2-yl)but-3-en-2-ol (DHF) conversion is barely spontaneous at 298 K with ΔG value of -1.03 kcal/mol at B3LYP and -7.04 kcal/mol at M06-2X. However, with an increase in temperature, ΔG becomes positive at 698 K making it non-spontaneous (Figure 5.1.6(b)). A similar trend is observed for Gibb's free energy change in conversion of OAL to OOL where conversion is slightly spontaneous at 298 K but becomes unfavorable with an increase in temperature. Conversion of DHF to STHF and BTHF to OOL also show a similar trend; however, the conversion remains almost spontaneous even at high temperature. On the contrary, ΔG reduces by about 3 kcal/mol for STHF to BTHF, OOL to OCT and BTHF to OAL conversions at 698 K temperature resulting in an increase in the feasibility of the reaction. The change in ΔH is found to be favorable with the increase in temperature for all conversion steps of RS 5 except BTHF to OAL. The increment in ΔH with the increase in temperature decreases the exothermicity of conversion.

5.1.2 Single Point Energetics (SPE)

Single point energy change (ΔE) of each step of all pathways (RS 1- RS 5) is calculated in the aqueous phase and shown in Figure 5.1.8 at M05-2X/6-311++g(3df,2p) level of theory. As

shown by Dahlke et al. [160], the M05-2X functional is better at predicting single point energetics than its counterpart functionals reported in the study. Thus in this study, SPE simulations have been performed using M05-2X functional. The dehydration of XYL to FF is common in all the reaction schemes and has a ΔE value of 11.36 kcal/mol. In RS 1, the decarbonylation of FF to produce FRN appears to be the most energy-intensive step requiring 15.85 kcal/mol of energy change making the conversion less preferred than its predecessor. Further, when FRN is hydrogenated to THF, the energy requirement is calculated to be -80 kcal/mol making it the most exothermic conversion step in RS 1 (Figure 5.1.8(a)). The reaction energy for this conversion has been reported by Vlachos et al.[161] in the gas phase to be -48.88 kcal/mol. This makes it the most favorable step of RS 1. The energy change of further hydrogenation of THF to form BOL is calculated to be -42.10 kcal/mol. Finally, hydrogenation of BOL yielding BAN and a water molecule is calculated to have ΔE of -38.96 kcal/mol which is slightly less energetically favorable than THF to BOL conversion.

In RS 2, FF to FOL conversion requires -38.36 kcal/mol of energy change. The FOL is then hydrogenated to produce 2MF and a water molecule, a step which has ΔE of -42.39 kcal/mol. Further, hydrogenation of 2MF to produce MTHF is calculated to be the most negative energy change reaction step in RS 2 with ΔE of -79.25 kcal/mol making it highly favorable over other conversions. This can be further understood by the corresponding ΔG (see Figure 5.1.5(b)) and ΔH (Table 5.1.2) values. The high negative enthalpy change suggests an exothermic reaction, and the ΔG values increase with the increase in temperature suggesting lower temperature conditions are better for the reaction to proceed. Further, energy difference of MTHF to PAD conversion is calculated to be -15.82 kcal/mol and the same for MTHF to POL conversion is calculated to be -38.41 kcal/mol which is almost similar to ΔE of conversion of POL to PAN, i.e., -38.79 kcal/mol.

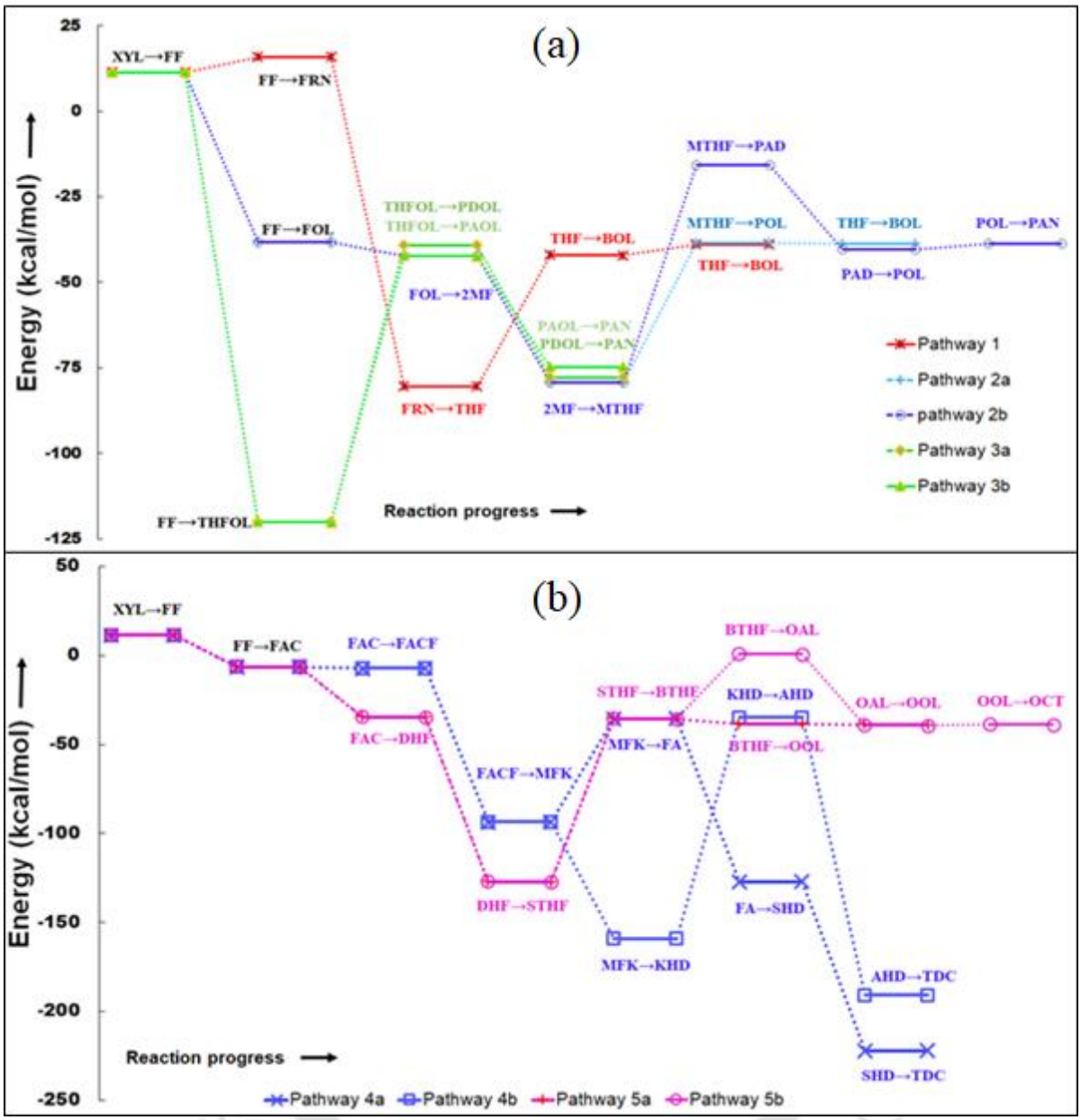

Figure 5.1.8: Single Point Energy difference (ΔE) diagram with M05-2X for (a) RS 1, 2 and 3 (b) RS 4 and RS 5.

In RS 3, ΔE for hydrogenation of FF to produce THFOL is calculated to be very high (-120.19 kcal/mol). Further in RS 3a, while reaction energy of hydrogenation of THFOL to produce PDOL is highly favorable with ΔE equal to -39.21 kcal/mol, it is slightly more favorable when compared to the conversion of THFOL to PAOL in RS 3b with ΔE of -42.33 kcal/mol. This favorability for pentane-1,5-diol is also reported by Chen et al. [162] in the energy profile of conversion of THFOL to PAN over Rh (111) catalyst in the gas phase.

Table 5.1.5: Gibbs free energy change (ΔG) in Kcal/mol for all conversion steps at varying temperature using B3LYP and M06-2X functional.

	298 K		**398 K**		**498 K**		**598 K**		**698 K**	
	M06-2X	B3LYP	M06-2X	B3LYP	M06-2X	B3LYP	M06-2X	B3LYP	M06-2X	B3LYP
XYL → FF	-28.63	-46.45	-39.81	-59.03	-51.07	-69.95	-62.31	-80.85	-73.48	-91.68
FF → FRN	3.43	6.82	-0.22	3.34	-3.87	-0.31	-7.51	-3.96	-11.12	-7.57
FRN → THF	-26.47	-22.83	-20.72	-18.18	-14.74	-12.23	-8.61	-6.15	-2.39	0.02
THF → BOL	-19.34	-18.99	-17.20	-17.33	-15.04	-15.16	-12.88	-12.99	-10.71	-10.81
BOL → BAN	-25.12	-26.80	-25.59	-27.10	-26.00	-27.44	-26.34	-27.73	-26.63	-27.96
FF → FOL	-11.89	-5.70	-9.15	-3.35	-6.34	-0.56	-3.49	2.26	-0.61	5.11
FOL → 2MF	-28.53	-30.24	-29.18	-31.02	-29.76	-31.61	-30.27	-32.14	-30.74	-32.61
2MF → MTHF	-25.68	-20.55	-19.81	-15.26	-13.70	-9.15	-7.46	-2.89	-1.13	3.43
MTHF → POL	-14.22	-14.79	-11.97	-12.86	-9.69	-10.62	-7.39	-8.36	-5.07	-6.09
MTHF → PAD	-1.35	-6.47	-2.17	-7.28	-3.04	-8.18	-3.94	-9.11	-4.86	-10.05
PAD → POL	-12.87	-8.32	-9.81	-5.58	-6.65	-2.44	-3.44	0.74	-0.21	3.96
POL →PAN	-24.97	-26.98	-25.53	-27.63	-26.02	-28.10	-26.44	-28.51	-26.81	-28.86
FF → THFOL	-39.58	-27.67	-30.86	-19.96	-21.83	-10.97	-12.62	-1.82	-3.29	7.43
THFOL → PDOL	-14.96	-15.82	-12.77	-13.89	-10.54	-11.66	-8.29	-9.40	-6.03	-7.13
PDOL → PAN	-50.74	-54.78	-52.01	-56.27	-53.14	-57.41	-54.14	-58.42	-55.03	-59.33
THFOL → PAOL	-18.30	-18.17	-15.90	-16.15	-13.49	-13.86	-11.07	-11.55	-8.64	-9.24

PAOL → PAN	-47.41	-52.42	-48.88	-54.01	-50.19	-55.21	-51.36	-56.27	-52.42	-57.21
FF → FAC	-3.92	-3.14	-3.26	-2.83	-2.68	-2.37	-2.15	-1.95	-1.66	-1.57
FAC → FACF	-5.07	-3.08	-4.58	-2.42	-4.15	-1.93	-3.78	-1.50	-3.44	-1.10
FACF → MFK	-40.28	-26.97	-34.49	-21.91	-28.48	-16.06	-22.34	-10.09	-16.13	-4.05
MFK → FA	-8.38	-4.13	-5.42	-1.75	-2.37	1.02	0.74	3.84	3.87	6.68
FA → SHD	-44.75	-32.09	-35.15	-22.82	-25.13	-12.23	-14.87	-1.41	-4.45	9.55
SHD → TDC	-109.88	-110.23	-105.77	-107.11	-101.31	-102.46	-96.58	-97.53	-91.64	-92.38
MFK → KHD	-51.44	-40.48	-39.54	-29.30	-27.17	-16.44	-14.52	-3.26	-1.70	10.10
KHD → AHD	-7.04	-2.72	-3.88	-0.35	-0.61	2.40	2.71	5.15	6.06	7.89
AHD → TDC	-104.52	-103.25	-102.92	-102.03	-101.02	-99.63	-98.90	-96.98	-96.59	-94.15
FAC → DHF	-7.09	-1.03	-4.12	1.82	-1.06	4.89	2.05	7.99	5.18	11.11
DHF → STHF	-47.05	-36.74	-38.19	-28.82	-28.97	-19.64	-19.55	-10.27	-10.00	-0.79
STHF → BTHF	-21.27	-24.72	-21.93	-25.70	-22.49	-26.47	-22.98	-27.15	-23.41	-27.78
BTHF → OOL	-15.45	-15.35	-13.49	-13.32	-11.49	-10.98	-9.48	-8.63	-7.46	-6.27
OOL → OCT	-25.71	-27.81	-26.43	-28.70	-27.08	-29.41	-27.68	-30.05	-28.22	-30.64
BTHF → OAL	-2.76	-7.05	-3.55	-7.53	-4.39	-8.11	-5.26	-8.72	-6.16	-9.35
OAL → OOL	-12.68	-8.30	-9.94	-5.79	-7.11	-2.87	-4.22	0.09	-1.30	3.08

Similarly, with ΔE of -77.82 kcal/mol, the energetics of conversion of PDOL to PAN in RS 3a is only slightly less energy intensive than the conversion of PAOL to PAN in RS 3b (ΔE = -74.69 kcal).

ΔE of all reaction steps of RS 4 and RS 5 is shown in Figure 5.1.8(b). The reaction energy of the conversion of XYL to FF is again 11.36 kcal/mol. The FF is then converted to FAC with the addition of acetone and removal of water which requires ΔE of -6.35 kcal/mol making it slightly more energetically favorable. Again, conversion of FAC to FACF, which includes the addition of FF and removal of water in RS 4, has comparable ΔE of -7.10 kcal/mol with FF to FAC conversion, while reaction energy for hydrogenation of FACF to produce MFK is calculated as -93.45 kcal/mol suggesting highly favorable energetics. MFK is then hydrogenated *via* RS 4a in two steps to produce FA followed by SHD with reaction energies of -35.63 kcal/mol and -127.18 kcal/mol respectively. The formation of FA to SHD is highly favorable and from ΔG value of -44.75 kcal/mol, it can be seen that this step is fairly spontaneous as well. Similarly, in RS 4b, MFK is hydrogenated in two steps to produce KHD followed by AHD with ΔE of -159.07 kcal/mol and -34.93 kcal/mol respectively. In the last reaction step of both schemes (RS 4a and RS 4b), the conversion of SHD to TDC has ΔE of -221.98 kcal/mol and energy change of -190.79 kcal/mol is calculated in conversion AHD to TDC. This suggests that the final conversion step of both reaction schemes are highly favorable. This is also in agreement with the spontaneity of both conversions (Table 5.1.5). In RS 5, while energy change during hydrogenation of FAC to produce DHF is -34.56 kcal/mol, further hydrogenation to obtain STHF has calculated energy difference of -127.09 kcal/mol making DHF to STHF highly preferred reaction. Subsequent hydrogenation and dehydration of STHF yield BTHF which has ΔE of -35.45 kcal/mol. BTHF can be further directly hydrogenated *via* RS 5a to obtain OOL with ΔE of -38.72 kcal/mol. BTHF can also be converted into OAL but with ΔE equal to 0.74 kcal/mol, it is not the most favorable conversion. OAL can be further

hydrogenated to obtain OOL with an energy difference of -39.46 kcal/mol. Finally, the energy difference for the conversion of OOL to OCT is calculated to be -38.86 kcal/mol.

The conversion of XYL to four different alkanes- butane, pentane, tridecane, and octane has been studied using five different pathways using B3LYP and M06-2X functional. It is observed that the conversion of FF to FRN is not very spontaneous at low temperature which makes the scheme RS 1 not very feasible at 298 K. At high temperature (698 K), except RS 1, no other pathway can proceed to completion due to the fact that several intermediate reaction steps, such as FF to FOL, MFK to FA, etc. are not feasible at high temperature. The single point energy calculation of all reaction steps also concur with this observation. In the comparison between B3LYP and M06-2X functionals, the absolute difference went as. high as 20.57 kcal/mol for ΔH of conversion of XYL to FF. But at the same time, it was as low as 0.10 kcal/mol for ΔG of conversion of THF to BOL. The average absolute error is found to be in the acceptable range of errors (± 5 kcal/mol) for specific systems.

5.2 DFT Study on Dibenzofuran Conversion to Cyclohexane and Benzene in Gas, Water and Methanol Solvents

In this study, dibenzofuran (DBF) is converted to cyclohexane and benzene via a network of pathways. All the structures are given a number whereas all the reactions are identified by alphabets for easy reference. The individual reaction pathways are described using all the reactions labels that appear in the pathway in a sequence. For example, pathway **-h-l-m** describes the conversion of structure **1** to structure **7** with structure **9** and **11** as intermediates via reactions –**h**–, –**l**– and –**m**–.

Satterfield et al. [163] report that the upgrading proceeds via two major routes – one via saturation of phenyl ring to form 2-cyclohexylphenol, which further disintegrates into single-ring hydrocarbons. And the other where direct hydrogenolysis of DBF occurs to form 2-phenylphenol followed by saturation to form cyclohexyl benzene and biphenyl. Thus the reaction network here initiates with two major pathways **-a-b-c-d-e-** and **-h-l-m**. In pathway **-a-b-c-d-e-**, dibenzofuran (structure **1**) is first converted to 1,2,3,4,4a,9b-hexahydrodibenzo[b,d]furan (structure **2**) by saturation of one aromatic ring. Then, structure **2** is converted to 2-cyclohexylphenol (structure **3**) by the opening of the furan ring of structure **2**. Saturation of structure **3** produces bi(cyclohexan)-2-ol (structure **4**). In addition, structure **2** can be converted to structure **12** in reaction –**p**– by hydrogenation of the ring, which is further converted to structure **4** in reaction –**q**–. Structure **4** is then dehydrogenated to produce bicyclohexane (structure **5**) which is further hydrogenated to yield two molecules of cyclohexane (structure **8**). Alternatively, in pathway **-a-b-f-g-**, production of cyclohexylbenzene (structure **6**) can also be achieved by dehydroxylation of structure **3**. Further hydrogenolysis of structure **6** produces benzene (structure **7**) and cyclohexane (structure **8**) via the same pathway structure 6 can also be hydrogenated to produce structure **5** via reaction **-o-** to subsequently yield 2 molecules of structure **8**.

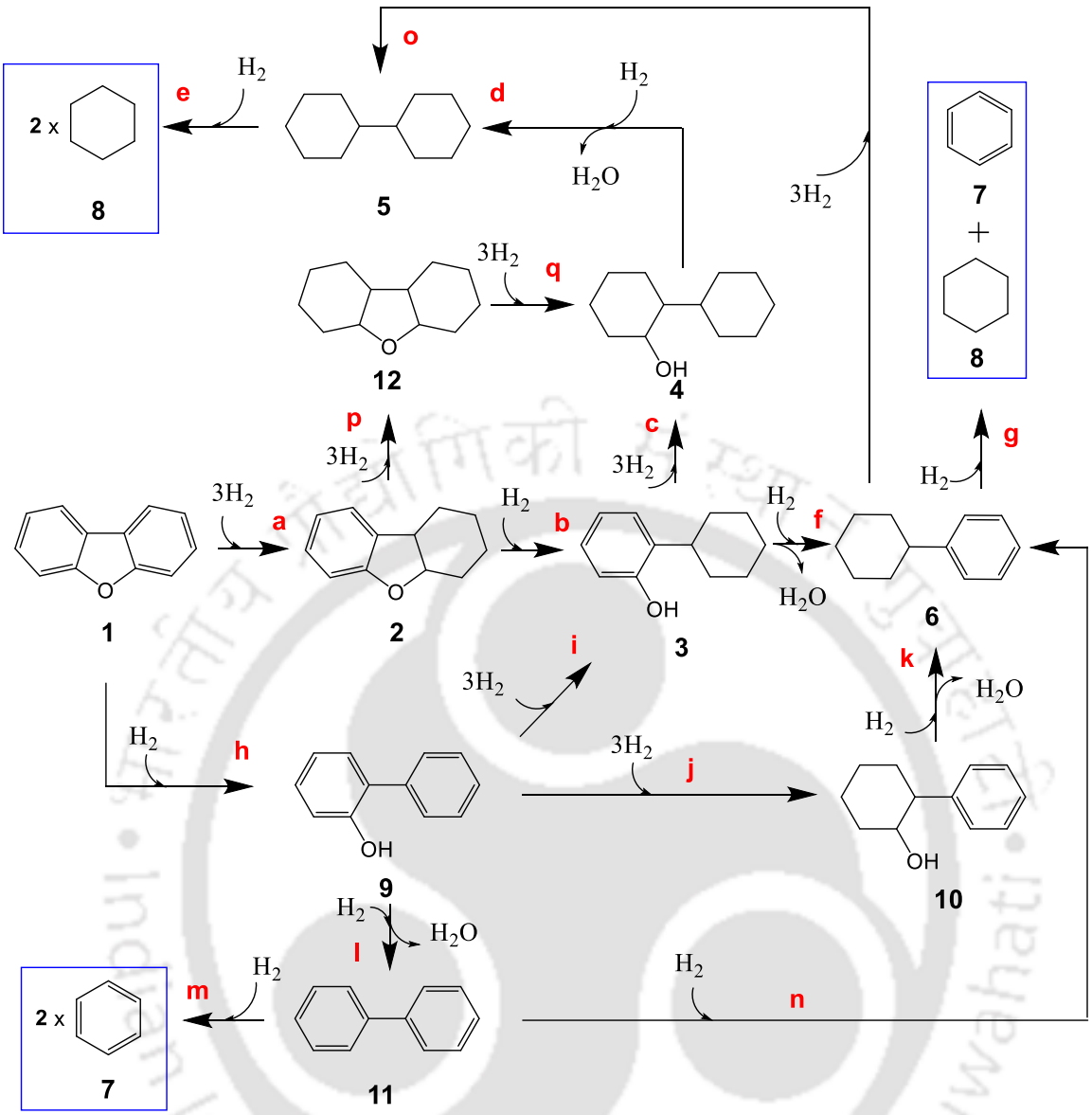

Reaction Scheme: All reactions describing the conversion of dibenzofuran to cyclohexane and benzene.

In pathway **-h-l-m**, dibenzofuran is converted to 2-phenylphenol (Structure **9**) by hydrogenolysis of C-O bond of structure **1** in reaction –**h**–. Structure **9** is then dehydroxylated to produce biphenyl (structure **11**) in reaction –**l**–**,** which is further hydrogenated to produce benzene. Structure **11** can also be saturated to form structure **6** through reaction –**n**–.

In pathways **-h-i-c-d-e-** and **-h-i-f-g-**, structure **9** undergoes saturation of one aromatic ring to produce structure **3** via reaction –**i**–. Dehydroxylation of structure **3** produce structure **6**

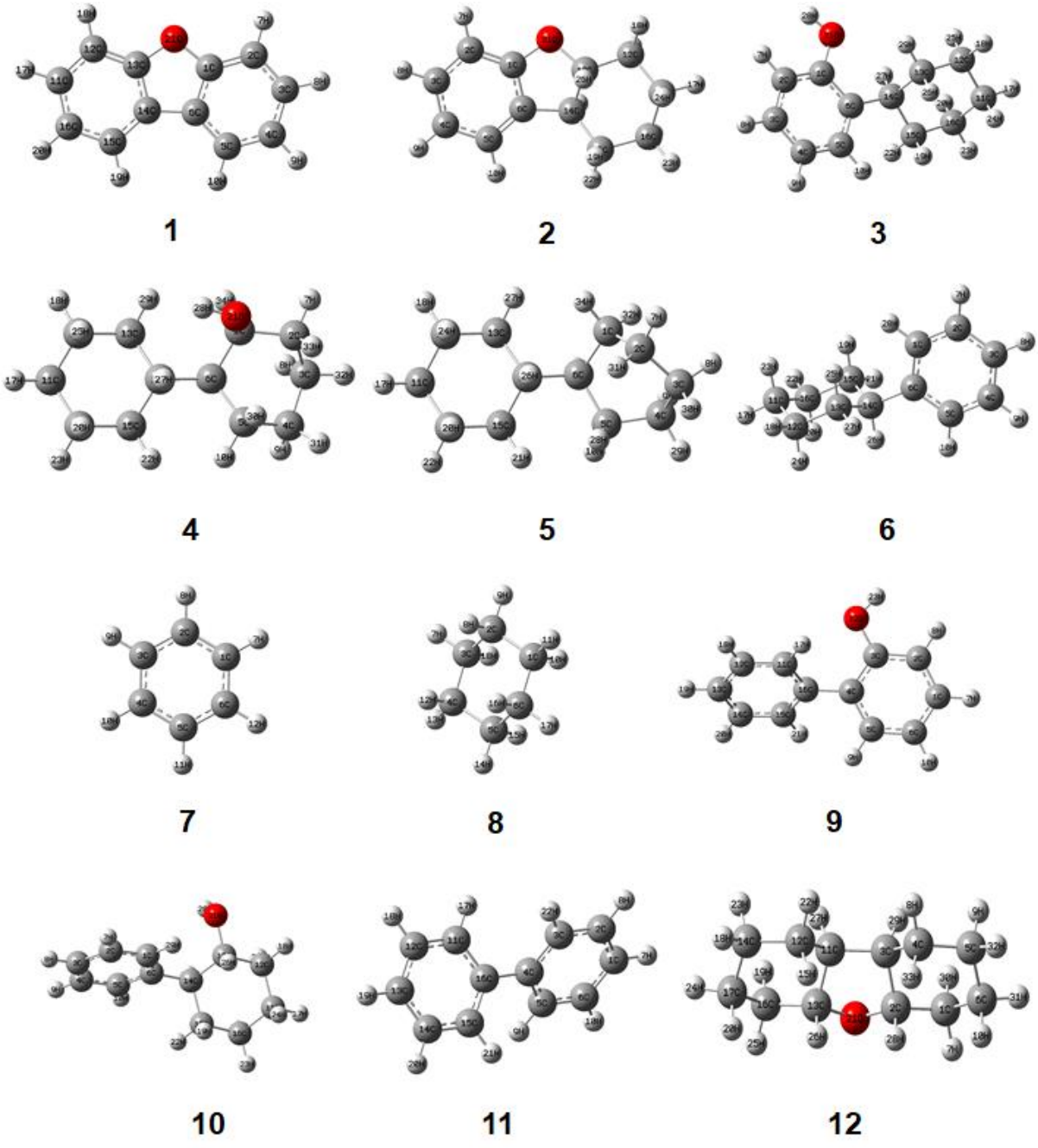

Figure 5.2.1: Molecular structure of all the reactants, intermediates and products optimized in gas phase.

in reaction –**f**– to further produce benzene and cyclohexane. Whereas, the saturation of structure **3** in reaction –**c**– produces structure **4** to yield cyclohexane as discussed in pathway **-a-b-c-d-e-**.

Finally, in pathway **-h-j-k-g-**, saturation of the phenol ring of structure **9** produce 2-phenylcyclohexan-1-ol (structure **10**) in reaction –**j**–. Dehydroxylation of structure **10** in reaction –**k**– yields structure **6** to produce structure **7** and **8**.

Density functional theory (DFT) is used to conduct all the simulations in this study. M06-2X functional [164] along with split-valence triple-zeta basis set with diffuse functions for all heavy atoms and polarization functions on non-hydrogen atom (6-311+g(d)) is used to conduct geometry optimization and frequency calculation in the gas phase. SMD solvation model [145] is used to incorporate the solvent effect with methanol and water as solvents.. Geometry optimization and frequency calculation are performed for all structures with SMD solvation model. Thermochemical parameters namely Gibbs free energy change (ΔG) and enthalpy change (ΔH) are calculated at 298 K to 598 K temperature at 1 atm pressure. Water and hydrogen molecules are also optimized at the above described level of theory in respective mediums and accounted for in the thermochemistry calculations. Finally, solvation free energy is calculated as:

$$\Delta G_{solv} = G_{solvent} - G_{gas} \tag{5.1}$$

Where ΔG_{solv} is the solvation free energy, $G_{solvent}$ is the sum of electronic and thermal free energies in the liquid phase, and G_{gas} is the sum of electronic and thermal free energies in the gas phase.

Single point energy is also calculated in the gas phase at M05-2X/6-31+g(3df,2p)//M06-2X/6-311+g(d) level of the theory under the DFT framework. All

simulations in this study are conducted with Gaussian 09 [147] using the ultrafine grid as recommended by the software manual for M05-2X and M06-2X functionals. Visualization of all structures is performed by GaussView 05 [154] software. The optimized molecular geometry of all structures in gas phase are presented in Figures 5.2.1

Table 5.2.1: Enthalpy change (ΔH) in kcal/mol of all the reactions from 298-598 K in the gas phase, as well as in water and methanol.

Reactions		**ΔH (kcal/mol)**			
	Temperature	**298**	**398**	**498**	**598**
a	gas	-44.31	-45.77	-46.93	-47.79
	water	-50.27	-51.71	-52.85	-53.69
	methanol	-46.82	-48.26	-49.40	-50.24
b	gas	-20.40	-20.57	-20.71	-20.80
	water	-24.26	-24.45	-24.60	-24.69
	methanol	-23.36	-23.55	-23.69	-23.78
c	gas	-45.87	-47.33	-48.49	-49.36
	water	-50.03	-51.48	-52.64	-53.49
	methanol	-46.20	-47.64	-48.79	-49.65
d	gas	-12.12	-12.46	-12.82	-13.19
	water	-18.02	-18.34	-18.69	-19.04
	methanol	-17.50	-17.82	-18.17	-18.52
e	gas	-14.53	-15.15	-15.73	-16.26
	water	-15.54	-16.19	-16.79	-17.34
	methanol	-15.94	-16.56	-17.14	-17.66
f	gas	-9.59	-9.97	-10.35	-10.73
	water	-17.09	-17.46	-17.84	-18.23
	methanol	-16.25	-16.61	-16.99	-17.37
g	gas	-6.39	-7.03	-7.61	-8.13
	water	-7.43	-8.08	-8.67	-9.20
	methanol	-7.40	-8.04	-8.63	-9.15
h	gas	-9.10	-9.31	-9.46	-9.55
	water	-15.97	-16.19	-16.35	-16.46
	methanol	-15.00	-15.22	-15.38	-15.49
i	gas	-55.60	-57.04	-58.18	-59.03
	water	-58.56	-59.97	-61.09	-61.92
	methanol	-55.18	-56.59	-57.71	-58.53
j	gas	-52.22	-53.65	-54.79	-55.64
	water	-58.29	-59.71	-60.83	-61.67
	methanol	-54.44	-55.86	-56.99	-57.83
k	gas	-12.97	-13.35	-13.74	-14.12
	water	-17.37	-17.73	-18.10	-18.48
	methanol	-16.99	-17.34	-17.71	-18.08

l	gas	-11.05	-11.42	-11.81	-12.19
	water	-17.91	-18.29	-18.69	-19.08
	methanol	-17.05	-17.42	-17.81	-18.19
m	gas	-4.01	-4.67	-5.25	-5.77
	water	-6.10	-6.75	-7.32	-7.83
	methanol	-5.78	-6.44	-7.03	-7.55
n	gas	-54.15	-55.58	-56.72	-57.58
	water	-57.75	-59.14	-60.25	-61.07
	methanol	-54.38	-55.78	-56.89	-57.71

5.2.1 Thermochemistry

The thermochemical parameters (ΔG, ΔH and K_{eq}) of all reactions presented in the scheme 1 are calculated at M06-2X/6-311+g(d) level of theory in the gas phase and with water and methanol as solvents using SMD implicit solvation model. The effect of temperature on all parameters is calculated from 298 K to 598 K temperature at 1 atm pressure. The pathways propose two routes of upgrading of DBF- via ring saturation in reaction –**a**– and via opening of the furan ring in –**h**–. The hydrogenation of structure **1** in reaction –**a**– is found to be more spontaneous in all phases over reaction –**h**–. Based on the intermediates obtained in the experimental works [96,98,163,165], The preference of reaction –**a**– over reaction –**h**– is extensively documented. However, the presence of structure **2** has been reported in the literature [166] with low selectivity. The high formation rate and low decomposition rate of structure **2** observed in this study could explain the reason for the same. Water is found to be most suitable solvent for reaction –**a**– with ΔG = -23.92 kcal/mol at 298 K among the three phases (Figure 5.2.2). In addition, the increase in temperature is found to be unfavourable with free energy becoming non-spontaneous (ΔG = 4.12 kcal/mol for water) at 598 K in all phases. This observation is in line with the works of Dong *et* al. [98] who report lower temperatures to be favourable for better conversion of DBF; as the temperature was reduced from 200 °C to 150 °C, the conversion of DBF dropped from 99% to 79%. However, the enthalpy change is not much affected by the temperature change and remains almost steady over the studied temperature range for both the reactions (–**a**– and –**h**–) in all phases as can be seen in Table

5.2.1. Thus, water appears to be a better choice for upgrading along the route of reaction –**a**–. But in order to be more certain of the solvent choice, one could look at the free energy of solvation (ΔG_{solv}) data which shows the ease of separation of compounds from the solvents. Here, structure **1** appears to be easier to separate from the solvents than structure **9** as can be seen in Table 5.2.2 with water being more favourable than methanol for separation. Further discussion on the upgrading is broken into two subsections. The first section discusses the upgrading along the ring saturation route and the second subsection discusses the upgrading route along the opening of furan ring of DBF.

Table 5.2.2: Free energy of solvation (ΔG_{solv}) values for all the structures described in the reaction scheme

Structure number	**ΔG_{solv} (kcal/mol)**	
	Water solvent	**Methanol solvent**
1	-3.95	-8.19
2	-4.74	-9.98
3	-6.89	-12.71
4	-5.60	-12.19
5	0.92	-6.71
6	-1.99	-8.62
7	-1.91	-5.19
8	0.80	-3.96
9	-9.19	-13.92
10	-9.77	-15.03
11	-3.37	-8.82
12	-4.36	-10.35

5.2.1.1 Ring saturation upgrading route of DBF

The formation of structure **2** from the DBF is proceeded by reaction –**b**– and –**p**– where structure **2** is further subjected to hydrogenolysis and hydrogenation respectively. In reaction -**p**-, structure **2** is hydrogenated, which is spontaneous in all the phases. The experimental works do not report the presence of structure **2** with high selectivity due to its quick subsequent conversion [98]. ΔG for this reaction is most negative for water and least negative for gas at all temperatures. The difference between the water and methanol spontaneity is ~5 kcal/mol at all

temperature. The increase in temperature is found to be unfavourable as the ln K reduce from 34.56 at 298 K to become –6.63 at 598 K in gas phase. Methanol solvent offers slight advantage over gas phase with difference of less than 1.5 kcal/mol in the ΔG of gas and methanol phase being at all temperatures. But the solvation free energy of structure **12** is found to be 2.37 times more negative for methanol than in water. This suggests that the separation of structure **12** will be more difficult from methanol than from water. The enthalpy change of reaction –**p**– is found to be exothermic in all mediums with water showing maximum favourability and gas phase

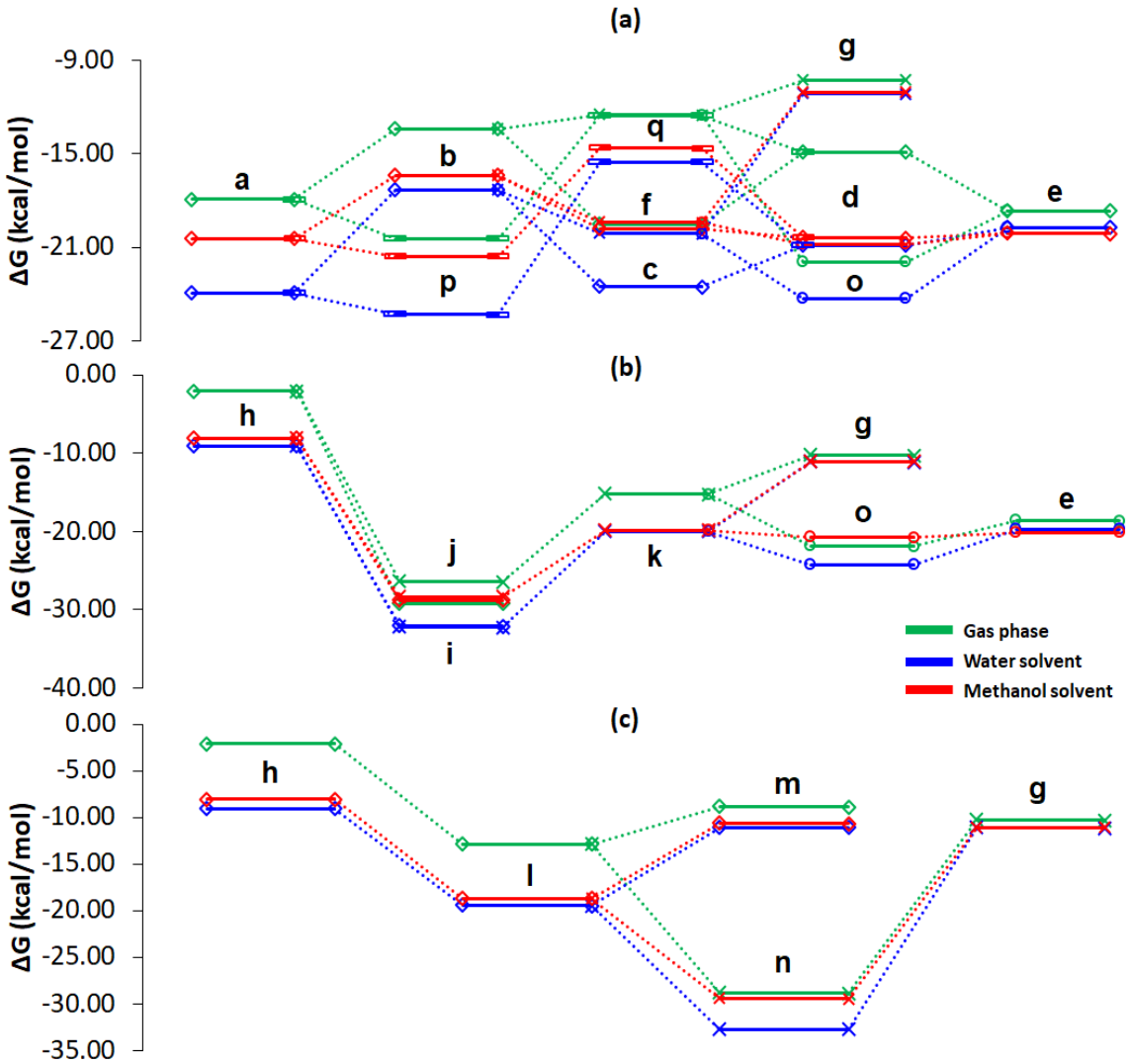

Figure 5.2.2: Gibbs free energy change (ΔG) plot for all reactions in gas, water and methanol at 298 K and 1 atm are shown in (a), (b) and (c).

showing the least (Figure 5.2.3). The difference in ΔH between the two mediums is found to be less than 5 kcal/mol at all temperatures. On the other hand, the conversion of structure **2** to structure **3** in reaction -**b**- shows the highest spontaneity of -17.31 kcal/mol in aqueous phase at 298 K. Thus, the reaction -**p**- is more likely to proceed to completion over reaction -**b**- at room temperature in aqueous phase. The observation of the formation of structure 3 via reaction -**p**- is consistent with several of the experimental reports [46,167,168]. However, this trend changes as the temperature is increased because reaction -**p**- becomes non-spontaneous at 598 K in all mediums. Subsequent conversion of structure **3** to structure **4** in reaction -**c**- is 1.79 kcal/mol more spontaneous than

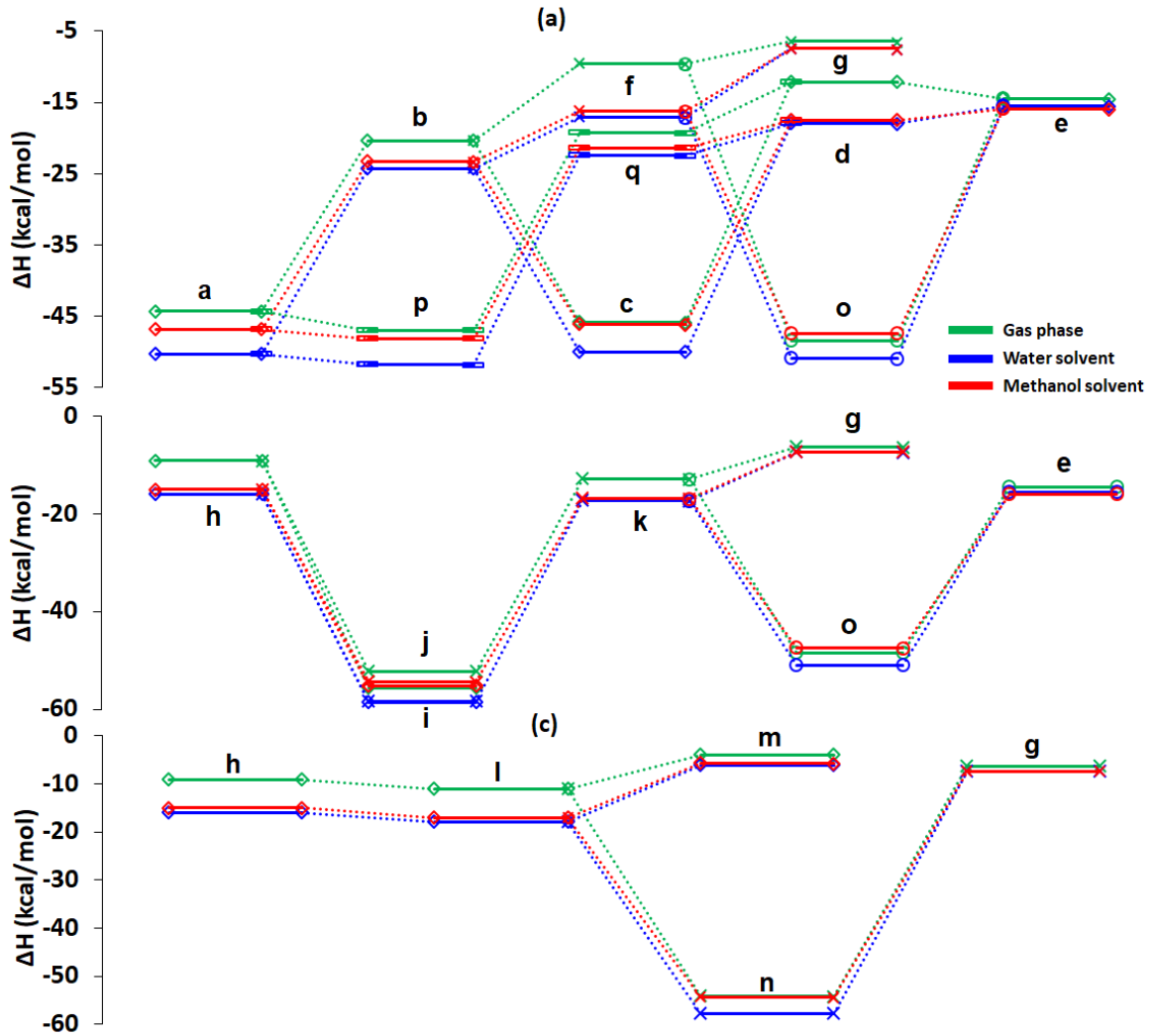

Figure 5.2.3: Free enthalpy change (ΔH) plot of all the reactions in gas, water and methanol solvent at 298 K temperature.

reaction -**q**- in all mediums at 298 K. This means that although reaction -**p**- will attain equilibrium faster than reaction -**b**-, reaction -**c**- would yield structure **4** quicker. The increase in temperature is found to be detrimental to reaction -**b**- as the ln K reduces to 8.55 at 598 K from 29.26 at 298 K. However, the enthalpy change is not affected and stays at constantly exothermicity throughout the studied temperature range in all mediums. With ΔG_{solv} of water being nearly half of methanol for structure **3**, it is again found to be better solvent for this reaction. The hydrogenation of structure **3** in reaction –**c**– is also very spontaneous in all mediums at 298 K. However, increase in temperature causes the spontaneity to decrease. The

Table 5.2.3: Entropy change (ΔS) in Kcal $mol^{-1}K^{-1}$ of all the reactions from 298-598 K in the gas phase, as well as in water and methanol

Reactions		**ΔS (kcal mol^{-1} K^{-1})**			
	Temperature	**298**	**398**	**498**	**598**
a	gas	-0.37	-0.52	-0.67	-0.81
	water	-0.37	-0.52	-0.67	-0.81
	methanol	-0.37	-0.52	-0.67	-0.81
b	gas	-0.10	-0.13	-0.17	-0.20
	water	-0.10	-0.13	-0.17	-0.20
	methanol	-0.10	-0.13	-0.17	-0.20
c	gas	-0.37	-0.52	-0.66	-0.81
	water	-0.37	-0.52	-0.67	-0.82
	methanol	-0.37	-0.52	-0.67	-0.81
d	gas	0.04	0.05	0.05	0.06
	water	0.04	0.05	0.05	0.06
	methanol	0.04	0.05	0.06	0.06
e	gas	0.06	0.07	0.08	0.08
	water	0.06	0.07	0.08	0.08
	methanol	0.06	0.07	0.08	0.08
f	gas	0.04	0.05	0.06	0.06
	water	0.04	0.05	0.06	0.06
	methanol	0.04	0.05	0.06	0.07
g	gas	0.05	0.06	0.07	0.08
	water	0.05	0.06	0.06	0.07

	methanol	0.05	0.06	0.06	0.07
h	gas	-0.10	-0.13	-0.17	-0.21
	water	-0.10	-0.13	-0.17	-0.20
	methanol	-0.10	-0.13	-0.17	-0.20
i	gas	-0.37	-0.52	-0.67	-0.81
	water	-0.37	-0.52	-0.67	-0.81
	methanol	-0.37	-0.52	-0.67	-0.81
j	gas	-0.36	-0.51	-0.65	-0.80
	water	-0.37	-0.51	-0.66	-0.80
	methanol	-0.37	-0.51	-0.66	-0.80
k	gas	0.03	0.04	0.04	0.04
	water	0.04	0.04	0.05	0.05
	methanol	0.04	0.05	0.05	0.06
l	gas	0.03	0.03	0.03	0.03
	water	0.02	0.02	0.02	0.02
	methanol	0.02	0.03	0.03	0.02
m	gas	0.07	0.08	0.09	0.10
	water	0.07	0.08	0.09	0.11
	methanol	0.07	0.08	0.09	0.10
n	gas	-0.35	-0.50	-0.64	-0.78
	water	-0.35	-0.49	-0.63	-0.77
	methanol	-0.35	-0.49	-0.63	-0.77
o	gas	-0.37	-0.52	-0.67	-0.81
	water	-0.37	-0.52	-0.67	-0.82
	methanol	-0.37	-0.52	-0.67	-0.82
p	gas	-0.37	-0.52	-0.67	-0.82
	water	-0.37	-0.52	-0.67	-0.82
	methanol	-0.37	-0.52	-0.67	-0.82
q	gas	-0.09	-0.13	-0.16	-0.20
	water	-0.10	-0.13	-0.17	-0.20
	methanol	-0.09	-0.13	-0.16	-0.20

ln K shows non-spontaneous reaction at 598 K. While the spontaneity of reaction is comparable in gas and methanol solvent, aqueous phase is better by about 4 kcal/mol than gas phase. Further conversion of structure **3** to structure **5** can proceed in two ways – via pathway **-c-d-** and via pathway **-f-o-**. The conversion via pathway **-f-o-** is discussed later in the section. From structure **4**, further conversion into structure **5** in reaction –**d**– is found to be equally spontaneous in water (ΔG = -20.85 kcal/mol) and methanol (ΔG = -20.38 kcal/mol) and is about 6 kcal/mol higher than gas phase (ΔG = -14.90 kcal/mol) at 298 K temperature. The enthalpy change is also found to be comparable between methanol and water solvent for this reaction (Figure 5.2.3). The

increase in temperature does not seem to have much effect on the equilibrium constant as can be seen in Figure 5.2.4. However, it may be worth noting here that the ΔG_{solv} indicate better separation of structure **5** from water solvent over methanol. Thus if the readers are interested in obtaining structure **5** as end product, it is recommended that water solvent be preferred over methanol. Further conversion of bicyclohexane to cyclohexane in reaction –**e**– is found to be spontaneous and exothermic in all three mediums. The free energy change difference between the least spontaneous gas phase and most spontaneous methanol solvent is less than 3 kcal/mol at all temperatures. However, the increase in temperature is not favourable as seen in the ln K plot in Figure 5.2.4. Thus, lower temperatures are favourable for this reaction. the solvation free energy for product structure **8** again suggests water to be favourable medium with respect to separation from the solvent.

In pathway -**a**-**b**-**f**-**o**-**e**-, the conversion of DBF to structure **3** has already been described above. Conversion of structure **3** to structure **6** in reaction –**f**– is also found to be more spontaneous by 7.57 kcal/mol in water solvent, and 6.87 kcal/mol in methanol solvent than in gas phase at 298 K. The enthalpy change for the same reaction is also found to be more favourable with water and methanol solvent over gas phase by the same margin as free energy. Although the increase in temperature increases the spontaneity for this reaction, the ln K is found to decrease from 33.98 at 298 K to 19.17 at 598 K in water solvent. Similarly, ln K for methanol solvent also decrease from 32.80 kcal/mol at 298 K to 18.70 kcal/mol at 598 K suggesting slower reaction at high temperature. The enthalpy change for reaction –**f**– is found to be highest for water solvent, and increases by less than 1.5 kcal/mol from 298 K to 598 K. But among the two solvents, the free energy of solvation shows water to be better medium for separation of structure **6**. Further hydrogenation of the phenyl ring of cyclohexylbenzene (structure 6) yields structure **5** in reaction –**o**– which is again found to be most spontaneous in water solvent at 298 K. However, the difference between the three phases is less than 3.48

kcal/mol at 298 K making them comparable in all phases. The increase in temperature decreases the ln K in all phases and the free energy change is found to be positive at 598 K in all phases showing no possibility of reaction at high temperature. The enthalpy change for the same reaction is found to be exothermic at all temperatures in all mediums.

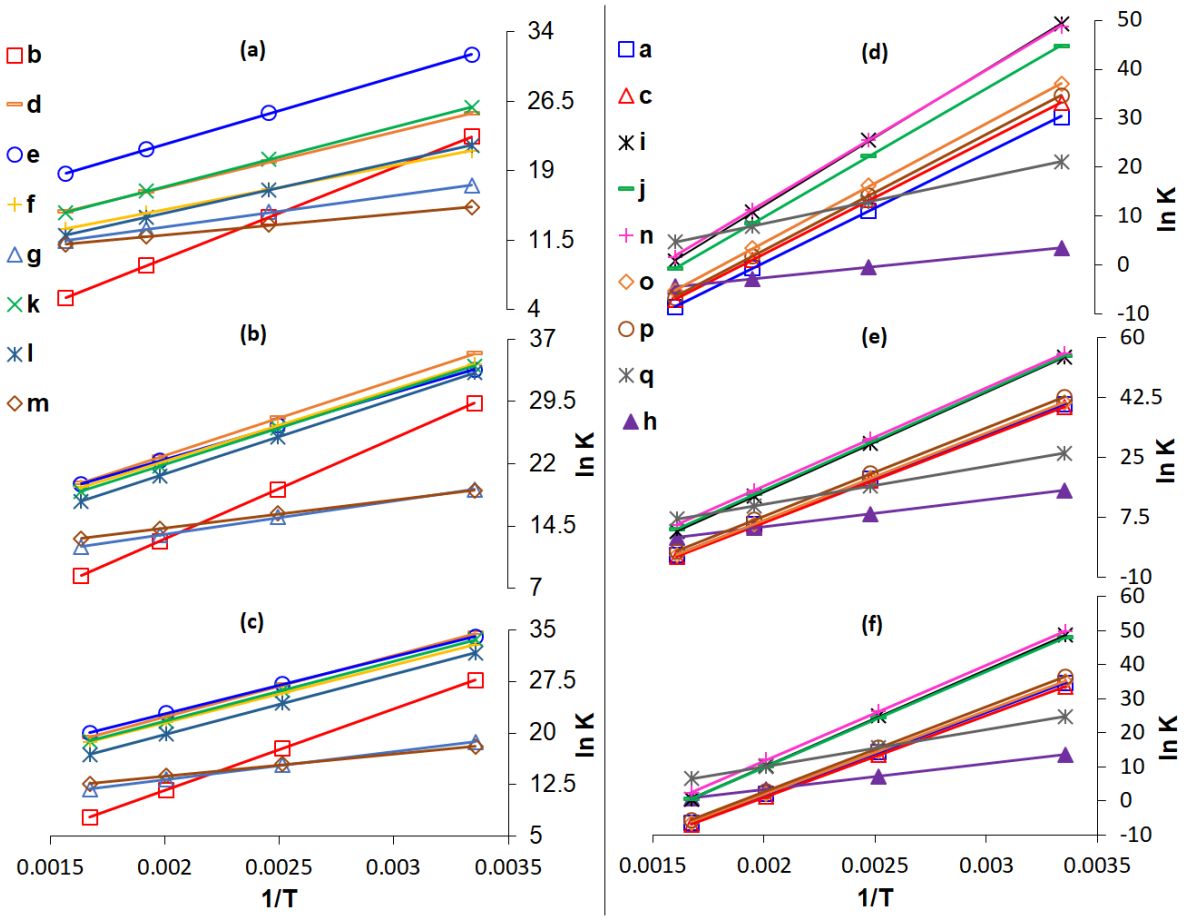

Figure 5.2.4: Equilibrium rate constant as a function of temperature for all the reactions in (a),(d) gas phase, (b,),(e) water solvent and (c),(f) methanol solvent.

In conversion of structure **3** to **5**, among the two pathway– **-c-d-** and **-f-o-**, it is observed that pathway **-c-d-** is less energy intensive and more spontaneous than pathway **-f-o-**. Thus, the reaction is more likely to proceed to completion via former pathway than the latter. The preference route -c-d- is also documented in the literature [96,165] over the Ni_2P

catalyst, and more deoxygenated products are obtained as the temperature is increased from 200 °C to 300 °C.

5.2.1.2 Furan-ring opening route of DBF upgrading

The less preferred upgrading route of DBF via reaction –**h**– initiates with the opening of furan ring of DBF to yield structure **9**. The reaction is found to be most spontaneous in water phase, followed by methanol and finally in water at all temperatures. The increase in temperature is also found to negatively influence the reaction thermochemistry which ln K reaching 0 or less at 598 K in all phases. Structure **9** is also found to be difficult to separate from either of the solvents in comparison to other structures discussed so far.

Further conversion of structure **9** to structure **6** can proceed via three different routes- pathway -**i**-**f**-, pathway -**j**-**k**- and pathway -**l**-**n**-. the conversion of structure **9** in reaction –**j**– is found to be most spontaneous, closely followed by reaction –**i**– and significantly more spontaneous than reaction –**l**– in all medium. Among different mediums, reaction –**j**– is calculated to have highest spontaneity in water (ΔG = -32.27 kcal/mol) at 298 K which decreases to -4.59 kcal/mol at 598 K. The ln K for other mediums also reach close to 0 at 598 K suggesting lower temperatures to be better for this conversion. The enthalpy change for this reaction is found to be exothermic for all mediums at all conditions. However, the solvation free energy suggests the product to be least separable among all other structures of this study in both the solvents. In the next step, conversion of structure **10** to structure **6** in reaction –**k**– is found to be equally spontaneous in water and methanol solvent with comparable enthalpy change in the two phases. Reaction –**k**– has been found to be dominant in catalytic works with Pt supported over mesoporous zeolite [95]. However, solvation free energy for structure **6** is more favourable in water than methanol for separation as mentioned in the previous section. Structure **6** can be converted to 2 molecules of cyclohexane via pathway -**o**-**e**- as discussed in

the section. Alternatively, it can be converted into benzene and cyclohexane via reaction –**g**– which is equally spontaneous in all phases with comparable free energy. The enthalpy change is also found to be comparable in all phases at all temperatures. Water can be a preferred solvent in this reaction due to its higher ΔG_{solv} suggesting better separation of products at infinite dilution. Although the increase in temperature increases the free energy of the reaction, it does not affect ln K much suggesting no advantage in reaching equilibrium with increase in temperature.

Very similar to the thermochemistry of reaction –**j**–, reaction –**i**– is also favourable in water medium at 298 K with ΔG = -32.14 kcal/mol. For this reaction, methanol is found to be the least favourable medium with ΔG = -28.75 kcal/mol at the same temperature. The enthalpy change is found be highly negative and shows water as the most favourable medium and methanol as least favourable for this reaction. Increase in temperature is found to be unfavourable as ln K reaches close to 0 at 598 K in all mediums. Further upgrading of structure 3 has already been discussed via pathway **-f-g-** , **-f-o-** and **-c-d-e-** .

Conversion of structure **9** to structure **11** in reaction –**l**– is spontaneous and exothermic in all mediums at all temperatures. The aqueous medium is found to be most favourable for free energy at all temperatures closely followed by the methanol solvent. ΔG at 298 K in water is found to be -19.49 kcal/mol whereas for methanol, ΔG = -18.71 kcal/mol. Spontaneity increases with temperature and at 598, ΔG = -20.64 kcal/mol and –19.93 kcal/mol in water and methanol respectively, but the ln K value stays relatively constant with increase in temperature. Thus increase in the temperature may not be cost effective for this reaction since the enthalpy change for water and methanol also show the decrease by mere 1.5 kcal/mol. From structure **11**, reaction –**m**– and –**n**– produce structure **7** and **6** respectively. The hydrogenation of structure **11** to produce structure **6** in reaction –**n**– is more spontaneous and exothermic in all phases over

reaction –**m**– to produce structure **7**. The ΔG of reaction –**n**– in least favourable gas phase is -28.90 kcal/mol at 298 K whereas the ΔG of reaction –**m**– is -8.89 kcal/mol at the same temperature. The most favourable is the aqueous phase for both the reactions with ΔG=32.75 kcal/mol for reaction –**n**– and -11.08 kcal/mol for reaction –**m**–. The enthalpy change is also found to have similar trend with highest ΔH = -57.75 kcal/mol for reaction –**n**– in aqueous phase and -6.10 kcal/mol for reaction –**m**– in the same phase at 298 K. However, with increase in temperature ln K is found to decrease from 55.36 at 298 K to 5.16 at 598 K for reaction –**n**– sharply whereas it remains relatively flat (Δ = 3.99) from 298 K to 598 K for reaction -m- for all phases. Thus depending on desirable product, temperature can be tuned to obtained optimum product distribution. The solvation free energy is similar for structure **6** and **7** for both the solvents, with better ΔG_{solv} in water for separation. Further upgrading of structure **6** obtained in reaction –**n**– has already been discussed above.

5.2.2 Single point energetics (SPE)

The single point energy of all the reactions is calculated in the gas phase using M05-2X/6-31+g(3df,2p)//M06-2X/6-311+g(d) level of theory. Figure 5.2.5 describes the ΔE plot of all reactions of scheme 1.

In pathway **-a-b-c-d-e-**, the SPE analysis of the conversion of dibenzofuran to structure **2** via reaction –**a**– has ΔE = -61.72 kcal/mol which increases to -28.17 in the conversion of structure **2** to structure **3** in reaction –**b**–. Conversion of structure **3** to structure **4** is similar to reaction –**a**– with ΔE = -63.57 kcal/mol in reaction –**c**–. This is in accordance with the literature [163] which report the saturation of ring to be a more favourable step over the breaking of C-O bond. Further dehydroxylation of structure **4** in reaction –**d**– is energetically less favourable with ΔE = -20.74 kcal/mol. Finally, in reaction –**e**–, structure **5** is converted to cyclohexane with ΔE = -18.99 kcal/mol.

In pathway **-a-b-f-g-,** the energetics of conversion of reaction –**a**– and –**b**– are identical to pathway **-a-b-c-d-e-**. After reaction –**b**–, ΔE of reaction –**f**– is calculated as -18.75 kcal/mol to produce structure **6** from structure **3**. Further conversion of structure **6** to cyclohexane and benzene are also energetically less favoured with ΔE = -11.03 kcal/mol.

In pathway **-h-i-c-d-e-**, the conversion of structure **1** to structure **9** by hydrogenolysis of furan ring is found to have ΔE = -17.12 kcal/mol. Further conversion of structure **9** to structure **3** in reaction –**i**– is found to be highly favourable with ΔE = -72.77 kcal/mol. Thus, reaction –i- is found to be energetically more favourable by 44.6 kcal/mol over reaction -b which reflects the preference of hydrogenation over hydrogenolysis during the HDO. The energetics of further conversion of structure **3** into cyclohexane has already been discussed above via reaction –**c**–, –**d**– and –**e**–.

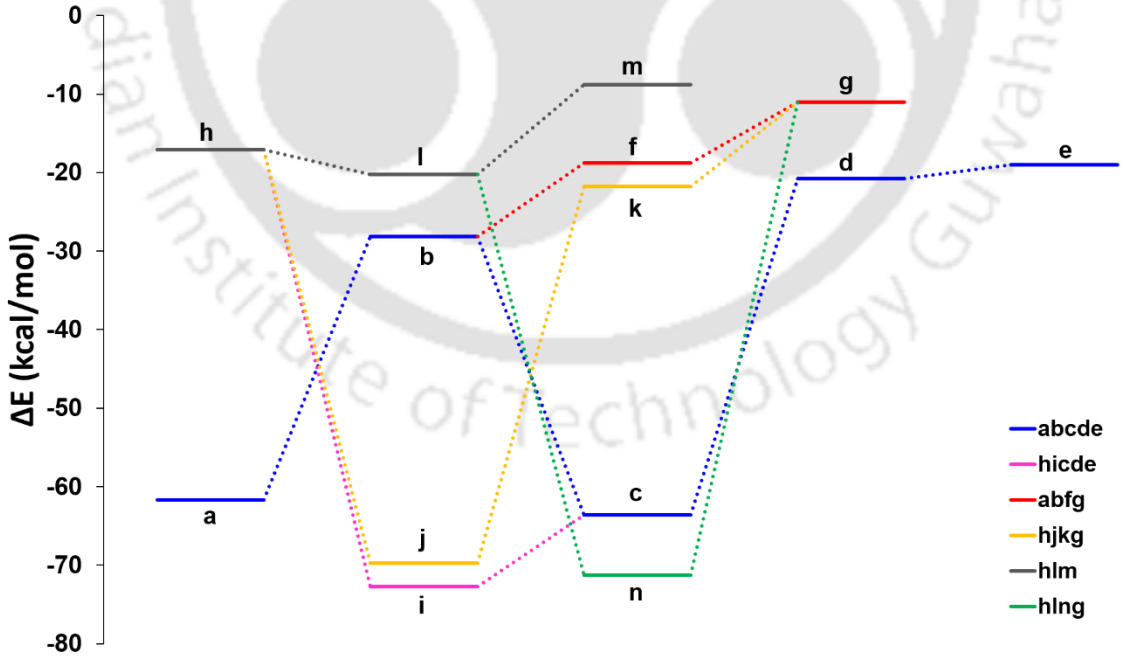

Figure 5.2.5: Single point energy change (ΔE) plot of all reactions of scheme 1.

In pathway **-h-j-k-g-**, the energetics of conversion of structure **9** to structure **10** in reaction –**j**– is highly favourable with ΔE = -69.74 kcal/mol. However, dehydroxylation of structure **10** to yield structure **6** has ΔE = -21.77 kcal/mol, which makes the formation of structure **6** energetically more favourable by reaction –**k**– than by reaction –**f**–. However, saturation of structure **11** to structure **6** in reaction –**n**– is found to be energetically most favourable with ΔE = -71.27 kcal/mol in pathway **-h-l-n-g-**. Finally, in pathway **-h-j-k-g-**, structure **6** is converted into cyclohexane and benzene in reaction –**g**–. In pathway **-h-l-m**, reaction –**l**– converts structure **9** to structure **11** with ΔE = -20.24 kcal/mol, which is 3.12 kcal/mol energetically more favourable than reaction –**h**–. Further breaking of biphenyl (structure **11**) to yield benzene is the least energy favourable reaction in the scheme with ΔE = -8.77 kcal/mol. Reaction –**n**– can further proceed to produce structure **5**, as proposed in the work of Hamid et al. [167]. Energetically, this step would require a change in ΔE of 50.53 kcal/mol.

It is observed that the reactions such as –**j**–, –**i**–, –**c**– and –**n**–**,** which involve saturation of the phenyl ring of the compounds were energetically more favourable than the rest of the reactions. These reactions are also found to be fairly spontaneous, which could be attributed to their highly negative entropy change (Table 5.2.3). On the other hand, reactions such as –**g**– and –**m**–, which involve breaking of dimer ring to produce smaller cyclic compounds are energetically less favourable.

5.3 Thermochemical Conversion of Guaiacol in Aqueous Phase by Density Functional Theory

Several reaction pathways to convert guaiacol to value added chemicals are proposed here. The general notation of these pathways used in this study is **X_Y**, where **Y** represents the reactant structure of the **X**th reaction scheme. For transition state structures, **TSY** notation is used to denote **Y**th transition state structure of the study. For example, structure **2_b1** denotes structure **b1** structure of reaction scheme **2**. Similarly, **A3_d** denotes reaction structure **d** of reaction scheme **A3**. Abbreviations used for important components involved in this study are **G** (guaiacol) and **P** (phenol).

All the simulations in this study are conducted using M06-2X functional with 6-311g+(d,p) basis set under DFT framework. SMD model [145] is used for implicit solvent effect with water as solvent in all the simulations. All associated molecular structures are first geometrically optimized in aqueous phase, then the frequency calculations are performed at the same level in the same aqueous phase and the corresponding zero-point energy (ZPE) is added. In case of a presence of an imaginary frequency, the transition state is determined which is further confirmed through intrinsic reaction coordinate (IRC) calculation. The IRC analysis confirms the saddle points to be reactants and products of the transition states. The bond dissociation energy (BDE) of various possible bond scissions of compounds of interest are also calculated. The BDE provides information about the energy requirement of the scission of bonds in the molecule. This helps in proposing possible reaction routes (irrespective of their favourability) of the model compound. The BDE is calculated as:

$$BDE_{R-A} = H_R + H_A - H_{R-A} \quad (5.2)$$

Where *H* refers to the enthalpy whereas subscript R and A represent species and R-A referred as molecule at 298 K.

The effects of temperature change on the thermochemical parameters such as Gibb's free energy change (ΔG) and enthalpy change (ΔH) of the reactions are also studied in the range of 298-598 K at each interval of 100 K at atmospheric pressure condition. Free energy landscape of best pathways are also calculated at 1-20 atm pressure from 298 K to 598 K temperature. All the simulations are performed using Gaussian 09 package [169] with the help of GaussView 5 visualization tool [170].

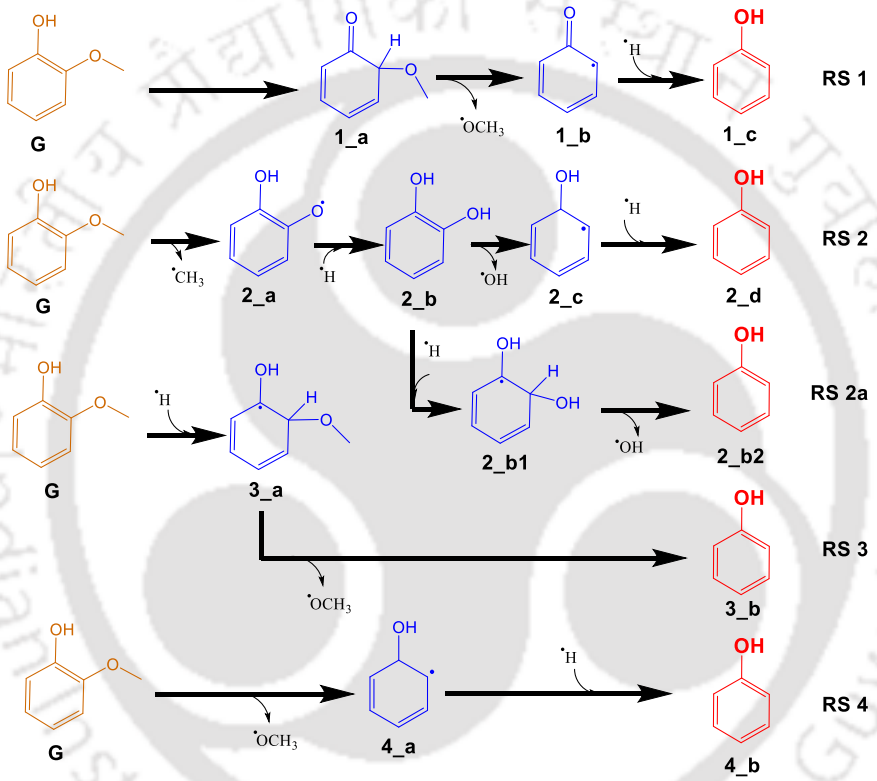

All the pathways present in scheme 1 are described here. In reaction scheme **1**, guaiacol (structure **G**) is converted into phenol by the elimination of methoxy group. In the first step, H˙ from hydroxyl group migrates to ortho position of **G** to produce structure **1_a**. Further, cleavage of methoxy group from structure **1_a** yields structure **1_b** which upon hydrogenation yields phenol (structure **1_c**). In a similar reaction scheme **3**, the hydrogenation of the guaiacol at its ortho position yields structure **3_a** followed by cleavage of methoxy group to produce phenol. Alternatively, guaiacol can first be subjected to demethoxylation followed by

hydrogenation in reaction scheme **4**. In reaction scheme **2** and **2a**, guaiacol is first subjected to demethylation of methoxy group to produce structure **2_a** which is then followed by hydrogenation to produce pyrocatechol (structure **2_b**). Hydrogenation of structure **2_b** followed by dehydroxygenation gives phenol *via* RS **2a**. Alternatively, dehydroxygenation of structure **2_b** followed by hydrogenation also yields phenol *via* reaction scheme **2**.

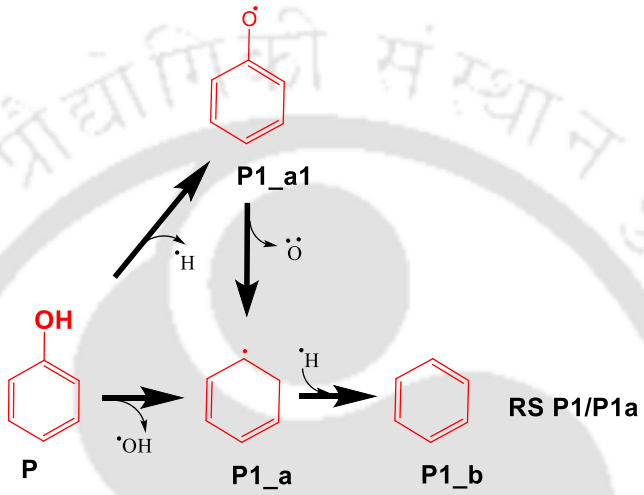

In reaction scheme **P1**, phenol is first dehydroxygenated and then protonated to produce benzene (structure **P1_b**). On the other hand, in **RS P1a**, removal of H˙ from hydroxyl group of phenol produces structure **1j** which is then cleaved of ö to produce structure **P1_a** which is further hydrogenated to produce benzene.

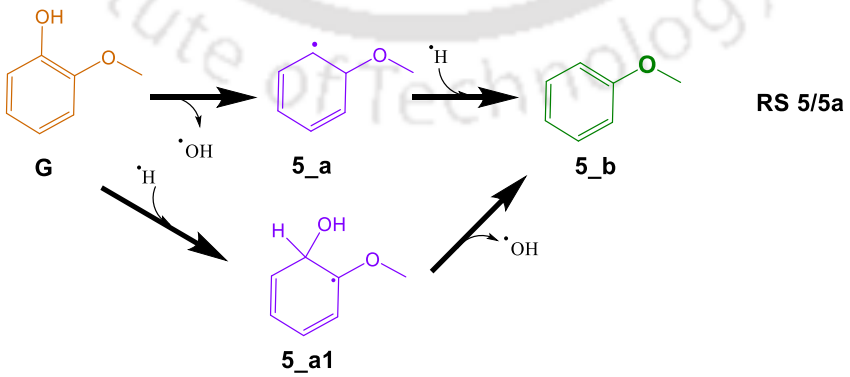

Pathways included in reaction scheme **5** and **5a** are described here. In reaction scheme **5** and **5a**, guaiacol is converted to anisole (structure **5_a1**). Guaiacol is first protonated, which

is followed by dehydroxylation *via* reaction scheme **5a** to yield anisole. Alternatively, guaiacol is first dehydroxylated, which is followed by protonation to yield anisole *via* reaction scheme **5**.

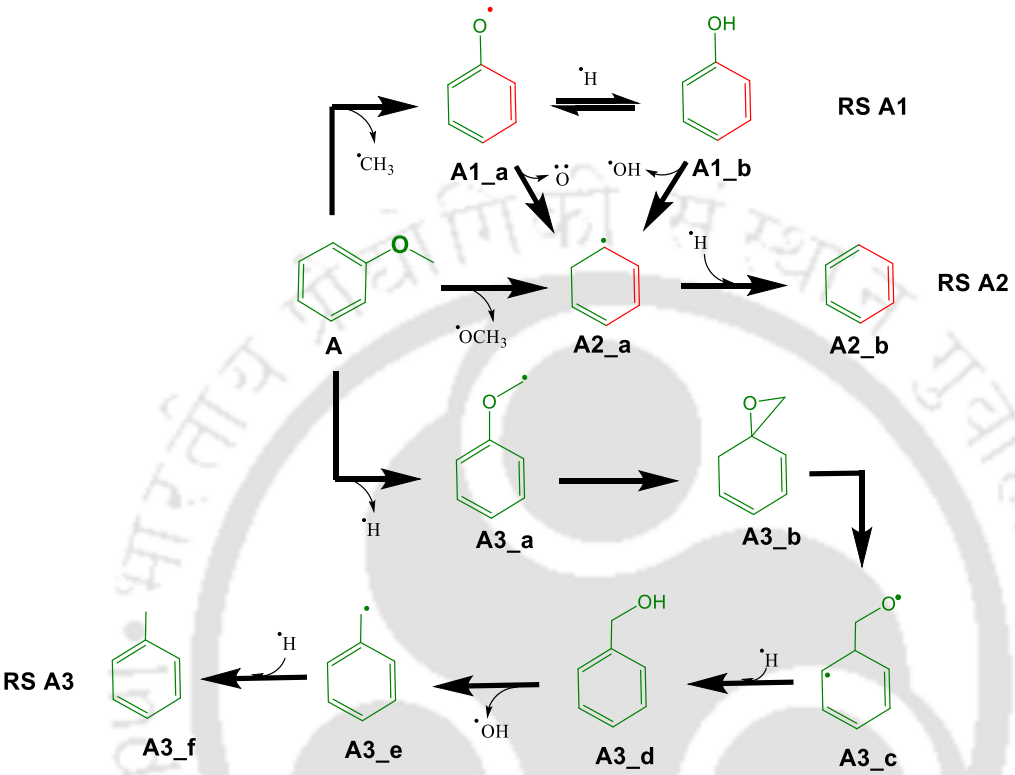

Anisole is then converted into toluene, phenol and benzene by three different pathways. In reaction scheme **A1**, the cleaving of methyl from methoxy group yields structure **A1_a** which is further protonated to produce phenol. Also, direct cleaving of methoxy group from anisole followed by protonation produces benzene *via* reaction scheme **A2**. In reaction scheme **A3**, the hydrogen atom of phenolic group is cleaved to form structure **A3_a**, which is further converted to structure **A3_c** in a two-step radical rearrangement. Structure **A3_c** is then protonated to produce phenylmethanol (structure **A3_d**) which upon dehydroxylation yields structure **A3_e** which is further protonated to produce toluene (structure **A3_f**).

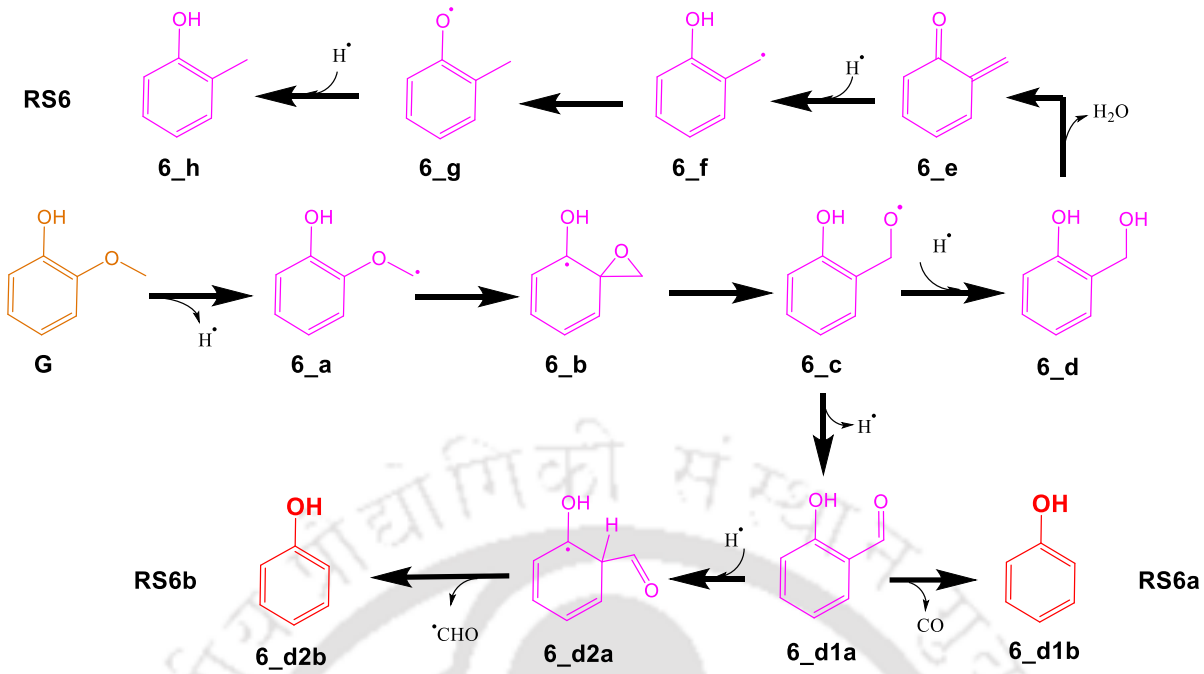

Similarly, reaction scheme **6**, **6a** and **6b** include pathways as described ahead. Reaction scheme **6a** and **6b** also propose the formation of phenol from guaiacol. First, methoxy group of guaiacol is deprotonated to produce structure **6_a**. Then, a two-step radical rearrangement produce structure **6_c**, which is further protonated to produce 2-hydroxybenzaldehyde (structure **6_d1a**). Finally, carbonyl group is cleaved from structure **6_d1a** to produce phenol *via* reaction scheme **6a**. Alternatively, protonation of structure **6_d1a** followed by cleaving of CHO also yields phenol *via* reaction scheme **6b**. Reaction scheme **6** proposes formation of o-cresol from guaiacol. In this trail, deprotonation of methoxy group of guaiacol followed by a two-step radical rearrangement yields structure **6_c** which upon further protonation produce salicyl alcohol (structure **6_d**). Further dehydration of structure **6_d** yields 5,6-dimethylenecyclohexa-1,3-diene (structure **6_e**) which upon protonation produce structure **6_f**. Finally, radical rearrangement of structure **6_f** followed by protonation produce o-cresol (structure **6_h**).

The conversion of guaiacol to three end products, namely benzene, toluene and o-cresol proceeds with the formation of several important intermediates such as anisole, catechol,

phenol, etc. Once the optimized structures of guaiacol, anisole and phenol are obtained, their BDE is calculated. Then on the basis of BDE analysis, further pathways are designed (as presented in reaction schemes 1-6) to produce platform chemicals.

5.3.1 Bond dissociation energy (BDE)

Bond dissociation energies for bond scission of guaiacol, anisole and phenol are calculated at M06-2X/6-311+g(d,p) level of theory in the aqueous phase using SMD solvation model.

5.3.1.1 Guaiacol

In BDE calculation of guaiacol, it is seen that the cleavage of $^{\bullet}CH_3$ radical (D2) from the methoxy group is the least energy demanding breakage with 60.88 kcal/mol of energy requirement (see Table 5.3.1). This is similar to the gas phase BDE of 59.40 kcal/mol for the same bond scission. With energy requirement of 85.22 kcal/mol, the breaking of $H^{\bullet}$ from hydroxyl group (D9) of guaiacol is the second least energy demanding bond breakage. This energy requirement in aqueous phase is slightly better than the gas phase BDE of 87.86 kcal/mol. Then the cleavage of methoxy group (D3) and breaking of $H^{\bullet}$ from methoxy group (D1) is found to have almost similar BDE of 99.84 kcal/mol and 100.42 kcal/mol respectively. D1 and D3 bond breaking are again better in gas aqueous phase by 3.24 kcal/mol and 2.62 kcal/mol respectively. The rest of the bonds have BDE above 111.00 kcal/mol which is quite high for the reaction to occur at low to moderate temperatures. The order of BDE is D2<D9<D3<D1<D8<D4<D5<D6<D7. On comparison with studies conducted in gas phase with B3LYP functional by Huang et al. [171] and Verma and Kishore [172] indicate that the BDE requirement for guaiacol increases in the aqueous medium. But since the functional used in their studies is different than this study, any quantitative comparison cannot be concluded with certainty.

Table 5.3.1. Bond Dissociation Energy (BDE) of Guaiacol

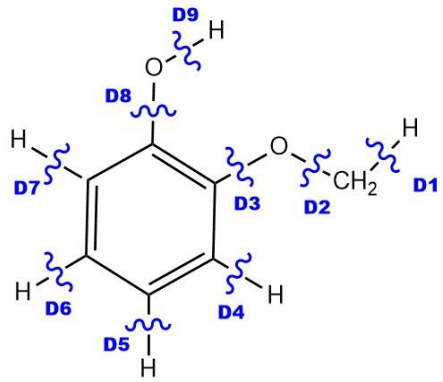

Bond Cleavage	BDE (kcal/mol)	BDE in gas phase (kcal/mol)
D1	100.42	97.18
D2	60.88	59.40
D3	99.83	102.45
D4	113.29	110.81
D5	113.37	111.74
D6	113.46	111.65
D7	114.90	113.34
D8	111.26	114.67
D9	85.22	87.86

5.3.1.2 Phenol

BDE calculation of phenol shows that the scission of H˙ of hydroxyl group (D1) is least energy demanding (see Table 5.3.2). When compared to gas phase BDE, several works, like that of Lucarini et al. [173] and Chandra & Uchimaru [174], report this BDE between 85.00 kcal/mol - 88 kcal/mol. The higher BDE of the PhO-H bond in aqueous phase is also reported by Bakalbassis et al. [175] . They report an increase of upto 8 kcal/mol in aqueous phase over gas phase. After D1, cleavage of hydroxyl group (D2) requires least BDE of 110.69 kcal/mol. The BDE of rest of the bonds are very competitive and high with cleavage of H˙ from ortho position (D7) being the highest at 114.70 kcal/mol. The order of bond dissociation energy for phenol molecule is D1<D2<D4<D6<D5<D3<D7. This could mean that D1 bond breaking can produce the most stable radical while D7 bond scission may produce the least stable radical.

5.3.1.3 Anisole

Bond dissociation energy analysis of anisole shows that the cleavage of ˙CH_3 from methoxy group (D2) is the least energy demanding bond scission amongst all (see Table 5.3.3). D2 bond breaking requires 67.19 kcal/mol of energy. This BDE is reported as 65.3 kcal/mol in the work of Pratt et al. [176] in gas phase suggesting similar energy requirement in both phases. The second lowest BDE (D3) requires 99.36 kcal/mol of energy to break H˙ from methoxy group

Table 5.3.2: Bond Dissociation Energy (BDE) of Phenol

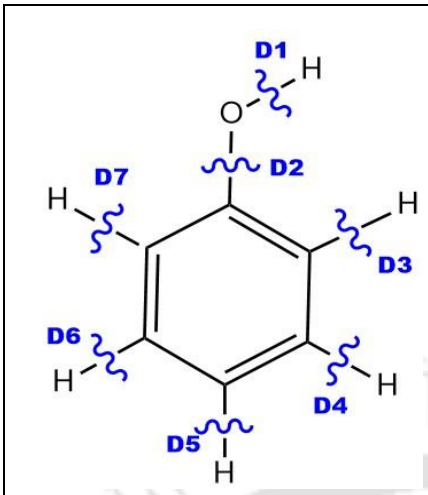

Bond Cleavage	BDE (kcal/mol)
D1	90.15
D2	110.69
D3	114.46
D4	112.49
D5	113.68
D6	112.64
D7	114.70

of anisole. The cleavage of methoxy group (D3) is almost of the same magnitude as the scission of H˙ from methoxy group (D1) with BDE of 100.20 kcal/mol. BDE of scission of rest of the bonds of anisole is quite high and almost of the same magnitude. The breaking of H˙ from ortho position (D8) is calculated to be 114.57 kcal/mol which is highest amongst all BDEs of anisole. The trend for BDE of anisole is D2<D3<D1<D5<D7<D4<D6<D8.

In summary it is observed that the breakage of bonds at the ortho position of the ring have high BDE whereas the cleavage of bonds from the functional groups attached to the rings have low BDE.

Table 5.3.3: Bond Dissociation Energy (BDE) of Anisole

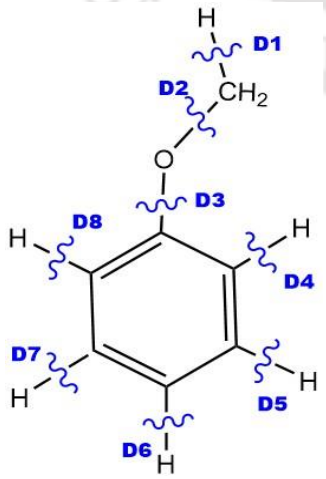

Bond Cleavage	BDE (kcal/mol)
D1	100.20
D2	67.19
D3	99.36
D4	113.02
D5	112.46
D6	113.71
D7	112.64
D8	114.57

5.3.2 Reaction Energy

5.3.2.1 Guaiacol to Phenol Conversion

The formation of phenol from guaiacol proceeds *via* several different pathways as described in the reaction schemes. As can be seen from BDE analysis, the direct cleavage of methyl group from guaiacol is the least energy demanding step requiring only 60.88 kcal/mol. Thus reaction scheme **2** and **2a** initiates with cleavage of $^{\bullet}CH_3$ from methoxy group to produce structure **2_a** which is then hydrogenated to produce catechol (structure **2_b**) exothermally as seen from its PES shown in Figure 5.3.1. The hydrogenation of structure **2_a** to catechol releases 83.34 kcal/mol of energy in aqueous phase which is about 8 kcal/mol higher than gas phase [172]. The cleavage of hydroxyl group from catechol to produce structure **2_c** requires a very high activation energy of 116.07 kcal/mol which makes this conversion feasible at high temperature conditions only. Further hydrogenation of structure **2_c** release 119.88 kcal/mol of energy to produce phenol. Alternatively, hydrogenation of catechol requires 6.83 kcal/mol of activation energy to produce structure **2_b1**. The gas phase activation energy for this conversion is almost equal with 8.1 kcal/mol [177]. Structure **2_b1** then undergoes dehydroxygenation to produce phenol releasing 17.32 kcal/mol of energy in aqueous phase as compared to 19.7 kcal/mol in gas phase [177]. Reaction scheme **2a** is more likely to proceed over reaction scheme **2** due to the lower activation energy of formation of structure **2_b1**. From Table 5.3.1 it can be seen that the cleavage of methoxy group is second most energy demanding BDE of any functional group from guaiacol. Cleavage of methoxy group from guaiacol require 99.83 kcal/mol and yield structure **4_a** which is further hydrogenated to produce phenol with a release of 119.88 kcal/mol of energy in RS 4. BDE analysis shows that the direct cleavage of any other functional group will require high energy. Thus in reaction scheme **3**, guaiacol is first hydrogenated to produce structure **3_a** which is energetically similar in gas phase [177]. Then the methoxy

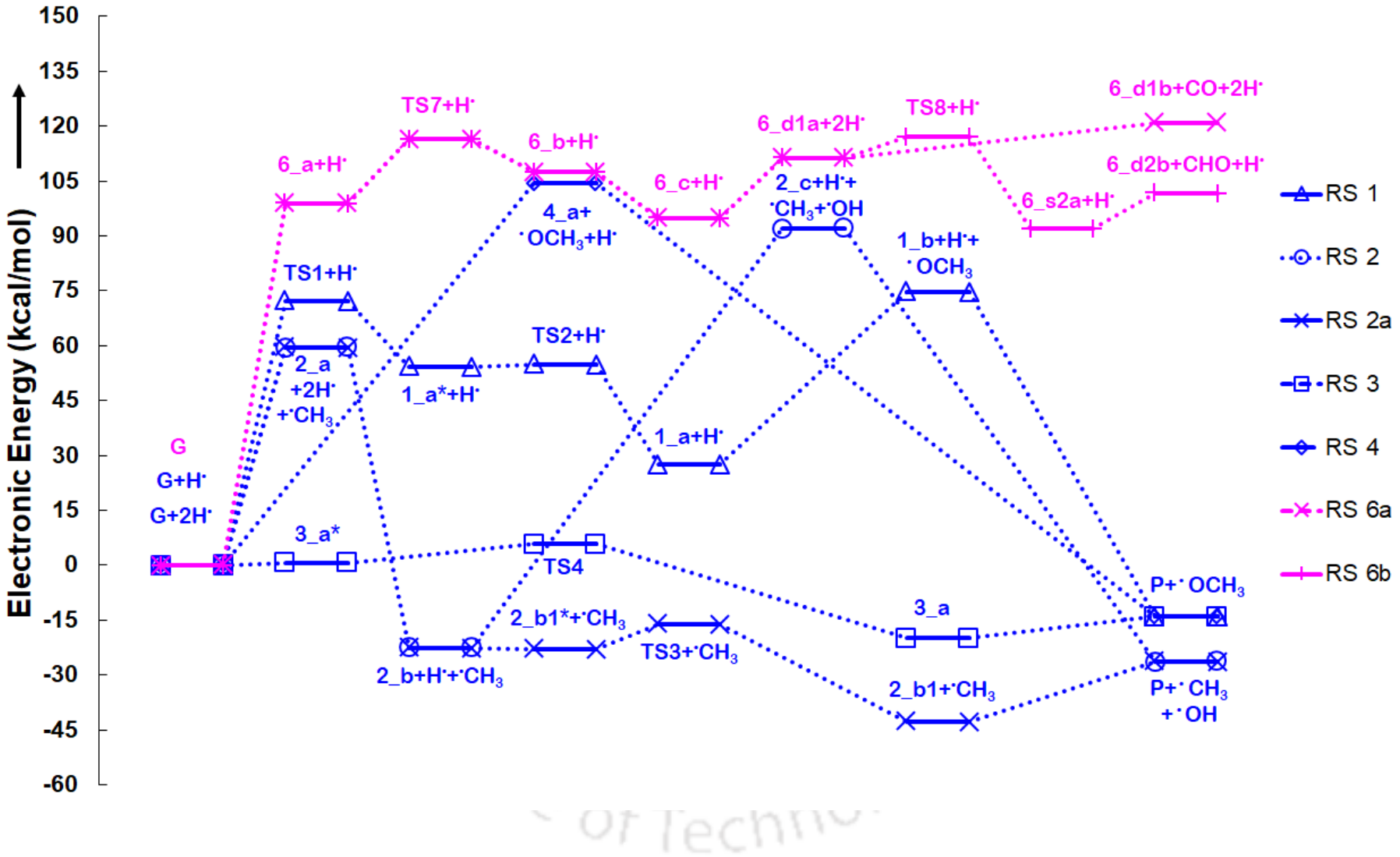

Figure 5.3.1: Potential energy surface (PES) of guaiacol to phenol conversion pathways with added zero-point energy.

group is cleaved from structure **3_a** which requires 6.93 kcal/mol of energy to produce phenol. By comparing with literature results, this reaction step is 5.86 kcal/mol more favourable in aqueous phase than in gas phase [177]. This reaction step is also significantly lower in energy requirement than direct BDE of methoxy group to yield phenol as discussed in reaction scheme **4**. Also, reaction scheme **1** initiates with rearrangement of H˙ from hydroxyl group to the ortho carbon position and requires 72.26 kcal/mol of energy to produce structure **1_a**. This step is again energetically more favourable in aqueous phase by about 15 kcal/mol [177]. This is important because the rearrangement step is the rate determining step of reaction scheme **1**. Further, the cleavage of methoxy group produce structure **1_b** which requires 48.02 kcal/mol of energy. Then, structure **1_b** is hydrogenated to produce phenol with the release of 90.15 kcal/mol of energy. From Table 5.3.1 it can be seen that the cleavage of H˙ from methoxy group of guaiacol requires 100.42 kcal/mol to produce structure **6_a**. The reaction further requires17.48 kcal/mol to overcome activation barrier and produce structure **6_c**. Dehydrogenation of structure **6_c** requires 17.59 kcal/mol to produce salicylaldehyde(structure **6_d1a**). Decarbonylation of salicylaldehyde in single step *via* reaction scheme **6a** to produce phenol require 10.55 kcal/mol. Alternatively, hydrogenation of salicylaldehyde followed by cleavage of CHO *via* reaction scheme **6b** require an activation barrier of 5.72 kcal/mol. From PES (Figure 5.3.1) it is evident that hydrogenation of salicylaldehyde is a preferred reaction step over decarbonylation. The phenol is further converted into benzene which is discussed below.

5.3.2.2 Phenol to Benzene Conversion

The conversion of phenol to benzene is proposed by two pathways – reaction scheme **P1** and **P1a** as per the BDE analysis (see Table 5.3.2). The cleavage of H˙ from hydroxyl group require 90.15 kcal/mol to yield structure **P1_a1** in RS **P1a**. As discussed in BDE section, the energy requirement for this scission in gas phase is almost of similar magnitude. Further scission of ö

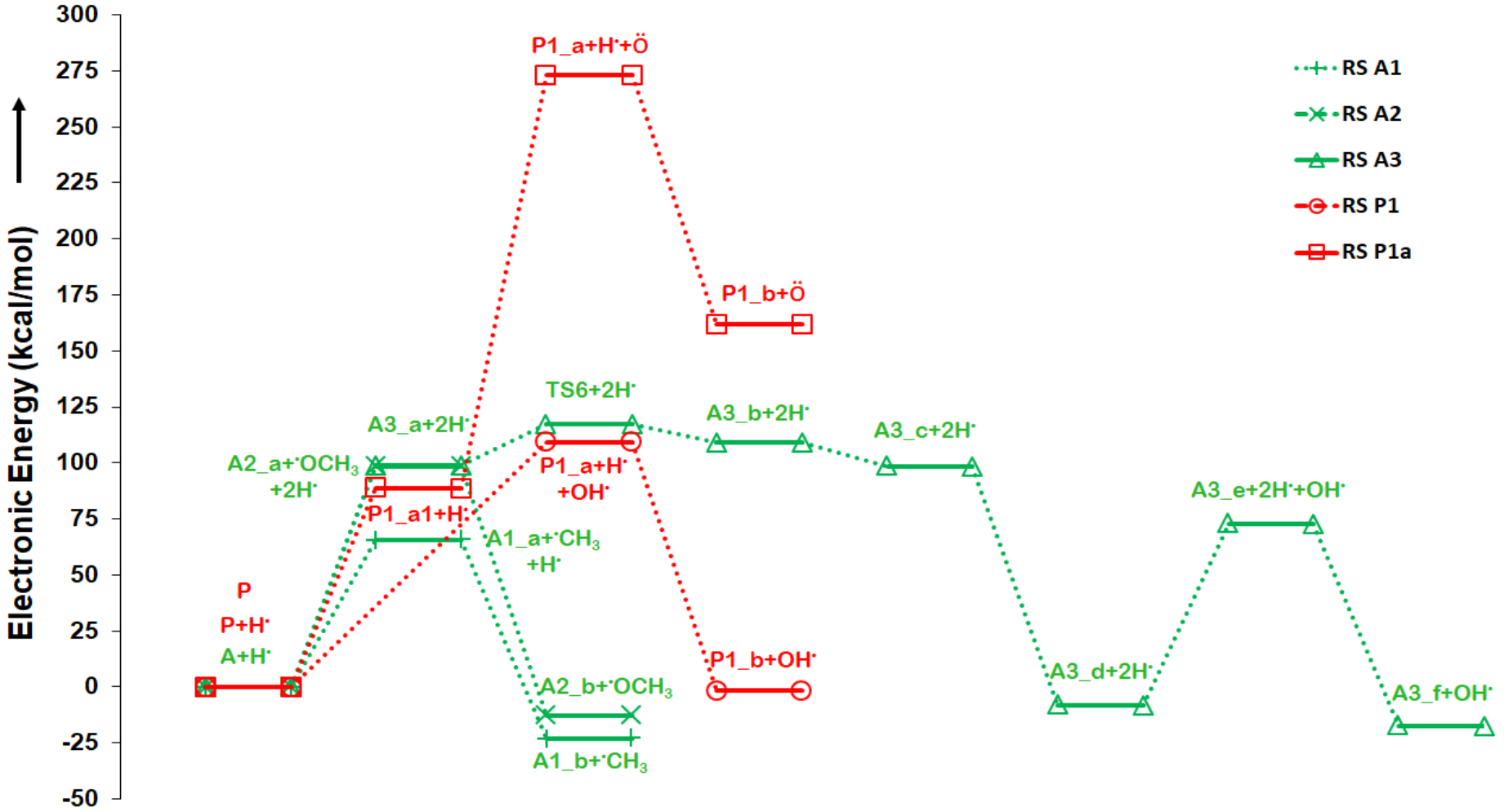

Figure 5.3.2: Potential energy surface (PES) of anisole to toluene, anisole to benzene, anisole to phenol and phenol to benzene conversions with added zero-point energy.

requires 185.09 kcal/mol of energy which is very high, and less likely to occur. Finally, structure **P1_a** is hydrogenated to produce benzene. In reaction scheme **P1**, the direct cleavage of hydroxyl group from phenol requires 110.69 kcal/mol to produce structure **P1_a**. Since the rate determining step for reaction scheme **P1a** requires 185.09 kcal/mol, the formation of benzene is more likely to proceed *via* reaction scheme **P1**.

5.3.2.3 Guaiacol to Anisole

The formation of anisole from guaiacol can occur *via* RS **5** and RS **5a**. The cleavage of hydroxyl group from guaiacol to produce structure **5_a** requires 111.26 kcal/mol which is slightly higher than in gas phase [172]. This is followed by hydrogenation to liberate 114.57 kcal/mol producing anisole *via* reaction scheme **5**, whereas in reaction scheme **5a**, guaiacol is hydrogenated with only 6.67 kcal/mol of energy to produce structure **5_a1**. The dehydroxygenation of structure **5_a1** further requires 18.59 kcal/mol. Thus anisole formation is more likely to proceed *via* reaction scheme **5a** over reaction scheme **5** due to its lower energy barrier.

5.3.2.4 Anisole to Phenol, Benzene and Toluene Conversion

The cleavage of $^{\bullet}CH_3$ from methoxy group requires 67.19 kcal/mol of energy to produce structure **A1_a** which is then hydrogenated to produce phenol *via* reaction scheme **A1**. The cleavage of $^{\bullet}OCH_3$ is the second least energy demanding bond breakage from anisole which requires 99.36 kcal/mol to produce structure **A2_a** in reaction scheme **A2** which is further hydrogenated to produce benzene. The cleavage of $H^{\bullet}$ from methoxy group of anisole requires 100.20 kcal/mol of energy to produce structure **A3_a**. The radical rearrangement of structure **A3_a** to produce structure **A3_c** require 18.59 kcal/mol of energy to cross its activation barrier. Further hydrogenation of structure **A3_c** liberate 107.95 kcal/mol to produce benzyl alcohol (structure **A3_d**). Dehydroxygenation of benzyl alcohol require activation energy of 82.24 kcal/mol to produce structure **A3_e** which upon further hydrogenation produce toluene. From

PES (see Figure 5.3.2), it is clear that guaiacol will most likely yield phenol *via* reaction scheme A1.

5.3.2.5 Guaiacol to o-cresol Conversion

The production of structure **6_c** from guaiacol has already been discussed in previous sub-section on "Guaiacol to phenol conversion". The hydrogenation of structure **6_c** produce salicyl alcohol liberating 105.99 kcal/mol of energy. Huang et al. [171] reported this energy liberation to be 100.0 kcal/mol in gas phase. The dehydration of salicyl alcohol require 23.46 kcal/mol in aqueous phase whereas 20.84 kcal./mol in gas phase [171] to produce structure **6_e**. Further successive hydrogenation of structure **6_e** produce o-cresol exothermally (Figure 5.3.3) liberating -88.07 kcal/mol. Huang et al. [171] report this step to be less favourable in gas phase by 9.19 kcal/mol.

5.3.3 Thermochemistry

Thermochemistry of all reaction pathways is studied at varying temperature (298 K - 598 K) and at atmospheric pressure and presented in Table 5.3.4 along with activation barrier and pre-exponential factor. Gibb's free energy change (ΔG) and reaction enthalpy change (ΔH) is calculated for all pathways. For pathways with same reactant and products (such as reaction scheme **3** and **1**), the thermochemical parameters are identical. However, in case of different side products (such as in reaction **1** and **2**), there is a change in thermochemical parameters which is also reported here. For the formation of phenol from guaiacol *via* RS **1**, RS **3** and RS **4**, the thermochemistry is identical. The Gibb's free energy change suggest favourable condition for these pathways and is calculated to be -19.32 kcal/mol at 298 K. Increase in temperature is also favourable as ΔG reduces to -23.58 kcal/mol at 598 K. The enthalpy change of the reaction also decreases from -14.63 kcal/mol at 298 K to -15.83 kcal/mol at 598 K. However, ΔG for RS **2** and RS **2a** are found to be more favourable (ΔG= -32.79 kcal/mol) at

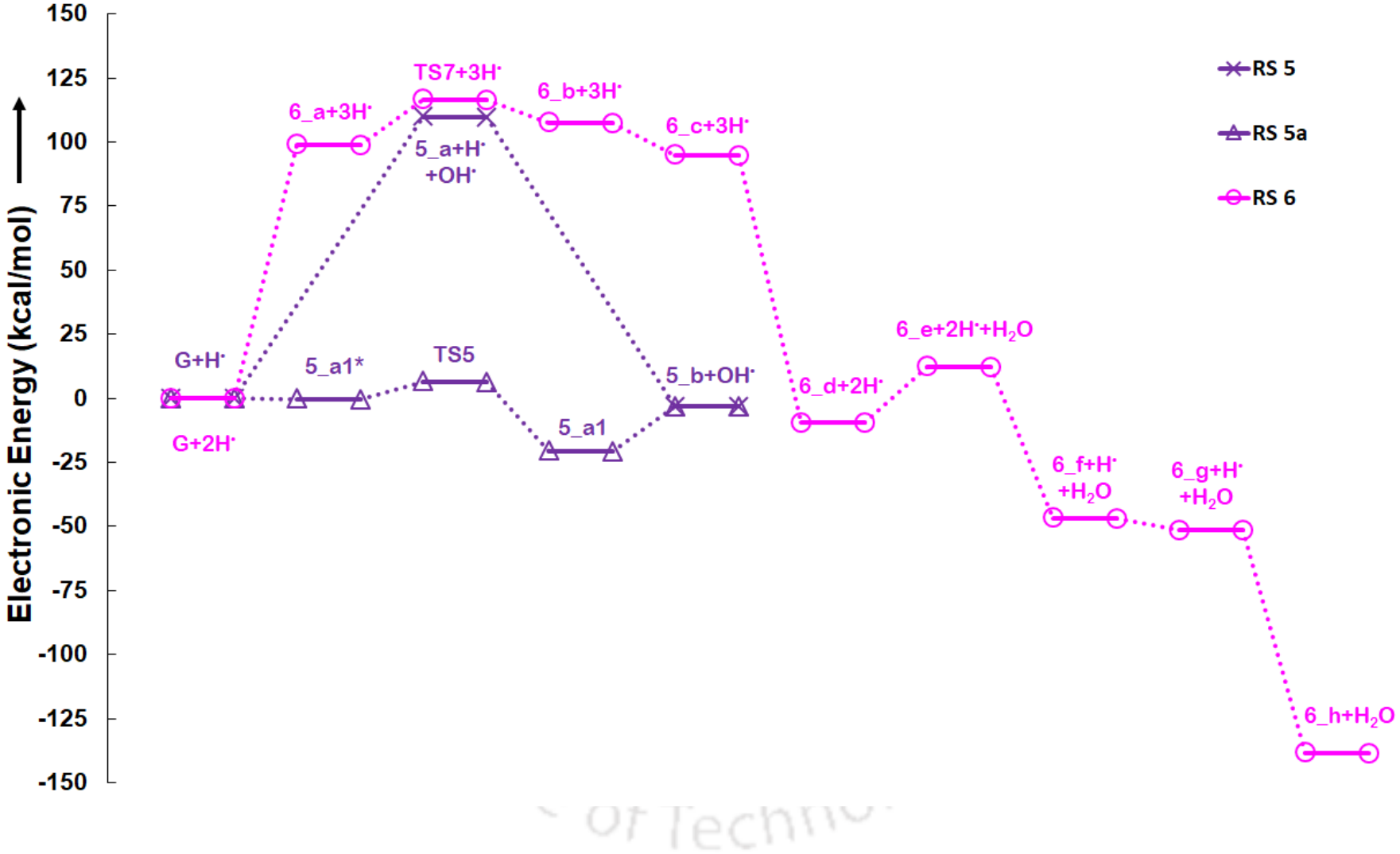

Figure 5.3.3: Potential energy surface (PES) curve of guaiacol to anisole and guaiacol to o-cresol conversion with added zero-point energy.

298 K. The spontaneity increases to -38.95 kcal/mol with increase in temperature at 598 K. The ΔH also decreases with increase in temperature. On the other hand, reaction scheme **6a** and **6b** show very high free energy change (98.08 kcal/mol and 83.87 kcal/mol respectively) at 298 K suggesting less likelihood of reaction progress. With increase in temperature, the spontaneity increases to 61.75 kcal/mol and 63.44 kcal/mol at 598 K for the respective pathways i.e., RS **6a** and RS **6b**. The enthalpy change is also observed to be very high at 298 K for reaction scheme **6a** (124 kcal/mol) as well as for reaction scheme **6b** (103.84 kcal/mol) and does not show much sensitivity to the increase in temperature. Further conversion of phenol to benzene *via* reaction scheme **P1a** has very high ΔG = 154.11 kcal/mol and ΔH =162.66 kcal/mol at 298 K. On the other hand, conversion *via* reaction scheme **P1** shows ΔG = -4.76 kcal/mol and ΔH = -1.89 kcal/mol at298 K. Though the increase in temperature decreases Gibb's free energy change and reaction enthalpy change for both pathways, the conversion can only occur *via* reaction scheme **P1**. For the formation of anisole *via* reaction scheme **5** and **5a**, ΔG is found to be -6.82 kcal/mol and ΔH is found to be -3.31 kcal/mol which decreases to -10.01 kcal/mol and -4.24 kcal/mol respectively at 598 K. Formation of phenol from anisole has ΔG = -25.97 kcal/mol and ΔH =-22.96 kcal/mol at 298K and increase in temperature shows increase in spontaneity and decrease in reaction enthalpy suggesting favourability. Formation of benzene and toluene from anisole show similar trend. At 298 K, ΔG for the formation of benzene is -17.26 kcal/mol and for the formation of toluene is -19.83 kcal/mol. At 298 K, ΔH for the same conversions are -13.21 kcal/mol and -17.19 kcal/mol respectively. Further increase in temperature increases the spontaneity and decreases the reaction enthalpy of both the reactions. The formation of o-cresol from guaiacol is found to be very spontaneous. ΔG at 298 K is -134.74 kcal/mol and ΔH at 298 K is -139.60 kcal/mol for this conversion of guaiacol to o-cresol. However, the spontaneity decreases with increase in temperature and ΔG increases to

-129.21 kcal/mol at 598 K. But ΔH decreases with increasing temperature and falls to -141.25 kcal/mol showing favourable condition.

Finally, in summary, the conversion of benzene from guaiacol will most likely proceed *via* reaction scheme **3** to form phenol followed by the formation of benzene *via* reaction scheme **P1**. The most favourable pathway for the formation of toluene will proceed *via* reaction scheme **5a** to form anisole followed by conversion of anisole to toluene *via* reaction scheme **A3**. The formation of o-cresol from guaiacol will most favourably proceed *via* **RS 6**. The formation of o-cresol is the most favourable product in this study. This is in agreement with the work of Lawson & Klein [111] who also reported the selectivity of o-cresol during guaiacol pyrolysis in water. The schematic representation of these favourable reactions along with their overall ΔG and ΔH at 298 K in aqueous phase are shown in Figure 5.3.4.

Table 5.3.4: Overall Free energy change (ΔG), enthalpy change (ΔH), activation energy (E_a) in kcal/mol; and pre-exponential factor (A) in s^{-1} of all reaction pathways.

Pathway(s)	Parameters	Temperature (K)			
		298	**398**	**498**	**598**
RS 1	ΔG	-19.32	-20.84	-22.25	-23.58
	E_a	74.73	74.73	74.73	74.73
	A	2.57E+22	2.34E+22	2.07E+22	1.80E+22
	ΔH	-14.63	-15.03	-15.42	-15.83
RS 2	ΔG	-32.79	-34.93	-36.99	-38.95
	E_a	92.15	92.15	92.15	92.15
	A	7.18E+23	1.10E+24	1.30E+24	1.30E+24
	ΔH	-26.27	-26.59	-27	-27.5
RS 2a	ΔG	-32.79	-34.93	-36.99	-38.95
	E_a	59.55	59.55	59.55	59.55
	A	2.74E+21	5.18E+21	7.57E+21	9.42E+21
	ΔH	-26.27	-26.59	-27	-27.5
RS 3	ΔG	-19.32	-20.84	-22.25	-23.58
	E_a	5.88	5.88	5.88	5.88
	A	8.98E+06	8.34E+06	8.32E+06	8.56E+06
	ΔH	-14.63	-15.03	-15.42	-15.83
RS 4	ΔG	-19.32	-20.84	-22.25	-23.58

	E_a	104.34	104.34	104.34	104.34
	A	3.24E+22	4.46E+22	5.32E+22	5.82E+22
	ΔH	-14.63	-15.03	-15.42	-15.83
RS 5	ΔG	-6.82	-7.95	-9.01	-10.01
	E_a	109.9	109.9	109.9	109.9
	A	3.72E+21	6.02E+21	7.96E+21	9.39E+21
	ΔH	-3.31	-3.59	-3.91	-4.24
RS 5a	ΔG	-6.82	-7.95	-9.01	-10.01
	E_a	6.37	6.37	6.37	6.37
	A	2.58E+07	2.52E+07	2.57E+07	2.69E+07
	ΔH	-3.31	-3.59	-3.91	-4.24
RS 6	ΔG	-134.74	-133.03	-131.18	-129.21
	E_a	116.45	116.45	116.45	116.45
	A	9.68E+17	2.04E+18	3.50E+18	5.15E+18
	ΔH	-139.6	-140.13	-140.68	-141.25
RS 6a	ΔG	98.08	89.19	80.12	70.96
	E_a	120.95	120.95	120.95	120.95
	A	1.09E+32	3.91E+32	8.89E+32	1.52E+33
	ΔH	124.33	125.01	125.54	125.92
RS 6b	ΔG	83.87	77.12	70.3	63.44
	E_a	116.97	116.97	116.97	116.97
	A	4.57E+18	1.26E+19	2.62E+19	4.47E+19
	ΔH	103.84	104.18	104.4	104.51
RS P	ΔG	-4.76	-5.67	-6.51	-7.28
	E_a	109.33	109.33	109.33	109.33
	A	6.78E+20	1.12E+21	1.48E+21	1.75E+21
	ΔH	-1.89	-2.19	-2.52	-2.86
RS Pa	ΔG	154.11	151.25	148.38	145.52
	E_a	272.99	272.99	272.99	272.99
	A	1.00E+25	2.54E+25	4.71E+25	7.27E+25
	ΔH	162.66	162.66	162.63	162.58
RS A1	ΔG	-25.97	-26.98	-27.97	-28.94
	E_a	98.46	98.46	98.46	98.46
	A	7.61E+20	1.57E+21	2.44E+21	3.15E+21
	ΔH	-22.96	-22.99	-23.09	-23.26
RS A2	ΔG	-17.26	-18.55	-19.75	-20.85
	E_a	65.73	65.73	65.73	65.73
	A	4.97E+21	7.02E+21	8.43E+21	9.27E+21
	ΔH	-13.21	-13.62	-14.03	-14.45
RS A3	ΔG	-19.83	-20.7	-21.52	-22.3
	E_a	117.07	117.07	117.07	117.07
	A	5.06E+17	1.10E+18	1.92E+18	2.86E+18
	ΔH	-17.19	-17.34	-17.53	-17.76

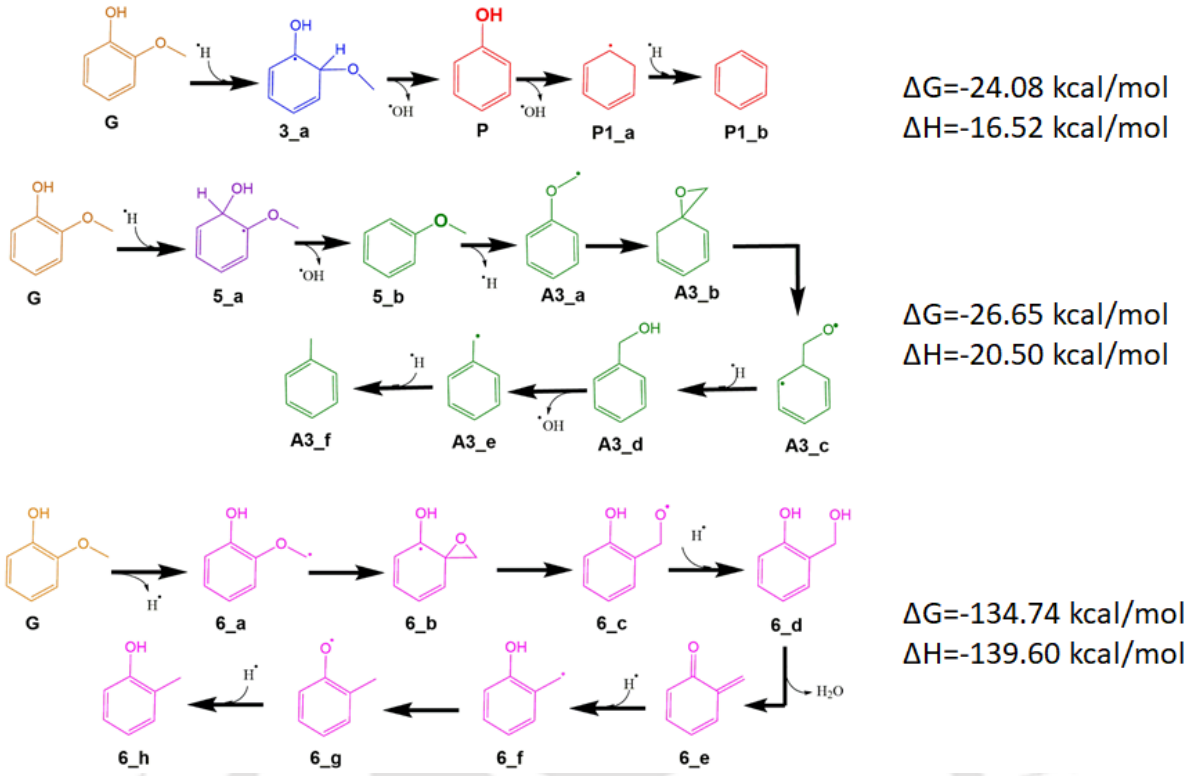

Figure 5.3.4: Most favourable paths for guaiacol to benzene, toluene and o-cresol production with overall ΔG and ΔH for each pathway.

In figure 5.3.5, the free energy plot of guaiacol to phenol conversion is described at 298 K and 598 K temperature and at 1atm and 20 atm pressure. It is seen that the conversion of structure P to P1_a is the least spontaneous reaction with ΔG as high as 82.17 kcal/mol at 298 K and 20 atm pressure. Whereas the conversion of structure P1_a to structure P1_b is the most spontaneous step with ΔG = -30.86 kcal/mol at 598 K at all pressures. The ΔG of conversion of guaiacol to structure 3_a is most favourable at 298 K temperature and 20 atm pressure whereas it is least favourable at 598 K temperature and 1 atm pressure. However, this trend reverses and formation of structure P is found to be more favourable at 598 K at all pressures and least favourable at 298 K at all pressures.

Similarly, in figure 5.3.6, the ΔG plot for the conversion of guaiacol to toluene is shown. The free energy change plot shows 298 K, 20 atm condition to be most favourable till the formation of anisole (structure 5_b) whereas 598 K, 1atm condition to be least spontaneous.

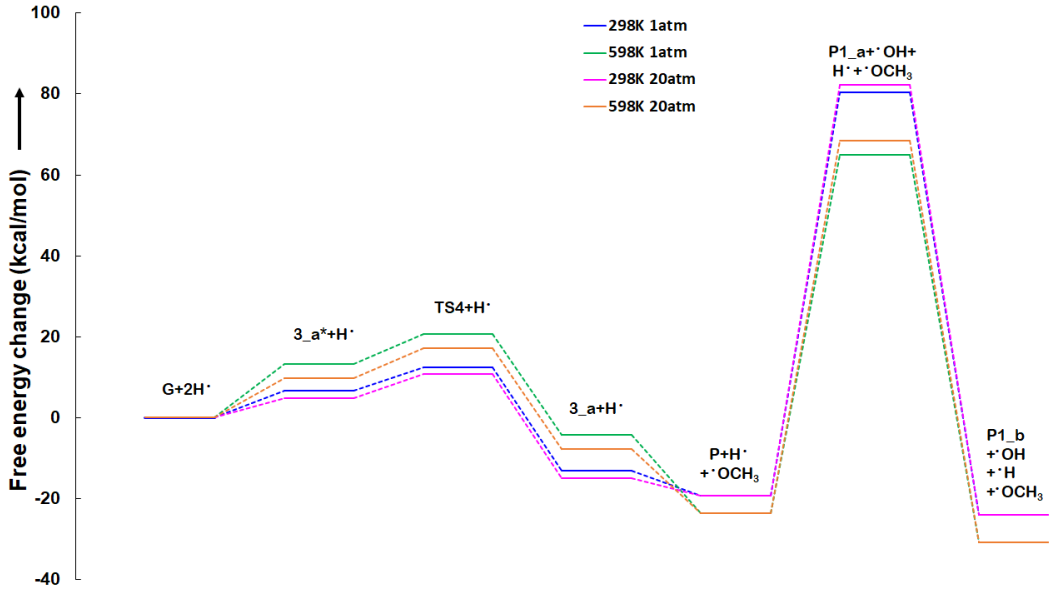

Figure 5.3.5: Free energy change landscape for conversion of guaiacol to benzene as described in figure 5.3.4.

Thereafter the trend is reversed and the formation of o-cresol is found to be most favourable at 598 K, 1atm condition. The rate controlling kinetics is observed in the conversion of structure A3_a to structure A3_b which proceeds via TS6. The ΔG for TS6 formation is most spontaneous at 598 K, 1atm condition with ΔG = 94.28 kcal/mol while the conversion is least spontaneous at 298 K , 20 atm with ΔG = 106.35 kcal/mol.

Figure 5.3.7 describes the free energy change plot of guaicol to o-cresol conversion. The ΔG for the conversion of structure 6_a to 6_b, which proceeds via transition state TS7 is the rate controlling step for this pathway and is most spontaneous at 598 K, 1 atm condition. ΔG for conversion of structure 6_a to TS7 is found to be 102.86 kcal/mol as the most favourable condition whereas ΔG is found to be 112.11 kcal/mol at 298 K, 20 atm condition which is least spontaneous. The formation of structure 6_d is not much affected by any change in parameters whereas significant change in ΔG of formation of structure 6_f and 6_g is observed only with

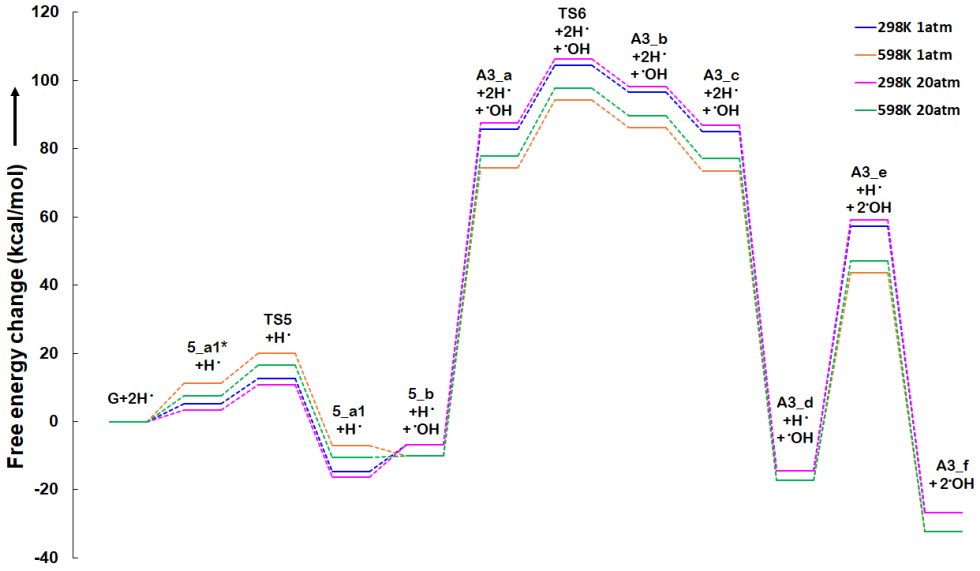

Figure 5.3.6: Free energy change landscape for conversion of guaiacol to toluene as described in figure 5.3.4.

change in temperature. From guaicol to formation of structure 6_g, 298 K temperature and 20 atm is least favourable condition; but thereafter, this condition becomes most favourable to yield structure 6_h with ΔG = -136.51 kcal/mol.

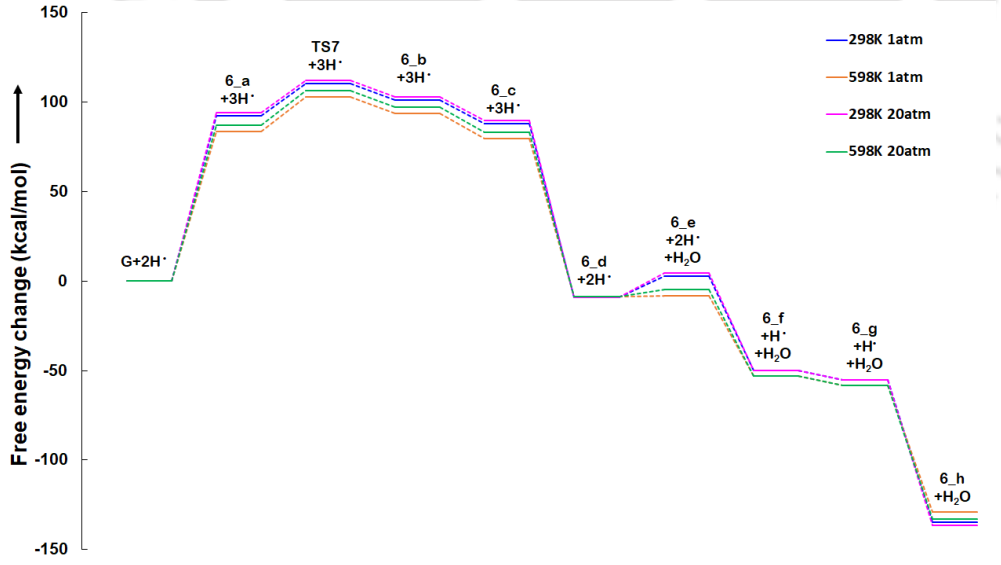

Figure 5.3.7: Free energy change landscape for conversion of guaiacol to o-cresol as described in figure 5.3.4.

5.4 Computational Study on Adsorption Characteristics of Phenol and Guaiacol Over Single and Multiple Nitrogen Doped Graphene

Density functional theory has emerged as a promising *ab initio* method in the past two decades for calculating the energies of molecular systems [134]. While most of the other first principle methods are computationally expensive, DFT considers all the electrons of the system as one entity - the electron density; and defines them with only three spatial variables [131]. This assumption simplifies the mathematics of energy calculation by reducing the total number of variables in the system and makes fairly accurate predictions at a reasonable computational cost [131]. Thus, it has emerged as the most suitable tool for studies where experimental observations are not feasible due to the scale of the system. In this study, the authors also employ the DFT to study the surface adsorption phenomenon over the N-doped graphene. To approximate the exchange-correlation potential of the DFT method, the M06-2X functional [164] from the meta-hybrid GGA class of functionals [139] is considered. This is because the M06-2X functional is reported to predict energies with less than 0.5 kcal/mol of error for organic systems [160]. All the structure optimization is performed using Pople's double zeta potential basis set with diffuse function for all non-hydrogen atoms and polarization functional for all atoms (6-31+g(d,p)) [151]. First, a 14 ring pure graphene sheet is prepared whose edges are closed with the dangling hydrogen atoms; and is optimized using the described functional and basis set. A doping site is then created in the central ring of the pure graphene by replacing a carbon atom with a nitrogen atom (Figure 5.4.1 (a)). A second graphene sheet is also considered with a pyridinic-like defect in a similar manner and is doped with one nitrogen atom, as shown in Figure 5.4.1 (b). To study multi-doping nitrogen effects, a third surface is also prepared by doping pristine graphene with 3 nitrogen atoms (Figure 5.4.1 (c)). The doped graphene sheets are then re-optimized at M06-2X/6-31+g(d,p) level of theory to obtain the

catalyst surface. The adsorption of model compounds is then carried out at different orientations on the optimized surfaces.

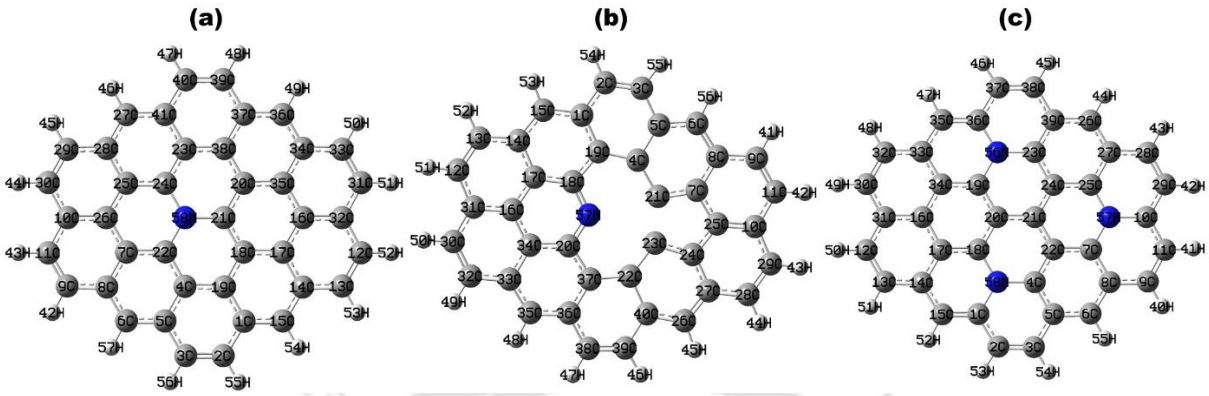

Figure 5.4.1: Optimized geometry of doped graphene sheets with (a) single doping on pristine graphene, (b) single nitrogen atom doping in pyridinic-like defective graphene and, (c) multi-doped graphene with three nitrogen atoms; where blue coloured atoms represent nitrogen, grey coloured atoms represent the carbon and white coloured atoms represent the hydrogen.

Once the geometries are optimized, the single point energy calculations are performed using Pople's triple zeta potential with diffuse and polarization function with M06-2X functional, i.e., M06-2X/6-311+g(d,p) with dispersion correction (D3) [178]. The adsorption energy (E_{ads}) is calculated as:

$$E_{ads} = E_{catalyst+substrate} - (E_{catalyst} + E_{substrate}) \quad (5.3)$$

where $E_{catalyst+substrate}$ is the energy of the system where the substrate is adsorbed over the catalyst surface. $E_{catalyst}$ and $E_{substrate}$ are individual energies of the catalyst and substrate, respectively.

To validate the prepared system, the authors reproduced the works of Fiorentine et al.[2] and studied the adsorption of CO_2 over N-doped graphene. For this, the catalyst surface was frozen, and the adsorption of CO_2 was conducted by keeping it relaxed. The adsorption energy was found to be -5.13 kcal/mol with dispersion correction, which is in excellent agreement with

the reported value of -5.65 kcal/mol. Similarly, the adsorption energy over pyridinic defect N-doped graphene was found to be -6.01 kcal/mol, similar to the reported value of -6.13 kcal/mol. The orientation and the location of the adsorption of CO_2 over the catalyst surface were also found to be identical to the reported results (Table 5.4.1 of the supplementary information). This "frozen catalyst surface and relaxed adsorbate" model is used throughout this study for determining the adsorption characteristics of bio-oil model compounds.

Table 5.4.1: Comparison of the present work with the literature work [2]

		Literature	This work
Graphitic defect	**Adsorption energy**	-5.65 kcal/mol	-5.13 kcal/mol
	Top view	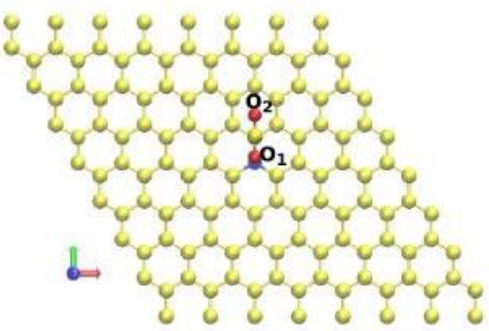	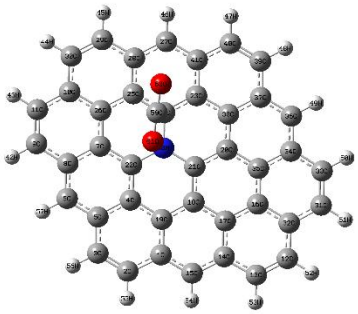
	Side view	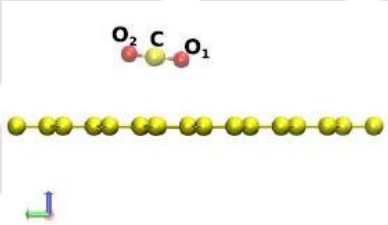	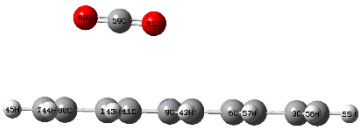
Pyridinic defect	**Adsorption energy**	-6.13 kcal/mol	-6.01 kcal/mol
	Top view	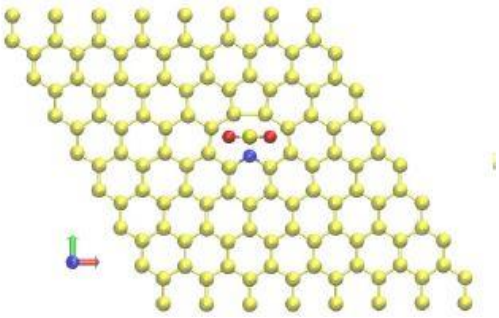	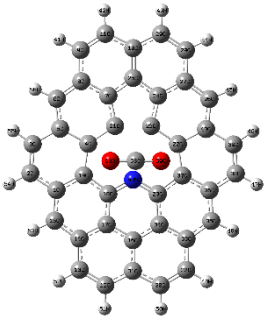

	Side view	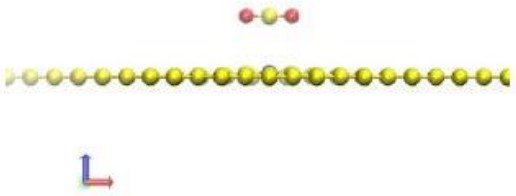	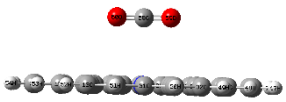

An important parameter to computationally characterize the adsorption over a catalyst is to study the distance between the adsorbate and the surface. The distance between the adsorbate and the surface is generally used to describe the strength of the two's interaction. However, in cases where the catalyst surface is not uniform or where the adsorbate molecule has multiple atoms interacting with the surface, the distance between the substrate and adsorbate's closest atoms does not accurately depict these interactions. To overcome this challenge, the authors devised a '*dipole moment change*' method. In this method, the dipole moment change is measured to quantify the approaching adsorbate's influence on the surface. The change in dipole moment ($\Delta\vec{\mu}$) is calculated as:

$$\Delta\vec{\mu} = \vec{\mu}_{\text{catalyst+substrate}} - \vec{\mu}_{\text{catalyst}} \tag{5.4}$$

Where $\vec{\mu}_{\text{catalyst+substrate}}$ is the dipole moment vector of the system where the substrate is adsorbed over the catalyst surface, and $\vec{\mu}_{\text{catalyst}}$ is the dipole moment vector of the bare catalyst. The magnitude ($\Delta\mu$) of the $\Delta\vec{\mu}$ provides a comparative analysis of adsorption of a species and their orientation on any surface. The '*dipole moment change*' method has an advantage in comparing the cases where the species are adsorbing on the catalyst in different orientations at a near-same distance from the surface. The orientation with a higher charge region of the adsorbate facing the surface will influence the surface more, and therefore the surface dipole more. Information about the influence of approaching charge on the surface can provide a better understanding of the adsorption characteristics than information on the closest distance between the surface and adsorbate.

All the calculations are performed using Gaussian 09 [169] with ultrafine grid setting, and the geometry management is done with the help of GaussView 05 [170]. For the density of state (DOS) and Fermi level calculations, GaussSum [179] and multiwfn [180] softwares are employed, respectively. Other properties like chemical potential (ν), chemical hardness (η), electrophilicity index (ω) and chemical softness (S) [181] are calculated as:

$$\nu = -(I+A)/2 \,, \tag{5.5}$$

$$\eta = (I-A)/2 \tag{5.6}$$

$$\omega = (\mu^2/2\eta) \,, \tag{5.7}$$

$$S = 1/2\eta \tag{5.8}$$

where I is the ionization potential, and A is the electron affinity. By Koopman's approximation [182], I is considered the negative of HOMO energy and A is considered the negative of LUMO energy.

First, the properties of pristine graphene and N-doped graphene are discussed to analyse the effect of nitrogen doping on the graphene. Thereafter, the adsorption characteristics of phenol and guaiacol are discussed over single atom doped graphene. Finally, the effect of multi-doped graphene is discussed to draw a comparison with single nitrogen-doped graphene.

5.4.1 Catalyst properties

A 14-ring pristine graphene catalyst surface is prepared by optimizing the structure at the given level of theory. The average bond length of the C-C bond in the ring is 1.42 Å which is in a perfect agreement with the experimental data [183]. The bond length for the single nitrogen-doped graphene (Q1) varies insignificantly from the pristine graphene near the doping site as the covalent radius of nitrogen is similar to carbon. A decrease of about 0.01 Å is observed in the length of C-N bonds. Bond lengths of different bonds in Q3 fluctuate within 0.02 Å from the pristine graphene bond lengths. Variations of such magnitude are reported in the literature

for nitrogen doping [69,184]; and are not at all uncommon in DFT studies. However, the P1 shows a lot of variation throughout the sheet. The C=N bond length is 1.31 Å, similar to the reported experimental bond length (1.30 Å) [185]. This is not uncommon given the five-ring (pyridine-like) loop in the sheet, which distorts the bond lengths significantly.

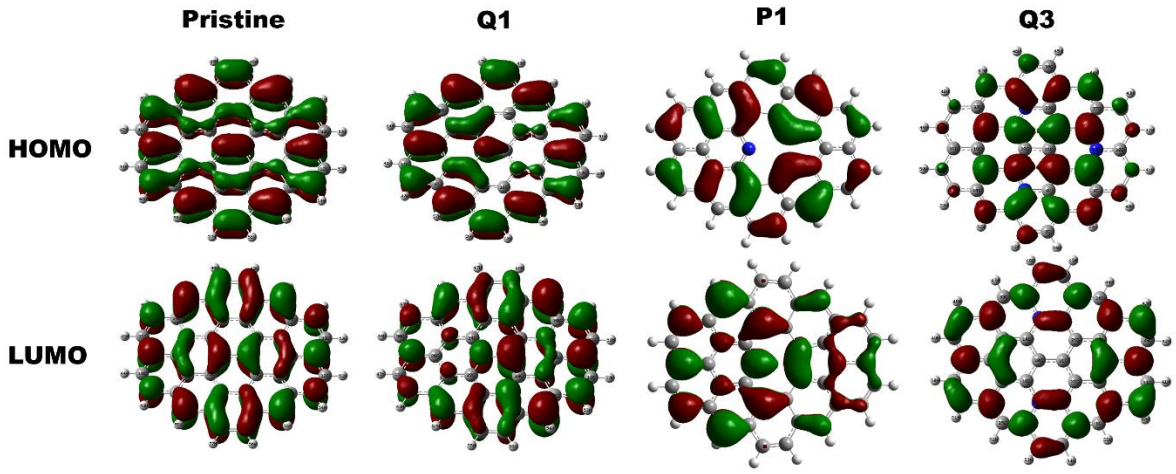

Figure 5.4.2: HOMO (top) and LUMO (bottom) orbitals for pristine, Q1, P1 and Q3 doped graphene sheets.

The HOMO and LUMO orbitals analysis (Figure 5.4.2) show that introducing nitrogen in the pristine graphene shifts the molecular orbitals significantly. In Q1, the nitrogen doped site show a HOMO localization, suggesting the site to be favourable for the transfer of electrons from the surface to the molecule. The 21st carbon atom adjacent to the nitrogen doping show a large LUMO localization. Thus, the site is favourable for accepting the electrons. In the P1 sheet, the HOMO is localized to the carbon atoms of the pyridinic-like ring near the defect site. Thus, the nitrogen site is not very electron donating, but the defect site is favourable for electron receiving entities. The LUMO orbitals show that the nitrogen has vacant orbitals; which can be filled by the adsorbing entity. The 21st and 23rd carbon atom which are located across the nitrogen atom towards the defect site, also has localization of LUMO orbitals. Thus the defect site is ideal for species with HOMO orbitals facing the site. In the Q3 sheet, the HOMO orbitals

appear in a zip like pattern in the centre. Thus, the adsorption can occur via the LUMO of the molecules in the central region. The LUMO orbitals of Q3 form a circular pattern around the centre and covers the nitrogen atoms. Thus, the adsorption via the HOMO orbitals of adsorbate is highly probable over the nitrogen atoms; however, less likely to occur over 21st carbon atom.

Table 5.4.2: Density of state of Pristine graphene, Q1 surface and Q3 surface near the fermi level.

Catalyst surface	Density of State	Fermi Level
Pristine	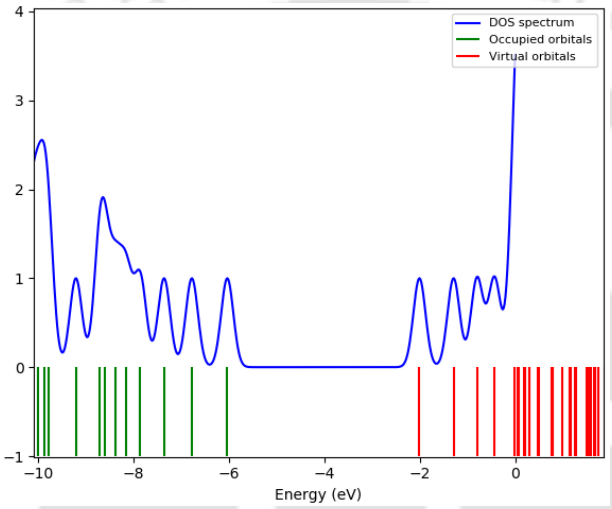	-6.03 eV
Q1	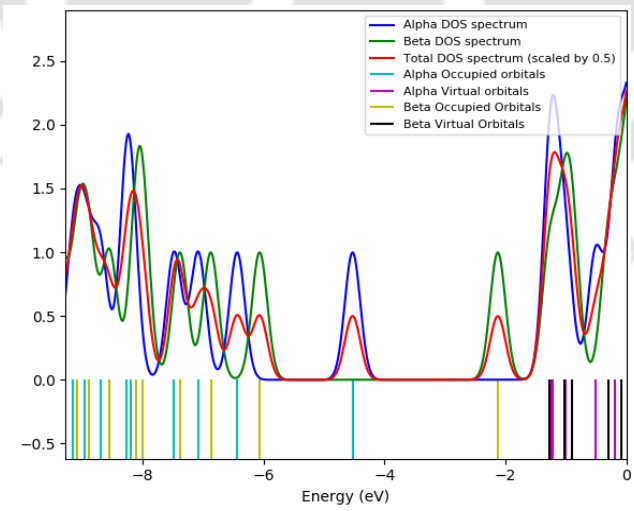	-4.52 eV

P1	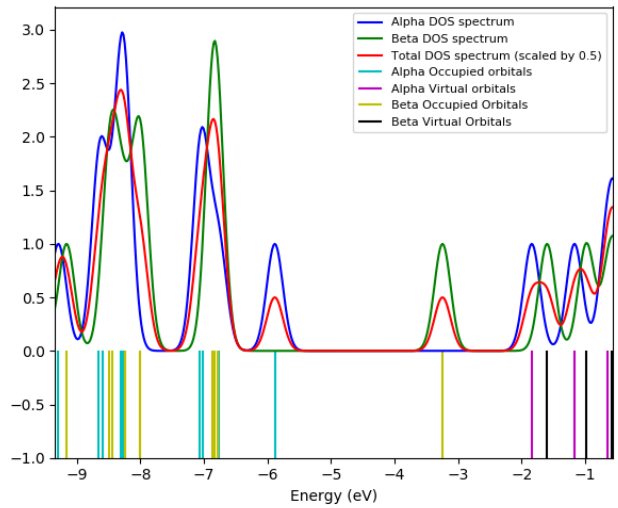	-5.88 eV
Q3	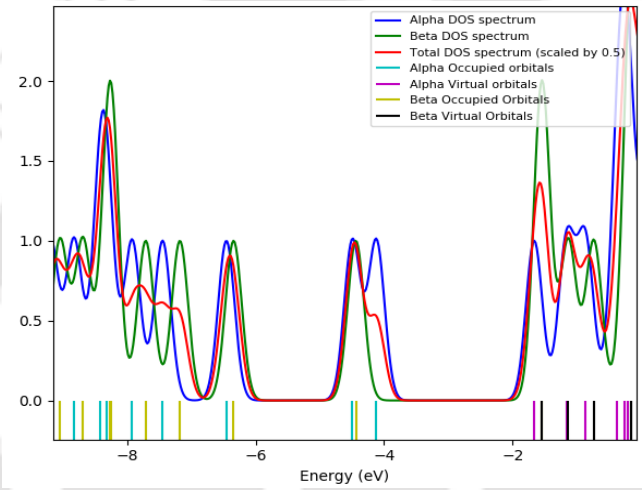	-4.12 eV

Fermi level (F_L) and electron density of state are also used to draw meaningful conclusions about the catalyst surface. While a higher F_L can denote a higher turnover frequency for any reaction, more electron density of state near the F_L is an indication of a better catalyst as many states are available for occupation [186]. The F_L for pristine graphene is found to be -6.03 eV which increases to -5.88 eV in P1, -4.52 eV in Q1 and -4.12 eV in Q3. However, the density of state (DOS) of all three catalysts is almost identical with Q3 having only one extra DOS near the F_L (Table 5.4.2). Based on F_L analysis, unlike the pristine graphene, P1, Q1 and Q3 catalysts possess some reactive sites on their surface. However, the DOS analysis suggests that from a single doped sheet of P1 and Q1 to multiple doped sheet Q3, there is no significant increase in these sites' reactivity.

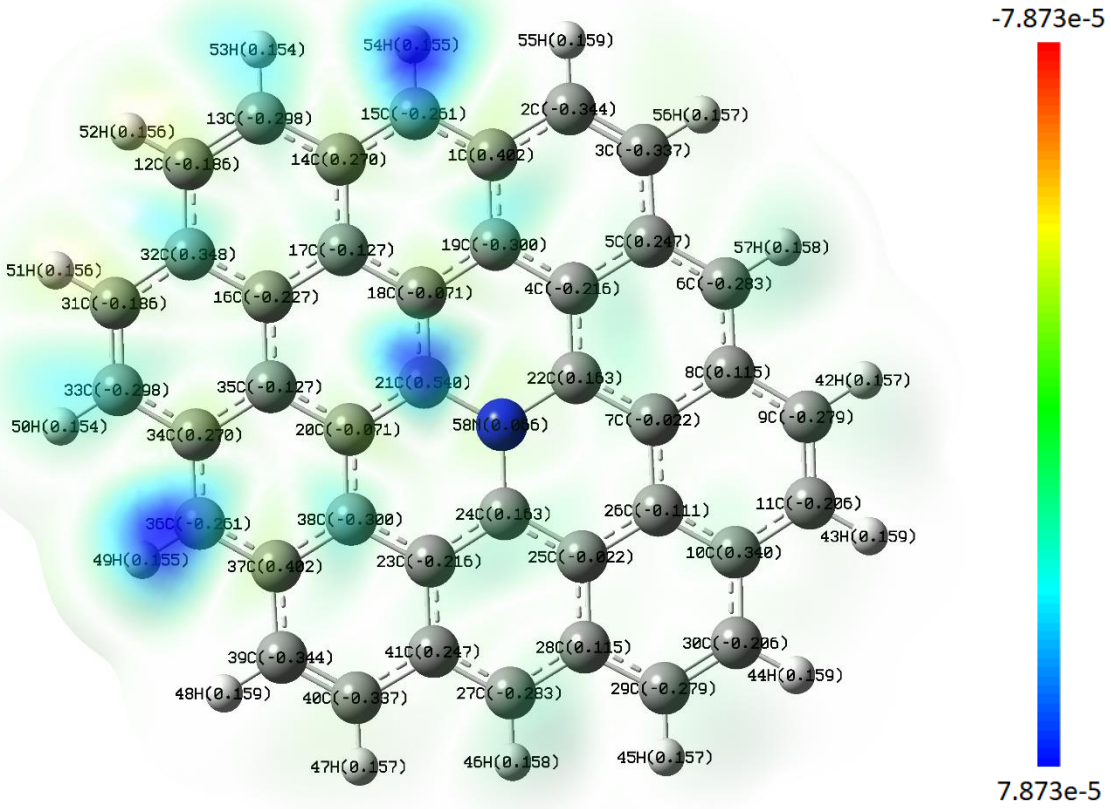

Figure 5.4.3: Spin density distribution (colour coded) and Mullikan charge distribution (in brackets) for Q1 surface.

The literature shows that high spin density and high charge serve as an ideal site for surface reactivity [115]. Spin density distribution describes the probability distribution of unpaired electrons over the surface. Therefore, to determine the location of the reactive sites on Q1, P1 and Q3, spin density analysis and Mullikan charge distribution analysis are conducted. Figure 5.4.3, 5.4.4 and 5.4.5 show spin density distribution and charge distribution for Q1, P1 and Q3, respectively. A high spin density distribution can be seen over 21st and 36th carbon atom along with 54th hydrogen atom for the Q1 catalyst. This could be attributed to the nitrogen's electronegative nature causing the nitrogen to pull electrons from the neighbouring atoms and giving 21C a high positive charge (0.540 a. u). The high spin density and high charge

make 21C an ideal site for catalytic activity. The bridge sites 15C-54H and 36C-49H also show high spin density distribution. However, since the catalytic activity at the boundary is a reasonably complex process, these sites are not considered for adsorption in the study.

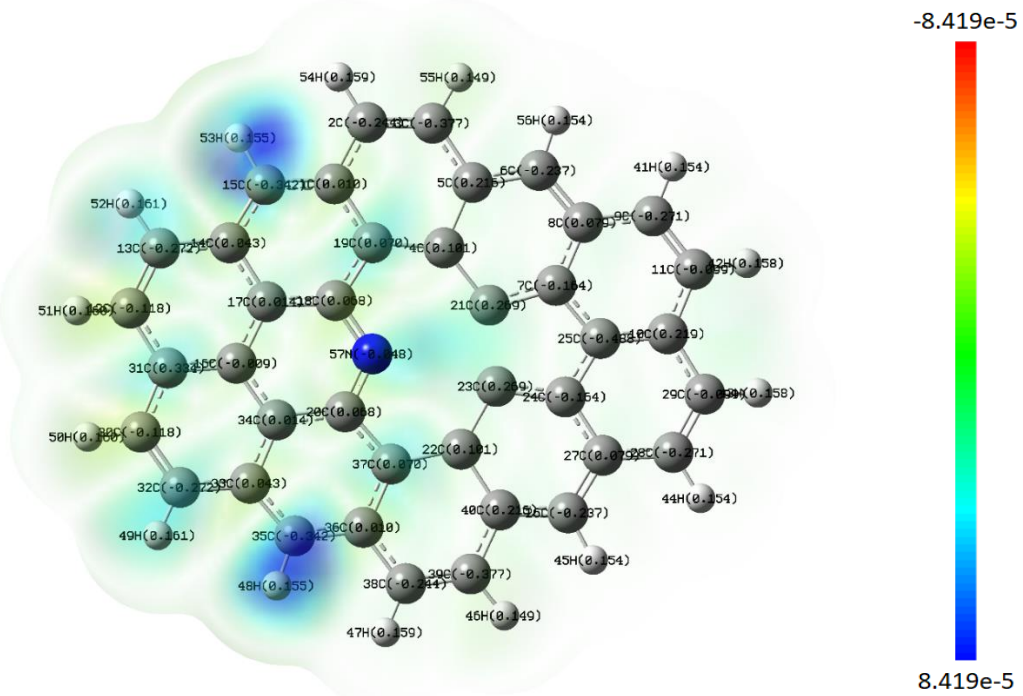

Figure 5.4.4: Spin density distribution (colour coded) and Mullikan charge distribution (in brackets) for P1 surface.

The spin density distribution for P1 is found to be high at the defect site between 57N and 23C/21C. This is again likely a result of the electronegative nature of the nitrogen atoms. The charge distribution of the adjacent atoms (23C and 21C) is again positive and high like the Q1 surface. The bridge site of 15C-53H and 35C-48H also shows favourable spin density similar to Q1 and has not been considered for adsorption in this study. Also, 19C, and 37C likewise show the fair spin distribution and positive charge, suggesting possible role in the adsorption process.

In Q3 (Figure 5.4.5), it can be seen that the number of high spin density sites increase due to a greater number of nitrogen-doping sites. The spin distribution is also more irregular and

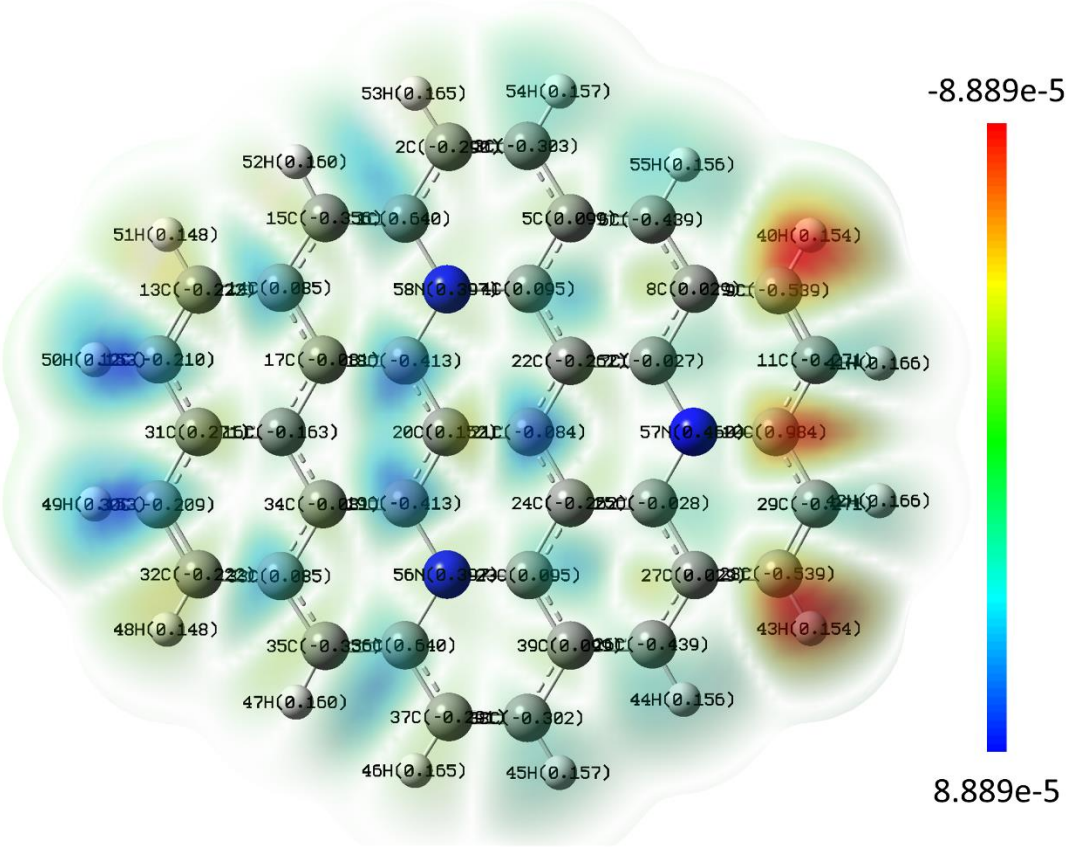

Figure 5.4.5: Spin density distribution (colour coded) and Mullikan charge distribution (in brackets) for Q3 surface.

unevenly distributed over Q3 than Q1 and P1. While the bridge sites 50H-12C and 49H-30C exhibit low spin density, 40H-9C and 28C-43H are highly deficit in unpaired electrons. The atoms around the nitrogen atoms - 18th, 19th and 20th carbon atom, has a low spin density with positive charge distribution making them suitable adsorption sites. In addition, 1C, 14C, 33C and 36C are also observed to have a spin density on the higher side with positive charge distribution and may contribute to the adsorption.

Another critical parameter for surface property determination is the Electrostatic Potential (ESP), which define the electrophilic and nucleophilic centres on a catalytic surface [187]. The ESP plots help determine the possible regions of adsorption on the catalyst by providing information about the nucleophilic and electrophilic regions based on the substrate's

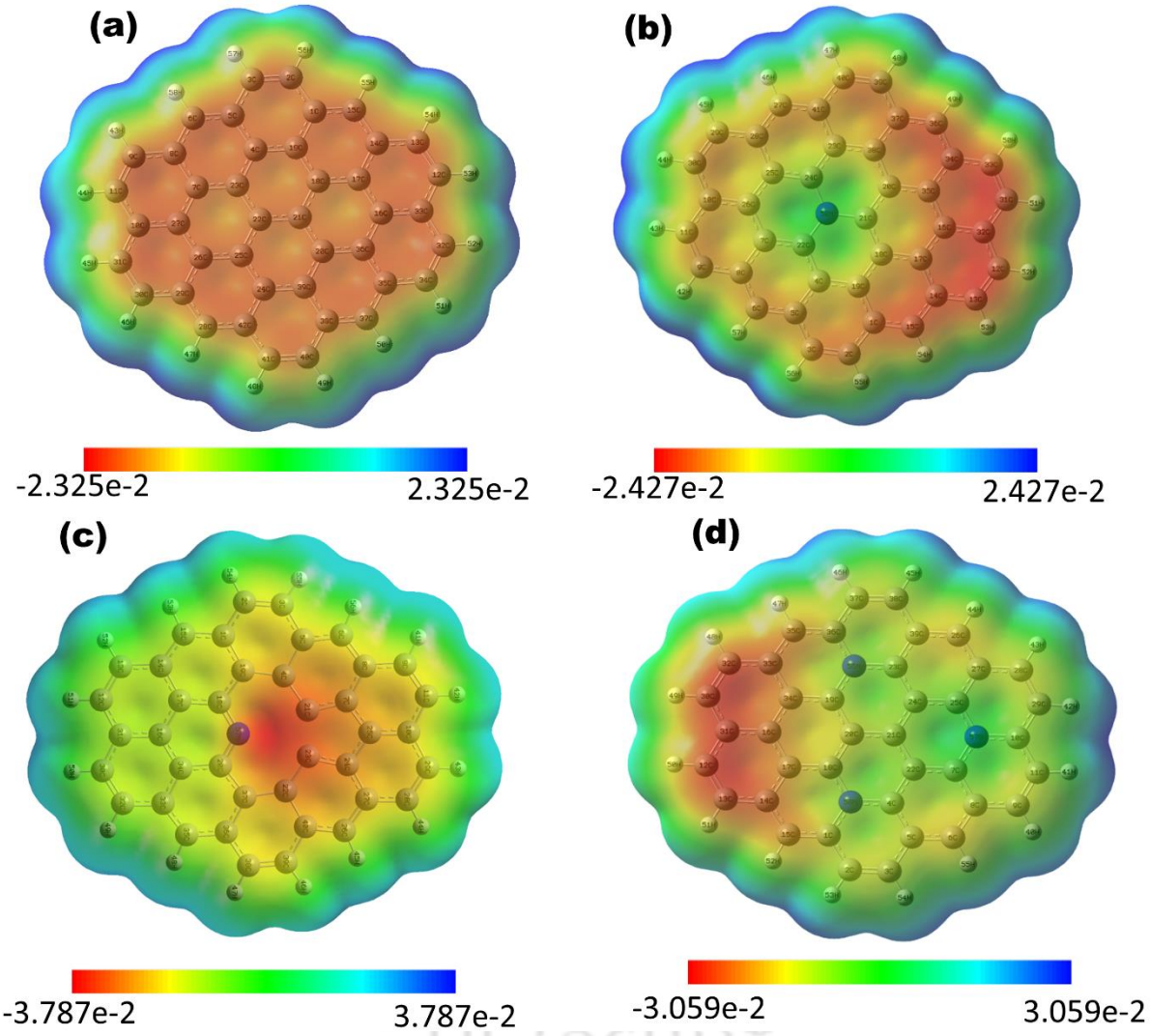

Figure 5.4.6: Electrostatic potential (ESP) map of (a) pristine graphene, (b) Q1 catalyst surface, (c) P1 catalyst surface and (d) Q3 catalyst surface showing nucleophilic regions (blue) and electrophilic regions (red).

charge distribution. Figure 5.4.6(b) shows that the part around 58N is fairly neutral while the atoms adjacent to the nitrogen atoms, including 21st carbon atom, are mildly rich in electron.

This contrasts with the pristine graphene (Figure 5.4.6(a)) where all carbon atoms possess the uniform potential of about -0.015 a.u. Increase in the distance from the nitrogen atom in Q1 increases the nucleophilicity of the carbon atoms making 31C and 12C the most electrophilic atoms. The nitrogen atom neutralizes the atom in its immediate vicinity. Similarly, the atoms around the nitrogen atoms in Q3 (Figure 5.4.6(b)) are also either neutral or mildly nucleophilic. High electron accumulation is observed over 30, 31 and 12 carbon atoms by virtue of them being farthest from the nitrogen atoms in Q3. However, in P1, the defect site 57N-21C/23C is highly electrophilic. This makes the region around 57N more favourable for adsorption of neutral entities and the region around 31C favourable towards electrophilic entities' adsorption.

Table 5.4.3: Ionization potential (I), electron affinity (A), chemical hardness (η), chemical potential (μ), chemical softness (S) and electrophilicity index (ω) for pristine graphene, Q1 surface, P1 surface and Q3 surface.

	I (eV)	**A (eV)**	**η (eV)**	**μ (eV)**	**S (eV^{-1})**	**ω (eV)**
Pristine	5.98	1.99	2.00	-3.98	0.25	3.97
Q1	4.49	1.24	1.62	-2.87	0.31	2.53
P1	5.84	1.82	2.01	-3.83	0.25	3.65
Q3	4.09	1.65	1.22	-2.87	0.41	3.38

Other global indices like chemical potential (ν), chemical hardness (η), electrophilicity index (ω) and chemical softness (S) are also determined for all four surfaces. While η is an indicator of the surface's resistance to an external electric field, S indicates the ease with each a surface deforms in the presence of external electric forces. η for pristine graphene is calculated as 2.00 eV, which decreases to 1.62 eV and 1.22 eV for Q1 and Q3, suggesting decreasing stability and increasing reactivity with an increase in nitrogen doping on the graphene sheets. On the contrary, η for the P1 surface is similar to the pristine surface with 2.01 eV and is therefore likely to retain its structure in the presence of an external potential. The chemical potential is the same for Q1 and Q3 surface (Table 5.4.3) and is higher than P1 and pristine

surfaces. Interestingly though, the ω of the Q3 is found to be higher than Q1, and ω of the P1 is found to be higher than Q3. Therefore, P1 is the most suitable surface for the adsorption of a nucleophilic entity among the three surfaces.

5.4.2 Adsorption of phenol

The adsorption of phenol is studied for 3 different configurations on Q1 (Figure 5.4.7). The phenol is adsorbed on the surface at the high spin density and high charge site (21C) in two orientations – via the ring (config 2) and the hydroxyl group (config 3). In addition, the third adsorption is also conducted over the nitrogen atom via the phenyl ring of phenol (config 1) to check any effect of nitrogen on the adsorption process.

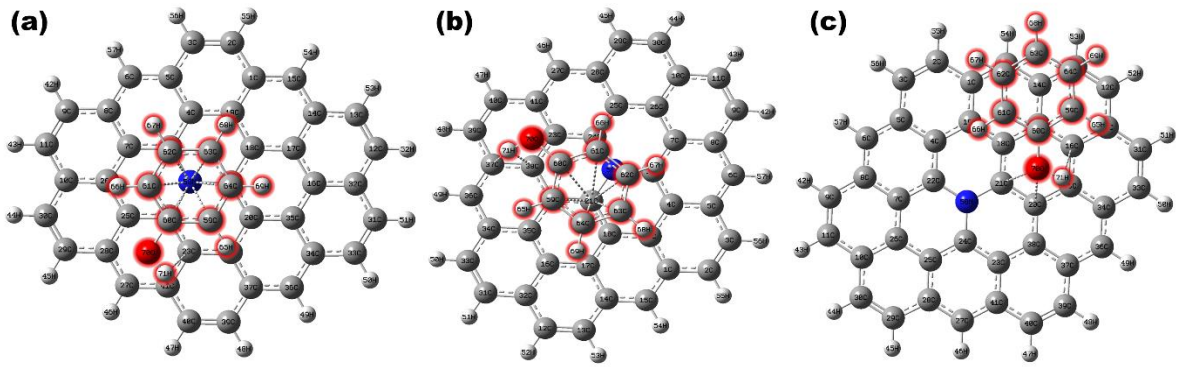

Figure 5.4.7: Adsorption of phenol on Q1 surface over (a) nitrogen atom via phenyl ring (b) 21C via phenyl ring and (c) 21C via OH group

It is observed that the adsorption of phenol over the nitrogen atom has the most favourable adsorption energy of all three configurations (Table 5.4.4). The change in the charge over the adjacent 21C atom of nitrogen atoms is the highest for this configuration among all three. This suggests that a strong charge delocalization occurs on the surface when the adsorption occurs via the nitrogen atom, which results in the strong adsorption. The charge transfer and the change in the dipole moment were moderate for this configuration. The weakest adsorption (E_{ads} = 13.21 kcal/mol) was observed for the third configuration where the

adsorption occurs by the hydroxyl group over 21C. The charge transfer for this reaction is found to be very small (0.067 a.u.). Consequently, the change in the highest positive and negative is also low; hence the weak adsorption. The pre-exponential factor for the adsorption is also calculated by the Hertz−Knudsen relation [188] as shown in table 5.4.4.

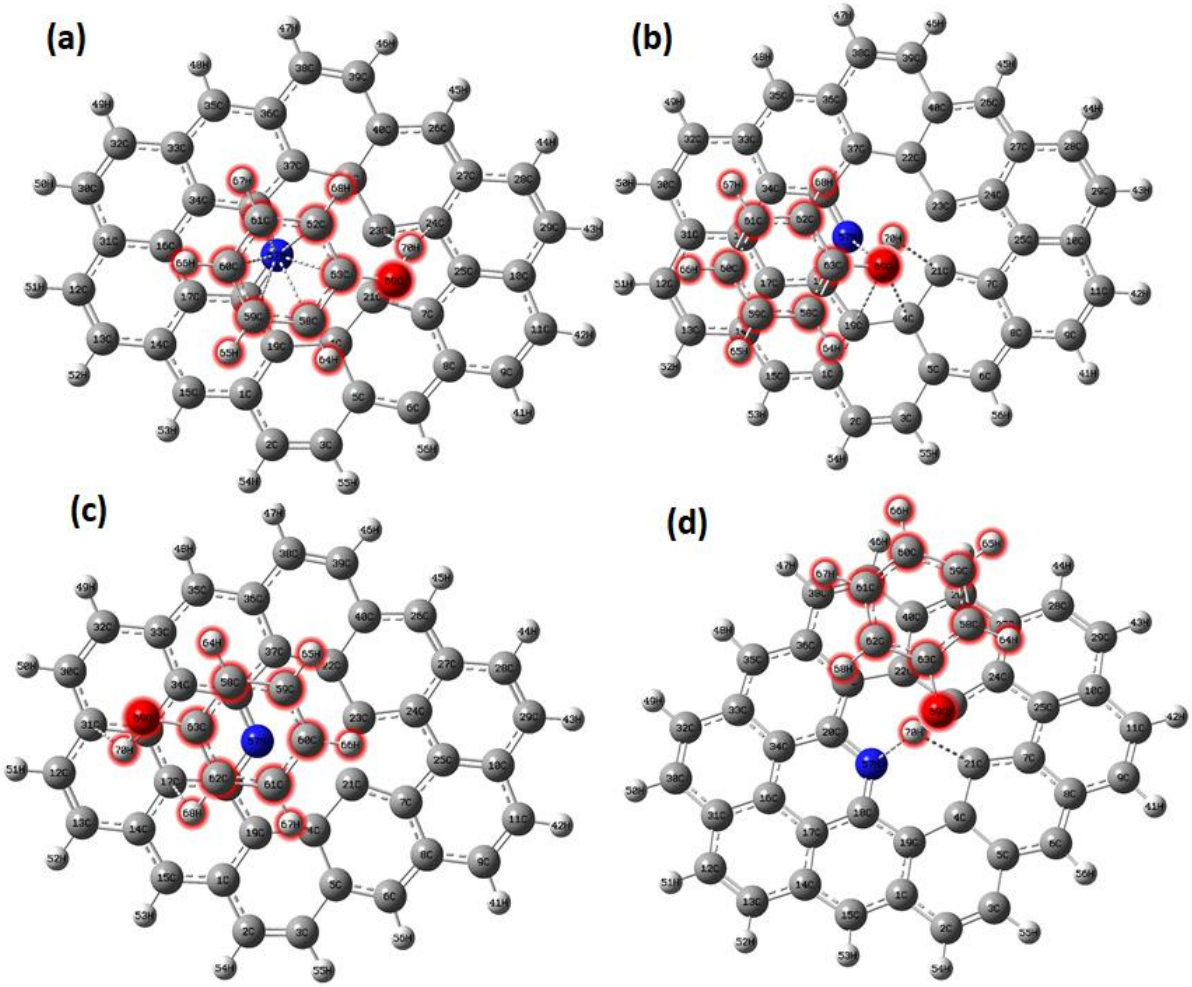

Figure 5.4.8: Adsorption of phenol on P1 surface over (a)nitrogen atom via phenyl ring, (b)nitrogen atom via hydroxyl group, (c) nitrogen atom with hydroxyl group facing away from the defect site, (d) defect site via hydroxyl group with phenyl ring facing away from the surface.

The adsorption of phenol is also studied over the P1 surface. Four configurations of phenol are adsorbed on the P1 surface at different locations (Figure 5.4.8). In the first configuration, the phenol is positioned so that the phenyl ring is positioned above the nitrogen

atom and the hydroxyl group is over the defect site. In the second configuration, the phenol is shifted such that the hydroxyl group is adsorbed over the nitrogen atoms. In the third configuration, the phenyl group is positioned over the nitrogen while the hydroxyl group faces away from the defect site. Finally, in the fourth configuration, the hydroxyl group is approached towards the defect site from above such that there is minimum interaction of the phenyl ring with the surface.

Table 5.4.4: Comparison of properties of different adsorption configurations of phenol over Q1 and P1 surface.

	Q1			P1			
	Config 1	Config 2	Config 3	Config 1	Config 2	Config 3	Config 4
E_{ads} (kcal/mol)	-17.28	-16.83	-13.21	-15.85	-16.28	-15.22	-13.16
Pre-exponential factor (s^{-1})	2.89E+04			2.87E+04			
Δμ (Debye)	0.93	1.01	0.99	1.19	1.31	1.09	1.58
Charge Transfer (a.u.)	0.135	0.182	0.067	0.141	0.233	0.171	0.142
Highest change in positive charge in a.u. (atom)	0.658 (58N)	0.827 (58N)	0.230 (2C)	0.349 (57N)	0.172 (57N)	0.506 (57N)	0.040 (57N)
Highest change in negative charge in a.u. (atom)	-0.798 (21C)	-0.792 (21C)	-0.315 (21C)	-0.478 (23C)	-0.361 (20C)	-0.333 (20C)	-0.298 (20C)

It is observed that the strongest adsorption takes place in the second configuration (E_{ads} = 16.28 kcal/mol) where the adsorption is occurring from the OH group facing the defect site. High charge transfer (0.233 a.u.) again plays a significant role in providing strong adsorption energy among the four configurations. However, large individual positive or negative charge change is not observed for this configuration. This implies that unlike the Q1 case, the charge transfer is more distributed and takes place through more than one atom between the surface and the adsorbate. The weakest adsorption occurs in the 4th configuration (E_{ads} = -13.16

kcal/mol) where the phenyl ring of phenol is facing away from the surface. The phenol orientation prohibits the interaction of the ring with the surface, leading to a smaller overall charge transfer. The most significant positive charge change is mere 0.040 a.u. over the nitrogen atom. However, the difference in the dipole moment is highest (1.58 D) in this case. Indeed, the highly polar hydroxyl group influences the surface dipole to a more considerable degree when facing the surface than being parallel to the surface in other configurations. Config 1 and config 3 also show adsorption on the stronger side; however, the relatively low charge transfer (0.141a.u. and 0.171 a.u. respectively) and low dipole moment change (1.19 D and 1.09 D respectively) leads to a lower E_{ads} than config 2.

5.4.3 Adsorption of guaiacol

The adsorption of guaiacol is studied for four different configurations on Q1 and P1 surface (Figure 5.4.9). Over the Q1 surface, the adsorption is conducted over the 21C atom via the phenyl ring, the hydroxyl group and the methoxy group in config 2, 3 and 4. In addition, similar to the phenol adsorption described above, config 1 shows guaiacol's adsorption over the nitrogen atom via the phenyl ring.

It is observed that the adsorption of guaiacol is strongest in the 1st configuration where the phenyl ring is adsorbing over nitrogen atom (Table 5.4.5). Although the charge transfer is not the highest in this case (0.166 a.u.), the negative change in the individual atom is very high (1.403 a.u.) over the adjacent 21C atom which suggests that a strong delocalization of the charge is occurring on the surface at the adsorption site. The delocalization of charge explains the strong adsorption (E_{ads} = -21.45 kcal/mol). Config 2 show moderate adsorption energy and have moderate charge transfer and dipole moment change. Config 3, on the other hand, has the weakest adsorption energy (E_{ads} = -18.20 kcal/mol) despite having a high dipole change (2.24 D). As the charge transfer is low, the polar hydroxyl and methoxy group influence the surface

dipole to a larger extend than in other cases where the charge transfer reduces the molecule's polarity. The largest charge transfer is observed in config 4. However, the adsorption energy is not the strongest as the dipole moment change is the lowest in this configuration.

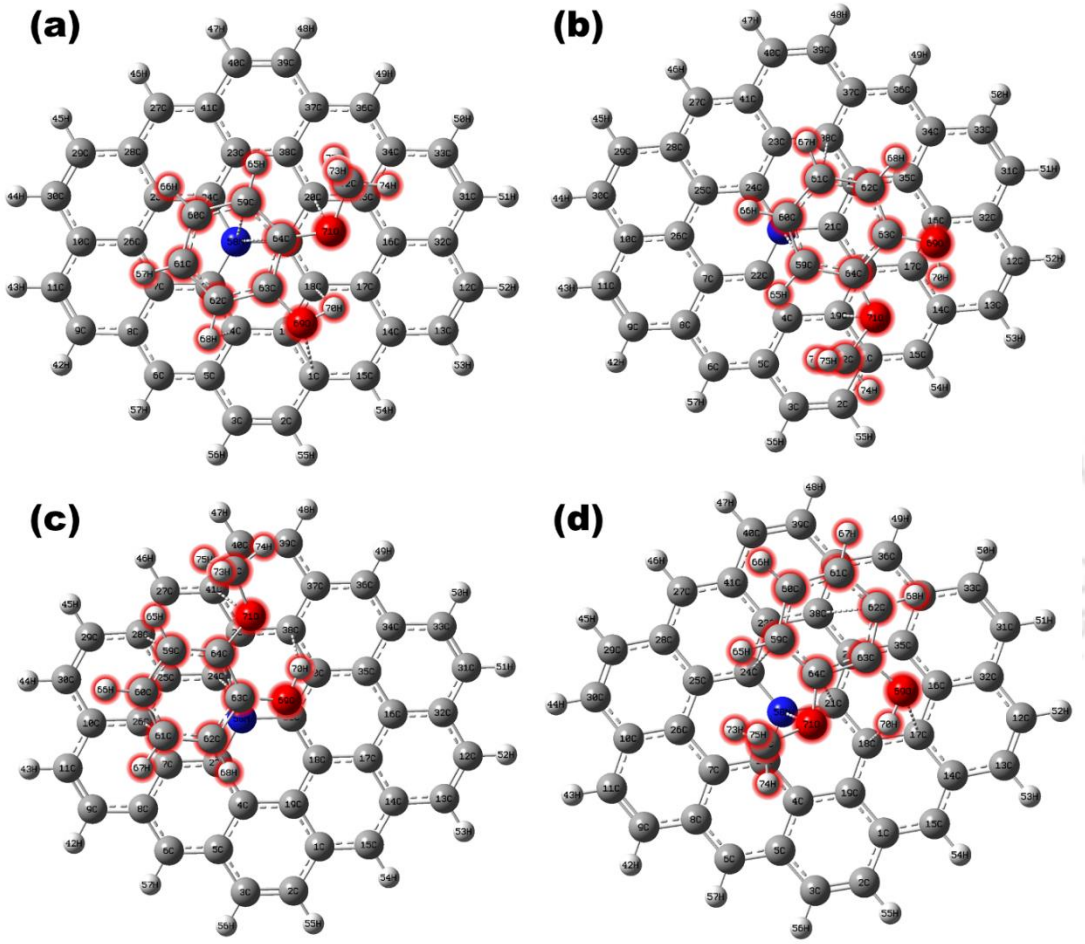

Figure 5.4.9: Adsorption of guaiacol on Q1 surface over (a) nitrogen atom via phenyl ring, (b) 21C atom via phenyl ring, (c) 21C atom via hydroxyl group, (d) 21C atom via methoxy group.

The adsorption of guaiacol over P1 surface was also conducted in four different configurations (Figure 5.4.10). In the first and second configuration, the methoxy group and the hydroxyl group were adsorbed over the nitrogen. In the third configuration, the phenyl ring of the guaiacol molecule was adsorbed over the nitrogen atom. Finally, in the fourth configuration,

the guaiacol molecules were placed in such a position that the phenyl ring adsorbed over the surface's defect site.

It was observed that the adsorption of guaiacol over the P1 surface was weaker than the adsorption over the Q1 surface. The strongest guaiacol adsorption energy over P1 is calculated

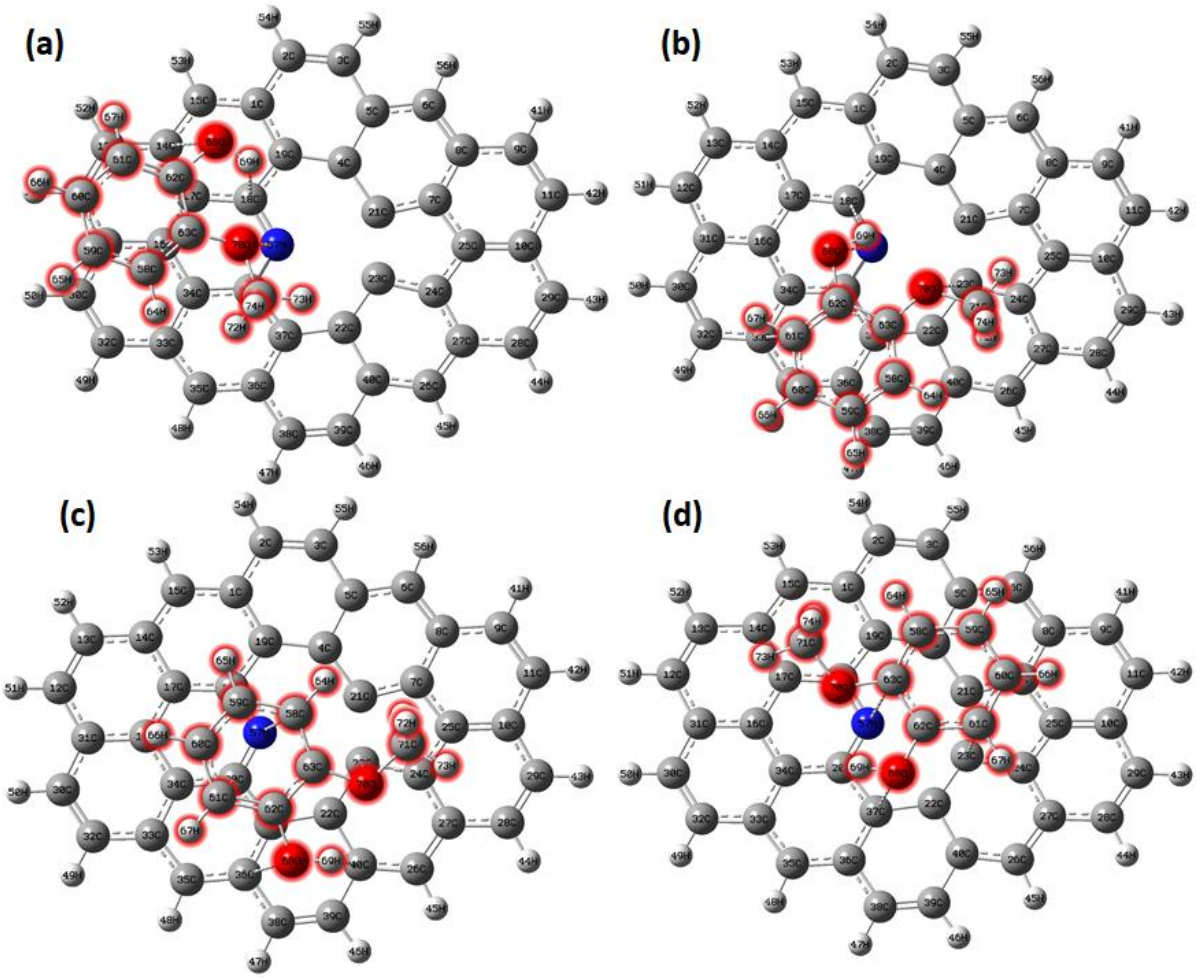

Figure 5.4.10: Adsorption of guaiacol on P1 surface over (a) nitrogen atom via the methoxy group, (b) nitrogen atom via the hydroxyl group, (c) nitrogen atom via the phenyl ring, (d) defect site via the phenyl ring.

to be -19.59 kcal/mol in 3rd configuration, which is 1.86 kcal/mol weaker than the strongest adsorption energy over Q1 surface. The high adsorption energy for the third configuration is surprising as neither the charge transfer nor the change in the charge of individual atoms of the

surface is very high. However, the dipole moment's difference is the highest for this configuration, indicating a strong interaction between the surface and the adsorbate. The weakest adsorption energy is observed for config 1 where the charge transfer is the smallest (0.109 a.u.). The change in the dipole moment is also the lowest in this configuration. The charge transfer for the second and fourth configuration are moderate, and therefore the E_{ads} is also found to lie between the E_{ads} of config 2 and config 4.

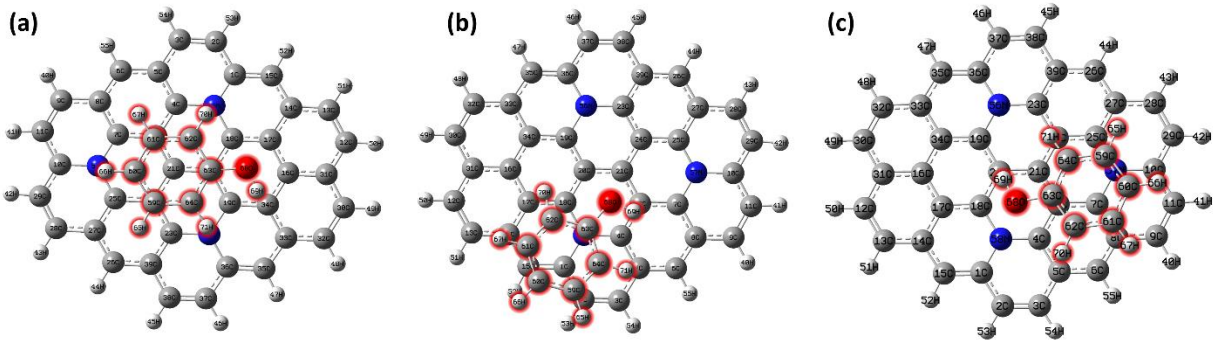

Figure 5.4.11: Adsorption of phenol on Q3 surface over (a) 21st carbon atom via the phenyl ring, (b) 21st carbon atom via the hydroxyl group, and (c) nitrogen atom via hydroxyl group.

Table 5.4.5: Comparison of properties of different adsorption configurations of guaiacol over Q1 and P1 surface

	Q1				P1			
	Config 1	Config 2	Config 3	Config 4	Config 1	Config 2	Config 3	Config 4
E_{ads} (kcal/mol)	-21.45	-19.97	-18.20	-19.28	-16.49	-18.31	-19.59	-18.58
Pre-exponential factor (s^{-1})	2.52E+04				2.50E+04			
Δμ (Debye)	1.75	1.74	2.24	1.60	1.66	1.98	2.07	1.68

Charge transfer (a.u.)	0.166	0.208	0.176	0.283	0.109	0.140	0.117	0.197
Highest change in negative charge in a.u. (atom)	-1.403 (21C)	-0.630 (21C)	-0.534 (24C)	-0.719 (21C)	-0.573 (20C)	-0.512 (20C)	-0.406 (20C)	-0.533 (20C)
Highest change in positive charge in a.u. (atom)	0.732 (58N)	0.886 (58N)	0.731 (58N)	0.812 (58N)	0.319 (57N)	0.281 (57N)	0.506 (57N)	0.367 (57N)

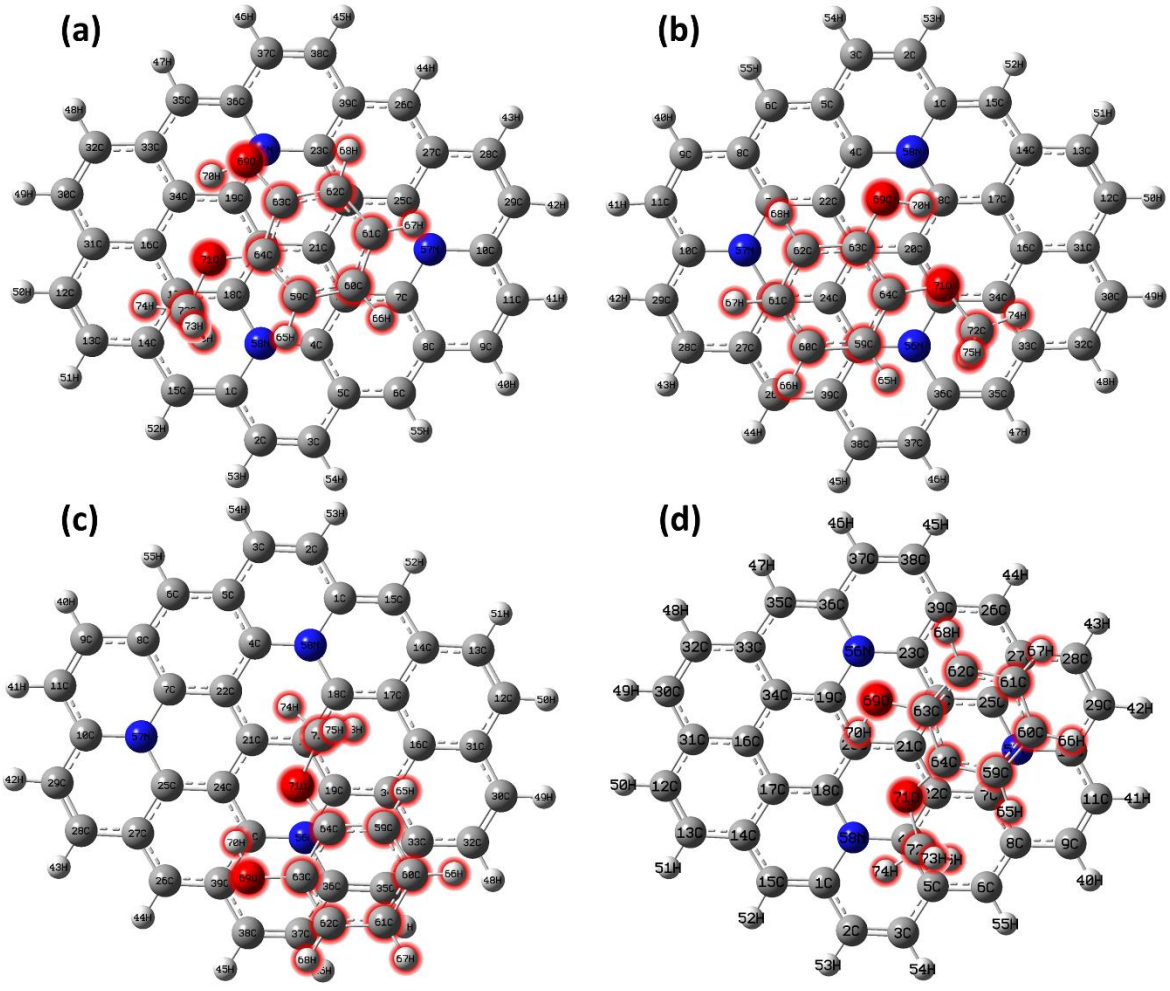

Figure 5.4.12: Adsorption of guaiacol on Q3 surface over (a) 21st carbon atom via phenyl ring, (b) 21st carbon atom via hydroxyl group, (c) 21st carbon atom via methoxy group, (d) nitrogen atom via methoxy group

5.4.4 Multi-site doping adsorption

To determine the effect of multiple nitrogen doping in the sheet, the adsorption of phenol and guaiacol was also studied on the Q3 surface. The adsorption of phenol was conducted in 3 different configurations (Figure 5.4.11). In the first configuration, the adsorption was conducted via the phenyl ring over the 21C atom. In the second configuration, the adsorption was conducted via the hydroxyl group over the same atom of the surface. Since phenol's best adsorption over Q1 surface was observed when the phenyl ring adsorbed over the nitrogen atom, a similar arrangement is considered in config 3 for Q3. The phenyl ring is adsorbed over the 57N atom (Table 5.4.6). The strongest adsorption (E_{ads} = -16.83) is observed for the first configuration which is a result of the high charge delocalization on the surface. In the third configuration, the phenyl ring shifted from over the 57th nitrogen atom and the adsorption occurred over the 56th nitrogen atom via the hydroxyl group. The high dipole moment change is observed because the polar hydroxyl group is facing the surface, similar to the 4th configuration of phenol over P1 surface.

The adsorption of guaiacol is also studied over Q3 in four different configurations (Figure 5.4.12). The first three configurations describe the adsorption over the 21C atom of the surface via the ring, the hydroxyl group and the methoxy group. In the fourth configuration, the adsorption is studied over the 57th atom (nitrogen) via the phenyl ring as the similar arrangement was found most favourable over Q1 surface. The guaiacol molecule was found to shift in the second configuration such that the oxygen atom of the methoxy group is placed over 18th carbon atom, which is found to have maximum change in its charge among all atoms (-1.065 a.u.). As a result, the strongest adsorption is observed for this case. The shifting of molecule was also observed in the fourth configuration. The guaiacol moved from over the 57th nitrogen atom such that the oxygen atom of the methoxy group drifted closer to the 58th nitrogen atom. But as the

charge transfer and the change in the charge over individual atoms are also low, this configuration did not show the strongest adsorption.

Table 5.4.6: Comparison of properties of different adsorption configurations of phenol and guaiacol over Q3 surface

	Phenol adsorption			Guaiacol adsorption			
	Config 1	Config 2	Config 3	Config 1	Config 2	Config 3	Config 4
E_{ads} with D3 (Kcal/mol)	-16.83	-13.45	-16.33	-21.24	-21.53	-16.94	-20.65
Pre-exponential factor (s^{-1})	2.88E+04			2.51E+04			
Δμ (Debye)	0.70	0.69	1.08	1.67	1.78	1.64	1.92
Charge transfer (a.u.)	0.018	0.074	0.009	0.146	0.113	0.044	0.132
Highest change in negative charge in a.u. (atom)	-1.038 (19C)	-0.852 (19C)	-0.773 (18C)	-0.958 (18C)	-1.065 (18C)	-0.786 (24C)	-0.355 (10C)
Highest change in positive charge in a.u. (atom)	0.785 (56N)	0.726 (58N)	0.796 (58N)	0.879 (56N)	0.799 (58N)	0.570 (58N)	0.288 (28C)

5.5 Dehydrogenation and Dehydration of Formic Acid over Orthorhombic Molybdenum Carbide

5.5.1 System setup

The decomposition of formic acid proceeds mainly via dehydration or dehydrogenation [189]. In the dehydration mechanism, formic acid decomposes to CO and H_2O, whereas in the dehydrogenation mechanism, CO_2 and H_2 are formed. A third mechanism is also reported for decomposition to formaldehyde (HCHO), which is observed in trace quantities in non-catalytic reactions [190]; however, since such a mechanism is not reported in catalytic investigations, the formaldehyde product has not been considered further.

All the elementary reactions considered for the dehydration and dehydrogenation mechanisms are shown in Figure 5.5.1. For ease of understanding, the reactants, products and transition states are herein referred to as *X*r, *X*p and *X*TS, respectively, where *X* is the reaction number in Figure 5.5.1. The surface site is represented by *, with an adsorbed species denoted by their chemical formula followed by *.

The reaction scheme begins with the adsorption of formic acid (1r) on to the surface to give 1p. As the cleavage of the C=O bond is energetically demanding (7.67 eV) [191,192] and therefore, low probability, the adsorbed formic acid (HCOOH*) can begin to break down in three ways:

The H atom can break from the hydroxyl group to give HCOO* and H* (Reaction 2);
Alternatively, the C-H bond can break to give H* and COOH* (Reaction 3);
The entire hydroxyl group can break apart from the C atom to give HCO* and OH* (Reaction 4).[191,192]

The HCOO* formed in reaction 2 can dehydrogenate in two ways to give CO_2: in reaction 5, the HCOO* breaks down to give CO_2* and H*; alternatively, the HCOO* can break

down to H* and CO_2*, and the H* then reacts with another H* on the surface to form H_2 in an associative desorption process. The final products obtained from the reaction are CO_2* and H_2 in the gas phase. Similarly, the COOH* formed in reaction 3 can produce CO_2, CO and H_2O in reaction 7, 8 and 9. In reaction 7, the H from the OH group of COOH* cleaves to form CO_2* and H*, while in reaction 8 the OH group cleaves from COOH* to form CO*; and in reaction 9, the COOH* reacts with H* to form carbon dioxide and water on the surface. Finally, the HCO formed in reaction 4 can be degraded on the surface in reaction 10 to give CO*.

To maintain an overall closed reaction cycle, further reactions are also included for the formation of small molecules. Reaction 11 and 12 describe the formation of water and hydrogen from the pseudo-stable moieties present on the surface, and all the formed molecules desorb from the surface in reactions 13 to 16 (CO_2, H_2O, CO and H_2, respectively).

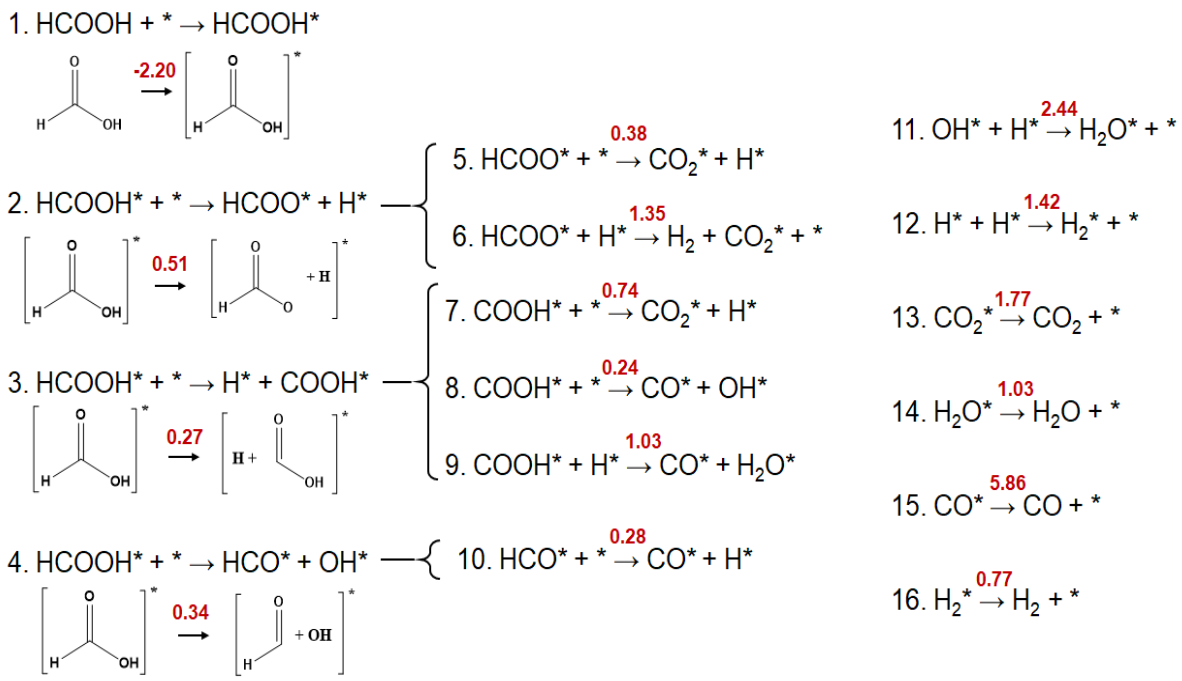

Figure 5.5.1: Complete reaction scheme, showing all the reactions considered in this study for the dehydration and dehydrogenation of HCOOH. The energy barrier (in eV) for each reaction, as calculated in this work, is presented in red.

5.5.1.1 Bulk

Density functional theory (DFT) simulations were performed using the "*Fritz Haber Institute ab initio molecular simulations*" (FHI-aims) software package [193], coupled with the "*Atomic Simulation Environment*" (ASE) Python package [194] for the management of model geometries.

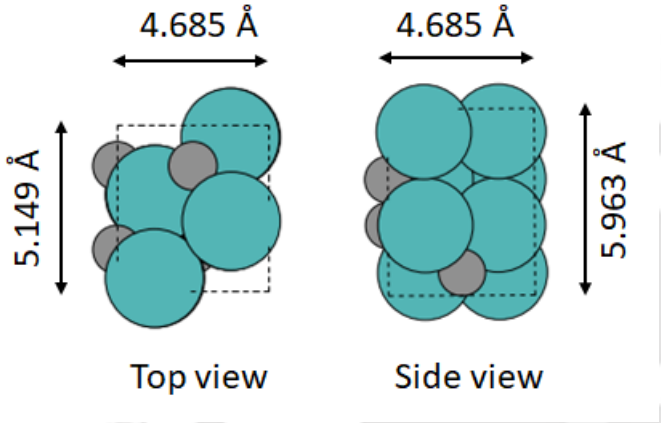

Figure 5.5.2: Top view and side view of the bulk β-Mo_2C with unit cell lengths, where Mo atoms are represented by teal colour, carbon atoms by grey colour and the dashed line show the unit cell.

The orthorhombic (β) structure of Mo_2C (Figure 5.5.2) is stable at a large range of temperatures [195], and thus, it has been considered as the catalytic form of the material during our investigation. A converged 5 × 5 × 4 **k**-grid was chosen for the periodic bulk calculations as, when performing convergence testing for the **k**-grid density, subsequent increments in **k**-grid sampling altered total energies by < 10 meV (1 kJ mol^{-1}) (Table 5.5.1). Relativistic effects were included using zeroth order regular approximation (ZORA) [193] as a scalar correction, and the spin and charge for the system were set to zero. Default FHI-aims convergence criteria was used for the self-consistent field (SCF) energy calculations, such that changes in the charge density ($\Delta\rho$) for the N atom system were:

$$\Delta\rho \leq 10^{-6} \times (N / 6)\ e\ a_0^{-3} \qquad (5.9)$$

To ensure energetic accuracy in a computationally efficient manner, the available basis sets of the FHI-aims package [193] were compared; the *light* basis set, which is equivalent to a Pople 6-31+G** basis set [151], was deemed appropriate as it provided converged accuracy in a tractable timeframe.

Table 5.5.1: Convergence testing of **k**-grid sampling. The energy change (ΔE) as a function of sampling is obtained for a unit cell of x = 4.754 Å, y=5.241 Å and z= 6.076 Å, with the selected converged settings highlighted in grey.

k-point density ($Å^{-1}$)	**k**-grid (*x*-axis)	**k**-grid (y-axis)	**k**-grid (z-axis)	Energy (eV)	ΔE (eV)
0.01	21	19	16	-894028.7805	-
0.02	11	10	8	-894028.7783	0.0022
0.03	7	6	5	-894028.7875	-0.0092
0.04	5	5	4	-894028.7916	-0.0040
0.05	4	4	3	-894028.7583	0.0333
0.06	4	3	3	-894028.7466	0.0117
0.07	3	3	2	-894028.6356	0.1110
0.08	3	2	2	-894028.5719	0.0637
0.09	2	2	2	-894028.9971	-0.4251
0.10	2	2	2	-894028.9971	0.0000

A range of exchange-correlation (XC) density functionals were compared for appropriateness towards modelling β-Mo_2C. For each XC, the bulk model was optimized using the trust-region method [196] until the force on each atom was less than 0.01 eV $Å^{-1}$; the unit cell vectors were also optimized, with the angles between the lattice vectors fixed (i.e. orthorhombic symmetry preserved). Comparison of the cohesive energy, formation energy, and unit cell parameters with literature for β-Mo_2C shows the PBE [3] XC functional with the Tkatchenko-Scheffler van der Waals correction [197] as providing favourable accuracy as well as computational efficiency (Table 5.5.2). The cohesive energy (E_{coh}) of the optimized β-Mo_2C bulk unit cell is calculated as:

$$E_{\text{coh}} = \frac{E_{\text{Mo}_2\text{C}}^{\text{bulk}} - n \cdot E_{\text{Mo}}^{\text{atom}} - m \cdot E_{\text{C}}^{\text{atom}}}{b} \tag{5.10}$$

where $E^{\text{bulk}}_{\text{Mo}_2\text{C}}$ is the energy of the bulk unit cell, $E^{\text{atom}}_{\text{Mo}}$ and $E^{\text{atom}}_{\text{C}}$ are the energy of a gas-phase molybdenum and carbon atom, respectively, *n* and *m* are the number of molybdenum and carbon atoms, respectively, and *b* is the number of units of Mo_2C in the bulk model [defined as $b = (n+m)/3$]. Similarly, the formation energy (E_{form}) of the *β*-Mo_2C structure is also calculated as:

$$E_{\text{form}} = E^{\text{bulk}}_{\text{Mo}_2\text{C}} - n \cdot E^{\text{bulk}}_{\text{Mo}} - m \cdot E^{\text{bulk}}_{\text{C}} \quad (5.11)$$

where $E^{\text{bulk}}_{\text{Mo}}$ and $E^{\text{bulk}}_{\text{C}}$ are the energy of a bulk Mo (bcc) and carbon atom (graphite), respectively, both in their respective ground state structures

Table 5.5.2: Comparison of the formation energy (E_{form}), cohesive energy (E_{coh}), bulk volume and lattice parameters calculated in this work for different functionals (PBE [3,4], M06-L [5], PBE0 [6,7] and B3LYP [8]) (*light* basis) with literature.

	Formation energy (eV)	Cohesive energy (eV)	Bulk Volume ($Å^{-3}$)	X (Å)	Y (Å)	Z (Å)
Computational Literature [198]	-0.46	-	-	-	-	-
Computational literature [199]	-0.30	-21.00	-	-	-	-
Experimental Literature [200]	-	-	147.46	4.724	5.199	6.004
PBE+TS	-0.74	-23.94	143.84	4.685	5.149	5.963
PBE	-1.74	-21.17	150.43	4.740	5.233	6.065
M06-L	-1.90	-22.40	149.48	4.769	5.192	6.037
B3LYP	Geometry optimisation unconverged after 8x computational cost					
PBE0	Geometry optimisation unconverged after 8x computational cost					

More extensive and computationally exhaustive functionals did not improve the target observables significantly. Thus, the PBE+TS XC functional is used for the continuation of this study.

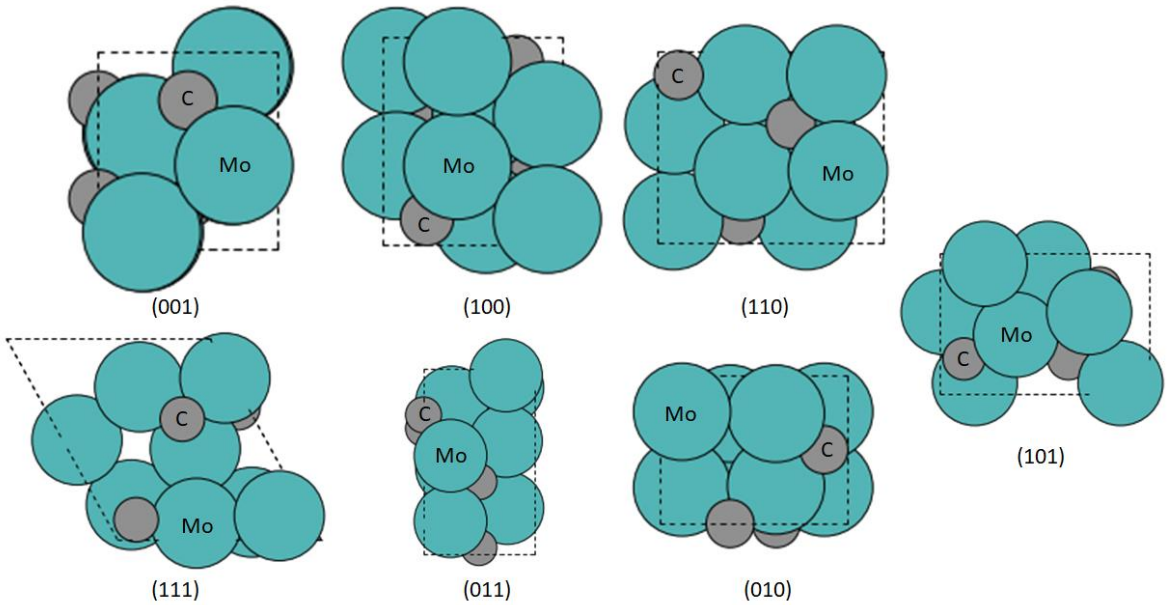

Figure 5.5.3: Top view (i.e. *xy* plane) of the investigated facets of *β*-Mo_2C with Mo terminations, where teal and grey circles represent molybdenum and carbon atoms, respectively, and the unit cell is represented by the dashed lines.

5.5.1.2 Surfaces

Seven different low-index vicinal surface facets (Figure 5.5.3) were created from the optimized bulk unit cell of *β*- Mo_2C: namely the (100), (110), (111), (101), (010), (001), and (011) facets. The Mo-terminated facets are reported to exhibit similar reactivity as that of Ru, Ni, and Pd metals [201]; in particular, the dissociation energy for a C-C bond on the *β*- Mo_2C surface is similar, and the dissociation of the C-O bond is thermodynamically more favourable. The carbon terminations are also known to reduce the C-O bond scission [202]. Therefore, only the metal terminations for the facets are considered herein. Furthermore, recent experimental and computational studies report that the (100) facet is highly active for hydrodeoxygenation (HDO) reactions [203,204]; the same surface has a high affinity towards hydrogen adsorption [205], which is a favourable characteristic for an HDO catalyst [206]. Furthermore, the Mo terminated (100) facet has the highest Mo surface density (0.130 atom $Å^{-2}$), providing higher coordination sites and resulting in better catalytic activity [207]. Experimentally, the surface can be

synthesized using the chemical vapour deposition technique [208], or through direct carburization of molybdenum [121] or molybdenum oxide [209]. Therefore, it is important to identify the relative stability of this surface, as it is used in all later work.

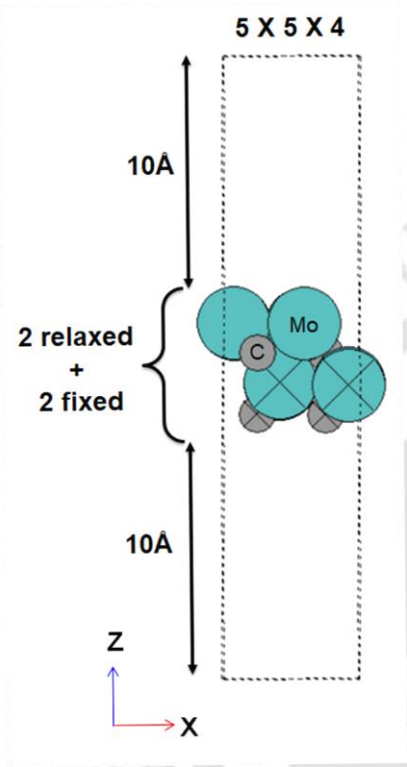

Figure 5.5.4: Profile of the (100) slab model, in the *xz*-plane. Colours are as per Figure 5.5.3, with fixed atoms noted with crosses. The 10Å vacuum above and below the slab (i.e. 20Å total) is also presented.

A 10 Å vacuum was introduced perpendicular to the *xy* plane, meaning that slab surfaces where separated by 20 Å in total (Figure 5.5.4). The large vacuum region eliminates self-interaction between slabs. In order to determine the relative stability of facets, the surface energy (γ_{hkl}) of each individual face, with miller indices (*hkl*), is calculated for a four-layer slab as:

$$\gamma_{hkl} = \frac{1}{2A}\left[E^{\text{surf}}_{Mo_2C} - s \cdot E^{\text{bulk}}_{Mo_2C}\right] \tag{5.12}$$

where $E^{surf}_{Mo_2C}$ and $E^{bulk}_{Mo_2C}$ are the total energy of the surface and bulk models, respectively, *s* is the number of bulk units in the slab model, and 2*A* is the surface area in the *xy* plane on the top and bottom of the slab.

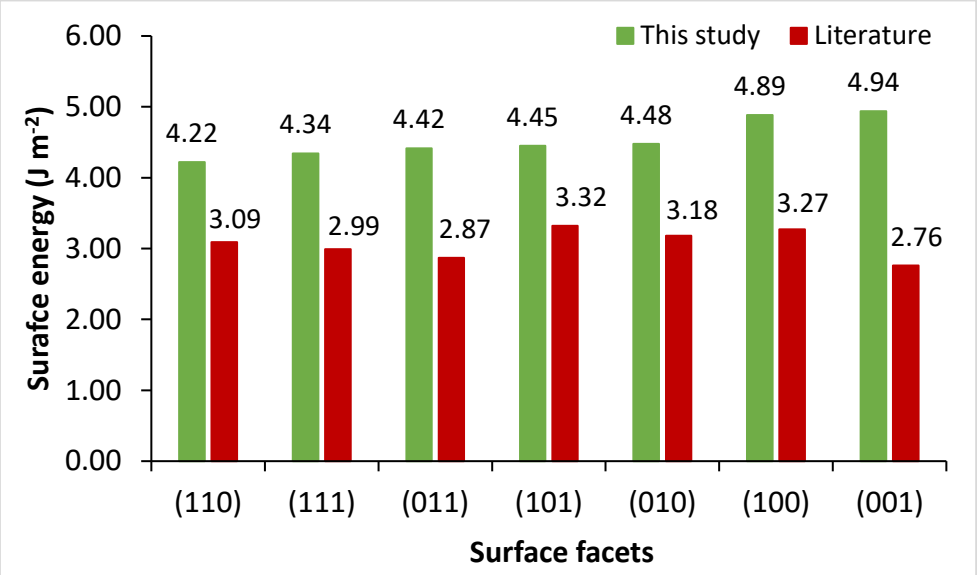

Figure 5.5.5: The surface energy (γ_{hkl}) of different surface facets, with Miller indices (*hkl*). Results from this study (green) are compared with previous computational studies (red) conducted using projector augmented wavefunction (PAW) method with the PBE functional [1].

For the considered surface facets, the lowest surface energy is calculated for γ_{110} (4.22 J m^{-2}) and the highest surface energy is calculated for γ_{001} (4.94 J m^{-2}, Figure 5.5.5), with a total range of 0.72 J m^{-2}. Whilst not the *most* energetically favourable [206], the Mo-terminated (100) facet is relatively stable and, therefore, investigated in the continuation of this study. To determine a chemically accurate thickness for the (100) slab model, γ_{100} was calculated as a function of slab thickness; γ_{100} differs by 0.47 J m^{-2} between two and four layers, and by less than 0.13 J m^{-2}, when comparing four, six and eight layers; thus, for a balance of computational efficiency and accuracy, subsequent calculations are performed with a four-layer model.

Table 5.5.3: The surface energy (γ_{100}, J m^{-2}) for models of the (100) surface with 2, 4, 6 and 8 layer slab thickness and varying constraints on the atoms furthest from the active surface.

Slab thickness (layers) / Unconstrained Layers	2	4	6	8
1	4.42	5.12	5.23	5.28
2	4.42	5.11	5.22	5.26
3	-	4.92	5.21	5.26
4	-	4.89	5.21	5.26
5	-	-	5.04	5.25
6	-	-	5.02	5.25
7	-	-	-	5.09
8	-	-	-	5.08

For the study of chemical reactions, a one-sided model of adsorption is favourable because it minimises calculation complexity. To compensate for the inhomogeneous electric field that arises in such one-sided calculations, a dipole correction applied. Furthermore, constraints are applied to ensure bulk structure at long-range from the adsorption site, i.e. on the side of the slab without an adsorbate. The model constraints were validated through impact on γ_{100}; for a model with four layers, constraints to the lower two layers alter γ_{100} by only 0.22 J m^{-2} compared to the fully relaxed slab (Table 5.5.3), and these constraints are applied herein.

Calculations were performed of the adsorption, reaction and desorption of the molecules, as outlined in the reaction scheme in Figure 5.5.1. The adsorption energy (E_{ads}) is calculated as:

$$E_{\text{ads}} = E_{\text{Mo}_2\text{C+Molecule}} - E^{\text{surf}}_{\text{Mo}_2\text{C}} - E_{\text{Molecule}} \quad (5.13)$$

where $E^{\text{surf}}_{\text{Mo}_2\text{C}}$ is the energy of the surface, $E_{Molecule}$ is the energy of the adsorbate and $E_{\text{Mo}_2\text{C+Molecule}}$ is the energy of the combined system. As with any thermodynamic process, the reverse action (i.e. desorption, E_{des}) can be calculated as $E_{\text{des}} = - E_{\text{ads}}$.

The adsorption energy of all the molecules was calculated at varying orientations on the different available surface sites: *on-top*, *bridge*, *fcc* and *hcp*. Two *hcp* sites (Mo-*hcp* and C-*hcp*) are considered depending on the type of atom present underneath the top layer. The most stable arrangement (i.e. most negative E_{ads}) are considered for the full reaction pathways, with the transition states calculated using a climbing image nudged elastic band (CI-NEB) method [210] with the molecular dynamics based Fast Inertial Relaxation Engine (FIRE) optimization algorithm [211]. A minimum of seven images (including reactants and products) were used in the transition state search, and the convergence criteria for the force on atoms was set to 0.06 eV $Å^{-1}$. To confirm the stability of individual minima and transition states, vibrational frequencies were calculated; the presence of exactly one imaginary frequency along the reaction pathway confirmed that transition states were first order saddle points on the potential energy landscape [22].

5.5.1.3 Microkinetics

Thermochemical analysis and microkinetic modelling of the reactions [212,213] was performed to determine the system behaviour [214] using our in-house modelling code [215]. The global partition function was calculated as $Q = q_{vibrational} \cdot q_{rotational} \cdot q_{translational} \cdot q_{electronic}$. The vibrational frequencies for each model were used to calculate the vibrational partition function ($q_{vibrational}$). The rotational ($q_{rotational}$) and translational ($q_{translational}$) contributions to Q were derived from the molecular structures and assume to be unity for adsorbed species as rotations and translations are frustrated. The electronic ($q_{electronic}$) partition function was set as the electron multiplicity in the ground state and assuming no excitations in the working temperature range. Subsequently, thermodynamics parameters (i.e. enthalpy, H, and entropy, S) were calculated at different temperatures (T) assuming the harmonic approach [214] and with the following relations:

$$S = k_B \ln Q + kT\left(\frac{\partial ln\, Q}{\partial T}\right)_V \qquad (5.14)$$

$$C_p = T\left[\frac{\partial S}{\partial T}\right]_p \quad (5.15)$$

$$H = E_{DFT} + E_{ZPE} + \int_0^T C_p \partial T \quad (5.16)$$

$$G = H - TS \quad (5.17)$$

where k_B is the Boltzmann constant, V is volume, p is pressure, E_{DFT} is the calculated DFT electronic energy, E_{ZPE} is the vibrational energy correction at 0 K, C_p is the heat capacity at constant pressure, and G is the Gibbs free energy. To validate our approach, the thermochemical parameters for the gas phase species were compared with literature [9,10], with all values in very good agreement (Table 5.5.4). The maximum difference in the C_p and S for the studied molecules are less than 7.65 J mol^{-1} K^{-1} in the studied temperature range, and the maximum difference in the enthalpy values is less than 3.62 kJ mol^{-1} (Table 5.5.4).

Table 5.5.4: The entropy (S) and heat capacity (C_p) as derived in this work and compared to the literature [9,10].

Gas phase species	T (K)	C_p (J mol^{-1} K^{-1})		S (J mol^{-1} K^{-1})		$H - H_{298.15}$ (kJ mol^{-1})	
		This work	Literature	This work	Literature	This work	Literature
CO	298.00	-	29.15	-	-	-	-
	300.00	28.95	29.15	196.91	197.84	0.00	0.06
	400.00	28.95	29.30	205.24	206.24	1.93	2.97
	500.00	28.95	29.82	211.70	212.83	4.05	5.93
H_2	298.00	-	28.84	-	130.67	-	-
	300.00	28.95	28.85	135.68	130.86	0.00	0.05
	400.00	28.95	29.18	144.01	139.22	1.33	2.96
	500.00	28.95	29.26	150.47	145.74	2.87	5.88
H_2O	298.00	-	33.59	-	188.82	-	-
	300.00	33.31	33.60	193.93	189.04	0.00	0.06
	400.00	33.96	34.26	203.59	198.79	1.57	3.45
	500.00	34.91	35.22	211.27	206.53	3.77	6.92
CO_2	298.00	-	37.12	-	213.79	-	-
	300.00	33.27	37.22	216.24	214.02	0.74	0.07
	400.00	35.30	41.34	226.10	225.31	2.37	4.00

	500.00	36.96	44.61	234.16	234.90	4.69	8.31
HCOOH	298.00	-	45.68 ± 0.07	-	248.70	-	-
	300.00	44.54	45.84	252.30	-	-	-
	400.00	51.66	54.52	266.11	-	-	-
	500.00	57.33	62.63	278.28	-	-	-

The rate constant (k) of each of the elementary reaction was calculated using the transition-state theory (TST) approximation of Eyring, Evans and Polanyi [216,217]. For this, the calculations were carried out using the relation:

$$k = A_0 \exp\left(\frac{-\Delta G^{\neq}}{k_B T}\right) = \frac{k_B T}{h}\frac{Q_{TS}}{Q_r}\exp\left(\frac{-\Delta G^{\neq}}{k_B T}\right) \quad (5.18)$$

where A_0 is the pre-exponential factor, $\Delta G^{\neq}$ is the activation free energy of the reaction, and Q_{TS} and Q_r are the partition functions of the transition state and reactant, respectively. Adsorption and desorption processes from the surface were considered barrier-less, but maintaining consideration of the variable degrees of freedom, e.g. 2D and 3D. Therefore, the adsorption rate constant ($k_{ads/des}$) was calculated from the Hertz−Knudsen relation [188] as:

$$k_{ads/des} = A_0 S_0(T) = \frac{A_{cat}}{\sqrt{2\pi m_i k_B T}} S_0(T) \quad (5.19)$$

where A_{cat} is the surface area of catalyst, *i.e.* the area in the simulation cell, and the sticking coefficient $S_0(T)$ is a temperature dependent term calculated from 3D and 2D degrees of freedom from the global partition function. The energy barrier for the diffusion of molecules on the surface was considered as negligible. To develop the kinetic model, the rate constants for the adsorption process were considered as

$$r_i = A_0 S_0(T) P_i \theta_i \quad (5.20)$$

and the rate constants for the surface reactions and desorption processes considered as

$$r_i = A_0 \exp\left(\frac{-\Delta G^{\neq}}{k_B T}\right)\theta_i \quad (5.21)$$

Here, P_i is the partial pressure of species *i*, and θ_i is the fractional surface coverage of the same species such that $\sum\theta_i = 1$ throughout. The differential equations were formulated as:

$$\frac{d\chi_i}{dt} = r_{x_i} \quad (5.22)$$

where χ_i is P_i for a gas phase species or θ_i for a surface species, and r_{x_i} is the net reaction rate for the formation of species *i*. Finally, the system of ordinary differential equations (ODEs) were solved to obtain a steady state solution for the system.

To complement the kinetic rate model, simulations of the temperature programmed desorption (TPD) technique were also considered. In this model, the temperature of the system was increased at the rate of 10 K s^{-1} and the surface was fractionally covered with hydrogen adatoms along with HCOOH. In line with experiments, where the gases are continuously removed from the reactor, re-adsorption of the evolved gases to the surface was not included in the ODEs. Overall, four different scenarios for initial HCOOH coverage on the surface were considered: 0.1, 0.4, 0.7 and 1.0 ML (monolayer).

5.5.2 Reaction profiles

The conversion of formic acid initiates with adsorption of the molecule on to the β-Mo_2C surface. Five non-equivalent sites were examined to determine the most stable adsorption configuration of formic acid over the surface, namely the *atop*, *bridge*, Mo-*hcp*, C-*hcp* and *fcc* positions, and three different arrangements were considered for the molecule, namely *lateral*, *C-up* and C-*down*, as shown in Figure 5.5.6(a).

The adsorption energies were calculated for each optimized configuration. The most stable adsorption of HCOOH occurs in the *lateral* configuration over the *bridge* site (figure 5.5.7), with an E_{ads} of -2.20 eV. On a pure transition metal, usually the C-*up* position is more

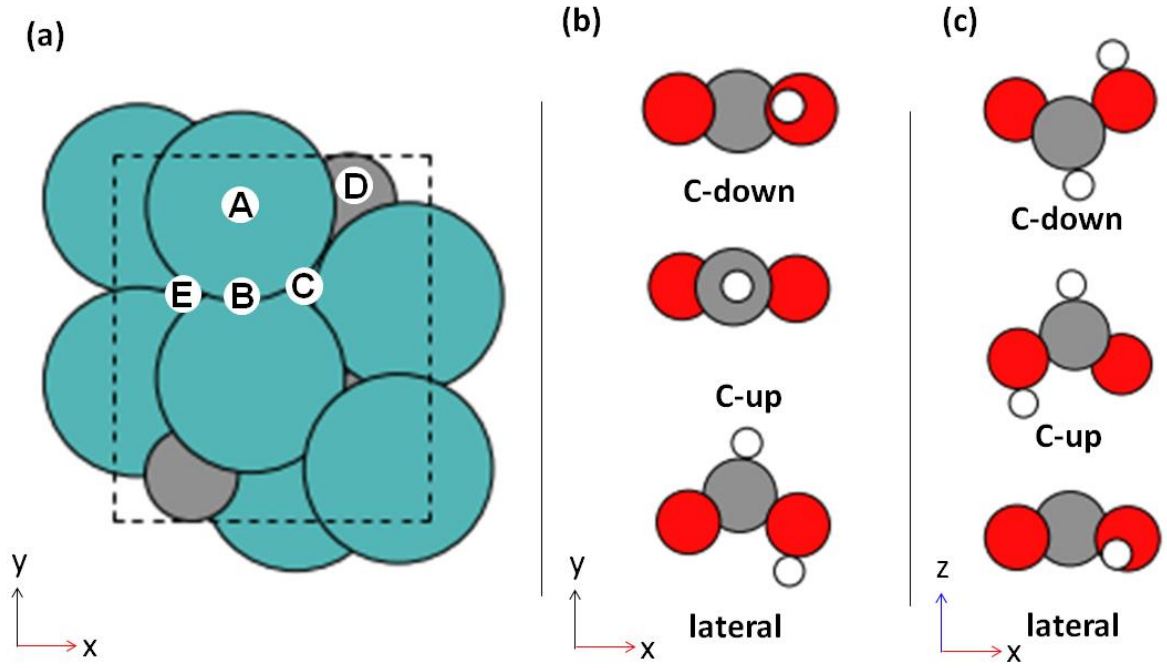

Figure 5.5.6: (a) Top view (*xy*-plane) of the catalyst surface where the possible adsorption sites are identified as: A, *atop*; B, *bridge*; C, Mo-*hcp*; D, C-*hcp* site; and E, *fcc*. Atom colours are as in Figure 5.5.3. (b) Top view (*xy*-plane) and (c) side view (*xz*-plane) of HCOOH in different arrangements considered for adsorption. Oxygen, carbon and hydrogen atoms are shown in red, grey and white, respectively.

stable as the oxygen atoms are able to bond with the metal surface with high coordination [218]; however, in carbides, the carbon atom of the adsorbate tends to shift towards the carbon deficit site [219]. Thus, during the geometry optimization, the molecule repositioned such that the carbon atom partially covered the *fcc* site and the oxygen atoms occupy the *atop* position. For the next most stable adsorption, which is with the molecule positioned *laterally* at the C-*hcp* site (E_{ads} = -2.11 eV), a similar relocation of the formic acid species occurs and the C atom again partially covers the Mo-*hcp* site. Initial and optimized structures are presented together

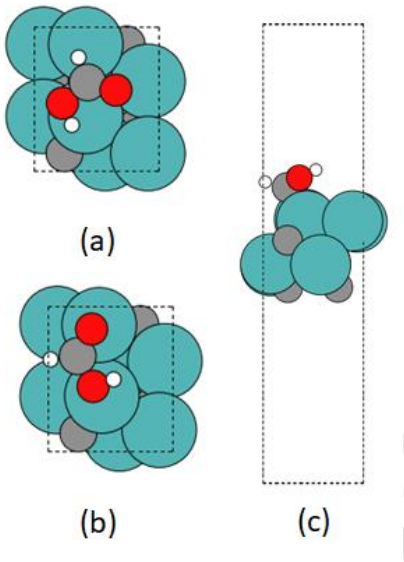

Figure 5.5.7: The configuration of HCOOH positioned *laterally* on the surface *bridge* site, which is deemed the most stable. (a) Initial geometry, viewed in the *xy*-plane; (b) optimized geometry, viewed in the *xy*- and (c) *xz*-plane. Atom colours are same as in Figure 5.5.6.

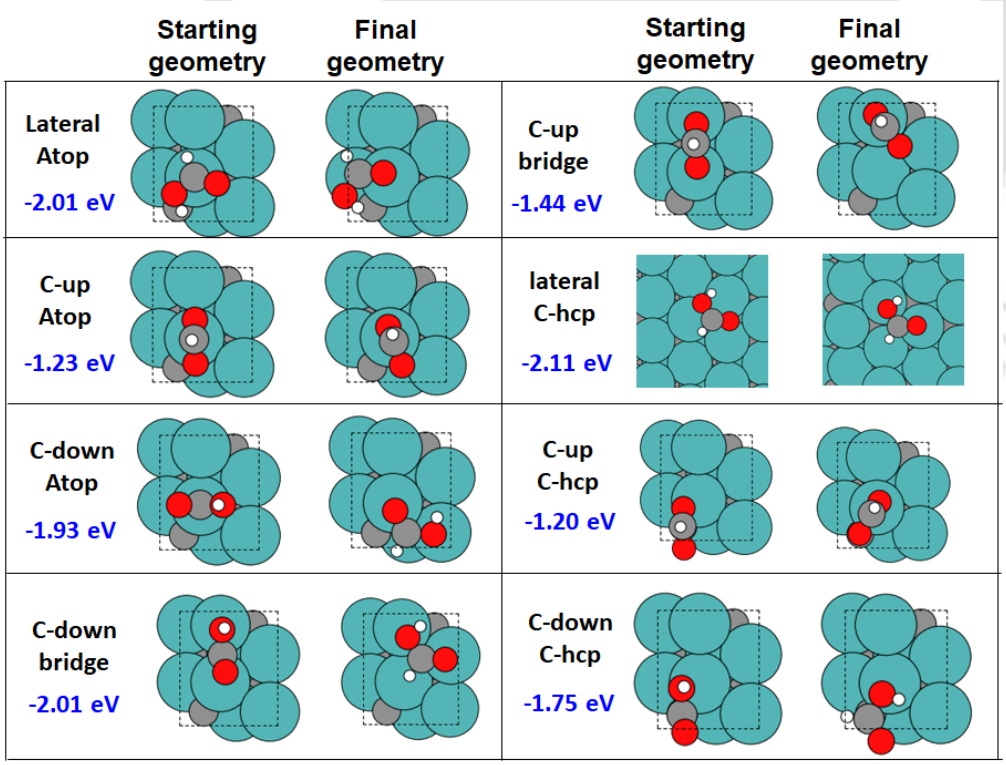

Figure 5.5.8: The initial and optimized configuration of HCOOH when adsorbed on the *β*-Mo_2C surface in the *atop*, *bridge* and *C-hcp* sites. E_{ads} is given in each case in blue font. Atom colours are as in Figure 5.5.6.

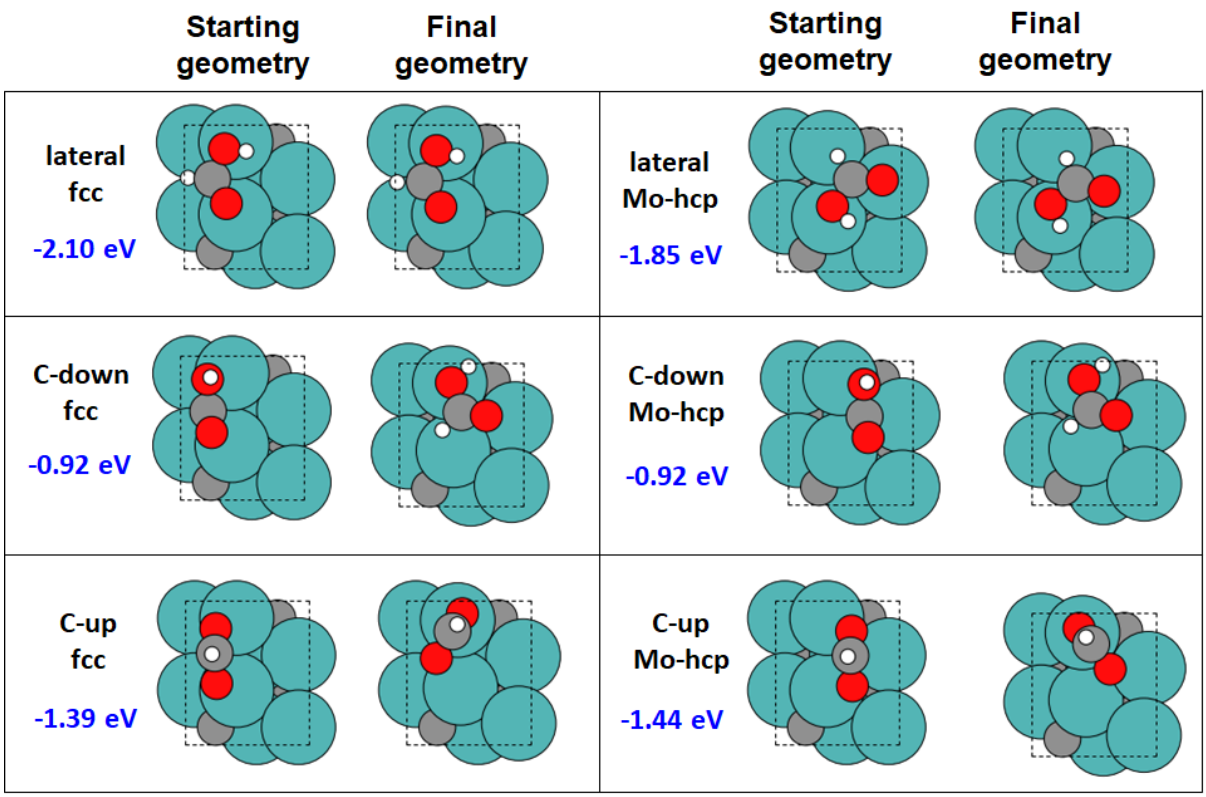

Figure 5.5.9: The initial and optimized configuration of HCOOH when adsorbed on the *β*-Mo_2C surface in the *fcc* and Mo-*hcp* sites. E_{ads} is given in each case in blue font. Atom colours are as in Figure 5.5.6.

in Figure 5.5.8 and 5.5.9. In general, the *lateral* configuration of HCOOH is the most stable for each adsorption site, with E_{ads} between -1.85 and -2.20 eV; furthermore, in several cases for the *C-up* and *C-down* configuration, the molecules optimise to a *lateral* configuration. Overall, the adsorption energy is considerably higher on *β*-Mo_2C than on other metal surfaces [218], which we attribute to the interaction of at least 3 atoms (2 oxygen and 1 carbon atom) interacting with the surface.

The conversion of formic acid has been considered via three different pathways: 1 (1a and 1b), 2 (2a, 2b and 2c) and 3a. In pathway 1 (Figure 5.5.10), the HCOOH dehydrogenation proceeds by cleavage of the O-H bond to produce formate (HCOO*) and hydrogen (H*) on the surface, with an activation energy of 0.51 eV. The formate (5p) can break down further to form

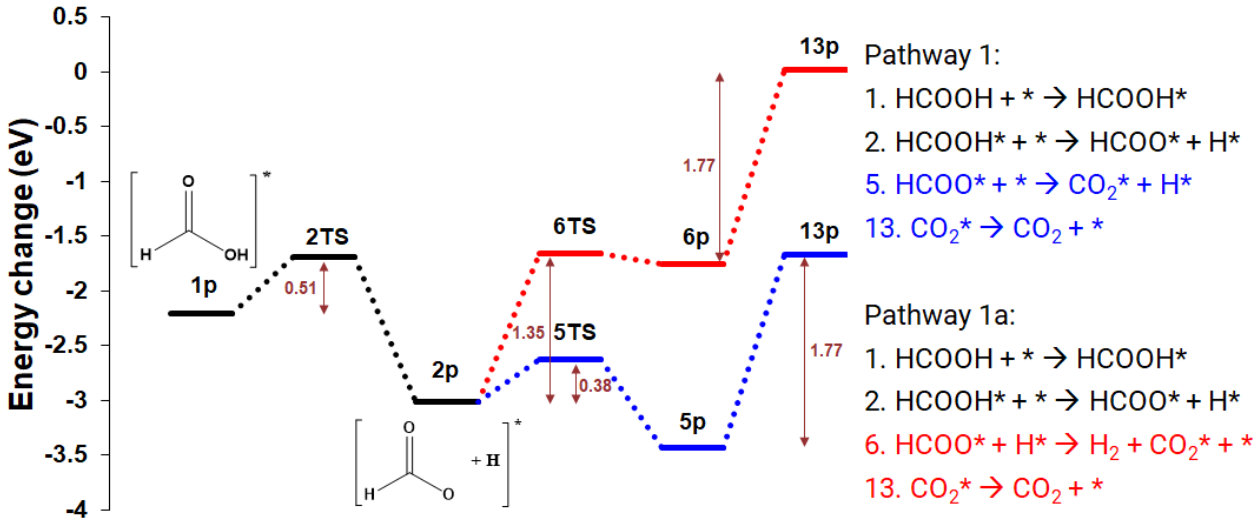

Figure 5.5.10: Potential energy surface (PES) of the dehydrogenation of HCOOH, via the formation of formate, to produce carbon dioxide via pathway 1a (blue) and 1b (red).

CO_2* and H* (Pathway 1a, E_{act} = 0.38 eV), or react with H* to form CO_2 on the surface and H_2 in the gas phase (Pathway 1b, E_{act} = 1.35 eV). The greater activation energy for pathway 1b suggests dehydrogenation via pathway 1a is most likely. The adsorption of CO_2 on the surface, calculated by systematically assessing the interaction of CO_2 with the five different surface sites and in *lateral* and *vertical* orientations (Figure 5.5.11), identifies that the most stable arrangement is in the partial *bridge* site (E_{ads} = -1.77 eV); the *vertical* configuration over the *fcc* site also realigns to this configuration during optimization. Interestingly, and contrastingly, adsorption in the *atop*, *lateral* configuration leads to the dissociation to CO and O on the surface with CO_2 dissociative adsorption highly favourable with (E_{ads} = -3.75 eV). The dissociation is unsurprising given Mo_2C is reported to be selective towards the cleavage of carbon and oxygen bonds [220]. For pathways 1a and 1b, the final desorption is considered to proceed as associated CO_2, with an E_{act} of 1.77 eV.

The second dissociative pathway (2) also commences with the adsorption of HCOOH (E_{ads}= -2.20 eV) and cleavage of the H-COOH bond, leading to the formation of co-adsorbed

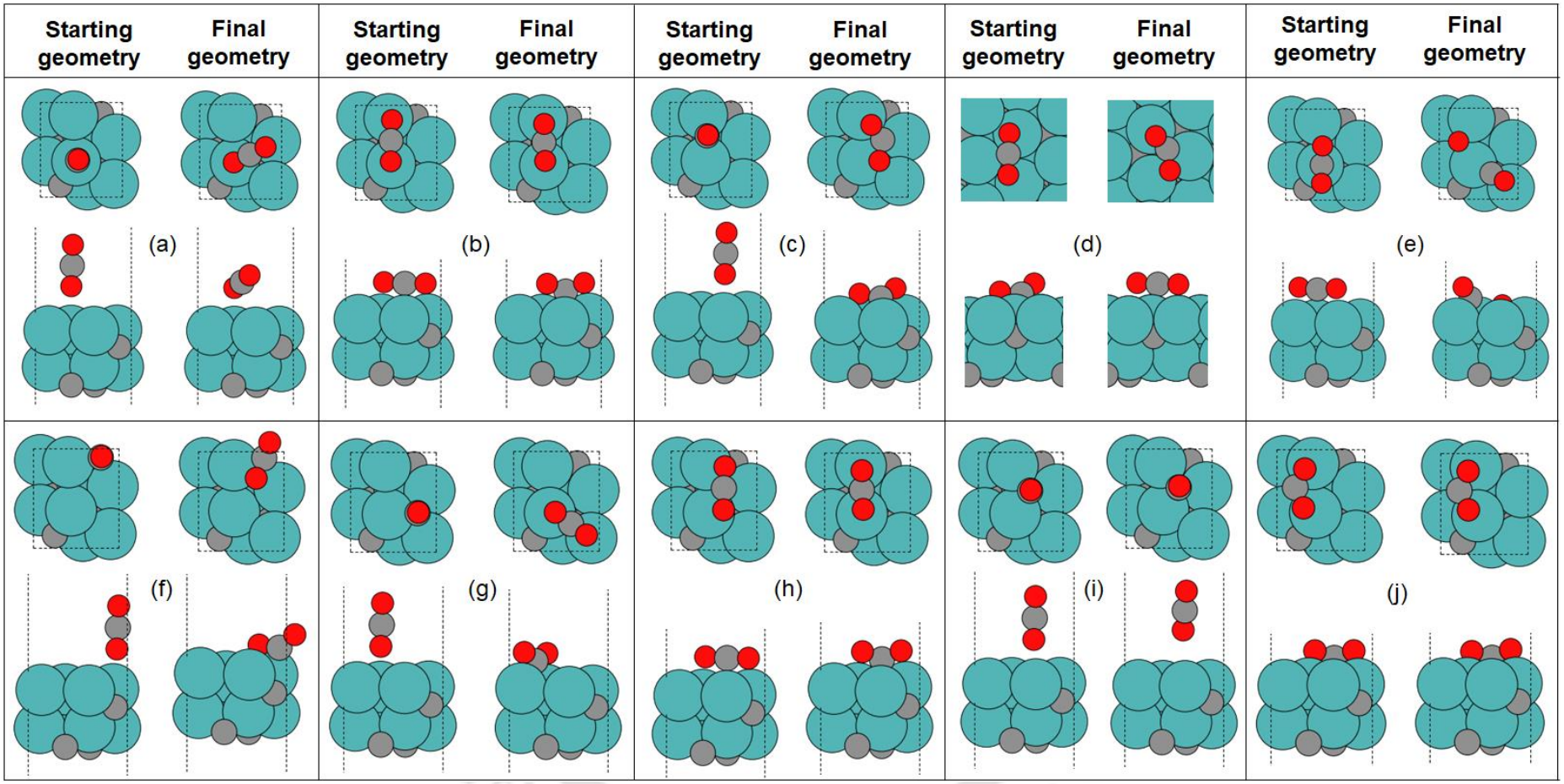

Figure 5.5.11: Configurations of CO_2 on the β-Mo_2C surface for each site and molecular configuration: (a) *atop*, *vertical*; (b) *bridge*, *lateral*; (c) *bridge*, *vertical*; (d) C-*hcp*, *lateral*; (e) *atop*, *lateral*; (f) *fcc*, *vertical*; (g) C-*hcp*, *vertical*; (h) Mo-*hcp*, *lateral*; (i) Mo-*hcp*, vertical; (j) *fcc*, *lateral*. Atom colours are as in Figure 5.5.6.

COOH* and H*. E_{act} for the breaking of the H-C bond is 0.27 eV, while the reaction energy is -0.76 eV, leading to the formation of 3p via a thermodynamically driven step. The COOH* can break down subsequently to CO_2 and CO in three different ways. In pathway 2a, the COOH* breaks down onto CO_2* and H* (E_{act} = 0.74 eV), with the CO_2* then desorbed as described in pathway 1a (Figure 5.5.12).

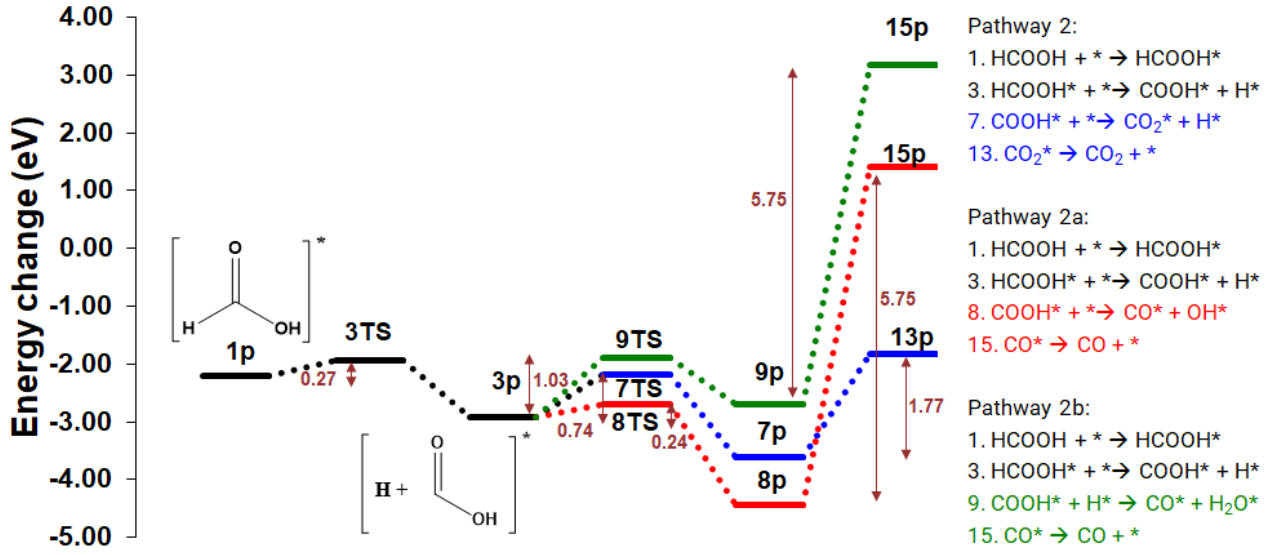

Figure 5.5.12: Potential energy surface (PES) for the dehydration and dehydrogenation of HCOOH on the catalyst surface to produce CO and CO2 in pathway 2a (blue), 2b (red) and 2c (green).

Alternatively, in pathway 2b, the COOH* dehydrates to CO* and OH* (E_{act} = 0.24 eV), which is lower than the reported activation energy on other precious metal surfaces: on the Au (100) surface, E_a is 0.70 eV [189]; on the Pd (111) surface, E_a = 1.20 eV [221]. On the Pt (111) and (100) surfaces, the reaction occurs via the formation of cis-COOH with E_{act} of 0.61 eV and 0.57 eV [222], respectively. In our results, the consequential reaction energy for the step is exothermic (-1.51 eV), which is again more favourable than on precious metal surfaces such as Au (100) [189], Pd (111) and Pt (111) [221]. For the CO molecule on the surface, a systematic study was conducted with two different configurations (*C-up* and *C-down*) on the five different sites previously identified (Figure 5.5.13). In general, it was observed that the CO stabilises at

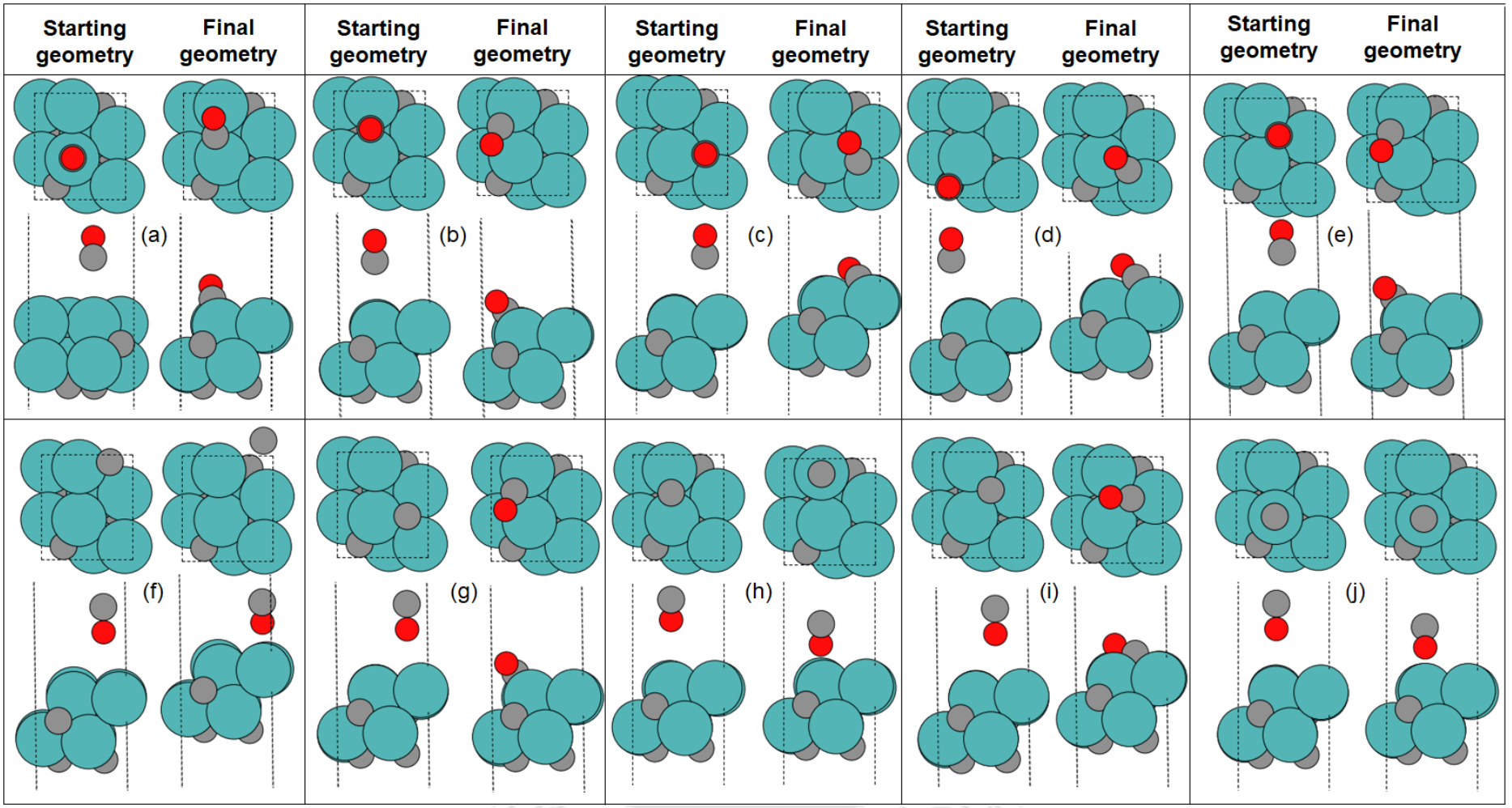

Figure 5.5.13: Configurations of CO on the β-Mo_2C surface for each site and molecular configuration (a) *atop*, *C-down*; (b) *bridge*, *C-down*; (c) C-*hcp*, *C-down*; (d) Mo-*hcp*, *C-down*; (e) *fcc*, *C-down*; (f) *fcc*, *C-up*; (g) C-*hcp*, *C-up*; (h) *bridge*, *C-up*; (i) Mo-*hcp*, *C-up*; (j) *atop*, *C-down*. Atom colours are as in Figure 5.5.6

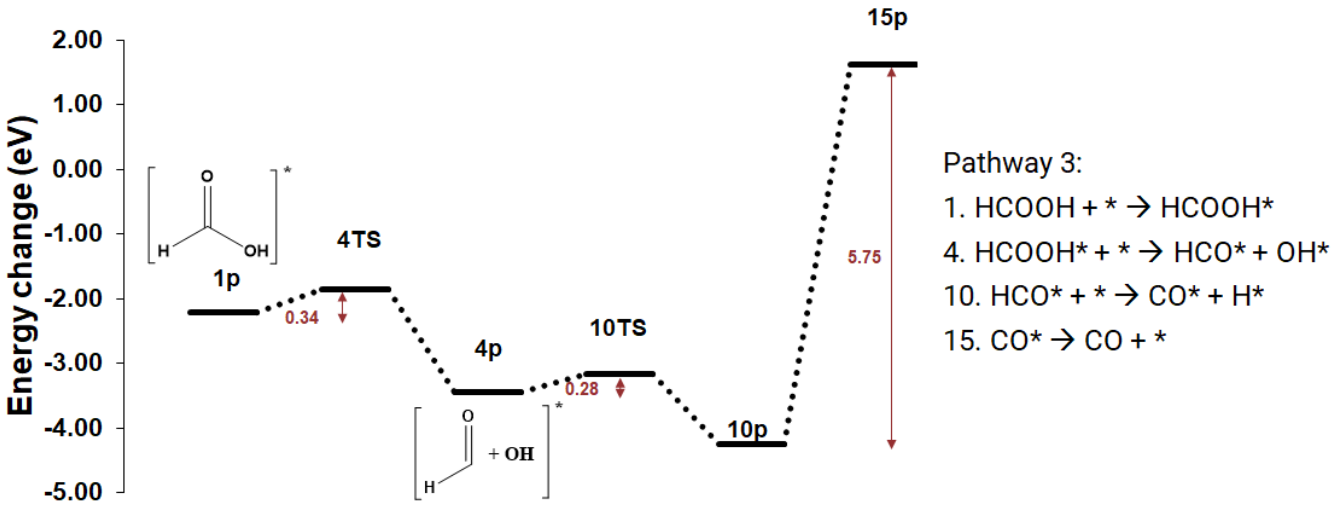

Figure 5.5.14: Potential energy surface (PES) for the most favourable pathway for the dehydration of HCOOH producing CO in pathway 3a.

carbon deficient sites with a strong adsorption energy (E_{ads} < -3.49 eV), in agreement with Nagai *et al.*[219]. The most stable CO adsorption is the *bridge*, *C-down* configuration but partially covering the *fcc* site (E_{ads} = -5.75 eV); Thus, the CO desorption energy is considered herein as requiring 5.75 eV (8p → 15p). The high desorption energy makes the β-Mo_2C (100) surface highly susceptible to CO poisoning, which is previously observed [223].

In pathway 2c, COOH* reacts with H* via 9TS to give CO and H_2O on the surface. The activation energy for this reaction is 1.03 eV, which is the most energy demanding pathway calculated for CO production. As discussed above, the CO desorption energy is high (9p → 15p, 5.75 eV) and would be the rate determining step in this reaction pathway; and the surface would be susceptible to poisoning.

In a third pathway, the HCO-OH bond is cleaved in reaction 4, as shown in pathway 3a of Figure 5.5.14. The transition state is 0.34 eV above reactants, making it the next most favourable conversion route after reaction 2. Further, the HCO* is broken down into CO* and H* on the surface in reaction 10, which is facile (E_{act} = 0.28 eV) and can be driven by the

exothermic reaction energy (-0.81 eV). As already highlighted, the subsequent desorption of CO is a very endothermic process.

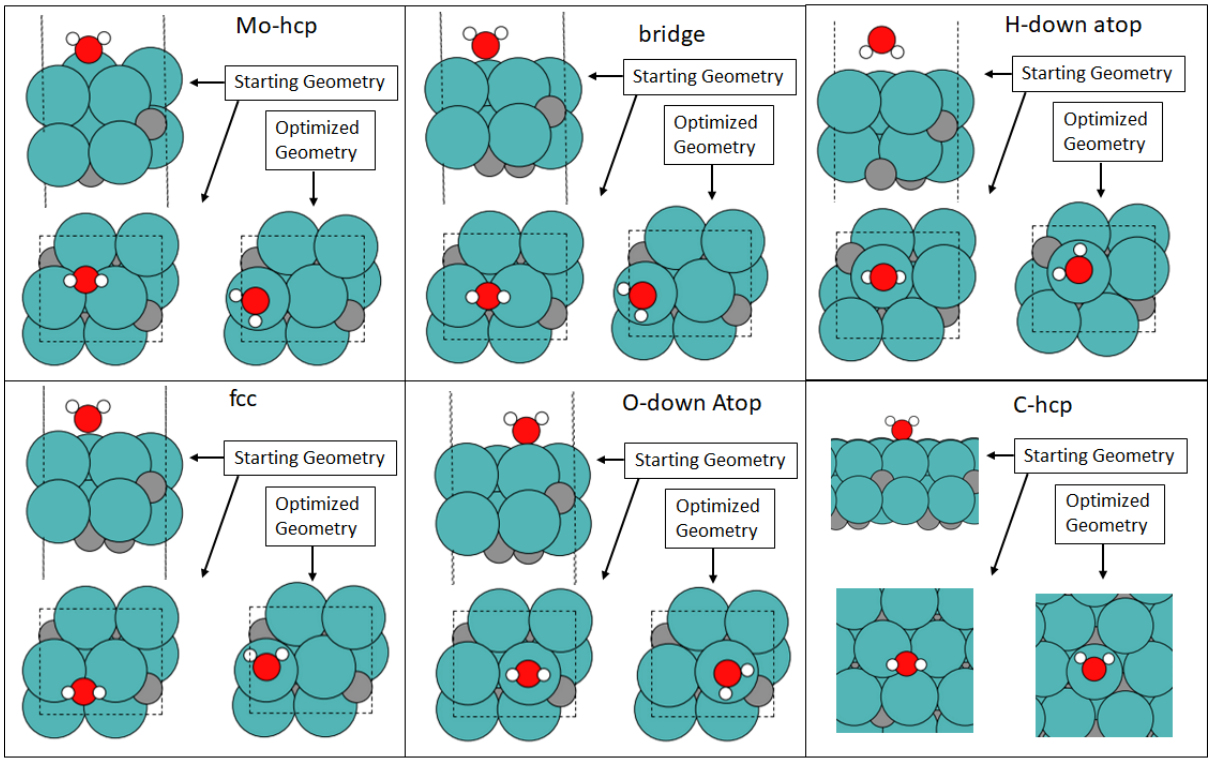

Figure 5.5.15: Configurations of H_2O adsorbed on β-Mo_2C at different catalyst sites, in different orientations, as labelled. Atom colours are as in Figure 5.5.6.

In several of the presented reaction schemes, H* and OH* form on the surface and can react to form either hydrogen or water molecules on the surface (Reaction 11 and 12, respectively, in Figure 5.5.1). The formation of H_2O* proceeds via transition state 11TS with E_{act} = 2.44 eV, whereas H_2* proceeds via 12TS with E_{act} = 1.42 eV. The H_2 stability on the surface is reportedly unaffected by the carburization of molybdenum carbide [224], with other transition metal carbides (TiC, VC, ZrC and NbC) favouring dissociation of hydrogen on the surface [225]. Here, β-Mo_2C exhibits similar behaviour, with only dissociative adsorption of H_2 observed (E_{ads} = -0.77 eV), i.e. the H_2 molecule is unstable, with the separated H atoms positioned on the *atop* position, in agreement with earlier reports [221]. The stability of the water molecule was confirmed by considering all adsorption sites and *O-up* and *O-down*

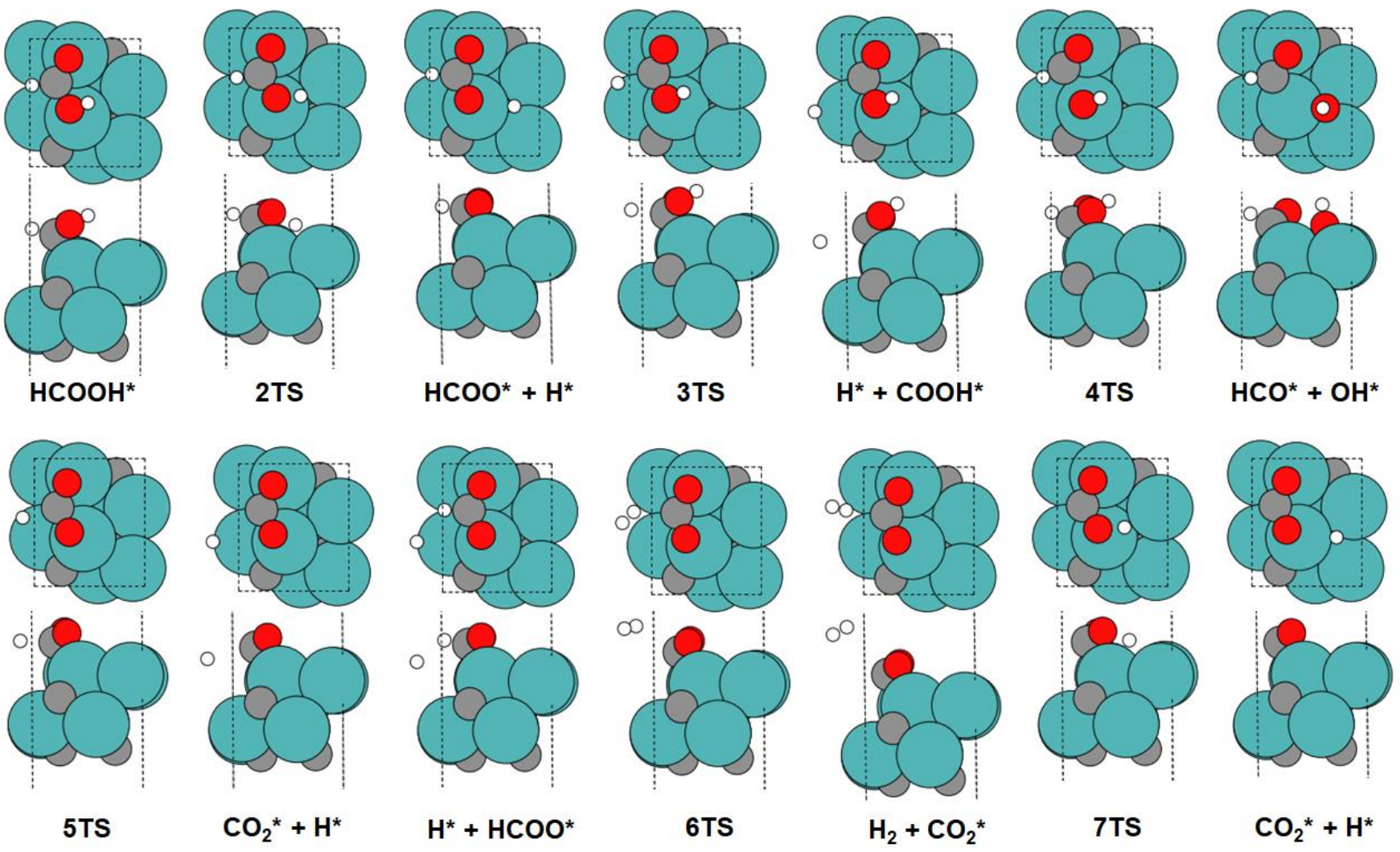

Figure 5.5.16: Optimized models of reactants, transition state and products on the β-Mo_2C (100) surface for reactions 1 through 7. Atom colours are as in Figure 5.5.6.

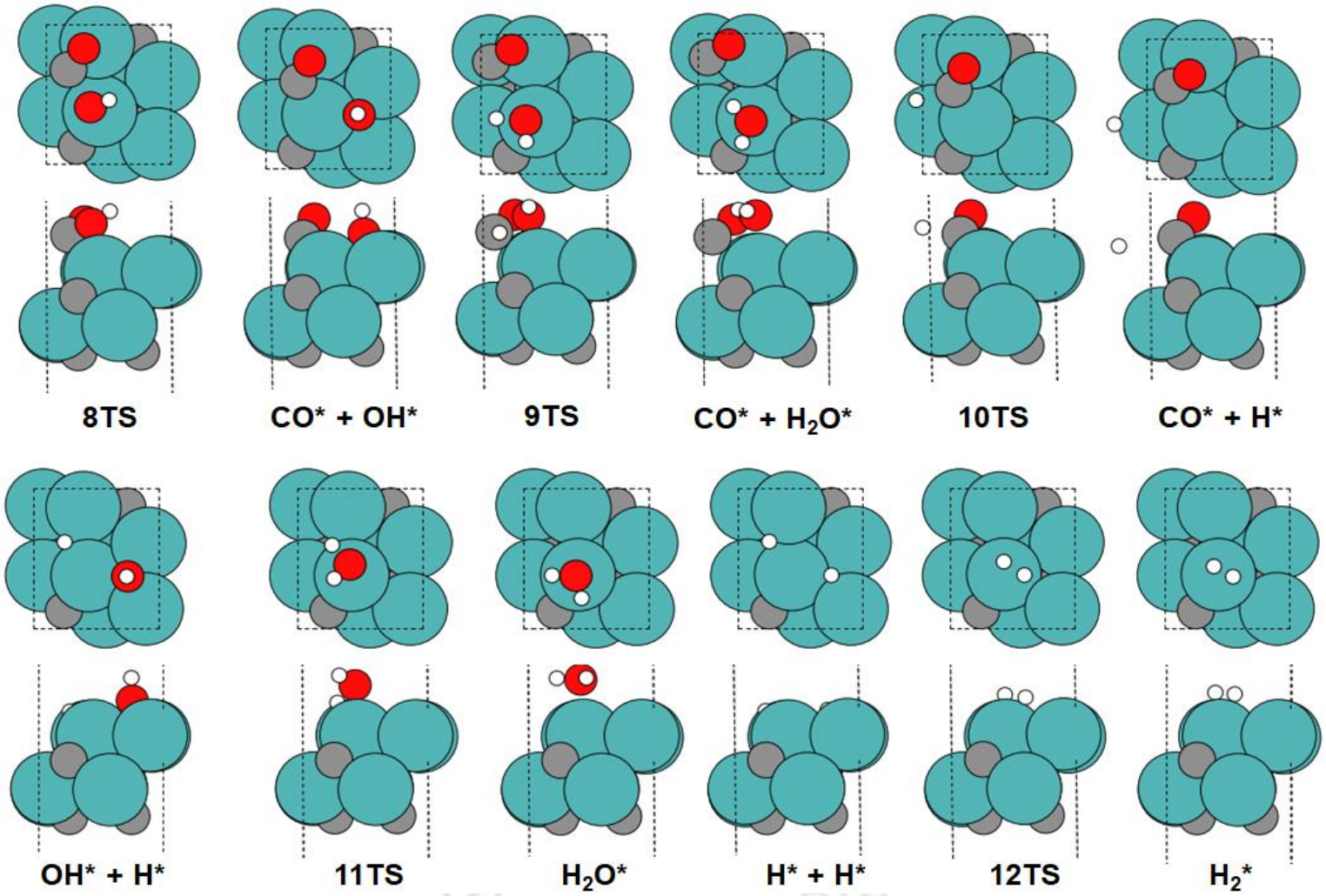

Figure 5.5.17: Optimized models of reactants, transition state and products on the β-Mo_2C (100) surface for reactions 8 through 12. Atom colours are as in Figure 5.5.6.

configurations (Figure 5.5.15); The most favourable position is clearly in the *atop lateral* position (E_{ads} = -1.03 eV), as all models converge to this configuration.

Table 5.5.5: Overall activation energy and pre-exponential factor for each reaction pathway.

Pathway	Activation energy (eV)	Pre-exponential factor (s^{-1})
1	0.53	1.26E+12
1a	2.22	1.26E+12
2	0.36	1.26E+12
2a	3.61	1.56E+12
2b	5.37	1.56E+12
3	3.81	1.56E+12

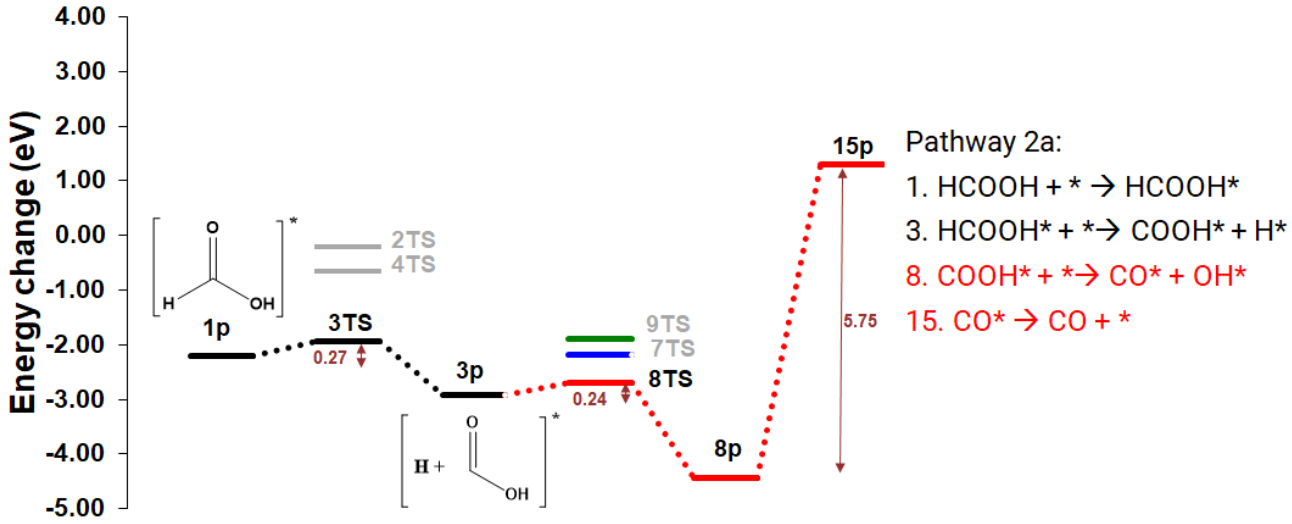

Figure 5.5.18: Most favourable pathway (2b, red) for the conversion of formic acid on β-Mo_2C surface. The crucial competing step that determines selectivity to CO_2 or CO is shown with alternative paths given in blue (pathway 2a) and green (pathway (2c).

The rate limiting step of each pathway decides the overall activation energy after adsorption of formic acid of the pathways. The activation energy after formic acid adsorption and the corresponding pre-exponential factor of each pathway is highlighted in Table 5.5.5. Overall, the most suitable pathway for the conversion of the formic acid is via reaction 3 to form COOH* on the surface, with all the optimized molecular geometries of all the reactants, transition states and products are given in Figure 5.5.16 and 5.5.17. The reaction requires 0.27 eV as initial activation energy, and subsequently formed COOH* degrades to CO* and OH (via

8TS*) with an activation energy of 0.24 eV. Whilst the final CO desorption from the surface requires 5.75 eV (Figure 5.5.18), the feasibility of this step is considered below with microkinetic modelling. Ideally, conditions would be sought that promote reaction 7, leading to CO_2 formation, over reaction 8, as the CO surface bond is extremely strong; alternatively, the surface could be modified such that the CO desorption energy is reduced, and the active site recycled, though this approach is not considered further here.

5.5.3 Microkinetics Modelling:

5.5.3.1 Batch reactor model

A batch reactor model with an initial HCOOH pressure:surface ratio of unity was considered in the temperature range of 300 - 500 K. All elementary steps listed in Table 5.5.6 were considered in the microkinetics simulations; at each temperature, the concentration of each species was calculated during the first second of the reaction, i.e. time period from 0 to 1 s in steps of 0.01 s. under the assumption that steady-state is reached within this time. For the adsorption reactions, the temperature dependent sticking coefficient ($S_0(T)$) was also calculated (Table 5.5.).

The rate constant (k) for the HCOOH adsorption process (reaction 1) is very small (of the order 10^{-4} s^{-1}), and therefore the concentration of formic acid on the surface is tiny (of the order 10^{-22} ML (monolayer) at 300 K) and remains steady (Figure 5.5.19). With an increase in temperature, the adsorption rate decreases for HCOOH and its concentration drops further as conversion increases. At 400 K and 500 K, the HCOOH* concentration at steady-state is of the order 10^{-24} ML and the surface is largely vacant, which agrees with the simulation model of low coverage. Since all the products are a result of the breakdown of HCOOH, the concentration of all the species is proportional to HCOOH*. The steady-state concentration of species 2p, 3p

Table 5.5.6: The energy barrier, reaction energy, sticking coefficient (S_0), pre-exponential factor (A_0) and rate constant (k) at 300 K, 400 K and 500 K, for all considered reactions. The reaction numbers are of the format $X.Y$ where Y represents all the reactions considered in the microkinetic model for reaction X of the Figure 5.5.1 in the main article.

Reaction number	Reaction	Energy barrier (eV)	Reaction energy (eV)	300 K			400 K			500 K		
				S_0	A_0	k (s^{-1})	S_0	A_0	k (s^{-1})	S_0	A_0	k (s^{-1})
1.1	HCOOH + * → HCOOH*	-	-2.20	7.94E-08	6.87E+03	5.46E-04	3.87E-08	5.95E+03	2.30E-04	2.21E-08	5.32E+03	1.18E-04
1.2	HCOOH* → HCOOH + *	-	2.20	-	8.99E+11	1.88E-05	-	3.20E+11	1.29E-03	-	1.26E+11	9.65E-02
2.1	HCOOH* → HCOO-H*	0.51	-0.80	-	8.54E+12	8.44E+08	-	7.78E+12	5.50E+08	-	7.20E+12	3.70E+08
2.2	HCOO-H* → HCOOH*	1.32	0.80	-	1.38E+13	1.41E+00	-	1.45E+13	1.38E+00	-	1.49E+13	1.37E+00
2.3	HCOO-H* + * → HCOO* + H*	-	-0.27	-	1.28E+13	1.03E+16	-	1.33E+13	1.07E+16	-	1.38E+13	1.13E+16
2.4	HCOO* + H* → HCOO-H* + *	-	0.27	-	8.46E+12	1.05E+10	-	8.15E+12	1.02E+10	-	7.88E+12	9.64E+09
3.1	HCOOH* → H-COOH*	0.27	-0.72	-	1.08E+13	1.19E+11	-	1.13E+13	1.01E+11	-	1.17E+13	9.00E+10
3.2	H-COOH* → HCOOH*	0.99	0.72	-	1.51E+13	2.76E+03	-	1.68E+13	3.05E+03	-	1.78E+13	3.35E+03
3.3	H-COOH* + * → H* + COOH*	-	-0.10	-	1.06E+13	1.49E+14	-	1.08E+13	1.48E+14	-	1.10E+13	1.51E+14
3.4	H* + COOH* → H-COOH*	-	0.10	-	1.03E+13	7.28E+11	-	1.01E+13	7.32E+11	-	9.85E+12	7.20E+11
4.1	HCOOH* → HCO-OH*	0.34	-1.23	-	1.36E+13	9.58E+09	-	1.45E+13	9.36E+09	-	1.50E+13	9.38E+09
4.2	HCO-OH* → HCOOH*	1.58	1.23	-	1.97E+13	3.13E-03	-	1.91E+13	3.11E-03	-	1.78E+13	2.88E-03
4.3	HCO-OH* + * → HCO* + OH*	-	-0.13	-	1.17E+13	4.10E+14	-	1.20E+13	4.18E+14	-	1.21E+13	4.21E+14
4.4	HCO* + OH* → HCO-OH* + *	-	0.13	-	9.25E+12	2.65E+11	-	9.06E+12	2.60E+11	-	8.95E+12	2.58E+11
5.1	HCOO* → H-COO*	0.38	-0.43	-	9.78E+12	7.55E+09	-	1.00E+13	6.17E+09	-	1.02E+13	5.28E+09
5.2	H-COO* → HCOO*	0.81	0.43	-	1.42E+13	1.50E+05	-	1.50E+13	1.55E+05	-	1.53E+13	1.59E+05
5.3	H-COO* + * → H* + CO_2*	-	-0.13	-	1.42E+13	4.06E+14	-	1.50E+13	4.43E+14	-	1.57E+13	4.86E+14

5.4	H* + CO_2* → H-COO*	-	0.13	-	7.65E+12	2.67E+11	-	7.23E+12	2.45E+11	-	6.92E+12	2.23E+11
6.1	HCOO*+ H* → HCOO*-H* + *	-	0.27	-	8.46E+12	1.05E+10	-	8.15E+12	1.02E+10	-	7.87E+12	9.62E+09
6.2	HCOO*-H* + * → HCOO* + H*	-	-0.27	-	1.28E+13	1.03E+16	-	1.33E+13	1.07E+16	-	1.38E+13	1.13E+16
6.3	HCOO*-H* → H2-COO*	1.35	1.25	-	8.66E+13	8.59E+00	-	1.61E+14	2.11E+01	-	2.58E+14	5.48E+01
6.4	H2-COO* → HCOO*-H*	0.09	-1.25	-	1.12E+13	1.34E+12	-	1.08E+13	1.28E+12	-	1.04E+13	1.23E+12
6.5	H2-COO* → H_2 + CO_2*	-	0.12	-	1.47E+12	7.63E+13	-	7.07E+11	5.00E+14	-	3.76E+11	3.87E+15
6.6	H_2 + CO_2* → H2-COO*	-	-0.12	-	3.69E+08	7.10E+06	-	2.80E+08	3.96E+05	-	2.41E+08	2.34E+04
7.1	COOH* → COO-H*	0.74	-0.68	-	8.59E+12	4.77E+06	-	8.00E+12	3.16E+06	-	7.54E+12	2.17E+06
7.2	COO-H* → COOH*	1.43	0.68	-	1.19E+13	9.85E-02	-	1.22E+13	9.19E-02	-	1.23E+13	8.67E-02
7.3	COO-H* + * → CO_2* + H*	-	-0.13	-	1.42E+13	4.05E+14	-	1.50E+13	4.42E+14	-	1.57E+13	4.85E+14
7.4	CO_2* + H* → COO-H*	-	0.13	-	7.65E+12	2.68E+11	-	7.23E+12	2.46E+11	-	6.92E+12	2.24E+11
8.1	COOH* → CO-OH*	0.24	-1.52	-	1.23E+13	7.24E+10	-	1.25E+13	6.79E+10	-	1.24E+13	6.41E+10
8.2	CO-OH* → COOH*	1.76	1.52	-	1.26E+13	2.18E-05	-	1.14E+13	1.87E-05	-	1.03E+13	1.54E-05
8.3	CO-OH* + * → CO* + OH*	-	-0.07	-	1.96E+13	1.24E+14	-	2.20E+13	1.59E+14	-	2.39E+13	1.99E+14
8.4	CO* + OH* → CO-OH*	-	0.07	-	5.55E+12	8.78E+11	-	4.93E+12	6.83E+11	-	4.54E+12	5.44E+11
9.1	H* + COOH* → H*-COOH* + *	-	0.10	-	1.03E+13	7.28E+11	-	1.01E+13	7.32E+11	-	9.85E+12	7.20E+11
9.2	H*-COOH* + * → H* + COOH*	-	-0.10	-	1.06E+13	1.49E+14	-	1.08E+13	1.48E+14	-	1.10E+13	1.51E+14
9.3	H*-COOH* → CO*-H_2O*	1.03	0.23	-	3.57E+13	1.02E+04	-	4.92E+13	1.52E+04	-	6.23E+13	2.32E+04
9.4	CO*-H_2O* → H*-COOH*	0.80	-0.23	-	3.68E+12	6.44E+05	-	3.02E+12	2.98E+05	-	2.64E+12	1.54E+05
9.5	CO*-H_2O* → CO* + H_2O*	-	-0.07	-	1.96E+13	1.24E+14	-	2.20E+13	1.59E+14	-	2.39E+13	1.99E+14
9.6	CO* + H_2O* → CO*-H_2O*	-	0.07	-	5.55E+12	8.78E+11	-	4.93E+12	6.83E+11	-	4.54E+12	5.44E+11

10.1	HCO* → H-CO*	0.28	-0.81	-	1.86E+13	1.54E+11	-	2.13E+13	1.66E+11	-	2.32E+13	1.78E+11
10.2	H-CO* → HCO*	1.08	0.81	-	6.70E+12	1.08E+02	-	6.73E+12	9.26E+01	-	6.70E+12	8.03E+01
10.3	H-CO* + * → H* + CO*	-	-0.24	-	6.40E+12	1.48E+15	-	6.07E+12	1.26E+15	-	5.89E+12	1.11E+15
10.4	H* + CO* → H-CO*	-	0.24	-	1.69E+13	7.35E+10	-	1.79E+13	8.61E+10	-	1.84E+13	9.82E+10
11.1	OH*-H* → H_2O*	2.44	1.94	-	3.13E+13	2.53E-11	-	3.61E+13	3.19E-11	-	3.88E+13	3.83E-11
11.2	H_2O* → OH*-H*	0.50	-1.94	-	2.40E+12	2.62E+08	-	1.82E+12	1.06E+08	-	1.49E+12	4.69E+07
11.3	H_2O* + * → OH* + H*	-	-0.04	-	1.12E+13	3.31E+13	-	1.14E+13	3.42E+13	-	1.16E+13	3.53E+13
11.4	OH* + H* → H_2O* + *	-	0.04	-	9.72E+12	3.28E+12	-	9.52E+12	3.17E+12	-	9.37E+12	3.07E+12
12.1	H*-H* → H_2*	1.42	1.42	-	2.41E+13	2.00E-01	-	3.17E+13	3.06E-01	-	3.82E+13	4.55E-01
12.2	H_2* → H*-H*	0.01	-1.42	-	1.03E+13	1.97E+13	-	9.68E+12	1.57E+13	-	9.08E+12	1.26E+13
12.3	H_2* → H* + H*	-	-0.02	-	1.04E+13	1.67E+13	-	1.05E+13	1.67E+13	-	1.05E+13	1.68E+13
12.4	H* + H* → H_2*	-	0.02	-	1.04E+13	6.51E+12	-	1.04E+13	6.50E+12	-	1.03E+13	6.48E+12
13.1	CO_2* → CO_2 + *	-	1.76	-	1.26E+12	1.67E-01	-	5.03E+11	5.89E+00	-	2.17E+11	2.22E+02
13.2	CO_2 + * → CO_2*	-	-1.76	2.76E-06	5.44E+03	1.50E-02	1.55E-06	5.44E+03	8.45E-03	9.93E-07	5.44E+03	5.41E-03
14.1	H_2O* → H_2O + *	-	0.86	-	3.31E+11	1.18E+07	-	1.19E+11	1.60E+08	-	4.87E+10	2.58E+09
14.2	H_2O + * → H_2O*	-	-0.86	4.06E-05	8.51E+03	3.45E-01	1.98E-05	8.51E+03	1.68E-01	1.13E-05	8.51E+03	9.63E-02
15.1	CO* → CO + *	-	5.75	-	1.56E+12	7.88E-42	-	7.33E+11	2.21E-40	-	3.70E+11	6.91E-39
15.2	CO + * → CO*	-	-5.75	2.13E-05	6.82E+03	1.46E-01	1.20E-05	6.82E+03	8.19E-02	7.68E-06	6.82E+03	5.24E-02
16.1	H_2* → H_2 + *	-	0.77	-	4.19E+12	3.98E+07	-	2.63E+12	3.91E+08	-	1.69E+12	4.58E+09
16.2	H_2 + * → H_2*	-	-0.77	9.37E-03	2.54E+04	2.38E+02	5.27E-03	2.54E+04	1.34E+02	3.37E-03	2.54E+04	8.58E+01

and 4p suggest that the most favourable mechanism of the HCOOH decay is reaction 3 followed by reaction 4, and finally reaction 2. As the temperature is increased from 300 K to 400 K, the steady-state concentration of 4p is steady compared to the change in the concentration of 2p and 3p, both of which decrease by an order of magnitude, which indicates that the path leading to 4p is mostly unaffected at this range of temperatures. However, from 400 K to 500 K, the trends reverse, i.e. the change in the concentration of 2p and 3p is minimal while the concentration of 4p decrease by 10^{-1} ML. This dramatic change is because the backward reaction rate for reaction 4 increases from 400 K, and therefore the concentration of 4p decreases.

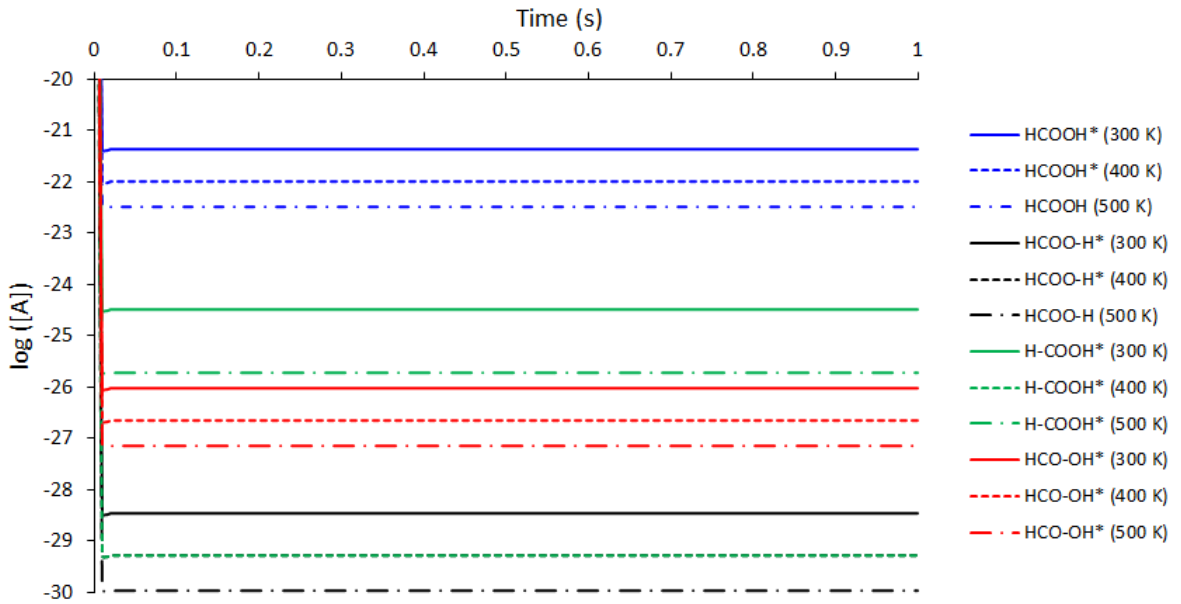

Figure 5.5.19: Plot of log of steady-state concentration [A] of 1p (HCOOH*), 2p (HCOO-H*), 3p (H-COOH*) and 4p(HCO-OH*) on the surface with time at 300 K, 400 K and 500 K.

Further degradation of 2p (HCOO-H*), 3p (H-COOH*) and 4p (HCO-OH*) to form CO and CO_2 species on the surface occurs as shown in Figure 5.5.20. At 300 K, the concentration of CO_2 on the surface rise steadily as the time progresses. This is due to the continuous formation of CO_2 on the surface from 2p and 3p via reaction 5, 6 and 7. As the

surface concentration of CO_2 increases, desorption of CO_2 from the surface into the gas phase also increases. At elevated temperatures (i.e. 400 K and 500 K), the formation of CO_2 on the surface decreases, which is attributed to two factors: (i) the formation of 2p and 3p decrease, and therefore there is less reactant for the formation of CO_2, and (ii), the rate constants of reaction 5 and 7 also decrease with increase in temperature (Table 5.5.6). Thereafter, whatever CO_2 is formed on the surface at 400 K and 500 K is desorbed almost immediately due to the high rate constant of reaction 13.

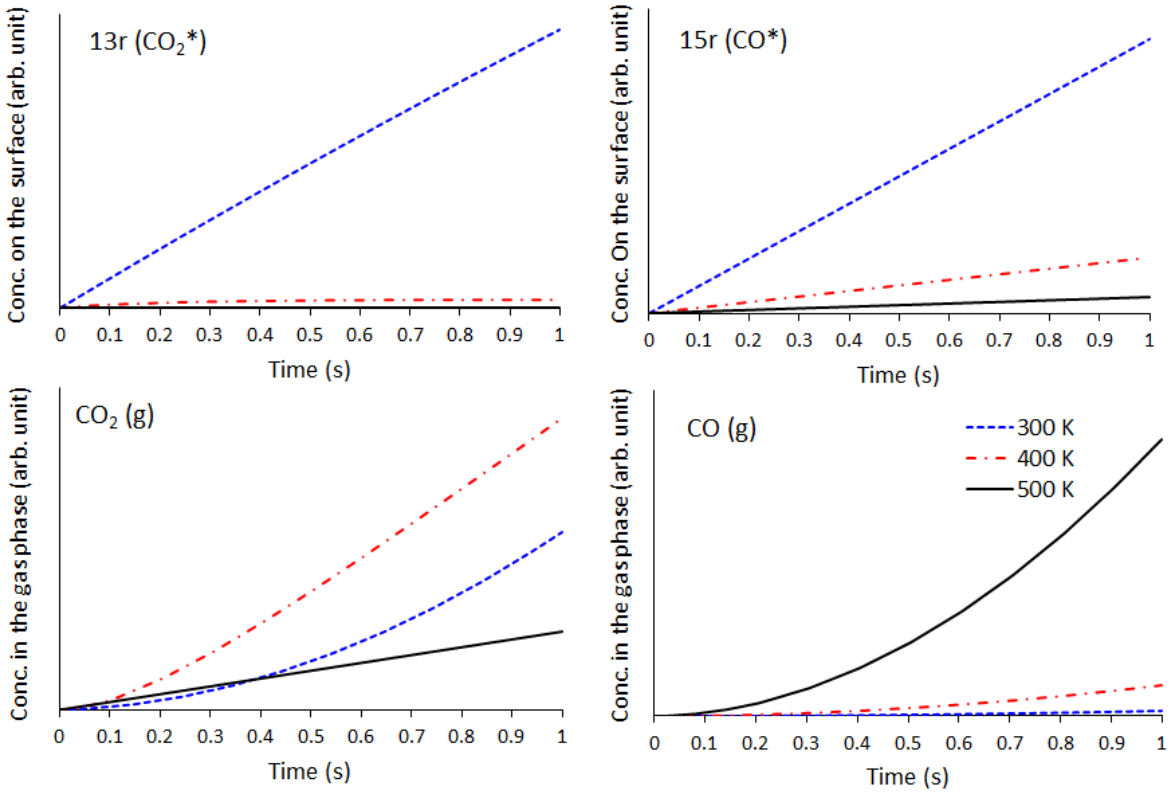

Figure 5.5.20: Plot of steady-state concentration of 13r and 15r on the surface, and CO and CO_2 in the gas phase, against time, at 300 K, 400 K and 500 K. The plots are showing the ratio between these gaseous species and the initial HCOOH, and are normalised by: 10^{-13} for 13r, 10^{-11} for 15r, 10^{-14} for CO_2(g) and 10^{-50} for CO(g).

From 3p and 4p, carbon monoxide is formed on the surface *via* reactions 8, 9 and 10, and accumulates on the surface at all the temperatures studied. At 300 K, 100 times more CO is produced on the surface than CO_2, and the *k* for CO formation increases faster with the

temperature than for CO_2. These, together with the very slow CO desorption, lead to a difference in the CO and CO_2 coverage of 10^5 at 500 K, presenting a ratio of 10^{-50} with the initial HCOOH at all temperatures. The extremely slow desorption kinetics (7.88×10^{-42} s^{-1}) of CO suggests that it could poison the surface at low to moderate temperatures.

5.5.3.2 Temperature Programmed Desorption (TPD) model

In order to see how HCOOH coverage affects the reactions, TPD modelling was conducted. Four different scenarios were considered with increasing initial formic acid surface coverage: 10 %, 40 %, 70 % and 100 %. The temperature was increased at the rate of 10 K s^{-1} and the change in the concentration of all the gas phase species was calculated with increasing temperature.

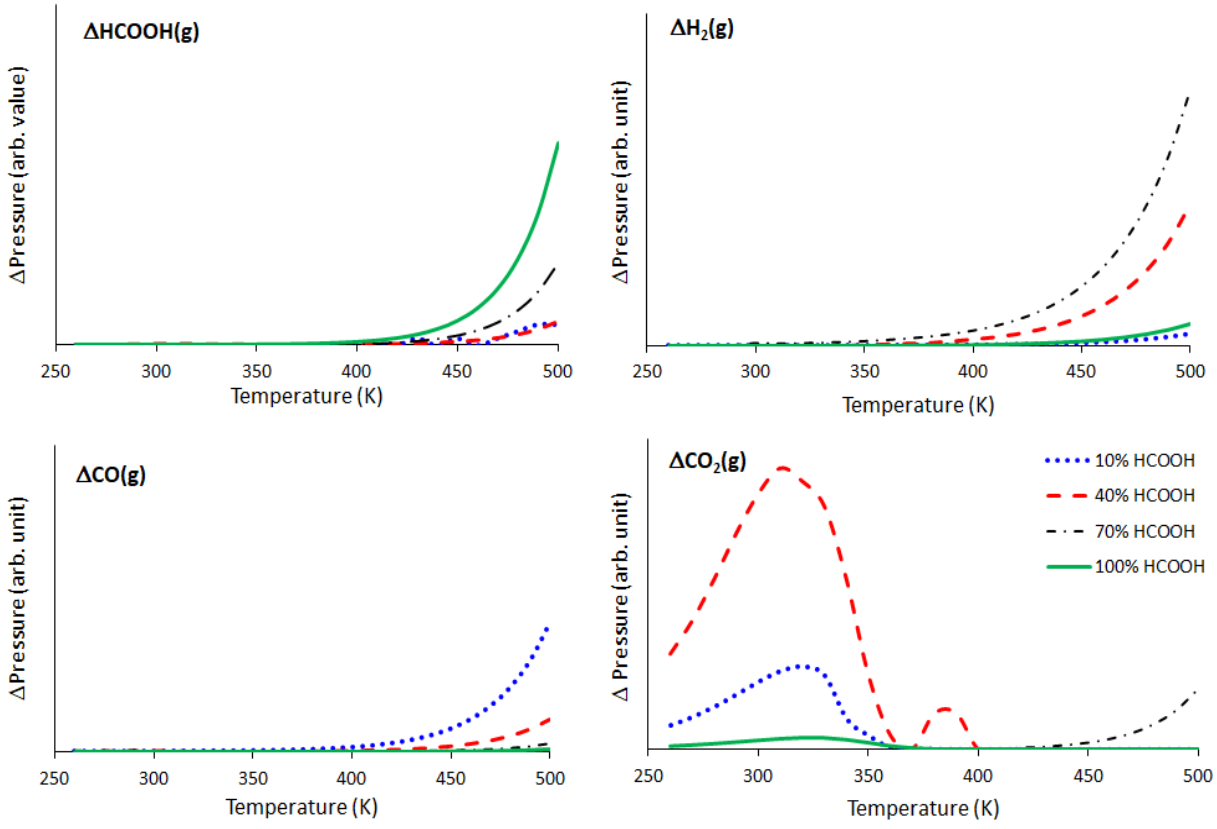

Figure 5.5.21: Plot of change in ratio of gaseous species (HCOOH, H_2, CO_2 and CO), with increasing temperature, for the different initial formic acid surface coverage.

Formic acid starts to appear in the gas phase after 400 K at all the four initial conditions (Figure 5.5.21). The change in CO_2 concentration begins at 260 K, reaches a peak at 340 K and falls thereafter for 10% and 40% HCOOH coverage. A tiny peak for CO_2 is also observed at 100% coverage condition between 300-350K; however, as vacant sites are not available for the reaction to occur, the peak is very small. The experimental TPD also reports the CO_2 desorption near this temperature for different transition metal at similar coverage [226,227]. On the Pd surface, CO_2 desorption from Zn is reported between 300 K and 400 K for 10% to 50% concentration [226]. Similarly, CO_2 is found to evolve at 295 K over oxygen exposed Pd (110) [227]. The evolution of CO_2 from our system suggests that the adsorbed formic acid is undergoing dehydrogenation from 260 K to 340 K through pathway 1. Above 400 K, CO is observed in gas phase indicating pathway 2 and 3 to be dominating the conversion route. The presence of CO at this temperature is in line with the experimental observations for other metals [226,228]. However, in the work of Flaherty et al.[202], the peak is observed before 400 K for CO over carbide of molybdenum. It is to be noted though that the species concentration in their case on the surface was 1.6 ML. Therefore, the molecules from the second layer could be desorbing into the gas phase at lower temperatures than 400 K. On a Zn loaded Pd surface, CO appears in the gas phase between 300 K and 520 K, depending on the amount of Zn loading [226]. Similarly, over a CeO_2 catalyst, CO appears from 450 K and peaks at 600 K [228]. Contrary to what is generally observed for metal catalysts [226,227], the change in the concentration of H_2 is not observed before 350 K. For metal catalysts, the electronegative hydrogen adatoms are stabilised by the electropositive metals as they move away from the surface [229] for associative desorption, but the presence of carbon in the Mo lattice in Mo_2C decreases the overall electropositivity of the surface and increases the work function [230,231]; Therefore, a higher temperature is required to facilitate the hydrogen atoms' associative desorption from the surface. The formation of H_2 on the surface (reaction 12) also has slow

kinetics (10^{-1} s^{-1}). At higher HCOOH coverage (70% and 100%), since very less or no sites are available for the conversion to proceed, no change in the concentration of CO and H_2 is observed in the gas phase. Only after 400 K, when HCOOH desorbs from the surface, does the concentration of CO, CO_2 and H_2 begin to change in increasing proportion. The rate of change of HCOOH in the gas phase increases sharply after 450 K, and is steeper for 70% and 100% coverage than for 10% and 40% coverage.

The selectivity analysis of the system shows that CO_2 is the preferred end product obtained in the gas phase, with almost 100% selectivity, which is very close to the reported experimental result of over 96% for the β-Mo_2C [232].

5.6 Hydrodeoxygenation of Guaiacol Over Orthorhombic Molybdenum Carbide: A DFT and Microkinetic Study

5.6.1 System Setup

All the simulations in this study were performed under the density functional theory (DFT) framework using the "*Fritz Haber Institute ab initio molecular simulations*" (FHI-aims) software package [193] in combination with the "*Atomic Simulation Environment*" (ASE) Python package [194] for geometry handling.; and the microkinetic modelling was conducted using our in-house code[212].

The orthorhombic (β) structure of molybdenum carbide was chosen as the bulk geometry due to its excellent thermal stability [195], which makes it suitable for usage in a wide temperature range. The (100) surface with molybdenum termination was chosen as catalytic surface because it shows favourable hydrogen adsorption properties [205]. Also, the (100) surface has been reported to be quite a suitable surface for HDO reactions in experimental works [203,204]. The Mo terminated (100) surface also has the highest surface metal density (0.130 atom $Å^{-2}$) of all terminations of (100) surface, resulting in higher coordination of this site at the surface. As a result, the electron-state fluctuations, which are involved in the breaking and formation of chemical bonds during catalytic reactions and are responsible for high turnover, are the highest at the Mo terminated surface [233].

To simulate the β-Mo_2C (100) surface, a 4-layer slab model was considered in a periodic environment (Figure 5.6.1). After convergence testing with respect to surface energies, it was deemed appropriate to constrain the bottom two layers of the slab, whilst the top two layers were unconstrained. A 10 Å vacuum was added above and below the plane of the slab (i.e. total vacuum of 20 Å), which prevent spurious self-interaction errors. To counterbalance any dipole arising out of the imbalanced electric field at the surface, a dipole correction was also applied.

A 5 × 5 × 4 sized **k**-grid was chosen for the periodic condition calculations. The PBE [3] functional with the Tkatchenko-Scheffler van der Waals correction [197] was used for electronic structure calculations, along with the "*light*" basis set of the FHI-aims package, which is equivalent to the Pople's 6-31+G** basis set [151]. In addition, zeroth order regular approximation (ZORA) [193] scaler corrections were incorporated to account for relativistic effects. The choice of all these parameters is a result of a systematic study described in our previous work [234].

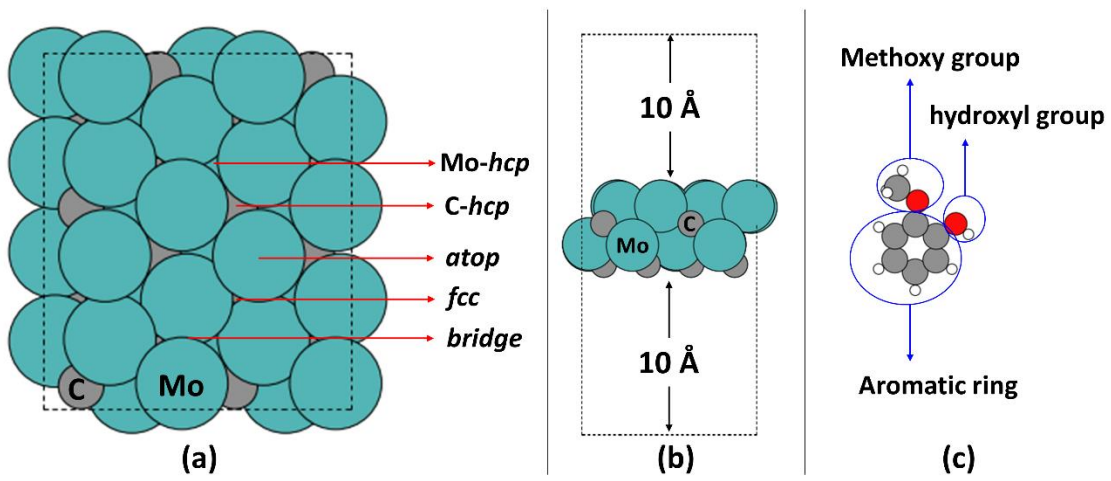

Figure 5.6.1: (a) Top view of the β-Mo_2C (100) slab showing adsorption sites, (b) side view of the β-Mo_2C (100) slab showing the vacuum, and (c) *methoxy* group, *hydroxyl* group and the aromatic *ring* of guaiacol; where the grey, teal, red and white coloured atoms represent carbon, molybdenum, oxygen and hydrogen, respectively.

Geometry optimization of all the structures was conducted using the trust region method [196] until the force on each atom was less than 0.01 eV $Å^{-1}$. For the transition state calculations, a minimum of 7 images were used in the Nudged Elastic Band (NEB) method calculations [210] with the molecular dynamics based Fast Inertial Relaxation Engine (FIRE) optimization algorithm [211]. The convergence criteria for the NEB calculations was set to 0.05 eV $Å^{-1}$ of force on each atom. This was followed by finite-difference frequency calculations for the transition state structures to confirm the validity of these structures, with one imaginary

frequency confirming a first-order saddle point. For cases where none or multiple imaginary frequencies were obtained, a machine learning NEB method [235] was used with 15 images to determine the correct transition state structure. In specific cases where obtaining the transition state was challenging, a complementary approach was used: the distance, *d*, between atom A (or a group of atoms) which react with the other atom B (a group of atoms) was calculated, and then divided into *n* equal parts (*n* =20 in this case). Atom(/group) A is then placed at a distance of *d/n* from atom(/group) B, for all values of n, generating a pathway that contains *n* different geometry samples. For each geometry, the distance between A and B is constrain whilst optimising all other degrees of freedom and, on plotting energy versus *d* for all the optimized geometries, the energy profile can be used to identify the transition state structure. Once we have the transition state structure, finite-difference frequency calculations confirmed the nature of the first-order saddle point by presenting a single imaginary frequency.

The adsorption energy (E_{ads}) of all the reactions describing an adsorption process in the reaction scheme was calculated as:

$$E_{\mathrm{ads}} = E_{\mathrm{Mo_2C+Molecule}} - E_{\mathrm{Mo_2C}} - E_{\mathrm{Molecule}} \tag{5.23}$$

Where E_{Molecule} is the energy of the adsorbate molecule in the gas phase, $E_{\mathrm{Mo_2C}}$ is the energy of the bare surface, and $E_{\mathrm{Mo_2C+Molecule}}$ is the energy of the system where the adsorbate is adsorbed on the surface. For the reactions describing the desorption of molecules from the surface, the desorption energy (E_{des}) was calculated as $E_{\mathrm{des}} = -E_{\mathrm{ads}}$.

The microkinetic modelling was conducted in the same manner as elsewhere [212]. Briefly, translations, rotations and vibrations were used to calculate the thermodynamic parameters, such as entropy, enthalpy and Gibbs free energy, based on a statistical thermodynamics approach [22]. These energetic quantities were then used to calculate the rate

constants for all the reactions using the transition-state theory (TST) approximation of Eyring, Evans and Polanyi [216,217]. For adsorption reactions, the rate constants were calculated using the Hertz−Knudsen relation [188]. Finally, the rate of reaction was described for each individual step and the system of ordinary differential equations (ODEs) were solved to obtain a steady state solution.

The mechanism proposed for the study initiates with the adsorption of guaiacol (GUA) on the surface. Guaiacol was considered interacting with the surface in three different orientations: via the aromatic *ring*, via the *methoxy* group and via the *hydroxyl* group as show in Figure 5.6.1(C). The adsorption was conducted on 4 different sites (*atop*, *bridge*, *fcc*, Mo-*hcp* and C-*hcp*) on the surface, as shown in Table 5.6.1-5.6.3 of the supplementary information. The strongest adsorption is via the aromatic *ring* over the C-*hcp* position of the surface, with an adsorption energy of -4.67 eV, which is at least 2.21 eV stronger compared to the precious metal surfaces such as Ru (E_{ads} = -2.46 eV)[56], Pd (E_{ads} = -1.43 eV)[236] and Pt (E_{ads} = -2.41 eV) [58]. However, for the carbide of tungsten from the same group, the adsorption energy is only 1.63 eV weaker than the molybdenum carbide [237]. In several cases, such as interaction in the *atop* position with the *methoxy* group, and in the *bridge* position via the aromatic *ring*, the molecule rearranged during optimizations to position over the C-*hcp* position via aromatic *ring*. The preference of the hollow site (similar to the C-*hcp* site) for adsorption of aromatic species, including guaiacol, is well documented [55]. As this was confirmed as the most stable adsorption site, all the subsequent calculations considering conversion of guaiacol were conducted at the C-*hcp* position. Further, kinetic calculations were conducted to obtain the sticking probability (σ) of aromatic compounds. The σ of phenol was found to be very close to unity at 90 K over Pt (111) and at 150 K over Ni (111) [238] and agrees with our calculated unity value in the similar temperature range. Similarly, over Ag (111) surface, the phenol σ is reported to be 0.56 at 163 K [239], which is 0.20 more than our calculated value at the same

temperature. For the similar molecule guaiacol, our kinetic calculations highlight the σ to be 0.76 at 170 K, which decrease to the order of 10^{-4} at 300 K, and to 3.23×10^{-7} at 500 K. As a result, the rate constant for adsorption decreases with increase in temperature; and therefore, low temperatures are favorable to promote the adsorption processes.

Table 5.6.1: Initial and final geometries of the adsorption of guaiacol via the *methoxy* group facing the surface at *atop*, *bridge*, C-*hcp*, Mo-*hcp* and *fcc* positions along with their respective adsorption energies (E_{ads}); the atoms are represented as: grey (Carbon), white (hydrogen), red (oxygen) and teal (molybdenum)

Position	Initial geometry	Final geometry	E_{ads} (eV)
atop	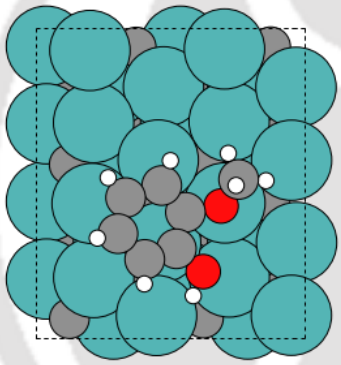	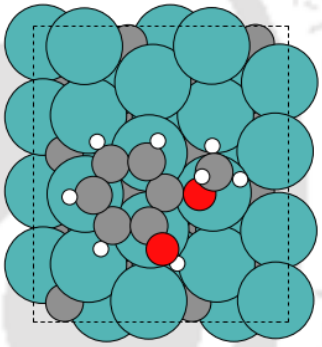	-4.67
bridge	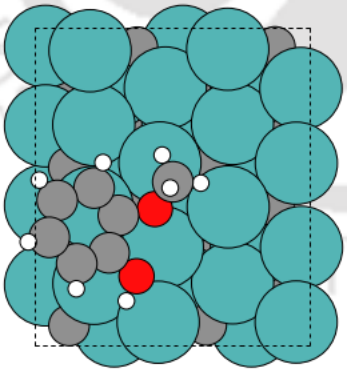	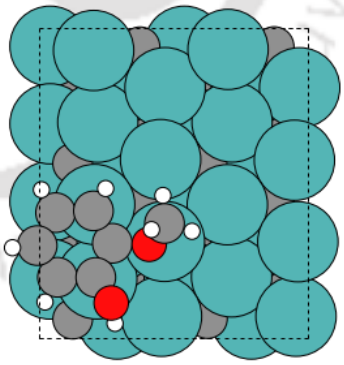	-4.49

C-*hcp*	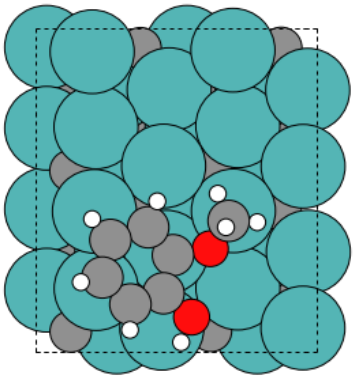	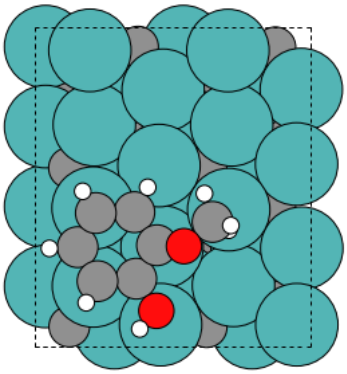	-4.67
Mo-*hcp*	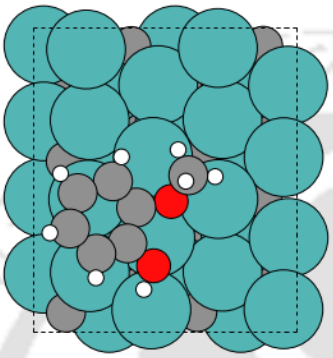	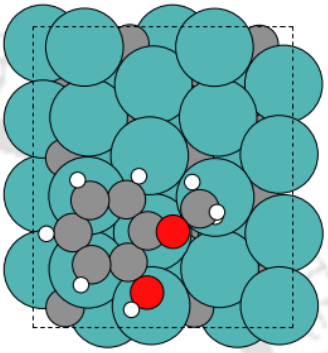	-4.66
fcc	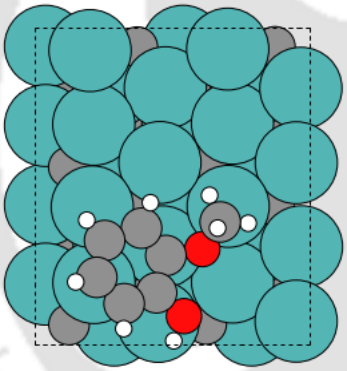	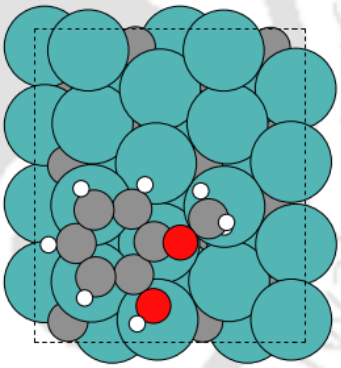	-4.60

Table 5.6.2: Initial and final geometries of the adsorption of guaiacol via the *hydroxyl* group facing the surface at *atop*, *bridge*, C-*hcp*, Mo-*hcp* and *fcc* positions along with their respective adsorption energies (E_{ads}); the atoms are represented as: grey (Carbon), white (hydrogen), red (oxygen) and teal (molybdenum)

	Initial geometry	Final geometry	E_{ads} (eV)

atop	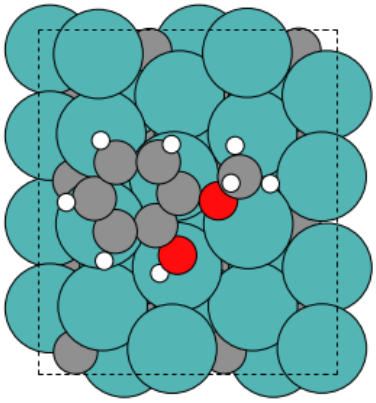	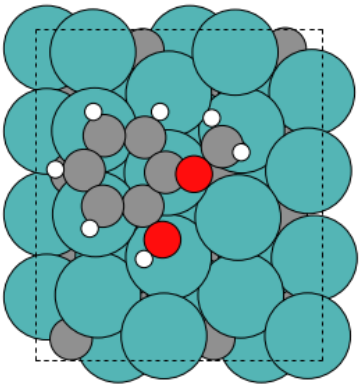	-4.17
bridge	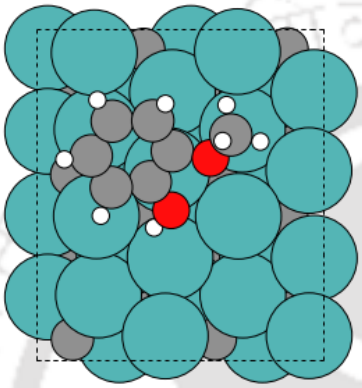	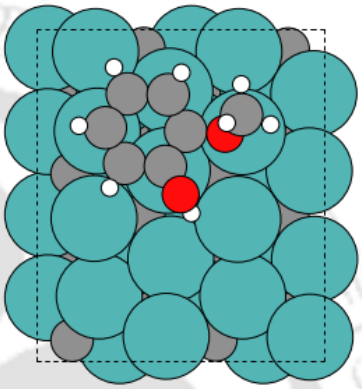	-4.50
C-*hcp*	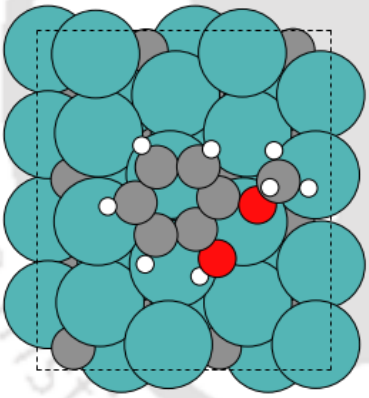	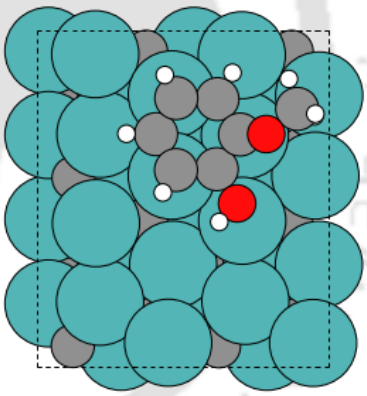	-4.66
Mo-*hcp*	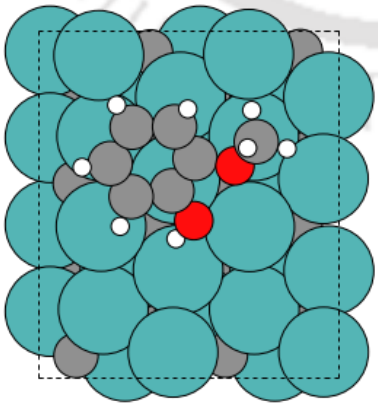	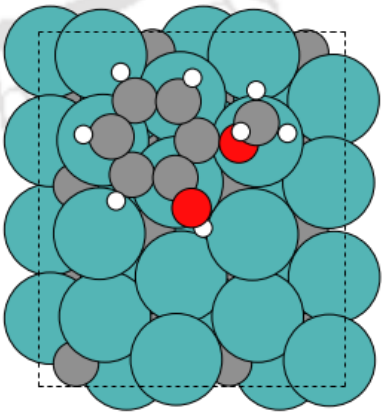	-4.50

fcc	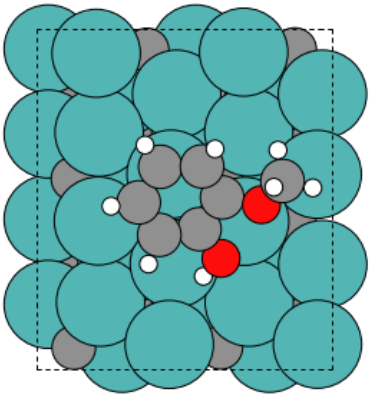	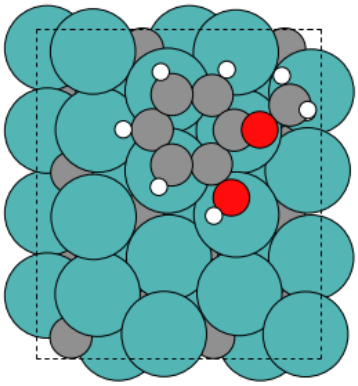	-4.66

Table 5.6.3: Initial and final geometries of the adsorption of guaiacol via the aromatic *ring* facing the surface at *atop*, *bridge*, C-*hcp*, Mo-*hcp* and *fcc* positions along with their respective adsorption energies (E_{ads}); the atoms are represented as: grey (Carbon), white (hydrogen), red (oxygen) and teal (molybdenum)

	Initial geometry	Final geometry	E_* (eV)
atop	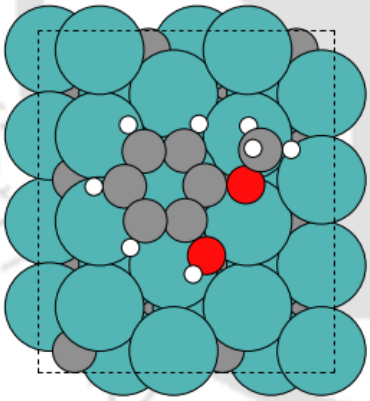	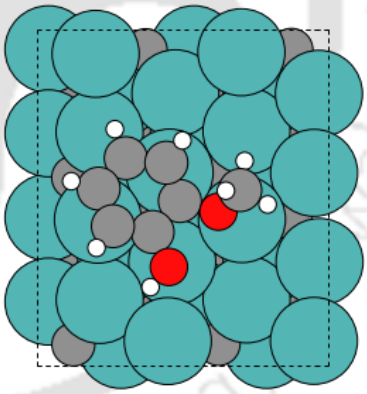	-4.09
bridge	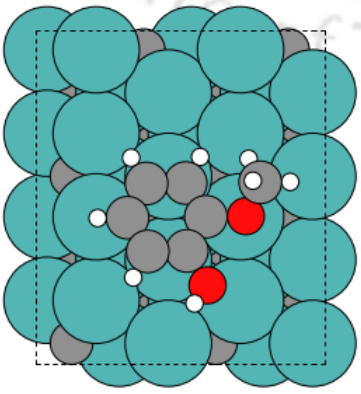	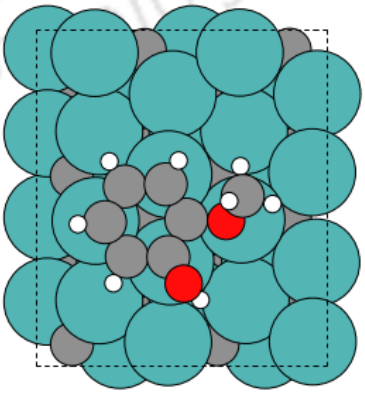	-4.67

C-*hcp*	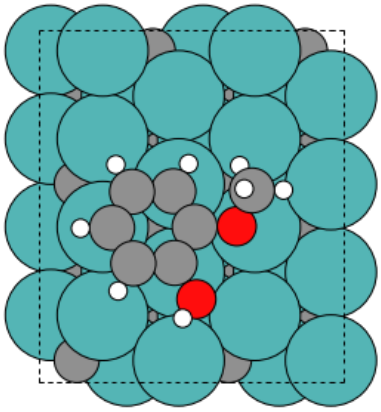	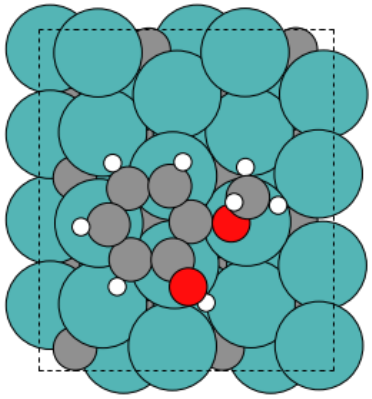	-4.67
Mo-*hcp*	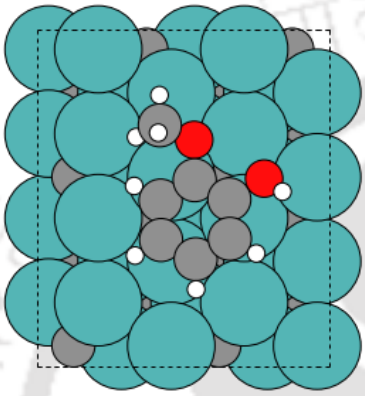	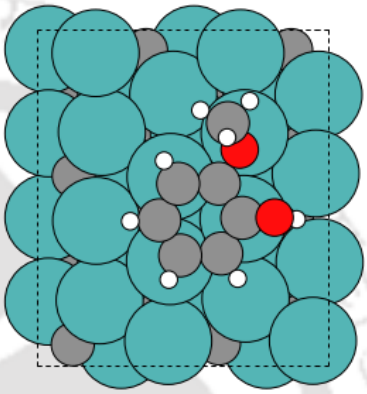	-4.26
fcc	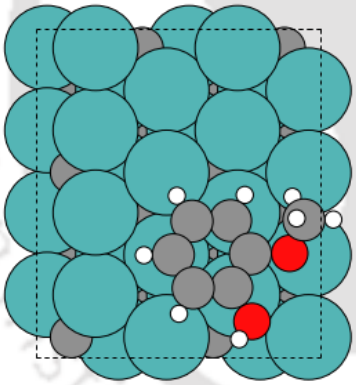	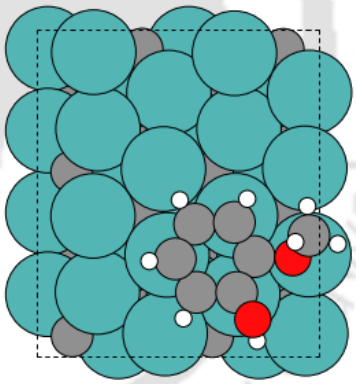	-4.49

5.6.2 Energy profile of the upgrading routes

The proposed mechanism describes the hydrogenation and deoxygenation of guaiacol in a series of elementary steps. Since the saturation of the aromatic ring are known to be quite endothermic [107], and therefore, unfeasible in the temperature range considered, it is not included here. Thus, the upgrading of the adsorbed guaiacol can begin in two different ways: the molecule can be hydrogenated at the α- or the β-position of the aromatic ring (structures S2 and S3 in

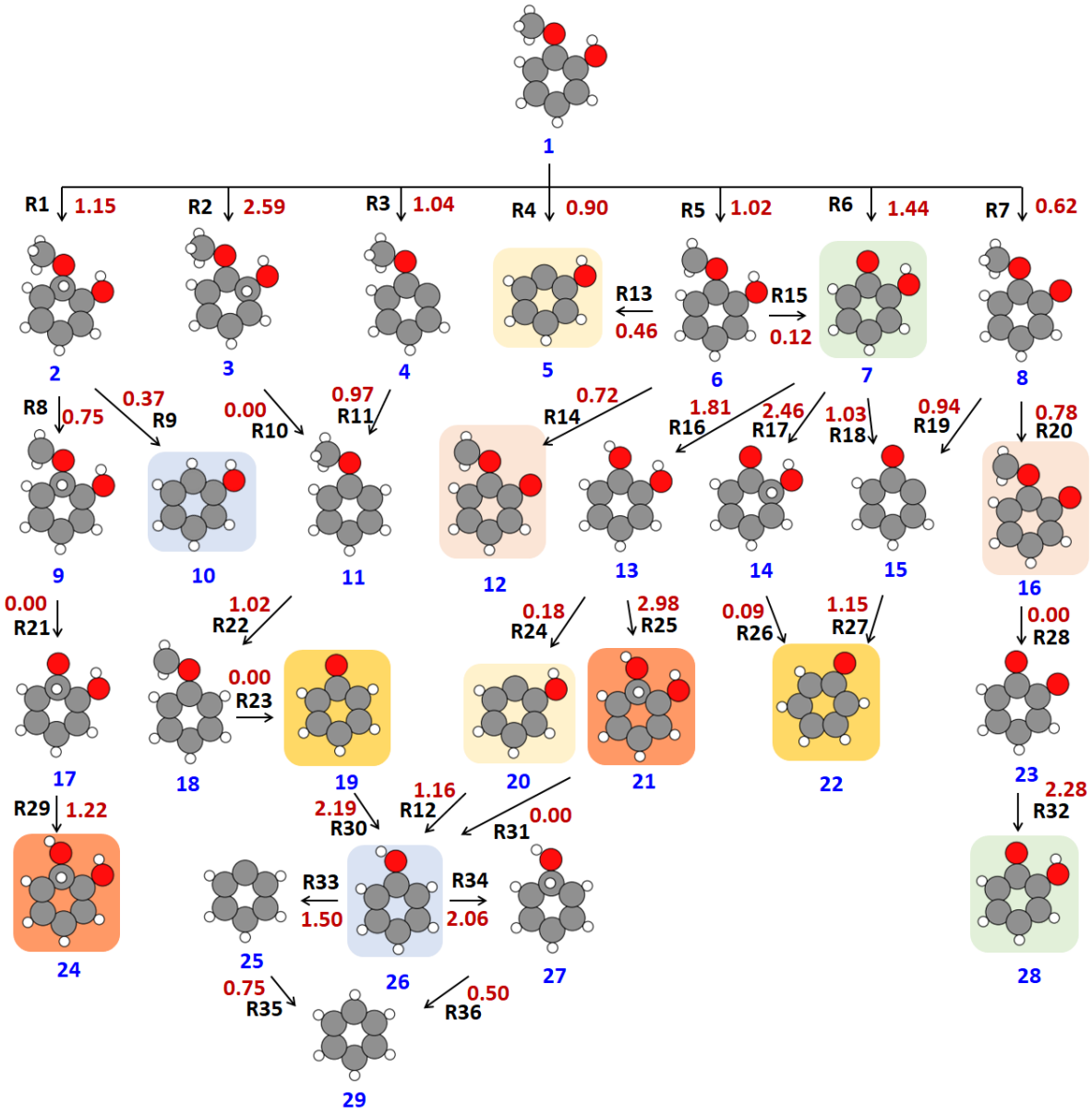

Figure 5.6.2: Reaction scheme of all the elementary steps for guaiacol upgrading; numbers given in red are the forward energy barriers of each reaction, in eV, whilst blue and black text show the structure (denoted in text as S) and reaction numbers, respectively. Equivalent structures are highlighted with identically coloured backgrounds.

Figure 5.6.2), or the methoxy and hydroxyl groups can dissociate from the molecule. Considering both options, there are seven routes (R1- R7) by which the upgrading can initiate (Figure 5.6.2). With respect to kinetic barriers, the dissociation of H from the hydroxyl group (R7) is the least energy demanding (0.62 eV), whereas thermodynamically, R6 is the most

favourable reaction (ΔE = -2.29 eV). The deprotonation of the hydroxyl group was previously observed as having the lowest energy barrier among R1-R7 on noble metal surfaces [56,107], showing similarity to our results. While the reported barrier over Pt (111) surface is 0.37 eV [107], it is 0.29 eV over the Ru (0001) surface [56] for the same reaction. The next most accessible reaction in our calculations is the cleavage of the methoxy group (R4), which has an activation energy of 0.90 eV. The kinetic calculations show the rate constant for R7 to be 100 times faster than R4, suggesting faster production of structure 8 (denoted here in as S) over S5/S20. The direct protonation of the molecule *via* R1 and R2 are highly energy demanding with energy barriers of 1.15 eV and 2.59 eV, respectively. Since the hydrogen cannot be transferred to the α- or β-position atom directly from the surface, due to steric hindrance, a concerted reaction mechanism is considered; here, a surface hydrogen migrates to the aromatic ring, and simultaneously a hydrogen from the ring shifts to the α- or β-position. Initially, the high activation barrier was suspected as arising due to hydrogen diffusion on the surface; However, reaction 49 or R49 (Table 5.6.4), which describes the diffusion and association of hydrogen atoms to form molecular hydrogen on the surface, show that the hydrogen diffusion is barrierless on the β-Mo_2C(100) surface. Therefore, the activation energy observed is associated with the second step in the concerted process, i.e. the migration of H from the aromatic ring to the α- or β-position.

The methoxy group of S8 undergoes further deprotonation in R20, with a reaction barrier of 0.78 eV, to give S16/S12; however, S16/S12 decomposes rapidly to S23 (R28) in a barrierless exothermic step (-2.31 eV). Kinetics simulations give a rate constant of ~10^{30} s^{-1} suggesting that the decomposition reaction is very fast. The carbene (CH_2) that separates from S16/S12 in R28 sits over a *fcc* site with the lowest carbon coordination in S23. Nagai *et al.* [219] reported similar behaviour for carbon monoxide (CO), with the strongest CO adsorption

Table 5.6.4: Activation energy (E_a), reaction energy (ΔE), Arrhenius factor (A_0) and forward rate constant (k_f) for reactions described in the reaction scheme. The notation used for the reactants (*X*r), transition states (TS*X*) and products (*X*p) uses *X* to represent the reaction number. The structures are denoted as S*Y*, as shown in Figure 5.6.2.

Rxn. No	Reactions	E_a (eV)	ΔE (eV)	500 K		600 K		700 K	
				A_0	k_f	A_0	k_f	A_0	k_f
ads	GUA + * >> GUA*	-	-4.67	1.30E+04	4.19E-03	1.18E+04	4.46E-04	1.10E+04	6.45E-05
R1	1r* > TS1 > 1p*	1.15	0.64	4.47E+13	1.78E+05	4.46E+13	2.15E+05	4.39E+13	2.50E+05
R2	2r > TS2 > 2p*	2.59	0.86	8.18E+13	1.78E-04	9.37E+13	2.35E-04	1.05E+14	3.13E-04
R3	GUA* > TS3 > 3p*	1.04	-0.69	4.03E+13	4.82E+06	4.69E+13	6.33E+06	5.34E+13	8.36E+06
R4	GUA* > TS4 > 4p*	0.90	0.59	7.62E+13	9.65E+07	8.67E+13	1.32E+08	9.60E+13	1.79E+08
R5	GUA* > TS5 > 5p*	1.02	-0.49	2.26E+13	6.76E+06	2.47E+13	7.09E+06	2.70E+13	7.78E+06
R6	GUA* > TS6 > 6p*	1.44	-2.29	1.41E+15	1.33E+06	2.09E+15	3.51E+06	2.87E+15	9.13E+06
R7	GUA* > TS7 > 7p*	0.62	-0.65	1.21E+13	2.01E+09	1.13E+13	1.56E+09	1.07E+13	1.24E+09
R8	1p* > TS8 > 8p*	0.75	-0.46	2.83E+13	4.32E+08	2.93E+13	4.59E+08	3.03E+13	4.98E+08
R9	1p* > TS9 > 9p*	0.37	-2.05	2.77E+14	3.68E+12	3.31E+14	6.24E+12	3.79E+14	1.04E+13
R10	2p* >> 10p*	-	-2.16	2.68E+13	9.58E+28	3.04E+13	1.23E+29	3.37E+13	1.58E+29
R11	11r* > TS11 >11p*	0.97	-0.29	7.06E+13	2.13E+07	8.24E+13	3.07E+07	9.31E+13	4.33E+07
R12	12r* > TS12 > S26*	1.16	-0.29	6.48E+13	7.57E+05	7.50E+13	1.08E+06	8.38E+13	1.49E+06
R13	S6* > TS13 > 13p*	0.79	-0.22	1.86E+15	8.08E+08	4.53E+15	9.85E+09	1.04E+16	1.19E+11
R14	S6* > TS14 > 14p*	0.82	-1.58	5.70E+14	3.63E+08	1.24E+15	3.05E+09	2.64E+15	2.63E+10
R15	S6* > TS15 > 15p*	0.49	-2.08	5.63E+14	2.43E+10	1.20E+15	2.16E+11	2.48E+15	1.92E+12
R16	16r* > TS16 > 16p*	1.81	1.43	1.94E+14	8.80E+01	2.30E+14	1.43E+02	2.61E+14	2.27E+02
R17	17r* > TS17 > 17p*	2.46	0.52	1.32E+13	1.11E-04	1.33E+13	9.74E-05	1.33E+13	8.60E-05
R18	S7* > TS18 > 18p*	1.03	-1.19	8.30E+13	1.44E+07	9.39E+13	2.00E+07	1.04E+14	2.80E+07
R19	S8* > TS19 > 19p*	0.39	-1.99	7.42E+13	5.60E+11	8.75E+13	7.82E+11	1.00E+14	1.09E+12
R20	S8* > TS20 > 20p*	0.78	-0.54	3.66E+13	7.88E+08	4.12E+13	9.15E+08	4.59E+13	1.10E+09
R21	S9* >> 21p*	-	-1.94	1.06E+13	2.45E+27	1.15E+13	2.49E+27	1.23E+13	2.57E+27
R22	S11* > TS22 > 22p*	1.02	-0.52	2.57E+13	8.67E+06	2.85E+13	9.34E+06	3.14E+13	1.05E+07

R23	S18* >> 23p*	-	-2.05	2.00E+13	2.97E+28	2.18E+13	3.33E+28	2.35E+13	3.73E+28
R24	16p* > TS24 > 24p*	0.18	-1.12	6.01E+13	9.12E+12	6.83E+13	1.22E+13	7.60E+13	1.65E+13
R25	25r* >> 25p*	-	2.98	1.58E+13	1.73E-08	1.55E+13	1.54E-08	1.52E+13	1.37E-08
R26	17p* > TS26 > 26p*	0.09	-1.87	1.64E+13	4.40E+12	1.68E+13	4.56E+12	1.71E+13	4.73E+12
R27	27r* > TS27 > S19*	1.15	0.23	7.30E+13	9.72E+05	8.63E+13	1.44E+06	9.81E+13	2.07E+06
R28	S12* >> 28p*	-	-2.31	1.87E+13	2.54E+30	2.09E+13	2.86E+30	2.30E+13	3.23E+30
R29	29r* > TS29 > 25p*	1.22	3.61	1.07E+14	5.05E+05	1.20E+14	7.15E+05	1.30E+14	9.89E+05
R30	30r* > TS30 > S26*	2.19	1.41	5.97E+13	3.00E-02	6.86E+13	4.11E-02	7.64E+13	5.54E-02
R31	25p* >> 31p*	-	-4.47	1.96E+13	4.79E+44	2.19E+13	6.78E+44	2.40E+13	9.44E+44
R32	32r* > TS32 > S7*	2.28	1.69	1.89E+14	2.99E-02	2.25E+14	4.95E-02	2.58E+14	7.98E-02
R33	S26* > TS33 > 33p*	1.50	-0.73	7.27E+13	6.05E+03	8.62E+13	8.53E+03	9.91E+13	1.20E+04
R34	34r* > TS34 > 34p*	2.06	0.57	1.66E+14	5.05E+00	1.98E+14	7.46E+00	2.29E+14	1.12E+01
R35	35r* > TS35 > 35p*	0.75	-0.5	5.26E+13	5.33E+08	6.09E+13	7.34E+08	6.81E+13	9.88E+08
R36	34p* > TS36 >36p*	0.5	-1.94	1.83E+13	6.63E+09	1.84E+13	6.39E+09	1.84E+13	6.17E+09
R37	37r* > TS37 > CH_3*	0.72	0.14	1.90E+13	1.08E+08	1.92E+13	1.16E+08	1.93E+13	1.22E+08
R38	38r* > TS38 > CH_4*	1.56	1.25	7.62E+13	7.04E+02	8.21E+13	9.37E+02	8.62E+13	1.21E+03
R39	39r* > TS39 > H_2O*	2.15	1.65	9.33E+13	1.10E-01	1.08E+14	1.58E-01	1.21E+14	2.25E-01
R40	40r* > TS40 > OCH_3*	0.85	0.17	5.36E+13	3.87E+07	5.91E+13	5.33E+07	6.32E+13	7.04E+07
R41	41r* > TS41 > CH_3OH*	2.45	2.14	3.77E+14	6.27E-03	4.75E+14	1.17E-02	5.66E+14	2.14E-02
R42	S26* >> phenol + *	-	4.45	8.91E+24	3.49E+01	8.24E+24	2.25E+03	7.41E+24	1.43E+05
R43	16p* >> catechol + *	-	4.26	9.24E+24	6.63E+02	8.24E+24	4.40E+04	7.20E+24	2.87E+06
R44	S29* >> benzene + *	-	4.06	2.18E+22	1.18E+00	1.79E+22	2.54E+01	1.46E+22	5.49E+02
R45	CH_4* >> CH_4 + *	-	0.38	1.19E+19	5.16E+21	1.04E+19	4.18E+22	9.06E+18	3.51E+23
R46	CH_3OH* >> CH_3OH + *	-	1.18	1.95E+22	1.31E+21	1.98E+22	3.82E+22	1.94E+22	1.13E+24
R47	H_2O* >> H_2O + *	-	1.07	4.19E+20	6.31E+18	4.73E+20	1.22E+20	5.08E+20	2.33E+21
R48	H_2* >> H_2 + *	-	0.79	4.91E+18	5.82E+16	6.88E+18	8.09E+17	8.82E+18	1.08E+19
R49	H* + H* > TS49 > H_2*	-	0	1.57E+13	1.38E+13	1.64E+13	1.55E+13	1.72E+13	1.76E+13

occurring at the carbon deficient site on the β-Mo_2C surface; experimental studies also report the surface to be selective to the cleavage of the C-O bond [120,125].

An oxygen atom of S23 can be protonated to produce S28 (R32), though a high energy barrier is calculated (2.28 eV) and the rate constant for this conversion is low (~10^{-2} s^{-1}). S28 can be formed from two more pathways: (i) the methyl radical from the guaiacol can directly cleave (R6) to form S7 (which is equivalent to S28); or (ii) the methoxy group of guaiacol can lose a hydrogen (R5), to give S6, followed by the dissociation of CH_2 moiety (R15) to again produce S7/S28. The conversion via R6 is 0.42 eV more energy demanding than R5, and kinetically slower than the R5 and R15 (Table 5.6.4). Therefore, the formation of S7/S28 will occur predominantly via R5 and R15. The preference of dehydrogenation over the deoxygenation in the methoxy group of guaiacol has also been reported by Lee *et al*. [58] over Pt (111) surface with E_a= 0.75 eV for R5 with the help of BEP correlation.

From S7/S28, there can be three possible reduction routes: in R16, hydrogenation yields catechol with an activation energy of 1.81 eV; in R17, the aromatic ring is hydrogenated with an activation energy of 2.46 eV; and in R18, the hydroxyl group is cleaved in a reaction with activation barrier of 1.03 eV. The kinetic modelling returns rate constants for R16 of ~10^1 s^{-1} and for R18 of ~10^7 s^{-1}, which suggests that the formation of catechol from guaiacol is very slow. Furthermore, the high barrier for R17 makes it unlikely. Thus, the reaction proceeds via R27 with an energy barrier of 1.15 eV to form S22/S19.

S22/S19 can also be formed via R2 and R3; the protonation of the β-carbon of guaiacol (R2) has an activation energy of 2.59 eV, and is kinetically very slow (~10^{-4} s^{-1}), whereas R3 (condensation) has a barrier of only 1.04 eV and is kinetically faster. Thus, S4 will be formed and converted to S11 via re-hydrogenation of the aromatic ring (R11). Further dehydrogenation

of the methoxy group (R22) requires only 1.02 eV of energy, which results in an unstable S18 that degrades to S19/S22 in a barrier-less exothermic step (-2.05 eV).

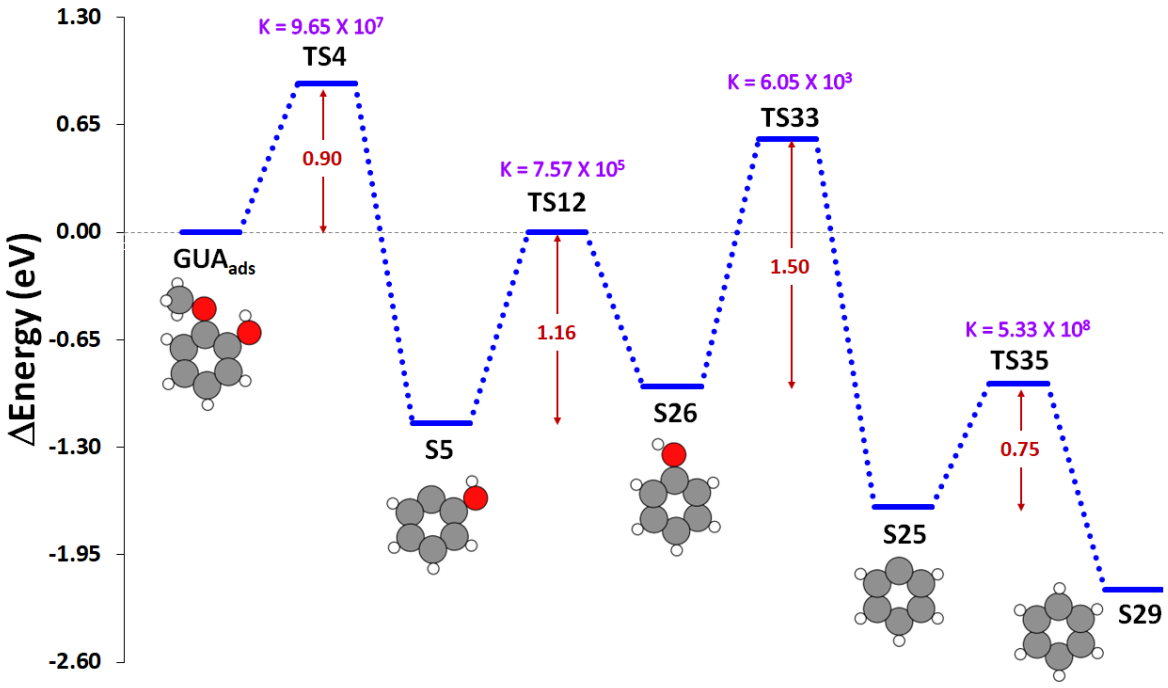

Figure 5.6.3: The reaction profile of the most favorable pathway of HDO of guaiacol over *β*-Mo_2C. The activation barrier for each step is given in red, in eV, and the rate constant of the conversion at 500 K is given in purple, in s^{-1}.

From S19/S22, protonation (R30) can yield phenol (S26/S10) in a very slow and energy demanding step (2.19 eV). The prohibitively high reaction barrier in R30 is in contradiction to experimental studies, which report high selectivity and quick appearance of phenol over pure and supported molybdenum carbides [78,240,241]. Therefore, phenol most likely forms by alternative route(s), of which two routes have been considered herein. One possibility is the direct methoxylation of guaiacol (R4, 0.90 eV) to give S5/S20, which is then followed by hydrogenation (R12, 1.16 eV). The other possibility considered is the protonation of guaiacol (R1) to form S2, which has an activation energy of 1.15 eV. The methoxy group can then directly cleave from S2 (R9) with a low activation energy of 0.37 eV producing phenol. R9 is kinetically very favorable, with a rate constant of 3.68×10^{12} s^{-1} at 500 K; however, S2 can also

convert to S9 through an activation energy of 0.75 eV, with the unstable CH_2 moiety in S9 leading to exothermic degradation (R21) to S17. The formation of S17 via R21 is kinetically favorable (2.45×10^{27} s^{-1} at 500 K) as the CH_2 radical dissociates, with a thermodynamic energy change of -1.94 eV. Protonation of S17 to S24/S21 (R29, E_a = 1.22 eV) results in a molecule that decomposes in a highly exothermic step (R31) to form phenol (-4.47 eV). Once formed, the desorption of phenol from the surface is kinetically slow (3.49×101 s^{-1} at 500 K) and energy demanding (E_{des} = 4.45 eV), which means it would be likely to accumulate on the surface. The adsorption energy, which can be calculated as the negative of the desorption energy, suggests that the adsorption of phenol on the surface is at least 2 eV stronger than that observed over transition metals [57,238,239,242,243].

The accumulated phenol can be converted to benzene, which is considered in two ways. One possibility is the cleavage of the –OH group (R33) with an energy barrier of 1.50 eV, while alternatively the phenol α-position can be protonated with an energy barrier of 2.06 eV to form S27 (R34). Kinetically, R34 is much slower than R33, with rate constants differing by ~10^3 s^{-1}. Therefore, the reaction will proceed via R33 to form S25, which will then be protonated to form benzene. The preference in our calculations towards dehydroxygenation of phenol rather than protonation is in strong agreement with observations involving noble metal catalysts [56,107,244], and in non-catalytic works [245].

The several smaller radicals formed during the outlined reaction mechanisms have been considered, as they will react together to form stable entities and desorb from the surface. In our work, R37 and R38 describe the formation of methane from CH_2; similarly, R40 and R41 describe the formation of methanol from OCH_2; and R39 describes the formation of water from OH and H. To comprehensively complete the catalytic cycle, R37 to R49 are used in the microkinetic modelling.

The overall activation energy for the formation of different important intermediates was also calculated as shown in Table 5.6.5. For the formation of benzene via reaction R4 – R12 – R33 and R35 show the activation energy to be 1.75 eV where reaction 33 is the rate limiting step. In the formation of catechol via reaction R5 – R15 and R16, the rate controlling step is found to be reaction R5, and the overall activation energy for the conversion is 1.02 eV. The formation of anisole via reaction R3 and R11 show the overall barrier to be 1.04 eV which is associated with the dehydroxylation of guaiacol in reaction R3. Finally, the conversion of guaiacol to phenol via reaction R1 and R9 is found to have an overall activation barrier of 1.15 eV during the hydrogenation of the adsorbed guaiacol.

Table 5.6.5: Overall activation barrier of the formation of benzene, catechol, anisole and phenol, and the corresponding pre-exponential factor.

Overall reaction	Considered path	Activation energy (eV)	Pre-exponential factor (s^{-1})
Formation of Benzene	R4-R12-R33-R35	1.75	6.48E+13
Formation of catechol	R5-R15-R16	1.02	2.26E+13
Formation of anisole	R3-R11	1.04	4.03E+13
Formation of phenol	R1-R9	1.15	4.47E+13

To summarise, the overall most favorable pathway for the formation of benzene is via cleavage of the methoxy group in guaiacol (R4) to give S5/S20, which is then protonated (R12) to give phenol (Figure 5.6.3). The hydroxyl group of the phenol is then cleaved (R33) with an energy barrier of 1.50 eV to yield S25, which is protonated to give benzene. All the reactions become faster with increase in temperature, except the guaiacol adsorption on the surface.

5.6.3 Microkinetic modelling

5.6.3.1 Batch-reactor model

Microkinetic modelling of the reaction network described in Section 5.6.2 has been performed, considering specifically a batch reactor model at temperatures ranging from 500 K to 700 K.

The rate constants obtained from the thermochemical analyses were used to write the rate equation for 184 elementary reactions (Annexure 1), and the set of coupled ordinary differential equations were solved. The initial ratio of hydrogen and guaiacol was set to unity, and in large excess with respect to the number of sites. The reaction profile was studied for the duration of 1 s from the initialization of the reaction (i.e. t = 0 s).

At 500 K, the concentration of guaiacol on the surface increases steeply at 0.02 s (Figure 5.6.4), as the guaiacol is adsorbed on the surface, to reach 1.45×10^{-18} ML (monolayer). During the same time interval, the concentration of surface bound phenol increases to about 28 times the concentration of the adsorbed guaiacol, suggesting that a large fraction of guaiacol immediately converts to phenol upon adsorption. The quick reaction occurs because the rate of formation of phenol is of the order 10^{12} s^{-1} in reaction 9 (Table 5.6.4), which leads to such high concentration of phenol forming in a short time interval. A corresponding increase of phenol is also observed in the gas phase, rising to 1.70×10^{-14} Pa in 0.02 s and maintaining a steady state thereafter. Since the catechol conversion kinetics competes with phenol formation, the catechol formation increases at an increasing rate to 4.71×10^{-29} ML at 0.36 s while the phenol conversion attains a steady state (1.64×10^{-17} ML) after 0.08 s. Hydrogenation of phenol produces benzene, which appears on the surface in a lower concentration (2.68×10^{-21} ML) as the kinetics of reaction 33 and 34 are much slower than phenol formation. Though, at 0.14 s, a sudden increase is noted in benzene's coverage. The gas phase concentration profile also shows an increase in the benzene at this time, suggesting higher desorption from the surface. As more catechol, phenol and benzene are produced, the concentration of guaiacol declines to 1.03×10^{-21} ML at 0.26 s; thereafter, the guaiacol starts to re-adsorb at the vacant surface sites formed by the desorption of the converted products, leading to a gradual increase in guaiacol surface concentration and attaining steady state near 0.5 s. All other species also achieve steady state after this time.

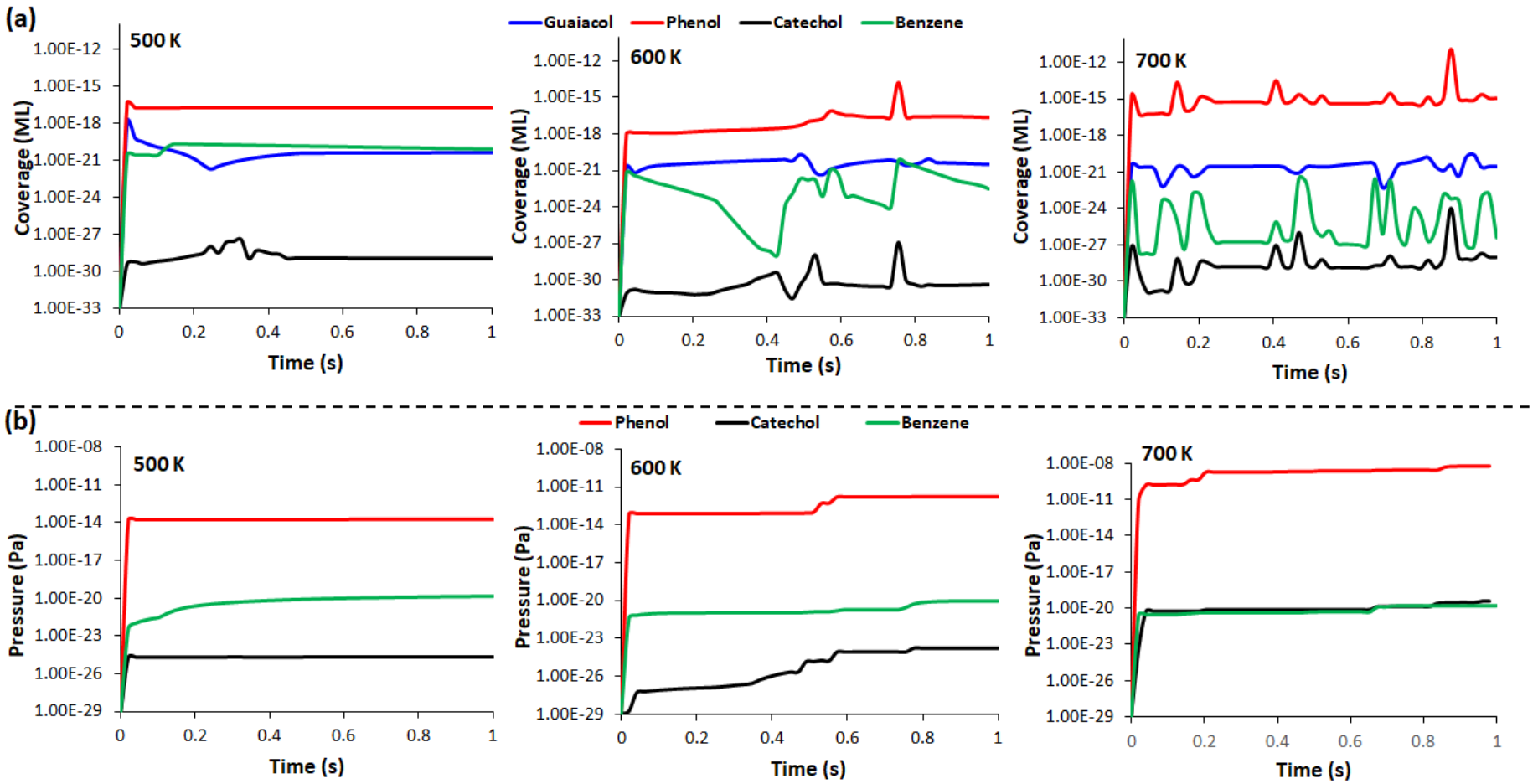

Figure 5.6.4: Plot of the concentration of guaiacol (blue), phenol (red), catechol (black) and benzene (green) (a) on the surface, and (b) in the gas phase at 500 K, 600 K and 700 K, for the reaction time of 1 s.

At 600 K, the concentration profile of all species exhibit more changes than at 500 K, due to the changes in the rate constants of all the reactions. As for 500 K, the concentration of phenol rises above that of guaiacol at 0.02 s; however, the coverage (1.09×10^{-18} ML) is marginally lower than at 500 K. The lower guaiacol adsorption rate is because the rate of adsorption decreases with increase in temperature. As less guaiacol adsorbs in the surface, the concentration of products formed is also lower; At 0.02 s, guaiacol coverage is slightly elevated to 2.00×10^{-21} ML, which then dips sharply at 0.04 s and rises back again at 0.1 s. While the dip in the guaiacol concentration was observed to be at 0.26 s at 500 K, the same is observed at 0.04 s at 600 K because the product formation and the desorption is faster at this temperature, due to higher reaction rates. The concentration of benzene is 6.70×10^{-22} ML at 0.02 s, due to quick phenol decomposition, but the concentration falls thereafter as the selectivity shifts towards catechol formation. After 0.26 s, the concentration of catechol starts to rise, resulting in a further decrease in the benzene concentration; however, the gas phase profile does not show any fluctuations in the benzene concentration at this time, suggesting that the rate of benzene desorption is much slower than the rate of formation of benzene on the surface. The concentration of catechol in gas phase increases at an increasing rate after 0.36 s, due to increased formation on the surface. After 0.4 s, as a result of the conversion of surface catechol to different products, the concentration of benzene and phenol begins to rise again. As more products are formed and desorbed from the surface, more guaiacol is adsorbed on the surface at 0.48 s. The adsorbed guaiacol again undergoes upgrading and the concentration peaks of all the products are again obtained thereafter. The gas phase profiles of all products also show an increased production of value-added products after 0.5 s.

The concentration profile of all the compounds shows a crest and trough pattern at 700 K throughout during the reaction. At 0.02 s, the concentration of guaiacol is expected to be lower than at lower T, due to decrease in the guaiacol adsorption rate constant (6.45×10^{-5} s^{-1}).

However, the concentration is 1.52×10^{-21} ML, which is higher than at 600 K. The higher surface coverage is because the reaction rate of almost all the reactions considered in the kinetic model increased at 700 K, leading to faster formation of products, and thus, faster desorption from the surface. The quicker rate of reaction recreates vacant surface sites in a short span of time than at lower T, and leads to a higher guaiacol adsorption. The higher product concentration observed in the gas phase at 0.02 s for 700 K, when compared to lower T, is the indicator of the quick desorption. From t=0 to t=0.28 s, the concentration profile follows a crest and trough pattern that is similar to that observed from t=0 to t=1 s at 600 K. After 0.28 s, the steady state is maintained till 0.38 s, from which time more products are desorbed from the surface, with more surface sites becoming available and subsequently resulting in higher phenol, catechol and benzene formation. The cycle of surface adsorption/desorption is repeated from 0.40 s to 0.68 s, and from 0.68 to 0.78; however, as more sites become occupied, the cycle time tends to get smaller and rapid product formation is observed near t=1 s, suggesting this temperature would provide maximum yield. Further analysis of the selectivity of products show that phenol will be the most likely product with over 99% selectivity at all times and at all temperatures. The concentration of other products is very low in comparison, over the surface and in the gas phase. In the literature [246], high selectivity of benzene (35%) followed by phenol (30%) is reported among all other aromatic/cyclic products over Mo_2C at 623 K and 27.48 bar. Tran *et al*. [247] report over 65 % selectivity for phenol at 50 bar pressure and 623 K temperature over activated carbon supported Mo, which also has strong similarities to our modelled reaction process. The high hydrogen pressure in the experimental work could be the likely reason for the reported high selectivity of benzene over phenol, as a high hydrogen pressure can hydrogenate the products to a greater extent. As the partial pressure of hydrogen is 0.5 in this study, high selectivity of phenol is obtained instead of full hydrogenation to benzene.

5.6.3.2 Temperature programmed desorption (TPD)

A temperature programmed desorption simulation was also conducted, where the initial guaiacol coverage on the catalyst surface was considered at 10 %, 40 %, 70 % and 100 %. The temperature of the system was increased at a rate of 10 K s^{-1}, and the concentration change of the species in the gas phase were recorded from 300 K to 700 K. No re-adsorption of the species was allowed during the analysis in line with the experimental procedure.

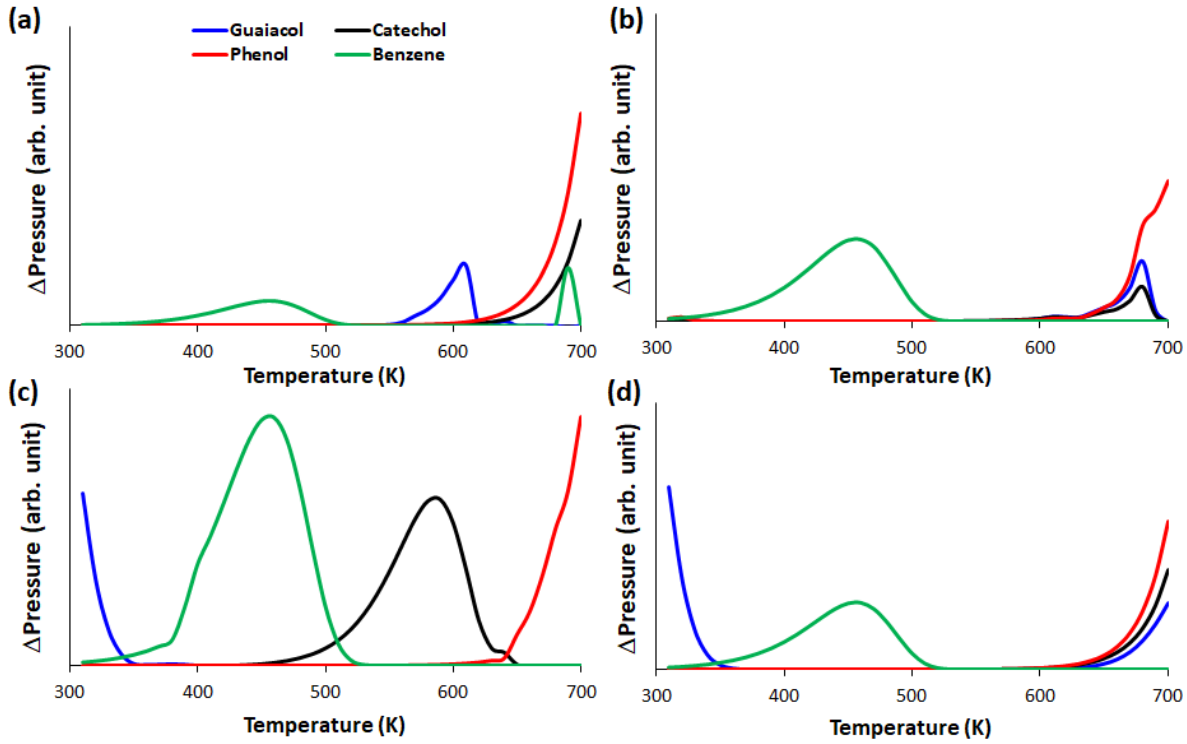

Figure 5.6.5: Change in concentration of guaiacol, catechol, phenol and benzene in gas phase shown in plot of change in partial pressure vs temperature for cases when the guaiacol coverages on the surface are (a) 10%, (b) 40%, (c) 70% and (d) 100%.

The TPD model shows that the desorption of benzene occurs near 450 K after it is produced from phenol at all coverage (Figure 5.6.5). Change in concentration of benzene is reported at temperatures above 250 K for a different surface (Pt and Pt_3Sn) at similar coverage [248], whilst, benzene is known to desorb at temperatures as low as 150 K from graphene [249]. Therefore, it is likely that the carbon-liking metal terminated surface investigated here binds

the benzene strongly to the surface [224]. Phenol on the other hand, stays on the surface till 600 K and starts desorbing thereafter. The desorption of phenol is known to occur at above 450 K at other surfaces [250–252]. At high coverage (70%), the desorption of benzene from the surface is large, as more benzene is formed on the surface from phenol. At the same coverage, catechol desorption is also observed in large proportion after 500K due to its formation and accumulation on the surface. Further increasing the guaiacol coverage (100%) is detrimental as the desorption rate of all species falls due to lack of sites for the generation of species on the surface.

CONCLUSIONS AND FUTURE SCOPE

6.1 Conclusions:

6.1.1 DFT Investigation on Thermochemical Analyses of Conversion of Xylose to Linear Alkanes in Aqueous Phase

In all the reaction scheme, it is observed that the reactions which involve saturation of furan ring present in the compounds are the most energy negative step. In RS 1, it is the FRN to THF conversion which involves saturation of two C=C bonds; in RS 2 it is the conversion of 2MF to MTHF, in RS 3 FF to THFOL conversion, in RS 4 MFK to 1,5-bis(tetrahydrofuran-2-yl)pentan-3-on and FA to SHD, and finally in RS 5, DHF to STHF; all these reactions had the saturation of C=C bond of the furan ring. In the scheme RS 4, the opening of the cyclic carbon atoms of SHD to produce TDC has the least energy requirement suggesting the SHD to be highly unstable in its form. It is observed that in general, Gibbs free energy change increases with increase in temperature for RS 5. For the rest of the schemes, it shows a mixed trend with the change in temperature. Also, the enthalpy change either decreases or remains almost constant with increase in temperature for all scheme. When aqueous phase results are compared with available gas phase data, it is observed that except XYL to FF conversion, all other conversions are more favorable in the aqueous phase by atleast 3 kcal/mol.

When the M06-2X and B3LYP functionals are compared with each other, it is observed that the absolute difference between the two functionals for thermochemical parameters is very small (≤ 2 kcal/mol) for ring opening reaction of saturated cyclic structures. On the other hand, the saturation step of cyclic structures has high absolute difference (≤ 10 kcal/mol) between the two functionals for free energy change and enthalpy change. When the absolute difference was very high (> 15 kcal/mol), both the functionals were compared with high accuracy methods (MP2 and G4MP2). It was observed that the absolute difference in the thermochemical

parameters was almost of the same magnitude. Therefore, large deviations are inevitable with B3LYP and M06-2X functionals and readers should be careful in selecting any particular functional. For simple molecules and saturated ring opening reactions, the difference between the two functionals are not large and hence both functionals can be interchangeably used for qualitative analysis. For the saturation step of cyclic structures, higher accuracy methods should be preferred. For all other reactions, M06-2X functional could be preferred due to its proven edge over other hybrid GGA functionals.

6.1.2 DFT Study on Dibenzofuran Conversion to Cyclohexane and Benzene in Gas, Water and Methanol Solvents

In the HDO of dibenzofuran in gas, water and methanol, it is observed that for most of the reactions, water is the best medium among the three whereas methanol shows better thermochemical parameters than the gas phase. However, water gives significantly better properties in few of the reactions such as –**a**–, –**c**– and –**n**–. The solvation free energy also suggests that the separation of products from water solvent would be easier than from the methanol solvent.

For the pathways, the upgrading of DBF is more likely to reach to completion via the saturation of phenyl ring to yield cyclohexane via pathway **-a-b-c-d-e**–/–**a-p-q-d-e-** over any other pathway. For this, lower temperature could be more favourable as the increase in temperature reduced the ln K for most of the reaction. It is also worth noting though that the harmonic oscillator and rigid rotor partition functions used in G09 are unlikely to be accurate near the high end of the studied temperature range.

It was also observed that, in general, the formation of single ring aromatics to be the most energy-intensive conversion for any pathway in all mediums. Whereas the saturation of

oxygenated intermediates such as reaction –**c**–, –**i**– and –**n**– was the least energy intensive conversion suggesting high reactivity of these intermediates.

6.1.3 Thermochemical Conversion of Guaiacol in Aqueous Phase by Density Functional Theory

Conversion of guaiacol to platform chemicals like o-cresol, toluene and benzene is studied in aqueous medium using M06-2X functional under the density functional theory framework. Several pathways are proposed for the conversion with important intermediates such as phenol, anisole, catechol and others. BDE analysis is conducted for guaiacol, phenol and anisole to understand scission of bonds of these compounds. The important conclusions of this study are as follows:

It is observed that BDE of bonds within the functional group is less energy demanding whereas the breakage of H˙ atoms from the 5th position in the ring have higher BDE.

In the proposed pathways, it is observed that conversion of guaiacol to phenol is most likely to occur by first hydrogenation of guaiacol followed by cleavage of ˙OCH_3. And the subsequent formation of benzene from phenol is most likely to occur *via* direct cleavage of hydroxyl group. Formation of anisole from guaiacol can most likely occur by protonation at $C_{aromatic}$-OH carbon followed by dehydroxylation. As per the reaction pathways discussed in this study, anisole is most likely to yield phenol.

1 It is evident that direct protonation of the model compound and intermediates is less energy demanding as compared to BDEs, and therefore are the favourable routes for conversion.

2 The thermochemistry is favourable for all conversions except reaction scheme **6a**, **6b** and **P1a**.

3 The overall thermochemistry also suggests the conversion of guaiacol to o-cresol to be the most favourable reaction with high spontaneity among all conversions.

4 Free energy change landscape of best reaction pathways shows the conversion of guaiacol to benzene to be kinetically most favourable with highest ΔG at 298 K, 20 atm condition for the rate controlling step.

5 In the free energy landscape of best reaction pathways, it is also observed that increase in pressure usually shifts the kinetics in unfavourable direction suggesting better spontaneity at lower pressures.

6.1.4 Computational Study on Adsorption Characteristics of Phenol and Guaiacol Over Single and Multiple Nitrogen Doped Graphene

In this study, the properties of nitrogen-doped graphene are studied using the density functional theory. Pristine graphene and pyridinic-like defect graphene are considered for doping with one nitrogen atom. In addition, a third surface is also prepared with three nitrogen-doped sites over a pristine graphene surface. The electronic properties of the surface are analysed to gain insight into the reactivity potential of the surface. The nitrogen doping disrupts the electronics of the pure graphene causing irregularity in the charge distribution, spin density, ESP and the molecular orbitals of the surface. It was also observed that the adjacent carbon atom of the doping site had high charge, rather than the doping itself. The adjoining carbon atoms were also found to have higher spin density than the nitrogen atom. Similarly, the electrostatic potential map showed that the region around the doping was neutral, except on the P1 surface. As the distance from the doping site increased, the surface became increasingly electronegative. The orbital analysis describes the HOMO and LUMO distribution over the surface. The adsorption of phenol and guaiacol was conducted over the identified locations on the surface, based on the charge distribution and spin density distribution. It was noted that for strong adsorption, either a high charge transfer or a strong delocalization of the charge on the surface is a necessary condition. Although the spin density distribution was found better on the adjacent carbon atoms of the nitrogen, the adsorption over the nitrogen atom via the phenyl

ring was the most favourable arrangement for both the molecules. Both Q1 and P1 were found to adsorb the molecules with almost similar E_{ads} as the difference between the E_{ads} of P1 and Q1 for the same molecule is within the DFT error margins. Guaiacol was found to adsorb more strongly than phenol. The dipole change was greater for guaiacol than phenol as the guaiacol contains two polar functional groups compared to phenol with only one polar functional group. The increase in the nitrogen doping altered the electronics of the surface to a greater degree than single doping.

6.1.5 Dehydrogenation and Dehydration of Formic Acid over Orthorhombic Molybdenum Carbide

The dehydration and dehydrogenation of formic acid is studied on the β-Mo_2C catalyst surface using density functional theory. Different orientations of formic acid, CO, CO_2 and H_2O are adsorbed on the surface at different surface sites to determine the most stable orientation and site for each molecule. The most stable structures are used to study the dehydration and dehydrogenation pathways of the conversion and the thermochemistry is analysed. Thermodynamically, it was observed that the conversion of the HCOOH is most likely to proceed by the breaking of H-COOH bond to yield CO as the end product (dehydration); however, the desorption energy for CO from the surface is very high (5.75 eV), which suggests that the surface is highly susceptible to CO poisoning.

Microkinetic analyses were also conducted for the batch reactor model and product distributions were calculated up to for 1 second between 300 to 500 K. The adsorption kinetics of formic acid were observed as very slow over the surface. As a result, much of the surface sites were vacant and the conversion inefficient. The concentration profile shows that the appearance of CO_2 will be kinetically faster than CO in the gas phase. The formation of CO will saturate the surface as the CO desorption step is very slow, and therefore rate limiting.

TPD analysis is also conducted to determine the concentration of different gas species in the system with increasing temperature and increasing concentration of adsorbed formic acid. At 10% and 40% formic acid coverage, HCOOH conversion occurs at low temperatures; CO_2 desorption is most favourable at 320 K, reaching a steady state at 370 K. All other species start desorbing from the surface after 400 K.

6.1.6 Hydrodeoxygenation of Guaiacol Over Orthorhombic Molybdenum Carbide: A DFT and Microkinetic Study

The HDO of guaiacol was studied over the (100) β-Mo_2C surface. A network of reaction pathways was proposed to produce benzene from guaiacol via phenol and catechol intermediates. The activation barriers and reaction energies were calculated using density functional theory. Through thermochemical analysis, increase in temperature was observed as not being very favorable for the adsorption of guaiacol on the surface. The most favourable pathway for guaiacol HDO is initiated with demethoxylation, which is the followed by hydrogenation to yield phenol. From phenol, the most favourable pathway for benzene formation is initiated with dehydroxylation, followed by protonation.

Overall, the protonation of molecules like guaiacol and phenol were observed to have higher energy barriers than the cleavage of functional groups. The carbon atoms of the functional group of the molecule, which were *sp2* or *sp* hybridized, were also noted as dissociating spontaneously, with minimum energy barriers, and the dissociated moieties occupy carbon deficient sites on the surface.

The microkinetic modelling of the system shows that, although the adsorption of guaiacol decreases with increase in temperature, higher temperatures are more favorable for further upgrading of guaiacol into valuable products such as phenol and benzene. The

temperature programmed desorption showed that the optimum surface coverage of guaiacol is ~70%, as the change in the concentration of all the products was highest in the gas phase.

6.2 Future Scope

In this study, it was observed that solvents had a favourable effect on the bio-oil upgrading in terms of thermochemistry and kinetics of the reactions occurring. However, this study only tested ethanol, in addition to water as a medium implicitly in the system. Therefore, further understanding of the solvation effects are required in an explicit model setting to determine the true mechanism occurring during the upgrading in solvents. Further, the future study could consider a hybrid system (also sometimes referred to as microsolvation model), where the solvent effects are incorporated by considering explicit water molecule, along with the polarized continuum implicitly. Such systems could be more accurate than implicit or explicit system alone.

In the second objective of the study, it was observed that the nitrogen-doping improved the adsorption properties of the model compounds when compared to the pristine graphene. However, it still could not facilitate a chemisorption of the model compounds on the surface. Therefore, the nitrogen-doped graphene could be further doped with metal or non-metal atoms to promote the catalytic properties of the material. Doping with minimal noble metal atoms may result in superior chemically modified graphene at a relatively lower cost, and could be a very exciting study. In addition, the metal carbides exhibited excellent catalytic performance in this study, but were susceptible to poisoning. Thus further doping the carbides to obtain a ternary or quaternary system could be explored to alleviate the shortcomings of such systems.

[1] T. Wang, Q. Luo, Y.W. Li, J. Wang, M. Beller, H. Jiao, Stable surface terminations of orthorhombic Mo2C catalysts and their CO activation mechanisms, Appl. Catal. A Gen. 478 (2014) 146–156. https://doi.org/10.1016/j.apcata.2014.03.042.

[2] M. Re Fiorentin, R. Gaspari, M. Quaglio, G. Massaglia, G. Saracco, Nitrogen doping and CO2 adsorption on graphene: A thermodynamical study, Phys. Rev. B. 97 (2018) 155428. https://doi.org/10.1103/PhysRevB.97.155428.

[3] J.P. Perdew, K. Burke, M. Ernzerhof, Generalized Gradient Approximation Made Simple, Phys. Rev. Lett. 77 (1996) 3865–3868. https://doi.org/10.1103/PhysRevLett.77.3865.

[4] J.P. Perdew, K. Burke, M. Ernzerhof, Generalized Gradient Approximation Made Simple [Phys. Rev. Lett. 77, 3865 (1996)], Phys. Rev. Lett. 78 (1997) 1396–1396. https://doi.org/10.1103/PhysRevLett.78.1396.

[5] Y. Zhao, D.G. Truhlar, A new local density functional for main-group thermochemistry, transition metal bonding, thermochemical kinetics, and noncovalent interactions, J. Chem. Phys. 125 (2006) 194101. https://doi.org/10.1063/1.2370993.

[6] J.P. Perdew, M. Ernzerhof, K. Burke, Rationale for mixing exact exchange with density functional approximations, J. Chem. Phys. 105 (1996) 9982–9985. https://doi.org/10.1063/1.472933.

[7] C. Adamo, V. Barone, Toward reliable density functional methods without adjustable parameters: The PBE0 model, J. Chem. Phys. 110 (1999) 6158–6170. https://doi.org/10.1063/1.478522.

[8] A.D. Becke, A new mixing of Hartree–Fock and local density-functional theories, J. Chem. Phys. 98 (1993) 1372–1377. https://doi.org/10.1063/1.464304.

[9] M. Chase, NIST-JANAF Thermochemical Tables, 4th Edition, J. Phys. Chem. Ref. Data,

Monogr. 9. (1998).

[10] J. Chao, K.R. Hall, K.N. Marsh, R.C. Wilhoit, Thermodynamic Properties of Key Organic Oxygen Compounds in the Carbon Range C1 to C4. Part 2. Ideal Gas Properties, J. Phys. Chem. Ref. Data. (1986). https://doi.org/10.1063/1.555769.

[11] Joint science academies' statement : Global response to climate change, (2005) 3–4. https://royalsociety.org/~/media/Royal_Society_Content/policy/publications/2005/9649.pdf.

[12] OECD/IEA, Global Energy & CO2 Status Report, Glob. Energy CO2 Status Rep. (2018) 1–15. http://www.iea.org/publications/freepublications/publication/GECO2017.pdf%0Ahttps://www.iea.org/publications/freepublications/publication/GECO2017.pdf.

[13] Eurostat, Energy statistics, 2018 (2017). http://admin.indiaenvironmentportal.org.in/files/file/Energy_Statistics_2018.pdf%0Ahttp://ec.europa.eu/eurostat/.

[14] R.W. Jenkins, C.M. Moore, T.A. Semelsberger, C.J. Chuck, J.C. Gordon, A.D. Sutton, The Effect of Functional Groups in Bio-Derived Fuel Candidates, ChemSusChem. 9 (2016) 922–931. https://doi.org/10.1002/cssc.201600159.

[15] V. Loo, Biomass for renewable energy, III (2002) 611–630.

[16] G.W. Huber, S. Iborra, A. Corma, Synthesis of transportation fuels from biomass: Chemistry, catalysts, and engineering, Chem. Rev. 106 (2006) 4044–4098. https://doi.org/10.1021/cr068360d.

[17] D.G. Christian, Biomass for Renewable Energy, Fuels, and Chemicals, J. Environ. Qual. 29 (2000) 193–212. https://doi.org/10.2134/jeq2000.00472425002900020040x.

[18] L. Petrus, M.A. Noordermeer, Biomass to biofuels, a chemical perspective, Green Chem. 8 (2006) 861. https://doi.org/10.1039/b605036k.

[19] P.M. Mortensen, J.D. Grunwaldt, P.A. Jensen, K.G. Knudsen, A.D. Jensen, A review of catalytic upgrading of bio-oil to engine fuels, Appl. Catal. A Gen. 407 (2011) 1–19. https://doi.org/10.1016/j.apcata.2011.08.046.

[20] A.R.K. Gollakota, M. Reddy, M.D. Subramanyam, N. Kishore, A review on the upgradation techniques of pyrolysis oil, Renew. Sustain. Energy Rev. 58 (2016) 1543–1568. https://doi.org/10.1016/j.rser.2015.12.180.

[21] A. V. Bridgwater, Review of fast pyrolysis of biomass and product upgrading, Biomass and Bioenergy. 38 (2012) 68–94. https://doi.org/10.1016/j.biombioe.2011.01.048.

[22] C.J. Cramer, Essentials of Computational Chemistry, Theories and Models, Wiley, 2004. https://www.wiley.com/en-us/Essentials+of+Computational+Chemistry%3A+Theories+and+Models%2C+2nd+Edition-p-9780470091821.

[23] J.B. Foresman, A. Frisch, Exploring Chemistry With Electronic Structure Methods.pdf, Explor. Chem. with Electron. Struct. Methods. (1996). https://doi.org/10.1002/adma.200400767.

[24] E.M. Rubin, Genomics of cellulosic biofuels, Nature. 454 (2008) 841–845. https://doi.org/10.1038/nature07190.

[25] G.W. Huber, I. Sara, A. Corma, Synthesis of Transportation Fuels from Biomass, Chem Rev. 2 (2006) 4044–4098. https://doi.org/10.1021/cr068360d.

[26] D.M. Alonso, J.Q. Bond, J.A. Dumesic, Catalytic conversion of biomass to biofuels, Green Chem. 12 (2010) 1493. https://doi.org/10.1039/c004654j.

[27] M. Stöcker, Biofuels and biomass-to-liquid fuels in the biorefinery: Catalytic conversion of lignocellulosic biomass using porous materials, Angew. Chemie - Int. Ed. 47 (2008) 9200–9211. https://doi.org/10.1002/anie.200801476.

[28] D. Wen, H. Jiang, K. Zhang, Supercritical fluids technology for clean biofuel production,

Prog. Nat. Sci. 19 (2009) 273–284. https://doi.org/10.1016/j.pnsc.2008.09.001.

[29] G.W. Huber, S. Iborra, A. Corma, Synthesis of transportation fuels from biomass: Chemistry, catalysts, and engineering, Chem. Rev. 106 (2006) 4044–4098. https://doi.org/10.1021/cr068360d.

[30] W. Mu, H. Ben, A. Ragauskas, Y. Deng, Lignin Pyrolysis Components and Upgrading-Technology Review, Bioenergy Res. 6 (2013) 1183–1204. https://doi.org/10.1007/s12155-013-9314-7.

[31] H. Wang, J. Male, Y. Wang, Recent Advances in Hydrotreating of Pyrolysis Bio-Oil and Its Oxygen-Containing Model Compounds, ACS Catal. 3 (2013) 1047–1070. https://doi.org/10.1021/cs400069z.

[32] J.N. Bowden, s, (1980). https://www.osti.gov/biblio/6922973.

[33] E. Furimsky, Chemistry of Catalytic Hydrodeoxygenation, Catal. Rev. 25 (1983) 421–458. https://doi.org/10.1080/01614948308078052.

[34] F. Fischer, H. Schrader, Über die Umwandlung der Kohle in Öle durch Hydrierung. II. Hydrierung von Kohlen durch Kohlenoxyd, Brennstof-Chem. 2 (1921) 255–261.

[35] E. Furimsky, Catalytic removal of sulfur, nitrogen, and oxygen from heavy gas oil, AIChE J. 25 (1979) 306–311. https://doi.org/10.1002/aic.690250213.

[36] D.C. Elliott, E.G. Baker, Upgrading biomass liquefaction products through hydrodeoxygenation, (1984). https://www.osti.gov/biblio/7124643.

[37] E. Furimsky, Catalytic hydrodeoxygenation, Appl. Catal. A Gen. 199 (2000) 147–190. https://doi.org/10.1016/S0926-860X(99)00555-4.

[38] J.D. Adjaye, N.N. Bakhshi, Production of hydrocarbons by catalytic upgrading of a fast pyrolysis bio-oil. Part I: Conversion over various catalysts, Fuel Process. Technol. 45 (1995) 161–183. https://doi.org/10.1016/0378-3820(95)00034-5.

[39] U. V. Mentzel, M.S. Holm, Utilization of biomass: Conversion of model compounds to

hydrocarbons over zeolite H-ZSM-5, Appl. Catal. A Gen. 396 (2011) 59–67. https://doi.org/10.1016/j.apcata.2011.01.040.

[40] D.D. Das, M.I. Schnitzer, C.M. Monreal, P. Mayer, Chemical composition of acid-base fractions separated from biooil derived by fast pyrolysis of chicken manure, Bioresour. Technol. 100 (2009) 6524–6532. https://doi.org/10.1016/j.biortech.2009.06.104.

[41] A.T. Madsen, E.H. Ahmed, C.H. Christensen, R. Fehrmann, A. Riisager, Hydrodeoxygenation of waste fat for diesel production: Study on model feed with Pt/alumina catalyst, Fuel. 90 (2011) 3433–3438. https://doi.org/https://doi.org/10.1016/j.fuel.2011.06.005.

[42] H.J. Park, K.H. Park, J.K. Jeon, J. Kim, R. Ryoo, K.E. Jeong, S.H. Park, Y.K. Park, Production of phenolics and aromatics by pyrolysis of miscanthus, Fuel. 97 (2012) 379–384. https://doi.org/10.1016/j.fuel.2012.01.075.

[43] L.D. Rollmann, Catalytic hydrogenation of model nitrogen, sulfur, and oxygen compounds, J. Catal. 46 (1977) 243–252. https://doi.org/10.1016/0021-9517(77)90206-8.

[44] E. Laurent, B. Delmon, A Study of the hydrodeoxygenation of carbonyl , carboxylic and guaiacyl groups over sulfided CoMo / y-A1203 and NiMo / 3 / -A1203 catalysts . I . Catalytic reaction schemes, 109 (1994) 77–96.

[45] A. Popov, E. Kondratieva, J. Gilson, L. Mariey, A. Travert, F. Maugé, IR study of the interaction of phenol with oxides and sulfided CoMo catalysts for bio-fuel hydrodeoxygenation, Catal. Today. 172 (2011) 132–135. https://doi.org/10.1016/j.cattod.2011.02.010.

[46] F.E. Massoth, P. Politzer, M.C. Concha, J.S. Murray, J. Jakowski, J. Simons, Catalytic Hydrodeoxygenation of Methyl-Substituted Phenols: Correlations of Kinetic Parameters with Molecular Properties, J. Phys. Chem. B. 110 (2006) 14283–14291.

https://doi.org/10.1021/jp057332g.

[47] E.M. Ryymin, M.L. Honkela, T.R. Viljava, A.O.I. Krause, Competitive reactions and mechanisms in the simultaneous HDO of phenol and methyl heptanoate over sulphided NiMo/γ-Al2O3, Appl. Catal. A Gen. 389 (2010) 114–121. https://doi.org/10.1016/j.apcata.2010.09.010.

[48] W. Baldauf, U. Balfanz, M. Rupp, Upgrading of flash pyrolysis oil and utilization in refineries, Biomass and Bioenergy. 7 (1994) 237–244. https://doi.org/https://doi.org/10.1016/0961-9534(94)00065-2.

[49] Y.-H.E. Sheu, R.G. Anthony, E.J. Soltes, Kinetic studies of upgrading pine pyrolytic oil by hydrotreatment, Fuel Process. Technol. 19 (1988) 31–50. https://doi.org/10.1016/0378-3820(88)90084-7.

[50] A. Gutierrez, R.K. Kaila, M.L. Honkela, R. Slioor, A.O.I. Krause, Hydrodeoxygenation of guaiacol on noble metal catalysts, Catal. Today. 147 (2009) 239–246. https://doi.org/10.1016/j.cattod.2008.10.037.

[51] Y. Xu, T. Wang, L. Ma, G. Chen, Upgrading of fast pyrolysis liquid fuel from biomass over Ru/γ-Al2O3catalyst, Energy Convers. Manag. 55 (2012) 172–177. https://doi.org/10.1016/j.enconman.2011.10.016.

[52] J. Gagnon, S. Kaliaguine, Catalytic Hydrotreatment of Vacuum Pyrolysis Oils from Wood, Ind. Eng. Chem. Res. 27 (1988) 1783–1788. https://doi.org/10.1021/ie00082a008.

[53] J. Payormhorm, K. Kangvansaichol, P. Reubroycharoen, P. Kuchonthara, N. Hinchiranan, Pt/Al2O3-catalytic deoxygenation for upgrading of Leucaena leucocephala-pyrolysis oil, Bioresour. Technol. 139 (2013) 128–135. https://doi.org/10.1016/j.biortech.2013.04.023.

[54] Y.K. Hong, D.W. Lee, H.J. Eom, K.Y. Lee, The catalytic activity of Pd/WOx/γ-

Al2O3for hydrodeoxygenation of guaiacol, Appl. Catal. B Environ. 150–151 (2014) 438–445. https://doi.org/10.1016/j.apcatb.2013.12.045.

[55] C. Chiu, A. Genest, A. Borgna, N. Rösch, Hydrodeoxygenation of Guaiacol over Ru(0001): A DFT Study, ACS Catal. 4 (2014) 4178–4188. https://doi.org/10.1021/cs500911j.

[56] J. Lu, A. Heyden, Theoretical investigation of the reaction mechanism of the hydrodeoxygenation of guaiacol over a Ru(0 0 0 1) model surface, J. Catal. 321 (2015) 39–50. https://doi.org/10.1016/j.jcat.2014.11.003.

[57] A.M. Verma, N. Kishore, Molecular Modelling Approach to Elucidate Gas Phase Hydrodeoxygenation of Guaiacol over Pd(111) Catalyst within DFT framework, J. Mol. Model. (2018). https://doi.org/10.1007/s00894-018-3803-8.

[58] K. Lee, G.H. Gu, C.A. Mullen, A.A. Boateng, D.G. Vlachos, Guaiacol hydrodeoxygenation mechanism on Pt(111): Insights from density functional theory and linear free energy relations, ChemSusChem. 8 (2015) 315–322. https://doi.org/10.1002/cssc.201402940.

[59] G. Li, J. Han, H. Wang, X. Zhu, Q. Ge, Role of dissociation of phenol in its selective hydrogenation on Pt(111) and Pd(111), ACS Catal. 5 (2015) 2009–2016. https://doi.org/10.1021/cs501805y.

[60] F. Liu, M. Wang, Y. Chen, J. Gao, Thermal stability of graphene in inert atmosphere at high temperature, J. Solid State Chem. 276 (2019) 100–103. https://doi.org/10.1016/j.jssc.2019.04.008.

[61] G. Wei, Y.E. Miao, C. Zhang, Z. Yang, Z. Liu, W.W. Tjiu, T. Liu, Ni-doped graphene/carbon cryogels and their applications as versatile sorbents for water purification, ACS Appl. Mater. Interfaces. 5 (2013) 7584–7591. https://doi.org/10.1021/am401887g.

[62] L. Gao, W. Yue, S. Tao, L. Fan, Novel strategy for preparation of graphene-Pd, Pt composite, and its enhanced electrocatalytic activity for alcohol oxidation, Langmuir. 29 (2013) 957–964. https://doi.org/10.1021/la303663x.

[63] M. Giovanni, H.L. Poh, A. Ambrosi, G. Zhao, Z. Sofer, F. Šaněk, B. Khezri, R.D. Webster, M. Pumera, Noble metal (Pd, Ru, Rh, Pt, Au, Ag) doped graphene hybrids for electrocatalysis, Nanoscale. 4 (2012) 5002–5008. https://doi.org/10.1039/c2nr31077e.

[64] X.Y. Xu, J. Li, H. Xu, X. Xu, C. Zhao, DFT investigation of Ni-doped graphene: Catalytic ability to CO oxidation, New J. Chem. 40 (2016) 9361–9369. https://doi.org/10.1039/c6nj00924g.

[65] B. Wanno, C. Tabtimsai, A DFT investigation of CO adsorption on VIIIB transition metal-doped graphene sheets, Superlattices Microstruct. 67 (2014) 110–117. https://doi.org/10.1016/j.spmi.2013.12.025.

[66] M.J. López, I. Cabria, J.A. Alonso, Palladium clusters anchored on graphene vacancies and their effect on the reversible adsorption of hydrogen, J. Phys. Chem. C. 118 (2014) 5081–5090. https://doi.org/10.1021/jp410262t.

[67] A.M. Verma, K. Agrawal, N. Kishore, Binding of phenolic model compounds with noble metal doped graphene sheets, Comput. Theor. Chem. 1134 (2018) 37–46. https://doi.org/10.1016/j.comptc.2018.05.001.

[68] M. Kunaseth, P. Poldorn, A. Junkeaw, J. Meeprasert, C. Rungnim, S. Namuangruk, N. Kungwan, C. Inntam, S. Jungsuttiwong, A DFT study of volatile organic compounds adsorption on transition metal deposited graphene, Appl. Surf. Sci. 396 (2017) 1712–1718. https://doi.org/10.1016/j.apsusc.2016.11.238.

[69] L.S. Panchakarla, K.S. Subrahmanyam, S.K. Saha, A. Govindaraj, H.R. Krishnamurthy, U. V. Waghmare, C.N.R. Rao, Synthesis, structure, and properties of boron- and nitrogen-doped graphene, Adv. Mater. 21 (2009) 4726–4730.

https://doi.org/10.1002/adma.200901285.

[70] A. Ghosh, D.J. Late, L.S. Panchakarla, A. Govindaraj, C.N.R. Rao, NO 2 and humidity sensing characteristics of few-layer graphenes, J. Exp. Nanosci. 4 (2009) 313–322. https://doi.org/10.1080/17458080903115379.

[71] D. Wei, Y. Liu, Y. Wang, H. Zhang, L. Huang, G. Yu, Synthesis of n-doped graphene by chemical vapor deposition and its electrical properties, Nano Lett. 9 (2009) 1752–1758. https://doi.org/10.1021/nl803279.

[72] C. Zhang, L. Fu, N. Liu, M. Liu, Y. Wang, Z. Liu, Synthesis of nitrogen-doped graphene using embedded carbon and nitrogen sources, Adv. Mater. 23 (2011) 1020–1024. https://doi.org/10.1002/adma.201004110.

[73] B. Guo, Q. Liu, E. Chen, H. Zhu, L. Fang, J.R. Gong, Controllable N-doping of graphene, Nano Lett. 10 (2010) 4975–4980. https://doi.org/10.1021/nl103079j.

[74] D. Golberg, Y. Bando, L. Bourgeois, K. Kurashima, T. Sato, Large-scale synthesis and HRTEM analysis of single-walled B- and N-doped carbon nanotube bundles, Carbon N. Y. 38 (2000) 2017–2027. https://doi.org/10.1016/S0008-6223(00)00058-0.

[75] B. Hammer, J.K. Norskov, Why gold is the noblest of all the metals, Nature. 376 (1995) 238–240. https://doi.org/10.1038/376238a0.

[76] J.K. Norskov, F. Abild-Pedersen, F. Studt, T. Bligaard, Density functional theory in surface chemistry and catalysis, Proc. Natl. Acad. Sci. 108 (2011) 937–943. https://doi.org/10.1073/pnas.1006652108.

[77] R.B. Levy, M. Boudart, Platinum-Like Behavior of Tungsten Carbide in Surface Catalysis, Science (80-.). 181 (1973) 547–549. https://doi.org/10.1126/science.181.4099.547.

[78] R. Moreira, E. Ochoa, J.L. Pinilla, A. Portugal, I. Suelves, Liquid-phase hydrodeoxygenation of guaiacol over Mo2C supported on commercial CNF. Effects of

operating conditions on conversion and product selectivity, Catalysts. 8 (2018). https://doi.org/10.3390/catal8040127.

[79] H. Fang, A. Roldan, C. Tian, Y. Zheng, X. Duan, K. Chen, L. Ye, S. Leoni, Y. Yuan, Structural tuning and catalysis of tungsten carbides for the regioselective cleavage of C-O bonds, J. Catal. 369 (2019) 283–295. https://doi.org/10.1016/j.jcat.2018.11.020.

[80] J.-S. Choi, G. Bugli, G. Djéga-Mariadassou, Influence of the Degree of Carburization on the Density of Sites and Hydrogenating Activity of Molybdenum Carbides, J. Catal. 193 (2000) 238–247. https://doi.org/10.1006/jcat.2000.2894.

[81] A.J. Ragauskas, C.K. Williams, B.H. Davison, G. Britovsek, J. Cairney, C.A. Eckert, W.J. Frederick Jr., J.P. Hallett, D.J. Leak, C.L. Liotta, J.R. Mielenz, R. Murphy, R. Templer, T. Tschaplinski, The Path Forward for Biofuels and Biomaterials, Science (80-.). 311 (2006) 484–489. https://doi.org/10.1126/science.1114736.

[82] R.A. LeCouteur, Handbook of Pulp, Wiley-VCH Verlag GmbH, Weinheim, Germany, 2006. https://doi.org/10.1002/9783527619887.

[83] V. Choudhary, S.I. Sandler, D.G. Vlachos, Conversion of xylose to furfural using Lewis and Bronsted acid catalysts in aqueous media, ACS Catal. 2 (2012) 2022–2028. https://doi.org/10.1021/cs300265d.

[84] W. Zhang, Catalytic conversion of sugar mixtures into furan products in ionic liquid media with organic solvent extraction, The University of Toledo, 2012. http://utdr.utoledo.edu/cgi/viewcontent.cgi?article=1512&context=theses-dissertations.

[85] I. Agirrezabal-Telleria, Y. Guo, F. Hemmann, P.L. Arias, E. Kemnitz, Dehydration of xylose and glucose to furan derivatives using bifunctional partially hydroxylated MgF2 catalysts and N2 stripping, Catal. Sci. Technol. 4 (2014) 1357–1368. https://doi.org/10.1039/C4CY00129J.

[86] B. Pholjaroen, N. Li, J. Yang, G. Li, W. Wang, A. Wang, Y. Cong, X. Wang, T. Zhang,

Production of renewable jet fuel range branched alkanes with xylose and methyl isobutyl ketone, Ind. Eng. Chem. Res. 53 (2014) 13618–13625. https://doi.org/10.1021/ie5016365.

[87] R. Xing, A. V. Subrahmanyam, H. Olcay, W. Qi, G.P. van Walsum, H. Pendse, G.W. Huber, Production of jet and diesel fuel range alkanes from waste hemicellulose-derived aqueous solutions, Green Chem. 12 (2010) 1933. https://doi.org/10.1039/c0gc00263a.

[88] B. Op de Beeck, M. Dusselier, J. Geboers, J. Holsbeek, E. Morré, S. Oswald, L. Giebeler, B.F. Sels, Direct catalytic conversion of cellulose to liquid straight-chain alkanes, Energy Environ. Sci. 8 (2015) 230–240. https://doi.org/10.1039/C4EE01523A.

[89] Y. Osaka, Y. Ikeda, D. Hashizume, M. Iwamoto, Direct hydrodeoxygenation of cellulose and xylan to lower alkanes on ruthenium catalysts in subcritical water, Biomass and Bioenergy. 56 (2013) 1–7. https://doi.org/10.1016/j.biombioe.2013.04.012.

[90] G.W. Huber, J.N. Chheda, C.J. Barrett, J.A. Dumesic, Production of Liquid Alkanes by Aqueous-Phase Processing of Biomass-Derived Carbohydrates, Science (80-.). 308 (2005) 1446–1450. https://doi.org/10.1126/science.1111166.

[91] C. Liu, R.S. Assary, L.A. Curtiss, Investigation of thermochemistry associated with the carbon-carbon coupling reactions of furan and furfural using ab initio methods, J. Phys. Chem. A. 118 (2014) 4392–4404. https://doi.org/10.1021/jp503702t.

[92] A.M. Verma, N. Kishore, Thermochemistry analyses for transformation of C6 glucose compound into C9, C12 and C15 alkanes using density functional theory, Mol. Phys. 115 (2017) 413–423. https://doi.org/10.1080/00268976.2016.1269962.

[93] S. Krishnamurthy, S. Panvelker, Y.T. Shah, Hydrodeoxygenation of dibenzofuran and related compounds, AIChE J. 27 (1981) 994–1001. https://doi.org/10.1002/aic.690270616.

[94] L. Wang, H. Wan, S. Jin, X. Chen, C. Li, C. Liang, Hydrodeoxygenation of dibenzofuran

over SiO2, Al2O3/SiO2 and ZrO2/SiO2 supported Pt catalysts, Catal. Sci. Technol. 5 (2015) 465–474. https://doi.org/10.1039/c4cy00859f.

[95] H.W. Lee, B.R. Jun, H. Kim, D.H. Kim, J.K. Jeon, S.H. Park, C.H. Ko, T.W. Kim, Y.K. Park, Catalytic hydrodeoxygenation of 2-methoxy phenol and dibenzofuran over Pt/mesoporous zeolites, Energy. 81 (2015) 33–40. https://doi.org/10.1016/j.energy.2014.11.058.

[96] J.A. Cecilia, A. Infantes-Molina, E. Rodríguez-Castellón, A. Jiménez-López, S.T. Oyama, Oxygen-removal of dibenzofuran as a model compound in biomass derived bio-oil on nickel phosphide catalysts: Role of phosphorus, Appl. Catal. B Environ. 136–137 (2013) 140–149. https://doi.org/10.1016/j.apcatb.2013.01.047.

[97] M. Altarawneh, E.M. Kennedy, B.Z. Dlugogorski, J.C. Mackie, Computational study of the oxidation and decomposition of dibenzofuran under atmospheric conditions, J. Phys. Chem. A. 112 (2008) 6960–6967. https://doi.org/10.1021/jp800093j.

[98] P. Dong, G.P. Lu, C. Cai, Effective hydrodeoxygenation of dibenzofuran by a bimetallic catalyst in water, New J. Chem. 40 (2016) 1605–1609. https://doi.org/10.1039/c5nj02164b.

[99] M. Zhou, Y. Wang, Y. Wang, G. Xiao, Catalytic conversion of guaiacol to alcohols for bio-oil upgrading, J. Energy Chem. 24 (2015) 425–431. https://doi.org/10.1016/j.jechem.2015.06.012.

[100] M. V. Bykova, O.A. Bulavchenko, D.Y. Ermakov, M.Y. Lebedev, V.A. Yakovlev, V.N. Parmon, Guaiacol hydrodeoxygenation in the presence of Ni-containing catalysts, Catal. Ind. 3 (2011) 15–22. https://doi.org/10.1134/S2070050411010028.

[101] M. V. Bykova, S.G. Zavarukhin, L.I. Trusov, V.A. Yakovlev, Guaiacol hydrodeoxygenation kinetics with catalyst deactivation taken into consideration, Kinet. Catal. 54 (2013) 40–48. https://doi.org/10.1134/S0023158413010023.

[102] V.N. Bui, D. Laurenti, P. Afanasiev, C. Geantet, Hydrodeoxygenation of guaiacol with CoMo catalysts. Part I: Promoting effect of cobalt on HDO selectivity and activity, Appl. Catal. B Environ. 101 (2011) 239–245. https://doi.org/10.1016/j.apcatb.2010.10.025.

[103] V.N. Bui, D. Laurenti, P. Delichère, C. Geantet, Hydrodeoxygenation of guaiacol. Part II: Support effect for CoMoS catalysts on HDO activity and selectivity, Appl. Catal. B Environ. 101 (2011) 246–255. https://doi.org/10.1016/j.apcatb.2010.10.031.

[104] E.A. Roldugina, E.R. Naranov, A.L. Maximov, E.A. Karakhanov, Hydrodeoxygenation of guaiacol as a model compound of bio-oil in methanol over mesoporous noble metal catalysts, Appl. Catal. A Gen. 553 (2018) 24–35. https://doi.org/10.1016/j.apcata.2018.01.008.

[105] Wahyudiono, M. Sasaki, M. Goto, Thermal decomposition of guaiacol in sub- and supercritical water and its kinetic analysis, J. Mater. Cycles Waste Manag. 13 (2011) 68–79. https://doi.org/10.1007/s10163-010-0309-6.

[106] R. Ma, K. Cui, L. Yang, X. Ma, Y. Li, Selective catalytic conversion of guaiacol to phenols over a molybdenum carbide catalyst, Chem. Commun. 51 (2015) 10299–10301. https://doi.org/10.1039/c5cc01900a.

[107] J. Lu, S. Behtash, O. Mamun, A. Heyden, Theoretical Investigation of the Reaction Mechanism of the Guaiacol Hydrogenation over a Pt(111) Catalyst, ACS Catal. 5 (2015) 2423–2435. https://doi.org/10.1021/cs5016244.

[108] D. Gao, Y. Xiao, A. Varma, Guaiacol Hydrodeoxygenation over Platinum Catalyst: Reaction Pathways and Kinetics, Ind. Eng. Chem. Res. 54 (2015) 10638–10644. https://doi.org/10.1021/acs.iecr.5b02940.

[109] A. Kruse, N. Dahmen, Water - A magic solvent for biomass conversion, J. Supercrit. Fluids. 96 (2015) 36–45. https://doi.org/10.1016/j.supflu.2014.09.038.

[110] M. Zhou, J. Ye, P. Liu, J. Xu, J. Jiang, Water-Assisted Selective Hydrodeoxygenation of

Guaiacol to Cyclohexanol over Supported Ni and Co Bimetallic Catalysts, ACS Sustain. Chem. Eng. 5 (2017) 8824–8835. https://doi.org/10.1021/acssuschemeng.7b01615.

[111] J.J.R. Lawson, M.M.T. Klein, Influence of Water on Guaiacol Pyrolysis, Ind. Eng. Chem. Fundam. 24 (1985) 203–208. https://doi.org/10.1021/i100018a012.

[112] H. Wang, T. Maiyalagan, X. Wang, Review on recent progress in nitrogen-doped graphene: Synthesis, characterization, and its potential applications, ACS Catal. 2 (2012) 781–794. https://doi.org/10.1021/cs200652y.

[113] Z. Hou, X. Wang, T. Ikeda, K. Terakura, M. Oshima, M.A. Kakimoto, S. Miyata, Interplay between nitrogen dopants and native point defects in graphene, Phys. Rev. B - Condens. Matter Mater. Phys. 85 (2012) 1–9. https://doi.org/10.1103/PhysRevB.85.165439.

[114] R. Siburian, K. Sebayang, M. Supeno, H. Marpaung, Effect of N-Doped Graphene for Properties of Pt/N-Doped Graphene Catalyst, ChemistrySelect. 2 (2017) 1188–1195. https://doi.org/10.1002/slct.201601561.

[115] L. Zhang, Z. Xia, Mechanisms of oxygen reduction reaction on nitrogen-doped graphene for fuel cells, J. Phys. Chem. C. 115 (2011) 11170–11176. https://doi.org/10.1021/jp201991j.

[116] Y. Gao, G. Hu, J. Zhong, Z. Shi, Y. Zhu, D.S. Su, J. Wang, X. Bao, D. Ma, Nitrogen-doped sp2-hybridized carbon as a superior catalyst for selective oxidation, Angew. Chemie - Int. Ed. 52 (2013) 2109–2113. https://doi.org/10.1002/anie.201207918.

[117] L. Lai, J.R. Potts, D. Zhan, L. Wang, C.K. Poh, C. Tang, H. Gong, Z. Shen, J. Lin, R.S. Ruoff, Exploration of the active center structure of nitrogen-doped graphene-based catalysts for oxygen reduction reaction, Energy Environ. Sci. 5 (2012) 7936–7942. https://doi.org/10.1039/c2ee21802j.

[118] E.F. Mai, M.A. Machado, T.E. Davies, J.A. Lopez-Sanchez, V. Teixeira Da Silva,

Molybdenum carbide nanoparticles within carbon nanotubes as superior catalysts for γ-valerolactone production via levulinic acid hydrogenation, Green Chem. 16 (2014) 4092–4097. https://doi.org/10.1039/c4gc00920g.

[119] J. Han, J. Duan, P. Chen, H. Lou, X. Zheng, Molybdenum carbide-catalyzed conversion of renewable oils into diesel-like hydrocarbons, Adv. Synth. Catal. 353 (2011) 2577–2583. https://doi.org/10.1002/adsc.201100217.

[120] J.R. McManus, J.M. Vohs, Deoxygenation of glycolaldehyde and furfural on Mo2C/Mo(100), Surf. Sci. 630 (2014) 16–21. https://doi.org/10.1016/j.susc.2014.06.019.

[121] A.P. Farkas, F. Solymosi, Adsorption and reactions of ethanol on Mo2C/Mo(1 0 0), Surf. Sci. 601 (2007) 193–200. https://doi.org/10.1016/j.susc.2006.09.023.

[122] M.M. Sullivan, C.J. Chen, A. Bhan, Catalytic deoxygenation on transition metal carbide catalysts, Catal. Sci. Technol. 6 (2016) 602–616. https://doi.org/10.1039/c5cy01665g.

[123] Q. Lu, C.J. Chen, W. Luc, J.G. Chen, A. Bhan, F. Jiao, Ordered mesoporous metal carbides with enhanced anisole hydrodeoxygenation selectivity, ACS Catal. 6 (2016) 3506–3514. https://doi.org/10.1021/acscatal.6b00303.

[124] K. Xiong, W.S. Lee, A. Bhan, J.G. Chen, Molybdenum carbide as a highly selective deoxygenation catalyst for converting furfural to 2-methylfuran, ChemSusChem. 7 (2014) 2146–2149. https://doi.org/10.1002/cssc.201402033.

[125] W.S. Lee, Z. Wang, R.J. Wu, A. Bhan, Selective vapor-phase hydrodeoxygenation of anisole to benzene on molybdenum carbide catalysts, J. Catal. 319 (2014) 44–53. https://doi.org/10.1016/j.jcat.2014.07.025.

[126] M.M. Sullivan, A. Bhan, Acetone Hydrodeoxygenation over Bifunctional Metallic-Acidic Molybdenum Carbide Catalysts, ACS Catal. 6 (2016) 1145–1152. https://doi.org/10.1021/acscatal.5b02656.

[127] Y. Shi, Y. Yang, Y.W. Li, H. Jiao, Theoretical study about Mo2C(101)-catalyzed hydrodeoxygenation of butyric acid to butane for biomass conversion, Catal. Sci. Technol. 6 (2016) 4923–4936. https://doi.org/10.1039/c5cy02008e.

[128] Y. Shi, Y. Yang, Y.W. Li, H. Jiao, Mechanisms of Mo2C(101)-Catalyzed Furfural Selective Hydrodeoxygenation to 2-Methylfuran from Computation, ACS Catal. 6 (2016) 6790–6803. https://doi.org/10.1021/acscatal.6b02000.

[129] Q. Luo, T. Wang, G. Walther, M. Beller, H. Jiao, Molybdenum carbide catalysed hydrogen production from formic acid - A density functional theory study, J. Power Sources. 246 (2014) 548–555. https://doi.org/10.1016/j.jpowsour.2013.07.102.

[130] M. Born, R. Oppenheimer, On the Quantum Theory of Molecules (translation by H. Hettema), Ann. Phys. 84 (1927) 457–484.

[131] P. Hohenberg, W. Kohn, Inhomogeneous electron gas, Phys. Rev. 136 (1964) B864–B871. https://doi.org/10.1103/PhysRevB.7.1912.

[132] P.A.M. Dirac, Note on Exchange Phenomena in the Thomas Atom, Math. Proc. Cambridge Philos. Soc. 26 (1930) 376. https://doi.org/10.1017/S0305004100016108.

[133] Y. Tomishima, Theory with Correlation Correction*, Prog. Theor. Phys. 22 (1959) 1–11.

[134] K. Capelle, A bird's-eye view of density-functional theory, Brazilian J. Phys. 36 (2006) 1318–1343. https://doi.org/10.1590/S0103-97332006000700035.

[135] W. Kohn, L.J. Sham, Self-Consistent Equations Including Exchange and Correlation Effects, Phys. Rev. 140 (1965) A1133–A1138. https://doi.org/10.1103/PhysRev.140.A1133.

[136] R.G. Parr, Y. Weitao, Density-Functional Theory of Atoms and Molecules, Oxford University Press, New York, 1994.

[137] I.N. Levine, Quantum Chemistry, 7th ed., Pearson, 2012.

[138] G. Li, E.J.M. Hensen, E.A. Pidko, Reaction Pathways and Mechanisms in Thermocatalytic Biomass Conversion II, Springer Singapore, Singapore, 2016. https://doi.org/10.1007/978-981-287-769-7.

[139] N. Mardirossian, M. Head-Gordon, Thirty years of density functional theory in computational chemistry: An overview and extensive assessment of 200 density functionals, Mol. Phys. 115 (2017) 2315–2372. https://doi.org/10.1080/00268976.2017.1333644.

[140] V. Sinha, N. Govindarajan, B. De Bruin, E.J. Meijer, How Solvent Affects C-H Activation and Hydrogen Production Pathways in Homogeneous Ru-Catalyzed Methanol Dehydrogenation Reactions, ACS Catal. 8 (2018) 6908–6913. https://doi.org/10.1021/acscatal.8b01177.

[141] J. Tomasi, B. Mennucci, R. Cammi, Quantum mechanical continuum solvation models, Chem. Rev. 105 (2005) 2999–3093. https://doi.org/10.1021/cr9904009.

[142] L. Onsagbr, Electric Moments of Molecules in Liquids, J. Am. Chem. Soc. 58 (1936) 1486–1493. https://doi.org/10.1021/ja01299a050.

[143] C.J. Cramer, D.G. Truhlar, SMx continuum models for condensed phases, Trends Perspect. Mod. Comput. Sci. Maroulis, G.; Simos, TE, Eds.; Lect. Ser. Comput. Comput. Sci. 6 (2006) 112–140. https://doi.org/doi:10.1201/b12251-8.

[144] S. Miertuš, E. Scrocco, J. Tomasi, Electrostatic interaction of a solute with a continuum. A direct utilizaion of AB initio molecular potentials for the prevision of solvent effects, Chem. Phys. 55 (1981) 117–129. https://doi.org/10.1016/0301-0104(81)85090-2.

[145] A. V. Marenich, C.J. Cramer, D.G. Truhlar, Universal solvation model based on solute electron density and a continuum model of the solvent defined by the bulk dielectric constant and atomic surface tensions, J. Phys. Chem. B. 113 (2009) 6378–6396.

[146] J. Tomasi, B. Mennucci, E. Cancès, The IEF version of the PCM solvation method: An

overview of a new method addressed to study molecular solutes at the QM ab initio level, J. Mol. Struct. THEOCHEM. 464 (1999) 211–226. https://doi.org/10.1016/S0166-1280(98)00553-3.

[147] M.J. Frisch, G.W. Trucks, H.B. Schlegel, G.E. Scuseria, M.A. Robb, J.R. Cheeseman, G. Scalmani, V. Barone, B. Mennucci, G.A. Petersson, H. Nakatsuji, M. Caricato, X. Li, H.P. Hratchian, A.F. Izmaylov, J. Bloino, G. Zheng, J.L. Sonnenberg, M. Hada, M. Ehara, K. Toyota, R. Fukuda, J. Hasegawa, M. Ishida, T. Nakajima, Y. Honda, O. Kitao, H. Nakai, T. Vreven, J.A. Montgomery, J.E. Peralta, F. Ogliaro, M. Bearpark, J.J. Heyd, E. Brothers, K.N. Kudin, V.N. Staroverov, R. Kobayashi, J. Normand, K. Raghavachari, A. Rendell, J.C. Burant, S.S. Iyengar, J. Tomasi, M. Cossi, N. Rega, J.M. Millam, M. Klene, J.E. Knox, J.B. Cross, V. Bakken, C. Adamo, J. Jaramillo, R. Gomperts, R.E. Stratmann, O. Yazyev, A.J. Austin, R. Cammi, C. Pomelli, J.W. Ochterski, R.L. Martin, K. Morokuma, V.G. Zakrzewski, G.A. Voth, P. Salvador, J.J. Dannenberg, S. Dapprich, A.D. Daniels, Ö. Farkas, J.B. Foresman, J. V Ortiz, J. Cioslowski, D.J. Fox, Gaussian 09, Revision D, Gaussian 09, Revis. D, Gaussian, Inc., Wallingford CT. (2009).

[148] E.G. Lewars, Computational Chemistry, 2011. https://doi.org/10.1007/978-90-481-3862-3.

[149] J.W. Ochterski, Thermochemistry in Gaussian, 264 (2000) 1–19.

[150] D.A. McQuarrie, J.D. Simon, Molecular thermodynamics, 1999. https://doi.org/10.1016/0022-2860(80)80339-5.

[151] M.J. Frisch, J.A. Pople, J.S. Binkley, Self-consistent molecular orbital methods 25. Supplementary functions for Gaussian basis sets, J. Chem. Phys. 80 (1984) 3265–3269. https://doi.org/10.1063/1.447079.

[152] L. Simón, J.M. Goodman, L. Simon, J.M. Goodman, How reliable are DFT transition structures? Comparison of GGA, hybrid-meta-GGA and meta-GGA functionals, Org.

Biomol. Chem. 9 (2011) 689–700. https://doi.org/10.1039/C0OB00477D.

[153] Y. Zhao, N.E. Schultz, D.G. Truhlar, Design of density functionals by combining the method of constraint satisfaction with parametrization for thermochemistry, thermochemical kinetics, and noncovalent interactions, J. Chem. Theory Comput. 2 (2006) 364–382. https://doi.org/10.1021/ct0502763.

[154] R. Dennington, T. Keith, J. Millam, GaussView, Version 5, (2009) Semichem Inc., Shawnee Mission, KS.

[155] M. Walker, A.J.A. Harvey, A. Sen, C.E.H. Dessent, Performance of M06, M06-2X, and M06-HF density functionals for conformationally flexible anionic clusters: M06 functionals perform better than B3LYP for a model system with dispersion and ionic hydrogen-bonding interactions, J. Phys. Chem. A. 117 (2013) 12590–12600. https://doi.org/10.1021/jp408166m.

[156] R.S. Assary, P.C. Redfern, J.R. Hammond, J. Greeley, L.A. Curtiss, Predicted thermochemistry for chemical conversions of 5- hydroxymethylfurfural, Chem. Phys. Lett. 497 (2010) 123–128. https://doi.org/10.1016/j.cplett.2010.07.082.

[157] S. Wang, B. Ru, H. Lin, Z. Luo, Degradation mechanism of monosaccharides and xylan under pyrolytic conditions with theoretic modeling on the energy profiles, Bioresour. Technol. 143 (2013) 378–383. https://doi.org/10.1016/j.biortech.2013.06.026.

[158] M. Wang, C. Liu, Q. Li, X. Xu, Theoretical insight into the conversion of xylose to furfural in the gas phase and water, J. Mol. Model. 21 (2015). https://doi.org/10.1007/s00894-015-2843-6.

[159] A. Banerjee, S.H. Mushrif, Reaction Pathways for the Deoxygenation of Biomass-Pyrolysis-Derived Bio-oil on Ru: A DFT Study using Furfural as a Model Compound, ChemCatChem. 9 (2017) 2828–2838. https://doi.org/10.1002/cctc.201700036.

[160] E.E. Dahlke, R.M. Olson, H.R. Leverentz, D.G. Truhlar, Assessment of the accuracy of

density functionals for prediction of relative energies and geometries of low-lying isomers of water hexamers, J. Phys. Chem. A. 112 (2008) 3976–3984. https://doi.org/10.1021/jp077376k.

[161] S. Wang, V. Vorotnikov, D.G. Vlachos, A DFT study of furan hydrogenation and ring opening on Pd(111), Green Chem. 16 (2014) 736–747. https://doi.org/10.1039/c3gc41183d.

[162] J. Guan, J. Li, Y. Yu, X. Mu, A. Chen, DFT Studies of the Selective C-O Hydrogenolysis and Ring-Opening of Biomass-Derived Tetrahydrofurfuryl Alcohol over Rh(111) surfaces, J. Phys. Chem. C. 120 (2016) 19124–19134. https://doi.org/10.1021/acs.jpcc.6b05026.

[163] V. LaVopa, C.N. Satterfield, Catalytic Hydrodeoxygenation of Dibenzofuran, Energy and Fuels. 1 (1987) 323–331. https://doi.org/10.1021/ef00004a003.

[164] Y. Zhao, D.G. Truhlar, The M06 Suite of Density Functional s for Main Group Thermochemistry, Thermochemical Kinetics, Noncovalent Interactions, Excited States, and Transition Elements: Two New Functi onals and Systematic Testing of Four M06 Functionals and Twelve Other Function, Theor. Chem. Acc. 120 (2008) 215–241. https://doi.org/10.1007/s00214-007-0310-x.

[165] A. Infantes-Molina, E. Gralberg, J.A. Cecilia, E. Finocchio, E. Rodríguez-Castellón, Nickel and cobalt phosphides as effective catalysts for oxygen removal of dibenzofuran: Role of contact time, hydrogen pressure and hydrogen/feed molar ratio, Catal. Sci. Technol. 5 (2015) 3403–3415. https://doi.org/10.1039/c5cy00282f.

[166] E. Rodríguez-Aguado, A. Infantes-Molina, J.A. Cecilia, D. Ballesteros-Plata, R. López-Olmo, E. Rodríguez-Castellón, CoxPy Catalysts in HDO of Phenol and Dibenzofuran: Effect of P content, Top. Catal. 60 (2017) 1094–1107. https://doi.org/10.1007/s11244-017-0791-3.

[167] S. Gbadamasi, T.H. Ali, L.H. Voon, A.Y. Atta, P. Sudarsanam, S.K. Bhargava, S.B. Abd Hamid, Promising Ni/Al-SBA-15 catalysts for hydrodeoxygenation of dibenzofuran into fuel grade hydrocarbons: Synergetic effect of Ni and Al-SBA-15 support, RSC Adv. 6 (2016) 25992–26002. https://doi.org/10.1039/c5ra27526a.

[168] D.E. Resasco, What Should We Demand from the Catalysts Responsible for Upgrading Biomass Pyrolysis Oil?, J. Phys. Chem. Lett. 2 (2011) 2294–2295. https://doi.org/10.1021/jz201135x.

[169] M.J. Frisch, G.W. Trucks, H.B. Schlegel, G.E. Scuseria, M.A. Robb, J.R. Cheeseman, G. Scalmani, V. Barone, B. Mennucci, G.A. Petersson, H. Nakatsuji, M. Caricato, X. Li, H.P. Hratchian, A.F. Izmaylov, J. Bloino, G. Zheng, J.L. Sonnenberg, M. Hada, M. Ehara, K. Toyota, R. Fukuda, J. Hasegawa, M. Ishida, T. Nakajima, Y. Honda, O. Kitao, H. Nakai, T. Vreven, J. J. A. Montgomery, J.E. Peralta, F. Ogliaro, M. Bearpark, J.J. Heyd, E. Brothers, K.N. Kudin, V.N. Staroverov, R. Kobayashi, J. Normand, K. Raghavachari, A. Rendell, J.C. Burant, S.S. Iyengar, J. Tomasi, M. Cossi, N. Rega, J.M. Millam, M. Klene, J.E. Knox, J.B. Cross, V. Bakken, C. Adamo, J. Jaramillo, R. Gomperts, R.E. Stratmann, O. Yazyev, A.J. Austin, R. Cammi, C. Pomelli, J.W. Ochterski, R.L. Martin, K. Morokuma, V.G. Zakrzewski, G.A. Voth, P. Salvador, J.J. Dannenberg, S. Dapprich, A.D. Daniels, Ö. Farkas, J.B. Foresman, J. V. Ortiz, J. Cioslowski, D.J. Fox, Gaussian 09, Revision D.01, (2009).

[170] R. Dennington, T.A. Keith, J.M. Millam, GaussView 5, Version 5.0.8, (2009) Semichem Inc.

[171] J. Huang, X. Li, D. Wu, H. Tong, W. Li, Theoretical studies on pyrolysis mechanism of guaiacol as lignin model compound, J. Renew. Sustain. Energy. 5 (2013) 043112–043117. https://doi.org/10.1063/1.4816497.

[172] A.M. Verma, N. Kishore, DFT Analyses of Reaction Pathways and Temperature Effects

on various Guaiacol Conversion Reactions in Gas Phase Environment, ChemistrySelect. 1 (2016) 6196–6205. https://doi.org/10.1002/slct.201601139.

[173] M. Lucarini, P. Pedrielli, G.F. Pedulli, S. Cabiddu, C. Fattuoni, Bond dissociation energies of O-H bonds in substituted phenols from equilibration studies, J. Org. Chem. 61 (1996) 9259–9263. https://doi.org/10.1021/jo961039i.

[174] A.K. Chandra, T. Uchimaru, The O-H bond dissociation energies of substituted phenols and protonaffinities of substituted phenoxide ions: A DFT study, Int. J. Mol. Sci. 3 (2002) 407–422. https://doi.org/10.3390/i3040407.

[175] E.G. Bakalbassis, A.T. Lithoxoidou, A.P. Vafiadis, Theoretical calculation of accurate absolute and relative gas- and liquid-phase O-H bond dissociation enthalpies of 2-mono- and 2,6-disubstituted phenols, using DFT/B3LYP, J. Phys. Chem. A. 107 (2003) 8594–8606. https://doi.org/10.1021/jp034400v.

[176] D.A. Pratt, M.I. De Heer, P. Mulder, K.U. Ingold, Oxygen-Carbon bond dissociation enthalpies of benzyl phenyl ethers and anisoles. An example of temperature dependent substituent effects, J. Am. Chem. Soc. 123 (2001) 5518–5526. https://doi.org/10.1021/ja004081a.

[177] Y. Furutani, Y. Dohara, S. Kudo, J.I. Hayashi, K. Norinaga, Theoretical Study on the Kinetics of Thermal Decomposition of Guaiacol and Catechol, J. Phys. Chem. A. 121 (2017) 8495–8503. https://doi.org/10.1021/acs.jpca.7b08112.

[178] S. Grimme, J. Antony, S. Ehrlich, H. Krieg, A consistent and accurate ab initio parametrization of density functional dispersion correction (DFT-D) for the 94 elements H-Pu, J. Chem. Phys. 132 (2010) 154104. https://doi.org/10.1063/1.3382344.

[179] N.M. O'boyle, A.L. Tenderholt, K.M. Langner, cclib: A library for package-independent computational chemistry algorithms, J. Comput. Chem. 29 (2008) 839–845. https://doi.org/10.1002/jcc.20823.

[180] T. Lu, F. Chen, Multiwfn: A multifunctional wavefunction analyzer, J. Comput. Chem. 33 (2012) 580–592. https://doi.org/10.1002/jcc.22885.

[181] P.K. Chattaraj, U. Sarkar, D.R. Roy, Electrophilicity Index, Chem. Rev. 106 (2006) 2065–2091. https://doi.org/10.1021/cr040109f.

[182] J. Luo, Z.Q. Xue, W.M. Liu, J.L. Wu, Z.Q. Yang, Koopmans' Theorem for Large Molecular Systems within Density Functional Theory, J. Phys. Chem. A. 110 (2006) 12005–12009. https://doi.org/10.1021/jp063669m.

[183] D.R. Cooper, B. D'Anjou, N. Ghattamaneni, B. Harack, M. Hilke, A. Horth, N. Majlis, M. Massicotte, L. Vandsburger, E. Whiteway, V. Yu, Experimental Review of Graphene, ISRN Condens. Matter Phys. 2012 (2012) 1–56. https://doi.org/10.5402/2012/501686.

[184] N. Al-Aqtash, I. Vasiliev, Ab Initio Study of Boron- and Nitrogen-Doped Graphene and Carbon Nanotubes Functionalized with Carboxyl Groups, J. Phys. Chem. C. 115 (2011) 18500–18510. https://doi.org/10.1021/jp206196k.

[185] Y.-C. Lin, P.-Y. Teng, C.-H. Yeh, M. Koshino, P.-W. Chiu, K. Suenaga, Structural and Chemical Dynamics of Pyridinic-Nitrogen Defects in Graphene, Nano Lett. 15 (2015) 7408–7413. https://doi.org/10.1021/acs.nanolett.5b02831.

[186] Y.Y. Tong, A.J. Renouprez, G.A. Martin, J.J. van der Klink, Electron availability and the surface fermi level local density of states: an alternative way to see catalytic activity of metals, in: Stud. Surf. Sci. Catal., 1996: pp. 901–910. https://doi.org/10.1016/S0167-2991(96)80301-6.

[187] V.P. Gupta, Electron Density Analysis and Electrostatic Potential, in: Princ. Appl. Quantum Chem., Elsevier, 2016: pp. 195–214. https://doi.org/10.1016/B978-0-12-803478-1.00006-6.

[188] K.W. Kolasinski, Surface Science, Foundations of Catalysis and Nanoscience, 3rd ed.,

John Wiley & Sons, Ltd, Chichester, UK, 2012. https://doi.org/10.1002/9781119941798.

[189] S. Singh, S. Li, R. Carrasquillo-Flores, A.C. Alba-Rubio, J.A. Dumesic, M. Mavrikakis, Formic acid decomposition on Au catalysts: DFT, microkinetic modeling, and reaction kinetics experiments, AIChE J. 60 (2014) 1303–1319. https://doi.org/10.1002/aic.14401.

[190] P. Mars, J.J.F. Scholten, P. Zwietering, The Catalytic Decomposition of Formic Acid, in: J. Phys. Chem., 1963: pp. 35–113. https://doi.org/10.1016/S0360-0564(08)60338-7.

[191] R. Sanderson, Polar Covalence, Elsevier, 1983. https://doi.org/10.1016/B978-0-12-618080-0.X5001-9.

[192] R. Sanderson, Chemical Bonds and Bonds Energy, 2nd ed., Elsevier Ltd, 1976. https://www.elsevier.com/books/chemical-bonds-and-bonds-energy/sanderson/978-0-12-618060-2.

[193] V. Blum, R. Gehrke, F. Hanke, P. Havu, V. Havu, X. Ren, K. Reuter, M. Scheffler, Ab initio molecular simulations with numeric atom-centered orbitals, Comput. Phys. Commun. 180 (2009) 2175–2196. https://doi.org/10.1016/j.cpc.2009.06.022.

[194] A. Hjorth Larsen, J. Jørgen Mortensen, J. Blomqvist, I.E. Castelli, R. Christensen, M. Dułak, J. Friis, M.N. Groves, B. Hammer, C. Hargus, E.D. Hermes, P.C. Jennings, P. Bjerre Jensen, J. Kermode, J.R. Kitchin, E. Leonhard Kolsbjerg, J. Kubal, K. Kaasbjerg, S. Lysgaard, J. Bergmann Maronsson, T. Maxson, T. Olsen, L. Pastewka, A. Peterson, C. Rostgaard, J. Schiøtz, O. Schütt, M. Strange, K.S. Thygesen, T. Vegge, L. Vilhelmsen, M. Walter, Z. Zeng, K.W. Jacobsen, The atomic simulation environment—a Python library for working with atoms, J. Phys. Condens. Matter. 29 (2017) 273002. https://doi.org/10.1088/1361-648X/aa680e.

[195] T. Epicier, J. Dubois, C. Esnouf, G. Fantozzi, P. Convert, Neutron powder diffraction studies of transition metal hemicarbides M2C1−x—II. In situ high temperature study on W2C1−x and Mo2C1−x, Acta Metall. 36 (1988) 1903–1921.

https://doi.org/10.1016/0001-6160(88)90293-3.

[196] J. Nocedal, S.J. Wright, Trust-Region Methods, in: Numer. Optim., 2nd ed., Springer New York, 2006: pp. 66–100. https://doi.org/10.1007/978-0-387-40065-5_4.

[197] A. Tkatchenko, M. Scheffler, Accurate molecular van der Waals interactions from ground-state electron density and free-atom reference data, Phys. Rev. Lett. (2009). https://doi.org/10.1103/PhysRevLett.102.073005.

[198] F.Z. Abderrahim, H.I. Faraoun, T. Ouahrani, Structure, bonding and stability of semi-carbides M2C and sub-carbides M4C (M=V, Cr, Nb, Mo, Ta, W): A first principles investigation, Phys. B Condens. Matter. 407 (2012) 3833–3838. https://doi.org/10.1016/j.physb.2012.05.070.

[199] J.R.D.S. Politi, F. Viñes, J.A. Rodriguez, F. Illas, Atomic and electronic structure of molybdenum carbide phases: Bulk and low Miller-index surfaces, Phys. Chem. Chem. Phys. 15 (2013) 12617–12625. https://doi.org/10.1039/c3cp51389k.

[200] E. Parthé, V. Sadagopan, The structure of dimolybdenum carbide by neutron diffraction technique, Acta Crystallogr. 16 (1963) 202–205. https://doi.org/10.1107/S0365110X63000487.

[201] A.J. Medford, A. Vojvodic, F. Studt, F. Abild-Pedersen, J.K. Nørskov, Elementary steps of syngas reactions on Mo2C(001): Adsorption thermochemistry and bond dissociation, J. Catal. 290 (2012) 108–117. https://doi.org/10.1016/j.jcat.2012.03.007.

[202] D.W. Flaherty, S.P. Berglund, C.B. Mullins, Selective decomposition of formic acid on molybdenum carbide: A new reaction pathway, J. Catal. 269 (2010) 33–43. https://doi.org/10.1016/j.jcat.2009.10.012.

[203] R. Ma, K. Cui, L. Yang, X. Ma, Y. Li, Selective catalytic conversion of guaiacol to phenols over a molybdenum carbide catalyst, Chem. Commun. 51 (2015) 10299–10301. https://doi.org/10.1039/c5cc01900a.

[204] K. Xiong, W. Yu, D.G. Vlachos, J.G. Chen, Reaction Pathways of Biomass-Derived Oxygenates over Metals and Carbides: From Model Surfaces to Supported Catalysts, ChemCatChem. 7 (2015) 1402–1421. https://doi.org/10.1002/cctc.201403067.

[205] T. Wang, X. Tian, Y. Yang, Y.-W. Li, J. Wang, M. Beller, H. Jiao, Surface morphology of orthorhombic Mo2C catalyst and high coverage hydrogen adsorption, Surf. Sci. 651 (2016) 195–202. https://doi.org/10.1016/j.susc.2016.04.017.

[206] F. Morteo-Flores, J. Engel, A. Roldan, Biomass hydrodeoxygenation catalysts innovation from atomistic activity predictors, Philos. Trans. R. Soc. A Math. Phys. Eng. Sci. 378 (2020) 20200056. https://doi.org/10.1098/rsta.2020.0056.

[207] K.E. You, S.C. Ammal, Z. Lin, W. Wan, J.G. Chen, A. Heyden, Understanding the effect of Mo2C support on the activity of Cu for the hydrodeoxygenation of glycerol, J. Catal. 388 (2020) 141–153. https://doi.org/10.1016/j.jcat.2020.05.007.

[208] F. Turker, O.R. Caylan, N. Mehmood, T.S. Kasirga, C. Sevik, G. Cambaz Buke, CVD synthesis and characterization of thin Mo 2 C crystals, J. Am. Ceram. Soc. 103 (2020) 5586–5593. https://doi.org/10.1111/jace.17317.

[209] C.A. Wolden, A. Pickerell, T. Gawai, S. Parks, J. Hensley, J.D. Way, Synthesis of β-Mo2C Thin Films, ACS Appl. Mater. Interfaces. 3 (2011) 517–521. https://doi.org/10.1021/am101095h.

[210] G. Henkelman, B.P. Uberuaga, H. Jónsson, A climbing image nudged elastic band method for finding saddle points and minimum energy paths, J. Chem. Phys. 113 (2000) 9901–9904. https://doi.org/10.1063/1.1329672.

[211] E. Bitzek, P. Koskinen, F. Gähler, M. Moseler, P. Gumbsch, Structural Relaxation Made Simple, Phys. Rev. Lett. 97 (2006) 170201. https://doi.org/10.1103/PhysRevLett.97.170201.

[212] S.S. Tafreshi, A. Roldan, N.H. de Leeuw, Micro-kinetic simulations of the catalytic

decomposition of hydrazine on the Cu(111) surface, Faraday Discuss. 197 (2017) 41–57. https://doi.org/10.1039/C6FD00186F.

[213] A. Roldán, G. Novell, J.M. Ricart, F. Illas, Theoretical Simulation of Temperature Programmed Desorption of Molecular Oxygen on Isolated Au Nanoparticles from Density Functional Calculations and Microkinetics Models, J. Phys. Chem. C. 114 (2010) 5101–5106. https://doi.org/10.1021/jp911283j.

[214] I. Chorkendorff, J.W. Niemantsverdriet, Concepts of Modern Catalysis and Kinetics, 2003. https://doi.org/10.1002/3527602658.

[215] A. Roldan, Microkinetic Modelling, (n.d.). https://github.com/Roldan-Group/Kinetics.

[216] H. Eyring, The activated complex in chemical reactions, J. Chem. Phys. (1935). https://doi.org/10.1063/1.1749604.

[217] M.G. Evans, M. Polanyi, Some applications of the transition state method to the calculation of reaction velocities, especially in solution, Trans. Faraday Soc. (1935). https://doi.org/10.1039/tf9353100875.

[218] C.H. Lin, C.L. Chen, J.H. Wang, Mechanistic studies of water-gas-shift reaction on transition metals, J. Phys. Chem. C. 115 (2011) 18582–18588. https://doi.org/10.1021/jp2034467.

[219] M. Nagai, H. Tominaga, S. Omi, CO Adsorption on Molybdenum Carbides and Molecular Simulation, Langmuir. 16 (2000) 10215–10220. https://doi.org/10.1021/la000484c.

[220] H. Ren, W. Yu, M. Salciccioli, Y. Chen, Y. Huang, K. Xiong, D.G. Vlachos, J.G. Chen, Selective hydrodeoxygenation of biomass-derived oxygenates to unsaturated hydrocarbons using molybdenum carbide catalysts, ChemSusChem. 6 (2013) 798–801. https://doi.org/10.1002/cssc.201200991.

[221] J. Scaranto, M. Mavrikakis, Density functional theory studies of HCOOH decomposition

on Pd(111), Surf. Sci. 650 (2016) 111–120. https://doi.org/10.1016/j.susc.2015.11.020.

[222] S. Bhandari, S. Rangarajan, C.T. Maravelias, J.A. Dumesic, M. Mavrikakis, Reaction Mechanism of Vapor-Phase Formic Acid Decomposition over Platinum Catalysts: DFT, Reaction Kinetics Experiments, and Microkinetic Modeling, ACS Catal. 10 (2020) 4112–4126. https://doi.org/10.1021/acscatal.9b05424.

[223] M.T. Darby, E.C.H. Sykes, A. Michaelides, M. Stamatakis, Carbon Monoxide Poisoning Resistance and Structural Stability of Single Atom Alloys, Top. Catal. 61 (2018) 428–438. https://doi.org/10.1007/s11244-017-0882-1.

[224] T. Mo, J. Xu, Y. Yang, Y. Li, Effect of carburization protocols on molybdenum carbide synthesis and study on its performance in CO hydrogenation, Catal. Today. 261 (2016) 101–115. https://doi.org/10.1016/j.cattod.2015.07.014.

[225] F. Silveri, M.G. Quesne, A. Roldan, N.H. De Leeuw, C.R.A. Catlow, Hydrogen adsorption on transition metal carbides: A DFT study, Phys. Chem. Chem. Phys. 21 (2019) 5335–5343. https://doi.org/10.1039/c8cp05975f.

[226] E. Jeroro, J.M. Vohs, Reaction of formic acid on Zn-modified Pd(111), Catal. Letters. 130 (2009) 271–277. https://doi.org/10.1007/s10562-009-9955-5.

[227] N. Aas, Y. Li, M. Bowker, The adsorption and decomposition of formic acid on clean and oxygen-dosed Pd(110), J. Phys. Condens. Matter. 3 (1991) S281–S286. https://doi.org/10.1088/0953-8984/3/S/044.

[228] C. Diagne, H. Idriss, I. Pepin, J.P. Hindermann, A. Kiennemann, Temperature-programmed desorption studies on Pd/CeO2 after methanol and formic acid adsorption and carbon monoxide-hydrogen reaction, Appl. Catal. 50 (1989) 43–53. https://doi.org/10.1016/S0166-9834(00)80824-6.

[229] N. V. Petrova, I.N. Yakovkin, Hydrogen associative desorption from Ru(1010), Eur. Phys. J. B. 63 (2008) 17–24. https://doi.org/10.1140/epjb/e2008-00217-7.

[230] R.G. Wilson, W.E. McKee, Vacuum thermionic work functions and thermal stability of TaB2, ZrC, Mo2C, MoSi2, TaSi2, and WSi2, J. Appl. Phys. 38 (1967) 1716–1718. https://doi.org/10.1063/1.1709747.

[231] D.L. Jacobson, A.E. Campbell, Molybdenum work function determined by electron emission microscopy, Metall. Mater. Trans. B. 2 (1971) 3063–3066. https://doi.org/10.1007/BF02814955.

[232] D.H. Carrales-Alvarado, A.B. Dongil, J.M. Fernández-Morales, M. Fernández-García, A. Guerrero-Ruiz, I. Rodríguez-Ramos, Selective hydrogen production from formic acid decomposition over Mo carbides supported on carbon materials, Catal. Sci. Technol. 10 (2020) 6790–6799. https://doi.org/10.1039/D0CY01088J.

[233] L.M. Falicov, G.A. Somorjai, Correlation between catalytic activity and bonding and coordination number of atoms and molecules on transition metal surfaces: Theory and experimental evidence, Proc. Natl. Acad. Sci. 82 (1985) 2207–2211. https://doi.org/10.1073/pnas.82.8.2207.

[234] K. Agrawal, A. Roldan, N. Kishore, A.J. Logsdail, Dehydrogenation and dehydration of formic acid over orthorhombic molybdenum carbide, Catal. Today. (2021). https://doi.org/10.1016/j.cattod.2021.04.011.

[235] J.A. Garrido Torres, P.C. Jennings, M.H. Hansen, J.R. Boes, T. Bligaard, Low-Scaling Algorithm for Nudged Elastic Band Calculations Using a Surrogate Machine Learning Model, Phys. Rev. Lett. 122 (2019) 156001. https://doi.org/10.1103/PhysRevLett.122.156001.

[236] A.M. Verma, N. Kishore, Molecular Modelling Approach to Elucidate Gas Phase Hydrodeoxygenation of Guaiacol over Pd(111) Catalyst within DFT framework, J. Mol. Model. (2018). https://doi.org/10.1007/s00894-018-3803-8.

[237] H. Fang, A. Roldan, C. Tian, Y. Zheng, X. Duan, K. Chen, L. Ye, S. Leoni, Y. Yuan,

Structural tuning and catalysis of tungsten carbides for the regioselective cleavage of C–O bonds, J. Catal. 369 (2019) 283–295. https://doi.org/10.1016/j.jcat.2018.11.020.

[238] S.J. Carey, W. Zhao, Z. Mao, C.T. Campbell, Energetics of Adsorbed Phenol on Ni(111) and Pt(111) by Calorimetry, J. Phys. Chem. C. 123 (2019) 7627–7632. https://doi.org/10.1021/acs.jpcc.8b03155.

[239] J. Lee, S. Ryu, S.K. Kim, The adsorption and photochemistry of phenol on Ag(111), Surf. Sci. 481 (2001) 163–171. https://doi.org/10.1016/S0039-6028(01)01033-0.

[240] J. Chang, T. Danuthai, S. Dewiyanti, C. Wang, A. Borgna, Hydrodeoxygenation of guaiacol over carbon-supported metal catalysts, ChemCatChem. 5 (2013) 3041–3049. https://doi.org/10.1002/cctc.201300096.

[241] Z. Cai, F. Wang, X. Zhang, R. Ahishakiye, Y. Xie, Y. Shen, Selective hydrodeoxygenation of guaiacol to phenolics over activated carbon supported molybdenum catalysts, Mol. Catal. 441 (2017) 28–34. https://doi.org/10.1016/j.mcat.2017.07.024.

[242] F. Maldonado, L. Villamagua, R. Rivera, DFT Analysis of the Adsorption of Phenol on the Nonpolar ($10\bar{1}0$) ZnO Surface, J. Phys. Chem. C. 123 (2019) 12296–12304. https://doi.org/10.1021/acs.jpcc.9b01906.

[243] A.M. Verma, N. Kishore, Platinum catalyzed hydrodeoxygenation of guaiacol in illumination of cresol production: a density functional theory study, R. Soc. Open Sci. 4 (2017) 170650. https://doi.org/10.1098/rsos.170650.

[244] M. Saleheen, A.M. Verma, O. Mamun, J. Lu, A. Heyden, Investigation of solvent effects on the hydrodeoxygenation of guaiacol over Ru catalysts, Catal. Sci. Technol. 9 (2019) 6253–6273. https://doi.org/10.1039/c9cy01763a.

[245] K. Agrawal, A.M. Verma, N. Kishore, Thermochemical Conversion of Guaiacol in Aqueous Phase by Density Functional Theory, ChemistrySelect. 4 (2019) 6013–6025.

https://doi.org/10.1002/slct.201900437.

[246] C.C. Tran, Y. Han, M. Garcia-Perez, S. Kaliaguine, Synergistic effect of Mo-W carbides on selective hydrodeoxygenation of guaiacol to oxygen-free aromatic hydrocarbons, Catal. Sci. Technol. 9 (2019) 1387–1397. https://doi.org/10.1039/c8cy02184h.

[247] E. Blanco, C. Sepulveda, K. Cruces, J.L. García-Fierro, I.T. Ghampson, N. Escalona, Conversion of guaiacol over metal carbides supported on activated carbon catalysts, Catal. Today. 356 (2020) 376–383. https://doi.org/10.1016/j.cattod.2019.08.029.

[248] B.M. Wong, G. Collinge, A.J.R. Hensley, Y. Wang, J.-S. McEwen, Benchmarking the accuracy of coverage-dependent models: adsorption and desorption of benzene on Pt (1 1 1) and Pt3Sn (1 1 1) from first principles, Prog. Surf. Sci. 94 (2019) 100538. https://doi.org/10.1016/j.progsurf.2019.04.001.

[249] R.S. Smith, B.D. Kay, Desorption Kinetics of Benzene and Cyclohexane from a Graphene Surface, J. Phys. Chem. B. 122 (2018) 587–594. https://doi.org/10.1021/acs.jpcb.7b05102.

[250] E. Castillejos-López, D.M. Nevskaia, V. Muñoz, A. Guerrero-Ruiz, On the interactions of phenol, aniline and p-nitrophenol on activated carbon surfaces as detected by TPD, Carbon N. Y. 46 (2008) 870–875. https://doi.org/10.1016/j.carbon.2008.02.007.

[251] B.-Q. Xu, T. Yamaguchi, K. Tanabe, Temperature-programmed-desorption of phenol from oxide surfaces, Mater. Chem. Phys. 19 (1988) 291–297. https://doi.org/10.1016/0254-0584(88)90033-8.

[252] X. Xu, C.M. Friend, The role of coverage in determining adsorbate stability: phenol reactivity on rhodium(111), J. Phys. Chem. 93 (1989) 8072–8080. https://doi.org/10.1021/j100361a021.

Full papers:

[1] **K. Agrawal**, A.M. Verma, N. Kishore, DFT investigation on thermochemical analyses of conversion of xylose to linear alkanes in aqueous phase, J. Mol. Graph. Model. 90 (2019) 199–209. https://doi.org/10.1016/j.jmgm.2019.05.005.

[2] **K. Agrawal**, N. Kishore, DFT study on dibenzofuran conversion to cyclohexane and benzene in gas, water and methanol solvents, J. Mol. Graph. Model. 99 (2020). https://doi.org/10.1016/j.jmgm.2020.107629.

[3] **K. Agrawal**, A.M. Verma, N. Kishore, Thermochemical Conversion of Guaiacol in Aqueous Phase by Density Functional Theory, ChemistrySelect. 4 (2019) 6013–6025. https://doi.org/10.1002/slct.201900437.

[4] **K. Agrawal**, N. Kishore, Adsorption of bio-oil model compounds over nitrogen doped graphene using density functional theory, *Accepted - Chemistryselect.*

[5] **K. Agrawal**, A. Roldan, N. Kishore, A. Logsdail, Dehydrogenation and dehydration of formic acid over orthorhombic molybdenum carbide, Cat. Tod., (2021), https://doi.org/10.1016/j.cattod.2021.04.011

[6] **K. Agrawal**, A. Roldan, N. Kishore, A. Logsdail, Kinetics of HDO of Guaiacol over Orthorhombic Molybdenum Carbide Using Density Functional Theory, *manuscript under submission.*

Conference Paper:

[1] **K. Agrawal,** N. Kishore, Computational Study on Kinetics of Conversion of Bio-oil Model Compound – Anisole, to Platform Chemicals, J. Phys. Conf. Ser. 1276 (2019) 012071. https://doi.org/10.1088/1742-6596/1276/1/012071.

Conferences:

[1] ACS Spring Conference | online, 2021

Agrawal K, Logsdail A, Kishore N. DFT Study on Hydrodeoxygenation of Resorcinol over Molybdenum Carbide – Poster presentation

[2] ICEC | Manchester University, UK, 2020

Agrawal K, Logsdail A, and Kishore N. Reactivity Modelling of the Hydrodeoxygenation of Bio-oil Compounds over Metal Carbide Catalyst – Oral presentation

[3] Research Conclave | IIT Guwahati, India, 2019

Agrawal K, and Kishore N. A Density Functional Theory Study on Adsorption of Phenol and Guaiacol Over N-doped Graphene – Oral presentation

[4] ICAMEES | UPES Dehradun, India, 2018

Agrawal K, and Kishore N. Thermochemistry of the Conversion of Dibenzofuran to Benzene and Cyclohexane in Water and Methanol – Poster presentation

[5] iCRAFT | BITS Pilani Dubai Campus, Dubai, UAE, 2018

Agrawal K, Kishore N. Computational Study on Kinetics of Conversion of Bio-oil Model Compound – Anisole, to Platform Chemicals – Oral paper presentation

Workshops:

[1] GIAN Course | IIT Guwahati, 2018

Density Functional Theory for Heterogeneous catalysis – secured grade AA (Excellent)

[2] RAMOLS | IISc Bangalore, 2018

Recent Advances in Molecular Simulation - attended a 4-day discussion meeting

ANNEXURE 1

All reactions considered in the microkinetic modelling with activation energy (E_a), reaction energy (ΔE), sticking coefficient (S_0), Arrhenius factor (A_0) and the rate constant (K) at 500 K, 600 K and 700 K

Rxn. No	Reactions	E_a (eV)	ΔE (eV)	500 K			600 K			700 K		
				S_0	A_0	K	S_0	A_0	K	S_0	A_0	K
Ads	GUA + * >> GUA*	-	-4.66	3.23E-07	1.30E+04	4.19E-03	3.77E-08	1.18E+04	4.46E-04	5.88E-09	1.10E+04	6.45E-05
	GUA* >> GUA + *	-	4.66	-	2.18E+25	5.21E+00	-	1.93E+25	3.75E+02	-	1.68E+25	2.67E+04
R1	GUA* + H* >> 1r + *	-	0.25	-	1.67E+13	2.35E+11	-	1.73E+13	2.64E+11	-	1.80E+13	2.99E+11
	1r + * >> GUA* + H*	-	-0.25	-	1.28E+13	9.07E+14	-	1.23E+13	8.06E+14	-	1.18E+13	7.11E+14
	1r > TS1 > 1p	1.15	0.64	-	4.47E+13	1.78E+05	-	4.46E+13	2.15E+05	-	4.39E+13	2.50E+05
	1p > TS1 > 1r	0.5	-0.64	-	6.20E+13	4.18E+10	-	6.65E+13	5.26E+10	-	7.01E+13	6.53E+10
R2	GUA* + H* >> 2r *+ *	-	0.31	-	1.01E+13	3.96E+10	-	1.02E+13	4.10E+10	-	1.04E+13	4.29E+10
	2r* + * >> GUA* + H*	-	-0.31	-	2.12E+13	5.37E+15	-	2.09E+13	5.19E+15	-	2.04E+13	4.96E+15
	2r* > TS2 > 2p*	2.59	0.86	-	8.18E+13	1.78E-04	-	9.37E+13	2.35E-04	-	1.05E+14	3.13E-04
	2p* > TS2 > 2r*	1.73	-0.86	-	7.90E+13	5.44E+02	-	9.40E+13	7.06E+02	-	1.09E+14	9.46E+02
R3	GUA* > TS3 > 3p*	1.04	-0.69	-	4.03E+13	4.82E+06	-	4.69E+13	6.33E+06	-	5.34E+13	8.36E+06
	3p* > TS3 > GUA*	1.73	0.69	-	6.68E+13	7.72E+01	-	7.42E+13	1.02E+02	-	8.06E+13	1.34E+02
	3p* + * >> s4* + OH*	-	-0.37	-	5.59E+12	1.47E+15	-	4.79E+12	1.05E+15	-	4.20E+12	7.46E+14
	s4* + OH* >> 3p* + *	-	0.37	-	3.81E+13	1.45E+11	-	4.44E+13	2.03E+11	-	5.07E+13	2.85E+11
R4	GUA* > TS4 > 4p*	0.90	0.59	-	7.62E+13	9.65E+07	-	8.67E+13	1.32E+08	-	9.60E+13	1.79E+08
	4p* > TS4 > GUA*	0.31	-0.59	-	2.45E+13	2.62E+11	-	2.55E+13	2.84E+11	-	2.63E+13	3.07E+11
	4p* + * >> s5* + OCH3*	-	-1.93	-	3.81E+11	3.17E+25	-	2.48E+11	9.06E+24	-	1.72E+11	2.72E+24
	s5* + OCH3* >> 4p* + *	-	1.93	-	5.59E+14	6.70E+00	-	8.57E+14	2.35E+01	-	1.24E+15	7.83E+01
R5	GUA* > TS5 > 5p*	1.02	-0.49	-	2.26E+13	6.76E+06	-	2.47E+13	7.09E+06	-	2.70E+13	7.78E+06
	5p* > TS5 > GUA*	1.51	0.49	-	7.22E+13	1.83E+03	-	7.95E+13	2.49E+03	-	8.53E+13	3.31E+03

	5p* + * >> s6* + H*	-	-0.14	-	8.89E+11	1.85E+14	-	4.08E+11	2.05E+13	-	1.92E+11	2.24E+12
	s6* + H* >> 5p *	-	0.14	-	2.39E+14	1.15E+12	-	5.21E+14	1.04E+13	-	1.11E+15	9.51E+13
R6	GUA* > TS6 > 6p*	1.44	-2.29	-	1.41E+15	1.33E+06	-	2.09E+15	3.51E+06	-	2.87E+15	9.13E+06
	6p* > TS6 > GUA*	3.73	2.29	-	2.23E+15	2.08E-11	-	3.02E+15	5.48E-11	-	3.80E+15	1.38E-10
	6p* + * >> s7* + CH3*	-	0.07	-	7.78E+12	1.65E+12	-	6.82E+12	1.24E+12	-	6.06E+12	9.34E+11
	s7* + CH3* >> 6p* +*	-	-0.07	-	2.73E+13	1.29E+14	-	3.12E+13	1.71E+14	-	3.51E+13	2.28E+14
R7	GUA* > TS7 > 7p*	0.62	-0.65	-	1.21E+13	2.01E+09	-	1.13E+13	1.56E+09	-	1.07E+13	1.24E+09
	7p* > TS7 > GUA*	1.27	0.65	-	2.54E+13	3.69E+04	-	2.64E+13	3.83E+04	-	2.69E+13	3.94E+04
	7p* + * >> s8*+ H*	-	-0.36	-	1.49E+13	8.10E+15	-	1.43E+13	7.27E+15	-	1.38E+13	6.54E+15
	s8* + H* >> 7p+ *	-	0.36	-	1.43E+13	2.63E+10	-	1.48E+13	2.93E+10	-	1.54E+13	3.26E+10
R8	1p* > TS8 > 8p*	0.75	-0.46	-	2.83E+13	4.32E+08	-	2.93E+13	4.59E+08	-	3.03E+13	4.98E+08
	8p* > TS8 > 1p*	1.21	0.46	-	1.41E+14	3.78E+05	-	1.51E+14	5.62E+05	-	1.56E+14	7.90E+05
	8p* + * >> s9* +H*	-	-0.12	-	2.15E+13	2.71E+14	-	2.18E+13	2.70E+14	-	2.17E+13	2.64E+14
	s9* + H* >> 8p*+ *	-	0.12	-	9.89E+12	7.85E+11	-	9.77E+12	7.89E+11	-	9.79E+12	8.05E+11
R9	1p* > TS9 > 9p*	0.37	-2.05	-	2.77E+14	3.68E+12	-	3.31E+14	6.24E+12	-	3.79E+14	1.04E+13
	9p* > TS9 > 1p*	2.42	2.05	-	4.46E+13	3.28E-04	-	4.49E+13	3.73E-04	-	4.51E+13	4.23E-04
	9p* + * >> s26* + OCH3*	-	-0.5	-	1.15E+11	2.26E+14	-	7.06E+10	5.33E+13	-	4.67E+10	1.34E+13
	s26* + OCH3* >> 9p*+ *	-	0.5	-	1.85E+15	9.43E+11	-	3.01E+15	3.99E+12	-	4.56E+15	1.59E+13
R10	2p* >> 10p*	-	-2.16	-	2.68E+13	9.58E+28	-	3.04E+13	1.23E+29	-	3.37E+13	1.58E+29
	10p* >> 2p*	-	2.16	-	7.94E+12	2.22E-03	-	7.01E+12	1.73E-03	-	6.31E+12	1.34E-03
	10p* + * >> s11* +OH*	-	-0.4	-	3.48E+12	1.12E+15	-	2.96E+12	7.47E+14	-	2.58E+12	5.02E+14
	s11 + OH* >> 10p+ *	-	0.4	-	6.12E+13	1.91E+11	-	7.18E+13	2.85E+11	-	8.24E+13	4.24E+11
R11	s4+ H* >> 11r+ *	-	-0.04	-	1.58E+13	2.48E+13	-	1.65E+13	2.81E+13	-	1.74E+13	3.20E+13
	11r* + * >> s4*+ H*	-	0.04	-	1.35E+13	8.56E+12	-	1.29E+13	7.58E+12	-	1.22E+13	6.65E+12
	11r* > TS11 > 11p*	0.97	-0.29	-	7.06E+13	2.13E+07	-	8.24E+13	3.07E+07	-	9.31E+13	4.33E+07
	11p* > TS11 > 11r*	1.26	0.29	-	5.50E+13	4.94E+05	-	6.42E+13	6.22E+05	-	7.34E+13	7.95E+05
R12	s5* + H* >> 12r +*	-	-0.02	-	1.60E+13	2.07E+13	-	1.68E+13	2.36E+13	-	1.78E+13	2.71E+13
	12r* +* >> s5* +H*	-	0.02	-	1.33E+13	1.03E+13	-	1.26E+13	9.03E+12	-	1.20E+13	7.86E+12
	12r* > TS12 > s26*	1.16	-0.29	-	6.48E+13	7.57E+05	-	7.50E+13	1.08E+06	-	8.38E+13	1.49E+06

	s26* > TS12 > 12r*	1.45	0.29	-	1.43E+14	7.28E+04	-	1.77E+14	1.11E+05	-	2.11E+14	1.70E+05
R13	13r* > TS13 > 13p*	0.79	-0.22	-	1.86E+15	8.08E+08	-	4.53E+15	9.85E+09	-	1.04E+16	1.19E+11
	13p* > TS13 > 13r*	1.01	0.22	-	1.31E+14	2.06E+07	-	1.47E+14	3.02E+07	-	1.60E+14	4.34E+07
	13p * + * >> s5* +OCH2*	-	-0.78	-	1.04E+13	4.50E+18	-	9.21E+12	3.46E+18	-	8.24E+12	2.65E+18
	s5* +OCH2* >> 13p*+ *	-	0.78	-	2.05E+13	4.73E+07	-	2.31E+13	6.15E+07	-	2.58E+13	8.02E+07
R14	14r* > TS14 > 14p*	0.82	-1.58	-	5.70E+14	3.63E+08	-	1.24E+15	3.05E+09	-	2.64E+15	2.63E+10
	14p* > TS14 > 14r*	2.4	1.58	-	1.44E+14	2.50E-03	-	1.63E+14	3.77E-03	-	1.79E+14	5.51E-03
	14p*+ * >> s12*+ H*	-	0.14	-	1.31E+13	1.39E+12	-	1.23E+13	1.21E+12	-	1.16E+13	1.04E+12
	s12*+ H* >> 14p*+ *	-	-0.14	-	1.63E+13	1.53E+14	-	1.73E+13	1.76E+14	-	1.84E+13	2.04E+14
R15	15r* > TS15 > 15p*	0.49	-2.08	-	5.63E+14	2.43E+10	-	1.20E+15	2.16E+11	-	2.48E+15	1.92E+12
	15p* > TS15 > 15r*	2.57	2.08	-	1.96E+13	4.78E-06	-	1.76E+13	4.34E-06	-	1.60E+13	3.95E-06
	15p* + * >> s7*+ CH2*	-	0.08	-	7.86E+12	1.53E+12	-	6.91E+12	1.16E+12	-	6.15E+12	8.82E+11
	s7* + CH2* >> 15p*+ *	-	-0.08	-	2.71E+13	1.39E+14	-	3.08E+13	1.83E+14	-	3.46E+13	2.41E+14
R16	s7* + H* >> 16r* + *	-	-0.03	-	1.47E+13	2.23E+13	-	1.54E+13	2.49E+13	-	1.62E+13	2.83E+13
	16r* + * >> s7* +H*	-	0.03	-	1.45E+13	9.56E+12	-	1.38E+13	8.53E+12	-	1.31E+13	7.53E+12
	16r* > TS16 > 16p*	1.81	1.43	-	1.94E+14	8.80E+01	-	2.30E+14	1.43E+02	-	2.61E+14	2.27E+02
	16p* > TS16 > 16r*	0.38	-1.43	-	1.17E+14	3.13E+12	-	1.31E+14	4.06E+12	-	1.44E+14	5.37E+12
R17	s7* + H* >> 17r*+ *	-	0.54	-	1.14E+13	7.98E+08	-	1.15E+13	8.43E+08	-	1.17E+13	8.92E+08
	17r* + * >> s7* +H*	-	-0.54	-	1.86E+13	2.67E+17	-	1.85E+13	2.52E+17	-	1.82E+13	2.39E+17
	17r* > TS17 > 17p*	2.46	0.52	-	1.32E+13	1.11E-04	-	1.33E+13	9.74E-05	-	1.33E+13	8.60E-05
	17p* > TS17 > 17r*	1.95	-0.52	-	2.47E+13	4.31E+00	-	2.71E+13	4.17E+00	-	2.92E+13	4.11E+00
R18	18r* > TS18 > 18p*	1.03	-1.19	-	8.30E+13	1.44E+07	-	9.39E+13	2.00E+07	-	1.04E+14	2.80E+07
	18p* > TS18 > 18r*	2.22	1.19	-	2.32E+14	1.03E-01	-	2.59E+14	1.62E-01	-	2.82E+14	2.49E-01
	18p* + * >> s15* +OH*	-	0.22	-	8.64E+12	1.57E+11	-	7.68E+12	1.22E+11	-	6.90E+12	9.43E+10
	s15* + OH* >> 18p* +*	-	-0.22	-	2.46E+13	1.36E+15	-	2.77E+13	1.75E+15	-	3.08E+13	2.26E+15
R19	19r* > TS19 > 19p*	0.39	-1.99	-	7.42E+13	5.60E+11	-	8.75E+13	7.82E+11	-	1.00E+14	1.09E+12
	19p* > TS19 > 19r*	2.38	1.99	-	6.00E+13	1.23E-03	-	6.52E+13	1.56E-03	-	6.96E+13	1.97E-03
	19p* + * >> s15* +OCH3*	-	0.4	-	3.43E+11	3.98E+08	-	2.19E+11	1.10E+08	-	1.49E+11	3.18E+07
	s15* + OCH3* >> 19p* +*	-	-0.4	-	6.20E+14	5.34E+17	-	9.72E+14	1.94E+18	-	1.43E+15	6.69E+18

R20	20r* > TS20 > 20p*	0.78	-0.54	-	3.66E+13	7.88E+08	-	4.12E+13	9.15E+08	-	4.59E+13	1.10E+09
	20p* > TS20 > 20r*	1.32	0.54	-	1.83E+14	1.78E+05	-	2.12E+14	2.89E+05	-	2.35E+14	4.54E+05
	20p* + * >> s12* +H*	-	-0.53	-	1.02E+13	7.03E+16	-	9.91E+12	6.08E+16	-	9.57E+12	5.26E+16
	s12* + H* >> 20p* +*	-	0.53	-	2.08E+13	3.03E+09	-	2.15E+13	3.50E+09	-	2.22E+13	4.04E+09
R21	21r* >> 21p*	-	-1.94	-	1.06E+13	2.45E+27	-	1.15E+13	2.49E+27	-	1.23E+13	2.57E+27
	21p* >> 21r*	-	1.94	-	2.00E+13	8.70E-02	-	1.86E+13	8.55E-02	-	1.73E+13	8.29E-02
	21p* + * >> s17* +CH2*	-	-0.03	-	1.35E+13	1.82E+13	-	1.26E+13	1.59E+13	-	1.18E+13	1.38E+13
	s17* + CH2* >> 21p* +*	-	0.03	-	1.58E+13	1.17E+13	-	1.69E+13	1.34E+13	-	1.81E+13	1.54E+13
R22	11p* > TS22 > 22p*	1.02	-0.52	-	2.57E+13	8.67E+06	-	2.85E+13	9.34E+06	-	3.14E+13	1.05E+07
	22p* > TS22 > 11p*	1.54	0.52	-	7.36E+13	1.17E+03	-	8.19E+13	1.61E+03	-	8.87E+13	2.16E+03
	22p* + * >> s18*+ H*	-	-0.15	-	1.67E+13	3.21E+14	-	1.66E+13	3.01E+14	-	1.63E+13	2.81E+14
	s18* + H* >> 22p* +*	-	0.15	-	1.27E+13	6.64E+11	-	1.28E+13	7.06E+11	-	1.30E+13	7.58E+11
R23	23r* >> 23p*	-	-2.05	-	2.00E+13	2.97E+28	-	2.18E+13	3.33E+28	-	2.35E+13	3.73E+28
	23p* >> 23r*	-	2.05	-	1.06E+13	7.17E-03	-	9.74E+12	6.40E-03	-	9.04E+12	5.70E-03
	23p* + * >> s19*+ CH2*	-	0.07	-	7.96E+12	1.72E+12	-	7.02E+12	1.32E+12	-	6.27E+12	1.00E+12
	s19* + OCH3* >> 19p*+ *	-	-0.07	-	2.67E+13	1.23E+14	-	3.03E+13	1.62E+14	-	3.39E+13	2.12E+14
R24	16p* > TS24 > 24p*	0.18	-1.12	-	6.01E+13	9.12E+12	-	6.83E+13	1.22E+13	-	7.60E+13	1.65E+13
	24p* > TS24 > 16p*	1.3	1.12	-	4.89E+13	4.36E+04	-	5.12E+13	5.17E+04	-	5.30E+13	6.12E+04
	24p* + * >> s5* +OH*	-	0.01	-	8.68E+12	5.15E+12	-	7.67E+12	3.97E+12	-	6.86E+12	3.06E+12
	s5* + OH* >> 24p* +*	-	-0.01	-	2.45E+13	4.13E+13	-	2.77E+13	5.36E+13	-	3.10E+13	6.96E+13
R25	16p* + H* >> 25r* +*	-	0.44	-	1.34E+13	5.48E+09	-	1.36E+13	5.93E+09	-	1.38E+13	6.42E+09
	25r* + * >> 16p* +H*	-	-0.44	-	1.59E+13	3.88E+16	-	1.57E+13	3.59E+16	-	1.54E+13	3.31E+16
	25r* >> 25p*	-	2.98	-	1.58E+13	1.73E-08	-	1.55E+13	1.54E-08	-	1.52E+13	1.37E-08
	25p* >> 25r*	-	-2.98	-	1.35E+13	1.23E+34	-	1.37E+13	1.38E+34	-	1.40E+13	1.55E+34
R26	17p* > TS26 > 26p*	0.09	-1.87	-	1.64E+13	4.40E+12	-	1.68E+13	4.56E+12	-	1.71E+13	4.73E+12
	26p* > TS26 > 17p*	1.95	1.87	-	1.29E+13	9.27E-02	-	1.18E+13	8.16E-02	-	1.10E+13	7.16E-02
	26p* + * >> s19*+ OH*	-	-0.6	-	8.69E+12	1.53E+17	-	7.94E+12	1.22E+17	-	7.30E+12	9.75E+16
	s19* + OH* >> 26p*+ *	-	0.6	-	2.45E+13	1.39E+09	-	2.68E+13	1.74E+09	-	2.91E+13	2.18E+09
R27	s15* + H* >> 27r* +*	-	-0.66	-	1.22E+13	5.80E+17	-	1.27E+13	6.35E+17	-	1.34E+13	7.06E+17

	27r* + * >> s15* +H*	-	0.66	-	1.74E+13	3.67E+08	-	1.67E+13	3.35E+08	-	1.59E+13	3.01E+08
	27r* > TS27 > s19*	1.15	0.23	-	7.30E+13	9.72E+05	-	8.63E+13	1.44E+06	-	9.81E+13	2.07E+06
	s19* > TS27 > 27r*	0.92	-0.23	-	4.09E+13	8.27E+07	-	4.83E+13	1.03E+08	-	5.56E+13	1.29E+08
R28	28r* >> 28p*	-	-2.31	-	1.87E+13	2.54E+30	-	2.09E+13	2.86E+30	-	2.30E+13	3.23E+30
	28p* >> 28r*	-	2.31	-	1.14E+13	8.39E-05	-	1.02E+13	7.45E-05	-	9.25E+12	6.59E-05
	28p*+ * >> s23* +CH2*	-	0.06	-	7.75E+12	1.91E+12	-	6.83E+12	1.45E+12	-	6.10E+12	1.10E+12
	s23* + CH2* >> 28p* +*	-	-0.06	-	2.74E+13	1.11E+14	-	3.11E+13	1.46E+14	-	3.49E+13	1.93E+14
R29	s17* + H* >> 29r* +*	-	0.23	-	1.19E+13	2.25E+11	-	1.24E+13	2.42E+11	-	1.29E+13	2.64E+11
	29r* + * >> s17*+ H*	-	-0.23	-	1.78E+13	9.43E+14	-	1.72E+13	8.80E+14	-	1.65E+13	8.07E+14
	29r* > TS29 > 25p*	1.22	3.61	-	1.07E+14	5.05E+05	-	1.20E+14	7.15E+05	-	1.30E+14	9.89E+05
	25p* > TS29 > 29r*	-2.39	-3.61	-	2.92E+13	4.98E+30	-	3.08E+13	6.04E+30	-	3.24E+13	7.38E+30
R30	s19* + H* >> 30r* +*	-	-0.03	-	1.50E+13	2.19E+13	-	1.57E+13	2.46E+13	-	1.65E+13	2.79E+13
	30r* + * >> s19* +H*	-	0.03	-	1.42E+13	9.72E+12	-	1.35E+13	8.66E+12	-	1.29E+13	7.63E+12
	30r* > TS30 > s26*	2.19	1.41	-	5.97E+13	3.00E-02	-	6.86E+13	4.11E-02	-	7.64E+13	5.54E-02
	s26* > TS30 > 30r*	0.78	-1.41	-	3.19E+13	6.73E+08	-	3.46E+13	7.20E+08	-	3.74E+13	7.91E+08
R31	25p* >> 31p*	-	-4.47	-	1.96E+13	4.79E+44	-	2.19E+13	6.78E+44	-	2.40E+13	9.44E+44
	31p* >> 25p*	-	4.47	-	1.08E+13	4.44E-19	-	9.72E+12	3.14E-19	-	8.85E+12	2.25E-19
	31p*+ * >> s26* +OH*	-	-0.39	-	3.97E+12	1.09E+15	-	3.37E+12	7.39E+14	-	2.93E+12	5.02E+14
	s26* + OH* >> 31p*+ *	-	0.39	-	5.35E+13	1.95E+11	-	6.31E+13	2.88E+11	-	7.27E+13	4.24E+11
R32	s23*+ H* >> 32r*+ *	-	-0.01	-	1.54E+13	1.57E+13	-	1.62E+13	1.78E+13	-	1.70E+13	2.03E+13
	32r*+ * >> s23*+ H*	-	0.01	-	1.38E+13	1.35E+13	-	1.32E+13	1.20E+13	-	1.25E+13	1.05E+13
	32r* > TS32 > s7*	2.28	1.69	-	1.89E+14	2.99E-02	-	2.25E+14	4.95E-02	-	2.58E+14	7.98E-02
	s7* > TS32 > 32r*	0.58	-1.69	-	3.11E+13	1.91E+10	-	3.32E+13	2.00E+10	-	3.55E+13	2.16E+10
R33	s26* > TS33 > 33p*	1.5	-0.73	-	7.27E+13	6.05E+03	-	8.62E+13	8.53E+03	-	9.91E+13	1.20E+04
	33p* > TS33 > s26*	2.23	0.73	-	9.99E+13	3.06E-02	-	1.12E+14	4.26E-02	-	1.22E+14	5.82E-02
	33p* + * >> s25*+ OH*	-	-0.11	-	9.14E+12	4.20E+13	-	8.14E+12	3.28E+13	-	7.32E+12	2.56E+13
	s25* + OH* >> 33p*+ *	-	0.11	-	2.33E+13	5.06E+12	-	2.61E+13	6.48E+12	-	2.91E+13	8.32E+12
R34	s26*+ H* >> 34r*+ *	-	0.9	-	3.53E+13	1.30E+07	-	3.72E+13	1.64E+07	-	3.90E+13	2.06E+07
	34r* + * >> s26*+ H*	-	-0.9	-	6.03E+12	1.63E+19	-	5.72E+12	1.29E+19	-	5.46E+12	1.03E+19

	34r* > TS34 > 34p*	2.06	0.57	-	1.66E+14	5.05E+00	-	1.98E+14	7.46E+00	-	2.29E+14	1.12E+01
	34p* > TS34 > 34r*	1.49	-0.57	-	3.45E+14	6.53E+05	-	4.54E+14	1.09E+06	-	5.76E+14	1.90E+06
R35	s25* + H* >> 35r* +*	-	0.48	-	2.83E+13	1.33E+10	-	3.04E+13	1.64E+10	-	3.26E+13	2.04E+10
	35r* + * >> s25*+ H*	-	-0.48	-	7.52E+12	1.60E+16	-	6.99E+12	1.29E+16	-	6.52E+12	1.04E+16
	35r* > TS35 > 35p*	0.75	-0.5	-	5.26E+13	5.33E+08	-	6.09E+13	7.34E+08	-	6.81E+13	9.88E+08
	35p* > TS35 > 35r*	1.25	0.5	-	3.70E+13	4.16E+05	-	4.31E+13	4.96E+05	-	4.93E+13	6.02E+05
R36	34p* > TS36 > 36p*	0.5	-1.94	-	1.83E+13	6.63E+09	-	1.84E+13	6.39E+09	-	1.84E+13	6.17E+09
	36p* > TS36 > 34p*	2.45	1.94	-	4.58E+12	5.20E-06	-	3.70E+12	3.33E-06	-	3.07E+12	2.14E-06
	34p* + * >> s29* +OH*	-	-2.33	-	1.60E+13	1.42E+30	-	1.69E+13	1.44E+30	-	1.75E+13	1.47E+30
	s29* + OH* >> 34p* +*	-	2.33	-	1.33E+13	1.50E-04	-	1.26E+13	1.48E-04	-	1.21E+13	1.45E-04
R37	CH2*+ H* >> 37r+ *	-	0.28	-	1.85E+13	2.04E+11	-	2.01E+13	2.44E+11	-	2.17E+13	2.96E+11
	37r* + * >> CH2*+ H*	-	-0.28	-	1.15E+13	1.04E+15	-	1.06E+13	8.71E+14	-	9.79E+12	7.19E+14
	37r* > TS37 > CH3*	0.72	0.14	-	1.90E+13	1.08E+08	-	1.92E+13	1.16E+08	-	1.93E+13	1.22E+08
	CH3* > TS37 > 37r*	0.58	-0.14	-	2.11E+13	5.22E+09	-	2.30E+13	5.64E+09	-	2.48E+13	6.21E+09
R38	CH3* + H* >> 38r* +*	-	0.49	-	1.81E+13	4.65E+09	-	1.95E+13	5.62E+09	-	2.10E+13	6.78E+09
	38r* + * >> CH3*+ H*	-	-0.49	-	1.17E+13	4.57E+16	-	1.09E+13	3.79E+16	-	1.01E+13	3.14E+16
	38r* > TS38 > CH4*	1.56	1.25	-	7.62E+13	7.04E+02	-	8.21E+13	9.37E+02	-	8.62E+13	1.21E+03
	CH4* > TS38 > 38r*	0.3	-1.25	-	8.31E+11	9.00E+09	-	7.63E+11	5.19E+09	-	7.30E+11	3.19E+09
R39	OH* + H* >> 39r* +*	-	0.02	-	1.61E+13	1.09E+13	-	1.70E+13	1.25E+13	-	1.80E+13	1.44E+13
	39r + * >> OH*+H*	-	-0.02	-	1.32E+13	1.95E+13	-	1.25E+13	1.70E+13	-	1.18E+13	1.47E+13
	39r > TS39 > H2O*	2.15	1.65	-	9.33E+13	1.10E-01	-	1.08E+14	1.58E-01	-	1.21E+14	2.25E-01
	H2O* > TS39 > 39r*	0.5	-1.65	-	1.29E+13	2.09E+10	-	1.34E+13	1.90E+10	-	1.41E+13	1.81E+10
R40	OCH2* H* >> 40r *	-	0.11	-	1.68E+13	2.47E+12	-	1.80E+13	2.89E+12	-	1.93E+13	3.42E+12
	40r*+ * >> OCH2*+ H*	-	-0.11	-	1.27E+13	8.61E+13	-	1.18E+13	7.36E+13	-	1.10E+13	6.23E+13
	40r* > TS40 > OCH3*	0.85	0.17	-	5.36E+13	3.87E+07	-	5.91E+13	5.33E+07	-	6.32E+13	7.04E+07
	OCH3* > TS40 > 40r*	0.68	-0.17	-	1.46E+14	4.63E+09	-	2.12E+14	1.13E+10	-	2.95E+14	2.73E+10
R41	OCH3* H* >> 41r *	-	-0.01	-	1.51E+14	7.24E+13	-	2.07E+14	1.93E+14	-	2.73E+14	4.94E+14
	41r* + * >> OCH3* +H*	-	0.01	-	1.41E+12	2.94E+12	-	1.03E+12	1.10E+12	-	7.79E+11	4.30E+11
	41r* > TS41 > CH3OH*	2.45	2.14	-	3.77E+14	6.27E-03	-	4.75E+14	1.17E-02	-	5.66E+14	2.14E-02

	CH3OH* > TS41 > 41r*	0.31	-2.14	-	7.10E+13	5.58E+12	-	8.07E+13	6.91E+12	-	9.02E+13	8.74E+12
R42	s26* >> phenol+ *	-	4.45	-	8.91E+24	3.49E+01	-	8.24E+24	2.25E+03	-	7.41E+24	1.43E+05
	phenol + * >> s26*	-	-4.45	1.46E-05	1.26E+04	1.84E-01	3.82E-06	1.26E+04	4.81E-02	1.12E-06	1.26E+04	1.42E-02
R43	16p* >> catechol +*	-	4.26	-	9.24E+24	6.63E+02	-	8.24E+24	4.40E+04	-	7.20E+24	2.87E+06
	catechol + * >> 16p*	-	-4.26	2.59E-06	1.16E+04	3.01E-02	5.50E-07	1.16E+04	6.39E-03	1.35E-07	1.16E+04	1.58E-03
R44	s29* >> benzene +*	-	4.06	-	2.18E+22	1.18E+00	-	1.79E+22	2.54E+01	-	1.46E+22	5.49E+02
	benzene + * >> s29*	-	-4.06	8.83E-05	1.38E+04	1.22E+00	2.84E-05	1.38E+04	3.92E-01	1.00E-05	1.38E+04	1.38E-01
R45	CH4* >> CH4 +*	-	0.38	-	1.19E+19	5.16E+21	-	1.04E+19	4.18E+22	-	9.06E+18	3.51E+23
	CH4 + * >> CH4*	-	-0.38	9.82E-04	3.05E+04	2.99E+01	5.97E-04	3.05E+04	1.82E+01	3.87E-04	3.05E+04	1.18E+01
R46	CH3OH* >> CH3OH +*	-	1.18	-	1.95E+22	1.31E+21	-	1.98E+22	3.82E+22	-	1.94E+22	1.13E+24
	CH3OH + * >> CH3OH*	-	-1.18	2.74E-04	2.16E+04	5.91E+00	1.48E-04	2.16E+04	3.20E+00	8.60E-05	2.16E+04	1.86E+00
R47	H2O* >> H2O+ *	-	1.07	-	4.19E+20	6.31E+18	-	4.73E+20	1.22E+20	-	5.08E+20	2.33E+21
	H2O + * >> H2O*	-	-1.07	5.67E-04	2.88E+04	1.63E+01	3.96E-04	2.88E+04	1.14E+01	2.92E-04	2.88E+04	8.40E+00
R48	H2* >> H2+ *	-	0.79	-	4.91E+18	5.82E+16	-	6.88E+18	8.09E+17	-	8.82E+18	1.08E+19
	H2 + * >> H2*	-	-0.79	9.89E-04	8.60E+04	8.51E+01	7.53E-04	8.60E+04	6.47E+01	5.97E-04	8.60E+04	5.14E+01
R49	H* + H* >> 49r*+ *	-	0	-	1.57E+13	1.38E+13	-	1.64E+13	1.55E+13	-	1.72E+13	1.76E+13
	49r* + * >> H* +H*	-	0	-	1.35E+13	1.54E+13	-	1.29E+13	1.37E+13	-	1.23E+13	1.21E+13
R50	49r *>> H2*	-	1.46	-	3.83E+13	1.39E+03	-	4.29E+13	1.87E+03	-	4.64E+13	2.41E+03
	H2* >> 49r*	-	-1.46	-	5.55E+12	1.53E+23	-	4.96E+12	1.14E+23	-	4.58E+12	8.82E+22

Sample input DFT files for simulating solvated system, gas phase system and periodic catalytic system using Gaussian 09 and FHI-aims.

Geometry optimization and frequency calculation in solvated system for guaiacol in Gaussian 09:

```
%nprocshared=2
%mem=7GB
%chk=C:\Users\workstation\Desktop\min.chk
#   opt=calcfc   freq   6-311+g(d,p)   scrf=(smd,solvent=water)
geom=connectivity
int=ultrafine m062x

Title Card Required

0 1
 C                  0.32903380   -0.54748263   -0.24638613
 C                 -0.04544592    0.79145354   -0.07049742
 C                 -1.38600385    1.11761191    0.17536253
 C                 -2.35208145    0.10483378    0.24533755
 C                 -1.97760177   -1.23410236    0.06944860
 C                 -0.63704418   -1.56026056   -0.17641343
 H                 -1.67192745    2.13991940    0.30965732
 H                 -3.37562712    0.35386291    0.43305746
 H                 -2.71522349   -2.00738092    0.12287590
 H                 -0.35112054   -2.58256807   -0.31070796
 O                  1.69694981   -0.88029717   -0.49726511
 O                  0.94034817    1.82490027   -0.14189666
 H                  1.64244914    1.55669963   -0.73915928
 C                  1.78837079   -2.24956912   -0.89930557
 H                  1.21576780   -2.39851444   -1.79084419
 H                  2.81191634   -2.49859817   -1.08702621
 H                  1.40583414   -2.87615486   -0.12087381

 1 2 1.5 6 1.5 11 1.0
 2 3 1.5 12 1.0
 3 4 1.5 7 1.0
 4 5 1.5 8 1.0
 5 6 1.5 9 1.0
 6 10 1.0
 7
```

```
8
9
10
11 14 1.0
12 13 1.0
13
14 15 1.0 16 1.0 17 1.0
15
16
17
```

Transition state calculation and frequency calculation for the transition state by Berny method with only one guess image in solvated system in Gaussian 09:

```
%nprocshared=24
%mem=30GB
%chk=3.chk
#      opt=(calcfc,ts,maxcycles=250)      freq      6-311+g(d,p)
scrf=(smd,solvent=water)
m062x int=ultrafine

Title Card Required

0 2
 C                 -0.47635300   -0.75507900   -0.00675500
 C                 -0.53467400    0.65893000    0.05560200
 C                  0.65358400    1.40651500   -0.06001200
 C                  1.87872800    0.75894300   -0.04178600
 C                  1.92853200   -0.63965100   -0.00221900
 C                  0.75824800   -1.39426300    0.00359900
 H                  0.58974100    2.48755800   -0.11252600
 H                  2.88696400   -1.14526500    0.00357300
 H                  0.78383300   -2.47712800    0.00025500
 O                 -1.62051400   -1.47619500   -0.03346100
 H                 -2.36015500   -0.85172900   -0.06540300
 O                 -1.79429700    1.19854900   -0.18433600
 H                  2.79470100    1.33593500   -0.07946400
 H                 -1.95389100    1.93440400    0.41661000
 H                 -0.67108700    0.72502600    1.88876400
```

Transition state calculation and frequency calculation for the transition state by Synchronous Transit-Guided Quasi-Newton (QST2) method with reactant and product images:

```
%nprocshared=24
%mem=30GB
%chk=2i_aq.chk
# opt=(calcfc,qst2,maxcycles=250) freq 6-311+g(d,p)
scrf=(smd,solvent=water) m062x int=ultrafine

Title Card Required

0 2
 C                 -1.33046100    1.33014100    0.03244400
 C                 -2.23518500    0.27588100   -0.05991900
 C                 -1.76026400   -1.03734400   -0.07335900
 C                 -0.39608400   -1.29427000   -0.00365300
 C                  0.50101900   -0.22789900    0.07900200
 C                  0.04188700    1.08900100    0.10667100
 H                 -1.68922300    2.35301000    0.05786700
 H                 -3.29926800    0.47246200   -0.11554200
 H                 -2.45565500   -1.86631200   -0.14104200
 H                  0.73880600    1.91037200    0.21053700
 O                  1.83389400   -0.56578700    0.16113700
 C                  2.79275800    0.34678000   -0.14708500
 H                  2.56778400    1.09897500   -0.89419000
 H                  3.79285000   -0.03025900    0.00495800
 H                 -0.00846300   -2.30569300   -0.01629400

Title Card Required

0 2
 C                 -1.33046100    1.33014100    0.03244400
 C                 -2.23518500    0.27588100   -0.05991900
 C                 -1.76026400   -1.03734400   -0.07335900
 C                 -0.39608400   -1.29427000   -0.00365300
 C                  0.50101900   -0.22789900    0.07900200
 C                  0.04188700    1.08900100    0.10667100
 H                 -1.68922300    2.35301000    0.05786700
 H                 -3.29926800    0.47246200   -0.11554200
 H                 -2.45565500   -1.86631200   -0.14104200
 H                  0.73880600    1.91037200    0.21053700
 O                  1.87916900   -0.61408980    0.23761865
 C                  1.47580032    0.10057810   -1.01274164
```

H	1.31388099	-0.50389708	-1.89759665
H	2.23868676	0.86323961	-0.97018369
H	-0.00846300	-2.30569300	-0.01629400

Transition state calculation and frequency calculation for the transition state by Synchronous Transit-Guided Quasi-Newton (QST3) method with reactant, product and an intermediate guess image for solvated system in Gaussian 09:

```
%nprocshared=24
%mem=30GB
%chk=1.chk
# opt=(calcfc,qst3,maxcycles=250) freq 6-311+g(d,p)
scrf=(smd,solvent=water) geom=connectivity int=ultrafine m062x

Title Card Required

0 1
 C                  0.36848246   -0.50072671   -0.05103157
 C                 -0.06318500    0.83214678   -0.08317833
 C                 -1.42679597    1.13026313    0.04177655
 C                 -2.35873918    0.09550616    0.19888100
 C                 -1.92707177   -1.23736736    0.23102731
 C                 -0.56346110   -1.53548388    0.10606954
 H                 -1.75638359    2.14794166    0.01723244
 H                 -3.39988603    0.32312483    0.29429057
 H                 -2.63863097   -2.02742721    0.35098119
 H                 -0.23387367   -2.55316252    0.13061177
 O                  1.75992229   -0.80492704   -0.17853600
 O                  0.88777776    1.88802141   -0.24348612
 H                  1.63345739    1.57159646   -0.75869204
 C                  1.91328103   -2.08396927   -0.79936776
 H                  1.46176221   -2.06608976   -1.76927037
 H                  2.95442831   -2.31158770   -0.89477317
 H                  1.43840352   -2.83127594   -0.19859817

 1 2 1.5 6 1.5 11 1.0
 2 3 1.5 12 1.0
 3 4 1.5 7 1.0
 4 5 1.5 8 1.0
 5 6 1.5 9 1.0
 6 10 1.0
 7
 8
 9
 10
 11 14 1.0
 12 13 1.0
```

```
 13
 14 15 1.0 16 1.0 17 1.0
 15
 16
 17

Title Card Required

0 1
 C                  0.32759898   -0.56970860   -0.26760243
 C                 -0.10014323    0.74990171    0.00304569
 C                 -1.43654203    1.08311689    0.26091727
 C                 -2.39200244    0.13964975    0.26218023
 C                 -2.06419762   -1.13855129    0.01361928
 C                 -0.73588675   -1.50039474   -0.24743895
 H                 -1.69874633    2.10137352    0.45916544
 H                 -3.40946212    0.40504811    0.46026985
 H                 -2.82627091   -1.88964557    0.01491772
 H                 -0.51638800   -2.52966937   -0.44060734
 O                  1.28460703   -0.95049788    0.72438300
 O                  0.75958710    1.66878004    0.01289061
 H                  0.77998637   -0.58960282   -1.23706098
 C                  1.75454970   -2.27300818    0.45048448
 H                  0.93057051   -2.95535951    0.46932482
 H                  2.21408135   -2.29530125   -0.51555572
 H                  2.47063267   -2.55793442    1.19273930

 1 2 1.5 6 1.5 11 1.0 13 1.0
 2 3 1.5 12 2.0
 3 4 2.0 7 1.0
 4 5 2.0 8 1.0
 5 6 1.5 9 1.0
 6 10 1.0
 7
 8
 9
 10
 11 14 1.0
 12
 13
 14 15 1.0 16 1.0 17 1.0
 15
 16
 17
```

```
Title Card Required

0 1
 C                  0.53512056   -0.29825893   -0.50140686
 C                  0.02826671    0.99373314   -0.20979890
 C                 -1.28535629    1.23347036    0.21575192
 C                 -2.17229071    0.18276297    0.37448413
 C                 -1.73617804   -1.10301817    0.10539832
 C                 -0.42018843   -1.33048990   -0.31957320
 H                 -1.60441587    2.23434805    0.41908619
 H                 -3.17613891    0.36112201    0.69910211
 H                 -2.40752149   -1.92793351    0.22249940
 H                 -0.11979438   -2.33816596   -0.51769531
 O                  1.64379700   -0.55310073    0.36507581
 O                  0.80029798    1.97887619   -0.34030346
 H                  1.06350428    0.75270047   -0.84668005
 C                  2.19858969   -1.83635252    0.06445994
 H                  2.52994795   -1.85224111   -0.95281547
 H                  3.02815878   -2.02703834    0.71280710
 H                  1.45278694   -2.58997351    0.20845182

 1 2 1.5 6 1.5 11 1.0
 2 3 1.5 12 2.0
 3 4 2.0 7 1.0
 4 5 2.0 8 1.0
 5 6 1.5 9 1.0
 6 10 1.0
 7
 8
 9
 10
 11 14 1.0
 12
 13
 14 15 1.0 16 1.0 17 1.0
 15
 16
 17
```

Intrinsic reaction coordinate (IRC) calculation for the transition state for solvated system in Gaussian 09:

```
%nprocshared=24
%mem=30GB
%chk=2i_irc.chk
# irc=(maxpoints=210,recorrect=never,calcfc) 6-311+g(d,p)
scrf=(smd,solvent=water) int=ultrafine m062x

Title Card Required

0 2
 C                  1.44563500    1.21022600    0.04886700
 C                  2.13666400    0.00013400    0.17831500
 C                  1.44584900   -1.21008700    0.04896700
 C                  0.08221000   -1.22608700   -0.17724300
 C                 -0.62565600   -0.00013900   -0.23051100
 C                  0.08200300    1.22593900   -0.17736800
 H                  1.98481900    2.14853800    0.10940800
 H                  3.20575600    0.00023100    0.35034200
 H                  1.98520300   -2.14829700    0.10957300
 H                 -0.46629100    2.15346400   -0.29399300
 O                 -1.97392000   -0.00013400   -0.63209500
 C                 -2.16662400    0.00010200    0.75341900
 H                 -2.42644700   -0.94966700    1.20446900
 H                 -2.42630800    0.95000600    1.20425800
 H                 -0.46585800   -2.15373000   -0.29396500
```

Geometry optimization and frequency calculation for the gas phase system in Gaussian 09

```
%nprocshared=24
%mem=30GB
%chk=Q.chk
#     opt=calcfc     freq     6-31+g(d,p)     geom=connectivity
empiricaldispersion=gd3
int=ultrafine m062x

Title Card Required

0 2
 C                 -1.42567400    3.68003300   -0.00044900
 C                 -0.67441900    4.89973300   -0.00024800
 C                  0.68167400    4.89341400   -0.00002900
 C                  0.70670100    2.43837600   -0.00013700
 C                  1.42835100    3.67010400    0.00020200
 C                  2.81946800    3.66143000    0.00021100
 C                  2.81809300    1.22117200    0.00053300
 C                  3.52832800    2.46154700    0.00005400
 C                  4.95644700    2.42599300   -0.00005600
 C                  4.95022300    0.00000300   -0.00010700
 C                  5.63648100    1.24692300   -0.00017700
 C                 -5.64766200    1.24331800   -0.00029100
 C                 -4.96580900    2.42758400   -0.00040200
 C                 -3.53986500    2.46269800   -0.00062200
 C                 -2.82521700    3.66470100   -0.00050200
 C                 -3.54538000   -0.00000100   -0.00399300
 C                 -2.83080600    1.22264700    0.00490000
 C                 -1.40902000    1.22215000   -0.00262200
 C                 -0.71483800    2.45616100    0.00139700
 C                 -1.40901900   -1.22215300   -0.00262500
 C                 -0.70344600   -0.00000200    0.00225400
 C                  1.40831700    1.21656500    0.00001500
 C                  0.70670400   -2.43837800   -0.00013400
 C                  1.40831800   -1.21656600    0.00001700
 C                  2.81809400   -1.22117100    0.00053900
 C                  3.54376600    0.00000100   -0.00058300
 C                  2.81947300   -3.66142700    0.00022500
 C                  3.52833100   -2.46154400    0.00006600
 C                  4.95645000   -2.42598800   -0.00004000
 C                  5.63648300   -1.24691700   -0.00016700
 C                 -5.64766200   -1.24331800   -0.00030400
 C                 -4.96737700   -0.00000100    0.00054100
```

```
C                  -4.96580700   -2.42758600   -0.00042300
C                  -3.53986500   -2.46270000   -0.00063800
C                  -2.83080600   -1.22264900    0.00489200
C                  -2.82521500   -3.66470500   -0.00052100
C                  -1.42566900   -3.68003500   -0.00046000
C                  -0.71483500   -2.45616500    0.00139300
C                  -0.67441400   -4.89973300   -0.00025200
C                   0.68168000   -4.89341400   -0.00002300
C                   1.42835500   -3.67010400    0.00021000
H                   5.49258800    3.36971100   -0.00015200
H                   6.72242800    1.24244000   -0.00020500
H                   6.72243000   -1.24243200   -0.00019300
H                   5.49259200   -3.36970500   -0.00012900
H                   3.36099900   -4.60234300    0.00013400
H                   1.23452300   -5.82774100    0.00003700
H                  -1.21763900   -5.83991700   -0.00060800
H                  -3.36712300   -4.60568600   -0.00226800
H                  -5.50530500   -3.36961500   -0.00154500
H                  -6.73388800   -1.24158900    0.00019600
H                  -6.73388900    1.24158900    0.00021000
H                  -5.50530600    3.36961400   -0.00151500
H                  -3.36712600    4.60568200   -0.00224300
H                  -1.21764500    5.83991600   -0.00060100
H                   1.23451700    5.82774100    0.00002500
H                   3.36099200    4.60234600    0.00011500
N                   0.70760500   -0.00000100   -0.00016100

1 2 1.5 15 1.5 19 1.5
2 3 2.0 55 1.0
3 5 1.5 56 1.0
4 5 1.5 19 1.5 22 1.5
5 6 1.5
6 8 1.5 57 1.0
7 8 1.5 22 1.5 26 1.5
8 9 1.5
9 11 2.0 42 1.0
10 11 1.5 26 1.5 30 1.5
11 43 1.0
12 13 2.0 32 1.5 52 1.0
13 14 1.5 53 1.0
14 15 1.5 17 1.5
15 54 1.0
16 17 1.5 32 1.5 35 1.5
17 18 1.5
```

```
18 19 1.5 21 1.5
19
20 21 1.5 35 1.5 38 1.5
21 58 1.0
22 58 1.0
23 24 1.5 38 1.5 41 1.5
24 25 1.5 58 1.0
25 26 1.5 28 1.5
26
27 28 1.5 41 1.5 46 1.0
28 29 1.5
29 30 2.0 45 1.0
30 44 1.0
31 32 1.5 33 2.0 51 1.0
32
33 34 1.5 50 1.0
34 35 1.5 36 1.5
35
36 37 1.5 49 1.0
37 38 1.5 39 1.5
38
39 40 2.0 48 1.0
40 41 1.5 47 1.0
41
42
43
44
45
46
47
48
49
50
51
52
53
54
55
56
57
58
```

Single point energy calculation for the gas phase system in Gaussian 09

```
%nprocshared=24
%mem=30GB
%chk=Q_E.chk
#    6-311+g(d,p)    geom=connectivity    empiricaldispersion=gd3
int=ultrafine
m062x

Title Card Required

0 2
 C                  1.42826600   -3.68259400   -0.00003300
 C                  0.67353300   -4.90994400    0.00006500
 C                 -0.68073800   -4.90372100    0.00012600
 C                 -0.70991300   -2.44149900    0.00002900
 C                 -1.43100000   -3.67261100    0.00011500
 C                 -2.82211900   -3.66706600    0.00015200
 C                 -2.82197600   -1.22515900    0.00012700
 C                 -3.53089200   -2.46379100    0.00012300
 C                 -4.96496400   -2.42988800    0.00014600
 C                 -4.95309200    0.00000000    0.00011500
 C                 -5.64442900   -1.25106200    0.00013100
 C                  5.65533800   -1.24715200   -0.00032000
 C                  4.97447600   -2.43149300   -0.00024400
 C                  3.54296200   -2.46573900   -0.00019800
 C                  2.82831800   -3.67011200   -0.00008200
 C                  3.55231000    0.00000000   -0.00068300
 C                  2.83468700   -1.22586000    0.00040500
 C                  1.41106300   -1.22407900   -0.00032100
 C                  0.71792300   -2.45994700    0.00007000
 C                  1.41106300    1.22407900   -0.00032200
 C                  0.70305400    0.00000000    0.00015600
 C                 -1.41021200   -1.21849400    0.00004000
 C                 -0.70991300    2.44149900    0.00002800
 C                 -1.41021200    1.21849400    0.00004000
 C                 -2.82197600    1.22515900    0.00012700
 C                 -3.55152700    0.00000000    0.00004200
 C                 -2.82211900    3.66706600    0.00015100
 C                 -3.53089200    2.46379100    0.00012200
 C                 -4.96496400    2.42988800    0.00014600
 C                 -5.64442900    1.25106200    0.00013000
 C                  5.65533800    1.24715200   -0.00032100
 C                  4.97080900    0.00000000   -0.00019100
```

```
C                  4.97447600    2.43149300   -0.00024500
C                  3.54296200    2.46573900   -0.00019900
C                  2.83468700    1.22586000    0.00040500
C                  2.82831800    3.67011200   -0.00008300
C                  1.42826600    3.68259400   -0.00003400
C                  0.71792300    2.45994700    0.00006900
C                  0.67353300    4.90994400    0.00006400
C                 -0.68073800    4.90372100    0.00012500
C                 -1.43100000    3.67261100    0.00011400
H                 -5.49825100   -3.37595500    0.00016600
H                 -6.73106900   -1.24342700    0.00015000
H                 -6.73106900    1.24342700    0.00014900
H                 -5.49825100    3.37595500    0.00016500
H                 -3.36415300    4.60896200    0.00018200
H                 -1.23755300    5.83641600    0.00018100
H                  1.22036500    5.84880200    0.00006800
H                  3.37068600    4.61208400   -0.00020400
H                  5.51165700    3.37553500   -0.00034300
H                  6.74228000    1.24228900   -0.00034100
H                  6.74228000   -1.24228900   -0.00034100
H                  5.51165700   -3.37553500   -0.00034200
H                  3.37068600   -4.61208400   -0.00020300
H                  1.22036500   -5.84880200    0.00007000
H                 -1.23755300   -5.83641600    0.00018200
H                 -3.36415300   -4.60896200    0.00018300
N                 -0.70873300    0.00000000   -0.00003500

1 2 1.5 15 1.5 19 1.5
2 3 2.0 55 1.0
3 5 1.5 56 1.0
4 5 1.5 19 1.5 22 1.5
5 6 1.5
6 8 1.5 57 1.0
7 8 1.5 22 1.5 26 1.5
8 9 1.5
9 11 2.0 42 1.0
10 11 1.5 26 1.5 30 1.5
11 43 1.0
12 13 2.0 32 1.5 52 1.0
13 14 1.5 53 1.0
14 15 1.5 17 1.5
15 54 1.0
16 17 1.5 32 1.5 35 1.5
17 18 1.5
```

```
18 19 1.5 21 1.5
19
20 21 1.5 35 1.5 38 1.5
21 58 1.0
22 58 1.0
23 24 1.5 38 1.5 41 1.5
24 25 1.5 58 1.0
25 26 1.5 28 1.5
26
27 28 1.5 41 1.5 46 1.0
28 29 1.5
29 30 2.0 45 1.0
30 44 1.0
31 32 1.5 33 2.0 51 1.0
32
33 34 1.5 50 1.0
34 35 1.5 36 1.5
35
36 37 1.5 49 1.0
37 38 1.5 39 1.5
38
39 40 2.0 48 1.0
40 41 1.5 47 1.0
41
42
43
44
45
46
47
48
49
50
51
52
53
54
55
56
57
58
```

Geometry optimization for periodic system using ASE python package and FHI-aims calculator

```
from ase import Atoms
from ase.io import read, write
from ase.calculators.aims import Aims, AimsCube
from ase.constraints import FixAtoms
from ase.optimize import QuasiNewton

#read geometry
slab = read('geometry.in')

#define calculator
calc=Aims(k_grid='5 5 4',
          xc='pbe',
            vdw_correction_hirshfeld='true',
            spin="none",
            relativistic="atomic_zora scalar",
            sc_iter_limit="300",
            relax_geometry="trm 1E-2",
            use_dipole_correction="true",)

#set the calculator to work on slab
slab.set_calculator(calc)

#define the required output
e_slab=slab.get_potential_energy()
print(e_slab)
```

Frequency calculation for periodic system using ASE package of python and FHI-aims calculator

```
from ase import Atoms
from ase.optimize import BFGS
from ase.calculators.aims import Aims, AimsCube
from ase.vibrations import Vibrations
from ase.io import read,write

structure=read('ts.traj')
calc=Aims(k_grid='5 5 4',
          xc='pbe',
            vdw_correction_hirshfeld='true',
            spin="none",
            relativistic="atomic_zora scalar",
            sc_iter_limit="300",
            compute_forces="true",
            final_forces_cleaned='true',
            use_dipole_correction="true",)

structure.set_calculator(calc)
vib=Vibrations(structure,
indices=[48,49,50,51,52,53,54,55,56,57,58,59,60,61,62,63,64,65
])
vib.run()
vib.summary()
vib.write_jmol()
```

Nudged elastic band method calculation for transition state search for periodic system using ASE package of python and FHI-aims calculator

```
from ase.constraints import FixAtoms
from ase.io import read, write
from ase.calculators.aims import Aims, AimsCube
from ase.neb import NEB
from ase.optimize.fire import FIRE as QuasiNewton

#calculator settings
def calc():
     return Aims(k_grid='5 5 4',
            xc='pbe',
            vdw_correction_hirshfeld='true',
            spin="none",
            relativistic="atomic_zora scalar",
            sc_iter_limit="300",
            compute_forces="true",
            final_forces_cleaned='true',
            use_dipole_correction="true",)

# Read the previous configurations
initial = read('reac.traj')
final = read('prod.traj')

# Make total 7 images including the reactant and product
images = [initial.copy() for i in range(6)] + [final]

#define atoms to freeze
freeze=FixAtoms(indices=[12,36,14,38,18,42,16,40,0,24,2,26,6,3
0,4,28,45,21,47,23,33,9,35,11])

# Make the NEB object, interpolate to guess the intermediate
steps
neb = NEB(images)
neb.interpolate()

#slab.set_constraint(freeze)
for image in images:
     image.set_calculator(calc())
     image.set_constraint(freeze)

# optimize the NEB path:
```

```
minimizer = QuasiNewton(neb, trajectory='neb.traj')
minimizer.run(fmax=0.05)
```

Machine learning based Nudged elastic band method calculation for transition state search for periodic system using ASE package of python and FHI-aims calculator

```
from ase.io import read
from ase.neb import NEB
from ase.optimize import BFGS
from catlearn.optimize.mlneb import MLNEB
from ase.neb import NEBTools
from ase.calculators.aims import Aims, AimsCube

# Read the previous configurations
initial = read('reac.traj')
final = read('prod.traj')
seven=15

#run the neb
neb_catlearn = MLNEB(start=initial,
                     end=final,
                     ase_calc=Aims(k_grid='5 5 4',
                          xc='pbe',
                          vdw_correction_hirshfeld='true',
                          spin="none",
                          relativistic="atomic_zora scalar",
                          sc_iter_limit="300",
                          compute_forces="true",
                          final_forces_cleaned='true',
                          use_dipole_correction="true",),
                     n_images=seven,
                     interpolation='idpp', restart=True)

neb_catlearn.run(fmax=0.05, trajectory='ML-NEB.traj')
```